

Universität Augsburg
Zentrum für elektronische Korrelation
und Magnetismus
Lehrstuhl für Theoretische Physik III



Real-time dynamics of weakly correlated electrons

Dissertation

zur Erlangung des akademischen Grades

Dr. rer. nat.

eingereicht an der

Mathematisch-Naturwissenschaftlich-Technischen Fakultät
der Universität Augsburg

von

Marc Alexander

Augsburg, Juni 2021

Erstprüfer: PD Dr. Marcus Kollar

Zweitprüfer: Prof. Dr. Thilo Kopp

Tag der mündlichen Prüfung: 28.10.2021

Contents

I	Introduction	1
1	Motivation	1
2	Organization of the thesis	2
3	Hubbard model	3
4	Thermalization and prethermal steady states	6
II	Dynamical Friedel oscillations	12
1	Introduction to local quenches	12
	a) Impurity quench Hamiltonian	13
	b) Single-particle observable	14
2	Eigenstates of the Cayley tree	16
	a) Introduction to the Cayley tree	16
	b) Separation of Hilbert space	17
	c) Ansatz for eigenstates	20
	d) Site-resolved initial density	23
3	General lattices	26
	a) Post-quench eigenstates	26
	b) Shell-symmetric states	27
	c) Check for the Bethe lattice	31
	d) Critical impurity strength	32
	e) Evaluation and numerical procedure	35
4	Results for time-dependent quantities	38
	a) Single-particle expectation values	39
	b) Fermi-sea expectation values	43
	c) Wave-front propagation	45
	d) Steady-state Friedel oscillations	48
	e) Regular vs. generalized thermalization	50
5	Summary for local quenches	55
6	Technical Outlook	57
	a) Site-resolved computation	57
	b) From quenched to ramped and driven impurities	60
III	Prethermalization induced by weak interactions	64
1	Introduction to the perturbative expansion	64
2	General expansion in interaction strength	66
	a) Formal time integration	66

CONTENTS

	b)	Construction of constants of motion	72
	c)	Generalized Gibbs ensemble of the prethermal steady state . .	74
3		Interaction quenches, ramps and periodic drives	80
	a)	Effective model and general method	80
	b)	Hubbard model in infinite spatial dimensions	84
	c)	Nonequilibrium crossing points	91
	d)	Relaxation after interaction quenches	97
	e)	Ramps: Crossover from quench to adiabatic regime	101
	f)	Periodically driven system	105
4		Photoinduced prethermalization	113
	a)	Hamiltonian with homogeneous electric field	114
	b)	General method	115
	c)	Electric field pulse on the hypercubic lattice	119
	d)	Hubbard model with infinite spatial dimensions	121
	e)	Numerical results	127
	f)	Expansion in field strength	132
	g)	Linear response	137
	h)	Pump-probe conductivity	145
	i)	Scaled prethermal plateau	150
5		Summary for weakly interacting systems	158
6		Outlook: From prethermalization to thermalization	162
	a)	Derivation of the Boltzmann equation	162
	b)	Local in time formulation	167
IV		Conclusion	169
V		Appendix	173
	1	Evaluation of $a_3(b)$ and $a_4(b)$	173

I Introduction

1 Motivation

This thesis aims to develop a method to treat correlated electron systems close to an integrable point during the prethermalization regime. In particular, we will investigate various nonequilibrium protocols acting upon the weakly interacting Hubbard model. Our method will be based on two fundamental concepts of quantum mechanics. First, physical observables are represented by Hermitian operators, and their expectation values give the mean value of measuring the corresponding quantity in an experiment. Therefore, we aim to compute expectation values instead of other non-measurable quantities, e.g., the wave function. Second, there is an inverse relationship between time t and energy E , $t \sim \frac{\hbar}{E}$ according to the Schrödinger equation and the uncertainty relation. A weakly interacting system exhibit two different energy scales. The first is a “high” energy scale due to the hopping Hamiltonian, and the second is a “low” energy scale induced by the weak interactions. This separation of energy scales leads to a separation of time scales. We call the short time-scale prethermalization regime and the long one thermalization regime. We will expand the expectation values in the integrability-breaking parameter and compute the lowest-order nontrivial contributions. They will relax to a stationary value in the thermodynamic limit. In finite systems, there will be infinitely many recurrences, and no relaxation occurs. The cumulative effect of the integrability-breaking terms generates further relaxation processes. These processes are not captured by our method, and they induce thermalization at later times.¹⁻³

It is well established by now that there is a significant difference between the nonequilibrium dynamics of integrable and nonintegrable quantum systems.⁴ Nonintegrable or generic systems thermalize, meaning that observables relax towards stationary values described by a Gibbs ensemble with an effective temperature determined by the initial state.¹⁻³ The eigenstate thermalization hypothesis (ETH)⁵⁻⁹ tries to explain when and why this phenomenon occurs. On the other hand, integrable systems relax towards a generalized Gibbs ensemble (GGE),¹⁰⁻¹³ which retains an additional amount of information on the initial state. We focus on generic systems, which are close to an integrable point. The high-energy scale then corresponds to an integrable system, and thus we expect relaxation towards a GGE on the prethermalization time scale. At later times the weak interactions induce further dynamics, and thermal expectation values are reached.

Systems of ultracold atoms provide exceptional opportunities to study such nonequi-

I INTRODUCTION

librium problems experimentally because they are in almost perfect isolation from the environment. The primary time scale for the temporal evolution of ultracold atoms is orders of magnitudes slower (≈ 1 ms) than that for correlated electron systems (≈ 1 fs), making it much easier to keep track of the time evolution.¹⁴ Experimental progress in ultracold atom systems^{15–20} allows to measure the relaxation process of nonequilibrium dynamics. Some experimental setups exhibit nonthermal steady states,^{21–23} which were identified as prethermal states.

The generation of prethermal states is a generic feature and occurs in solids as well. However, the time window for observations closes more rapidly than in ultracold atom experiments, making it more challenging to detect the prethermal states. Our method will predict the properties of the prethermal state and the point in time of its creation. The theoretical prediction should act as a guide for experimental setups.

2 Organization of the thesis

We study correlated electrons in solid matter, which we model by interacting fermions in the thermodynamic limit.^{24–27} We compute the quantities of interest for the Hubbard model,^{28–30} which we introduce in section 3. We investigate a particular class of nonequilibrium problems. Initially, the system is in the ground state, and then a small time-dependent perturbation brings the system out of equilibrium, and the observables become time-dependent. Our general method is the expansion in interaction strength g around the integrable point of a noninteracting system. We calculate the first nontrivial contribution as in weak-coupling it dominates during the short time scale.

The quantity of interest is the zeroth, first or second-order term in g depending on the nonequilibrium protocol and observable. The power in g determines the observed features. We always encounter relaxation to a constant value. A prethermal or thermal state captures these constant values. On a larger time scale, the weak interactions lead to thermalization.^{1–3} We shortly explain thermalization induced by quasiparticle scattering in the outlook subsection III.6.a). We introduce the concepts of thermalization and prethermal states governed by a GGE in section 4.

This dissertation has two main chapters. In the first one, we investigate local potential quenches. We start from a translationally invariant state and break its symmetry by quenching an attractive impurity potential on a single site to generate dynamical Friedel oscillations in the site-resolved density of particles. Thus, we have a nontrivial time evolution in $O(g^0)$ and treat the problem as purely noninteracting. As a result,

the observables relax to a state described by a GGE¹⁰⁻¹³ as the system is integrable. Our main result is the distinction between two physically different regimes. In the first one, the GGE becomes the standard Gibbs ensemble, while in the second an additional conserved quantity becomes relevant.

In the second chapter, we study a time-dependent perturbation, which is uniform in space. Due to the symmetry, the purely noninteracting state is not affected, and we compute the first or second correction in g depending on the observable. We group the observables into two categories according to whether the linear term in g vanishes or not. Furthermore, we investigate two different classes of problems. First, we change the interaction strength by different protocols, including quenches, ramps, and periodic driving. The initial state is non- or weakly interacting. Second, an electric field pulse hits the weakly interacting system. Interactions induce nontrivial dynamics, and our method predicts a nonthermal steady state, which we expect to collapse on the thermalization time scale.

3 Hubbard model

In 1963 Gutzwiller,³⁰ Kanamori,²⁹ and Hubbard²⁸ independently proposed the same Hamiltonian \hat{H} . They studied the physics of transition and rare-earth metals with very localized outer electrons in d or f shells.²⁷ Nowadays, it is referred to as the Hubbard model, and it is the sum of two competing terms. The first one is an electronic hopping Hamiltonian and the second is a local interaction term. By studying this idealized model, one can find various interesting universality classes of strongly correlated electron systems.³¹

First, we set up the general electronic Hamilton operator of solid-state physics and gradually approximate it to the Hubbard Hamiltonian. We apply the Born-Oppenheimer approximation,³² which means that the motion of the ions is neglected. Thus, the effective Hamiltonian consists of the electrons' kinetic energy, the electron-ion interaction and

I INTRODUCTION

the electron-electron interaction. The first two parts are captured by a single-particle operator \hat{H}_0 and the electron-electron interaction by a two-particle operator \hat{V} ,

$$\begin{aligned}\hat{H} &= \hat{H}_0 + \hat{V} , \\ \hat{H}_0 &= - \sum_{\sigma=\uparrow\downarrow} \int \hat{\Psi}_\sigma^\dagger(\mathbf{r}) \left(\frac{\hbar^2}{2m} \Delta - V_{\text{ion}}(\mathbf{r}) \right) \hat{\Psi}_\sigma(\mathbf{r}) d\mathbf{r} , \\ \hat{V} &= \sum_{\sigma,\sigma'=\uparrow\downarrow} \iint \hat{\Psi}_\sigma^\dagger(\mathbf{r}) \hat{\Psi}_{\sigma'}^\dagger(\mathbf{r}') \frac{e^2}{8\pi\epsilon_0|\mathbf{r}-\mathbf{r}'|} \hat{\Psi}_{\sigma'}(\mathbf{r}') \hat{\Psi}_\sigma(\mathbf{r}) d\mathbf{r} d\mathbf{r}' .\end{aligned}$$

Our derivation follows mainly the book of Peter Fulde²⁶ and we consider only the nonrelativistic formulation. The field operators obey the anti-commutator relations,

$$\left\{ \hat{\Psi}_\sigma^\dagger(\mathbf{r}), \hat{\Psi}_{\sigma'}(\mathbf{r}') \right\} = \delta_{\sigma\sigma'} \delta(\mathbf{r} - \mathbf{r}') , \quad \left\{ \hat{\Psi}_\sigma(\mathbf{r}), \hat{\Psi}_{\sigma'}(\mathbf{r}') \right\} = \left\{ \hat{\Psi}_\sigma^\dagger(\mathbf{r}), \hat{\Psi}_{\sigma'}^\dagger(\mathbf{r}') \right\} = 0 .$$

Next, we insert orthonormal basis functions $f_i(\mathbf{r})$ to express the Hamiltonian in creation $\hat{c}_{\sigma i}^\dagger$ and annihilation operators $\hat{c}_{\sigma i}$,

$$\begin{aligned}\hat{H}_0 &= - \sum_{i,j} \sum_{\sigma} t_{ij} \hat{c}_{\sigma i}^\dagger \hat{c}_{\sigma j} , \quad t_{ij} = \int f_i^*(\mathbf{r}) \left(\frac{\hbar^2}{2m} \Delta - V_{\text{ion}}(\mathbf{r}) \right) f_j(\mathbf{r}) d\mathbf{r} , \\ \hat{V} &= \sum_{i,j,k,l} \sum_{\sigma,\sigma'} V_{ijkl} \hat{c}_{\sigma i}^\dagger \hat{c}_{\sigma' j}^\dagger \hat{c}_{\sigma' k} \hat{c}_{\sigma l} , \quad V_{ijkl} = \iint \frac{e^2 f_i^*(\mathbf{r}) f_j^*(\mathbf{r}') f_k(\mathbf{r}') f_l(\mathbf{r})}{8\pi\epsilon_0|\mathbf{r}-\mathbf{r}'|} d\mathbf{r} d\mathbf{r}' .\end{aligned}$$

The transformation and anti-commutator relations are

$$\begin{aligned}\hat{\Psi}_\sigma(\mathbf{r}) &= \sum_i f_i(\mathbf{r}) \hat{c}_{\sigma i} , \quad \hat{c}_{\sigma i} = \int f_i^*(\mathbf{r}) \hat{\Psi}_\sigma(\mathbf{r}) d\mathbf{r} , \\ \left\{ \hat{c}_{\sigma i}^\dagger, \hat{c}_{\sigma' j} \right\} &= \delta_{\sigma\sigma'} \delta_{ij} \quad \text{and} \quad \left\{ \hat{c}_{\sigma i}^\dagger, \hat{c}_{\sigma' j}^\dagger \right\} = \left\{ \hat{c}_{\sigma i}, \hat{c}_{\sigma' j} \right\} = 0 .\end{aligned}$$

It is common practice to choose an approximate reduced basis to make the problem feasible. Therefore, the quality of this description depends on the functional form of $f_i(\mathbf{r})$ as well as on their number.²⁶

The idea of the Hubbard model is to neglect all the parameters V_{ijkl} except for the ones with the highest magnitude. We assume localized functions $f_i(\mathbf{r})$, which implies that $|f_i(\mathbf{r})|^2$ decays fast with $|\mathbf{r} - \mathbf{r}_i|$ compared to the lattice constant. Then, naturally $V_{iiii} \equiv U_i$ has the highest magnitude. The potential energy \hat{V} simplifies to

$$\hat{V} = \sum_{i,j,k,l} \sum_{\sigma,\sigma'} U_i \delta_{i,l} \delta_{j,k} \delta_{i,j} \hat{c}_{\sigma i}^\dagger \hat{c}_{\sigma' j}^\dagger \hat{c}_{\sigma' k} \hat{c}_{\sigma l} = \sum_i U_i \hat{c}_{i\uparrow}^\dagger \hat{c}_{i\uparrow} \hat{c}_{i\downarrow}^\dagger \hat{c}_{i\downarrow} = \sum_i U_i \hat{n}_{i\uparrow} \hat{n}_{i\downarrow} .$$

If the lattice is translational invariant, then U_i becomes independent of the lattice site ($U_i \equiv U$) and the kinetic energy can be diagonalized by Fourier transformation,

$$\hat{c}_{\sigma\mathbf{k}} = \frac{1}{\sqrt{L}} \sum_j e^{i\mathbf{k}\cdot\mathbf{r}_j} \hat{c}_{\sigma j}, \quad t_{ij} \longrightarrow t_{i-j}, \quad \epsilon_{\mathbf{k}} = - \sum_{\delta} t_{\delta} e^{-i\mathbf{k}\cdot\mathbf{r}_{\delta}}.$$

The single-band Hubbard Hamiltonian for the translational invariant case is

$$\hat{H} = \sum_{\mathbf{k}} \sum_{\sigma=\uparrow\downarrow} \epsilon_{\mathbf{k}} \hat{c}_{\sigma\mathbf{k}}^{\dagger} \hat{c}_{\sigma\mathbf{k}} + U \sum_i \hat{n}_{\uparrow i} \hat{n}_{\downarrow i}. \quad (\text{I.1})$$

In reciprocal space, the double occupation can be reformulated,

$$\begin{aligned} \hat{D} &= \sum_i \hat{n}_{\uparrow i} \hat{n}_{\downarrow i} = \frac{1}{L} \sum_{\mathbf{k}_1, \mathbf{k}_2, \mathbf{k}_3, \mathbf{k}_4} \Delta_{\mathbf{k}_1 + \mathbf{k}_2 - \mathbf{k}_3 - \mathbf{k}_4} \hat{c}_{\sigma\mathbf{k}_1}^{\dagger} \hat{c}_{\bar{\sigma}\mathbf{k}_2}^{\dagger} \hat{c}_{\bar{\sigma}\mathbf{k}_3} \hat{c}_{\sigma\mathbf{k}_4}, \\ \Delta_{\mathbf{k}} &= \frac{1}{L} \sum_i e^{-i\mathbf{k}\cdot\mathbf{R}_i} = \sum_{\mathbf{G}} \delta_{\mathbf{k}\mathbf{G}}. \end{aligned}$$

In the remainder of this thesis, we mainly use the tight-binding Hamiltonian for the kinetic energy part. In the tight-binding approximation, electrons hop only from one site to the nearest neighboring site. Thus, the hopping amplitudes t_{ij} for nearest neighbors are finite, and the others vanish. This is reasonable in the case of localized wave functions as the nearest neighbor amplitudes have the highest magnitude of all t_{ij} . The on-site terms t_{ii} act as an energy offset, and therefore we may neglect them. For example, the dispersion relation $\epsilon_{\mathbf{k}}$ on the d -dimensional hyper-cubic lattice is

$$\epsilon_{\mathbf{k}} = -2t \sum_{n=1}^d \cos(k_n).$$

The main advantage of the tight-binding model with Hubbard interaction is that it has only two parameters, t and U .

In the textbook of Ashcroft and Mermin,³² the Hubbard model is described as “a highly oversimplified model” for strongly interacting electrons in a solid.³¹ Nevertheless, the Hubbard model is one of the most important models in theoretical condensed-matter physics. Despite its simple formulation, the Hubbard model is believed to exhibit various characteristic phenomena, including metal-insulator transitions, antiferromagnetism, ferrimagnetism, ferromagnetism, Landau-Fermi liquid and Tomonaga-Luttinger liquid behavior, and superconductivity.³¹ Exact solutions for all interaction strengths can

I INTRODUCTION

be obtained for the Hubbard model in one dimension.³³ The model can describe the Mott–Hubbard transition between an insulating and a metallic phase in infinite dimensions at half-filling.³³ On the one hand, one cannot expect that the Hubbard model itself properly describes an experimental situation in detail, further it is usually necessary to extend it properly. On the other hand, the model already contains the necessary terms to describe the basic properties of correlated electron systems.³³

4 Thermalization and prethermal steady states

Steady state

The concept of a steady state is intuitively clear in classical mechanics. If all masses do not move anymore, then the state is stationary. Hence, it corresponds to all observables being constant in time. In quantum mechanics, a system is regarded as steady if all expectation values of physical observables are constant in time. This is true if the quantum-mechanical wave function $|\Psi(t)\rangle$ is an eigenstate of the Hamiltonian,

$$\hat{H}|\Psi(t)\rangle = E|\Psi(t)\rangle .$$

We note that all observables are constant in time for an eigenstate, but not the wave function itself. According to the Schrödinger equation,

$$i\hbar\frac{\partial}{\partial t}|\Psi(t)\rangle = \hat{H}_t|\Psi(t)\rangle ,$$

the wave function still has a time-dependent complex phase. Hence, the wave function is not constant in time even if it is an eigenstate. We compute time-dependent expectation values and not wave functions. When we encounter representative observables, which become constant in time, we say that the system has reached a steady state. More complicated observables may not relax in this manner, so that is not a strict definition.

A classical analog to this situation is the dynamic of a fluid, for which the surface is an important observable. If the surface does not move, we speak of a steady state. The more complicated observables are the dynamics of water molecules, which are still moving, e.g., due to Brownian motion.

If a quantum-mechanical state relaxes to a steady state, it is described by the so-called diagonal ensemble.^{8,34–36} We recap its derivation for a quench from \hat{H}_0 to \hat{H} . Every eigenstate $|\alpha\rangle$ of the final Hamiltonian \hat{H} shall be described by its eigenenergy E and an additional quantum number λ . Usually, it is assumed that the spectrum of \hat{H} is

nondegenerate and incommensurate.^{35,36} We prefer to use the assumption by Kennes et al.³⁷ that \hat{H}_0 and \hat{H} share the same set of additional quantum numbers λ , i.e., the same related symmetries. Due to this assumption, the pre- and post-quench Hamiltonians share the quantum numbers λ , and we will use

$$\langle E', \lambda' | \Psi_0 \rangle \langle \Psi_0 | E, \lambda \rangle = \delta_{\lambda, \lambda'} \langle E', \lambda | \Psi_0 \rangle \langle \Psi_0 | E, \lambda \rangle . \quad (\text{I.2})$$

If it exists, the steady-state expectation value must be equal to the long-time average,

$$\begin{aligned} \overline{\langle \hat{O} \rangle} &\equiv \lim_{t \rightarrow \infty} \frac{1}{t} \int_0^t d\tau \langle \hat{O} \rangle_\tau \\ &= \sum_{E, E'} \sum_{\lambda, \lambda'} \langle \Psi_0 | E, \lambda \rangle \langle E, \lambda | \hat{O} | E', \lambda' \rangle \langle E', \lambda' | \Psi_0 \rangle \lim_{t \rightarrow \infty} \frac{1}{t} \int_0^t d\tau e^{i\tau(E-E')} \\ &\stackrel{(\text{I.2})}{=} \sum_{E, \lambda} |\langle \Psi_0 | E, \lambda \rangle|^2 \langle E, \lambda | \hat{O} | E, \lambda \rangle \\ &= \text{Tr} \left\{ \hat{\rho}_{\text{DE}} \hat{O} \right\} \equiv \langle \hat{O} \rangle_{\text{DE}} , \\ \hat{\rho}_{\text{DE}} &= \sum_{\alpha} |\alpha \rangle \langle \alpha | \hat{O} | \alpha \rangle \langle \alpha | . \end{aligned} \quad (\text{I.3})$$

Eigenstate thermalization hypothesis

A pure isolated state under unitary time evolution remains a pure state. However, the diagonal ensemble does not resemble a pure state, but not the thermal state either. The density matrix can only become thermal if the system has contact with a thermal bath. Nevertheless, it was observed that expectation values relax to their corresponding thermal values.¹⁻³ The eigenstate thermalization hypothesis (ETH)⁵⁻⁹ explains why a system can “thermalize” in this sense, as we now discuss.

A system thermalizes if the expectation values under investigation relax to their thermal values. The choice of proper observables is important as thermalization varies with the observables under investigation. E.g. it is expected that “local” observables thermalize faster than “global” observables. In subsection III.2.b), we formally construct constants of motion, which cannot relax and therefore are not expected to thermalize. The techni-

I INTRODUCTION

cal statement of ETH is that the diagonal ensemble and the microcanonical ensemble result in the same expectation values for certain cases,

$$\langle \hat{O} \rangle_{\text{DE}} = \langle \hat{O} \rangle_{\text{microcan.}}(E_0) \equiv \frac{1}{Z_{E_0, \Delta E}} \sum_{\substack{\alpha \\ |E_0 - E_\alpha| < \Delta E}} \langle \alpha | \hat{O} | \alpha \rangle, \quad (\text{I.4})$$

$$Z_{E_0, \Delta E} = \sum_{\substack{\alpha \\ |E_0 - E_\alpha| < \Delta E}} 1.$$

According to Rigol et al.⁸, there are three scenarios in which the ETH is applicable. First, the eigenstate expectation values $\langle \alpha | \hat{O} | \alpha \rangle$ do not fluctuate between eigenstates that are close in energy. In this case, equation (I.4) holds without exception for all initial states that are narrow in energy. Second, for physically interesting initial conditions, the eigenstate occupation numbers $|\langle \Psi_0 | \alpha \rangle|^2$ are equal for eigenstates that are close in energy. Therefore, equation (I.4) immediately follows. Third, for eigenstates close in energy, there are large eigenstate-to-eigenstate fluctuations of both $\langle \alpha | \hat{O} | \alpha \rangle$ and $|\langle \Psi_0 | \alpha \rangle|^2$. However, for physically interesting initial conditions, the fluctuations in the two quantities are uncorrelated, and a given initial state then performs an unbiased sampling from the distribution of $\langle \alpha | \hat{O} | \alpha \rangle$, resulting in equation (I.4).

Integrable models have an extensive set of constants of motion, which are conserved after a quench. This leads to correlation within the $\langle \alpha | \hat{O} | \alpha \rangle$ and $|\langle \Psi_0 | \alpha \rangle|^2$. Thus, the ETH is violated, and the long-time limit is a nonthermal value. Nevertheless, it may be captured by a statistical ensemble. The statistical ensemble is constructed as the thermal ensemble of a reduced Hilbert space. The Hilbert space is reduced to states with identical sets of constants of motion as the initial state. The ensemble is termed generalized Gibbs ensemble (GGE).^{10–13} This “generalized” thermalization has been observed in quenches of integrable models.³⁸ There is progress towards a unified treatment of the ETH in integrable and generic quantum systems.³⁹

Prethermalization

The expression prethermalization is used when observables relax on an intermediate time scale to a nonthermal value. It is believed that real systems are always nonintegrable and eventually thermalize. If approximations lead to an integrable model, then these approximations are only valid on a certain time scale. The relaxation to the GGE is then an intermediate step. However, the neglected integrability-breaking terms will then accumulate, and the expectation values may thus thermalize at a later stage. Thus, the GGE describes a state stable on the model time scale but breaks down on a larger time

scale. Therefore, the GGE state may be regarded as a prethermal state.

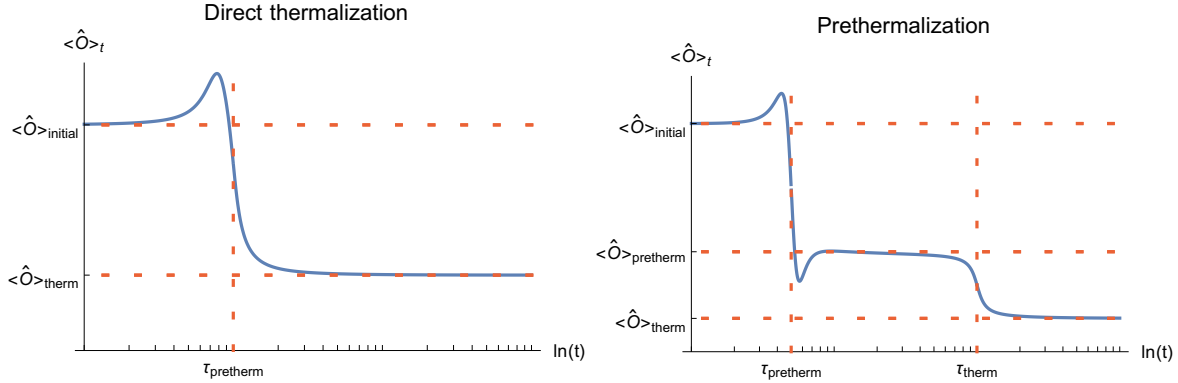


Figure 1: Schematic plot for direct thermalization (left) and prethermalization (right)

In figure 1, we depict the dynamics of direct thermalization and prethermalization schematically. The time axis in both plots is logarithmic to emphasize the separation of time scales.⁴⁰ In the left-hand plot, the observable relaxes during a single time scale and stays constant after reaching its thermal value. In the right-hand plot, the transient splits into two regimes. During the earlier times up to τ_{pretherm} relaxation to a nonthermal value occurs. On the much larger time scale τ_{therm} , slower processes lead to thermalization. During intermediate times τ with $\tau_{\text{pretherm}} \ll \tau \ll \tau_{\text{therm}}$ the system exhibits a plateau, which is the characteristic feature of a prethermal steady state.

The main prerequisite for prethermalization is this separation of time scales. The separation of time scales is a general phenomenon in many different systems and theories.⁴¹ We will investigate systems close to an integrable point. Therefore, we have an intrinsic separation of time scales. Our τ_{pretherm} will be given by the electron hopping between the crystal lattice sites.⁴² The τ_{therm} includes inverse orders of the weak integrability breaking parameter g .

Our method will be nonperturbative in the fast process and perturbatively in the slow processes. Thus, it will capture the time scale τ_{pretherm} , but it has no access to the time scale τ_{therm} . Consequently, our method will compute transient from the initial value $\langle \hat{O} \rangle_{\text{initial}}$ to the prethermal plateau value $\langle \hat{O} \rangle_{\text{pretherm}}$. We will encounter both cases of direct thermalization and prethermalization in this dissertation. In chapter II, the strength of the perturbation determines whether the local density relaxes to a thermal or a prethermal expectation value. In chapter III, the observable under investigation

I INTRODUCTION

determines the two cases. The occupation numbers relax to prethermal values. On the other hand, the kinetic energy, double occupation, and current relax to their thermal values.

Time scales after a pump pulse

Pump-probe spectroscopy has enabled the study of excitation and relaxation processes in correlated electron systems. Aoki et al.¹⁴ explain the dynamics after a pump pulse in three general phases. Their schematics are displayed in figure 2. First, photoirradiation excites the system. This is captured by Fermi's golden rule (linear-response theory) for weak pumps or the Schwinger mechanism (Landau-Zener tunneling) for strong fields. The system may also reach a nonequilibrium time-periodic steady state during the laser application, a so-called Floquet state.⁴³ The effective Floquet Hamiltonian can drastically differ from the original one. It is possible to generate a negative temperature ensemble⁴⁴ during the excitation phase.

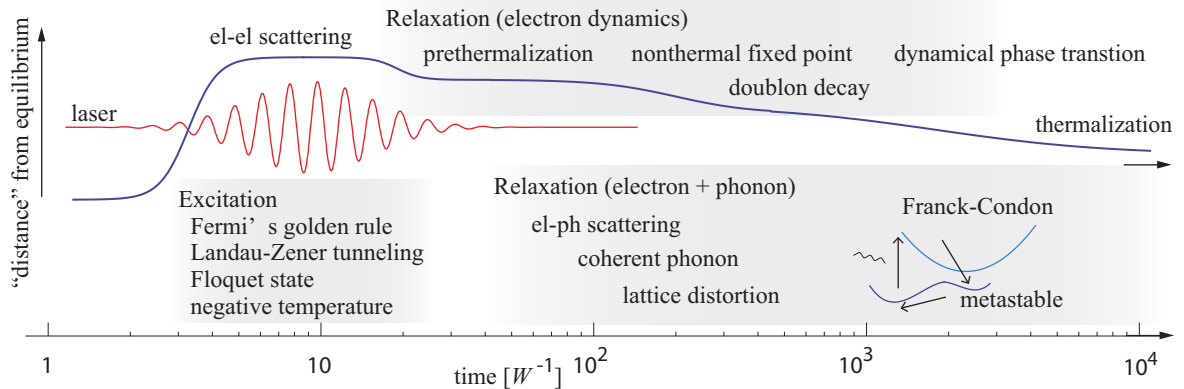


Figure 2: Schematic time evolution of a system in a pump-probe experiment. From reference¹⁴

Second, relaxation due to electron dynamics sets in. The early stages of electron-electron scattering are very distinct from the late time scattering for weakly interacting systems. We investigate the early stages in section III.4, which lead to a prethermal state for intermediate times. Later on, electron-electron scattering is governed by the Boltzmann equation,^{45–47} which leads to a thermal distribution as we will discuss in subsection III.6.a). The dynamic can passage nonthermal fixed points.⁴⁸ One might first expect that strong interactions give rise to fast interparticle scattering, which would restore equilibrium quickly. However, doublons and holes are created during the first stage in

Mott insulators, and these annihilate in pairs. The relaxation time of doublons in a gapped system can be orders of magnitude longer than the intrinsic time.⁴⁹ Certain nonequilibrium models exhibit a critical perturbation strength. If the excitations exceed that, then the dynamical features change spontaneously. This phenomenon is coined dynamical phase transition⁵⁰ as it resembles certain aspects of equilibrium phase transitions.

At a certain point, the relaxation process enters the third phase, and the electronic system couples to classical degrees of freedom. Usually, these are lattice distortions. The corresponding electron-phonon processes can be understood within the Franck-Condon picture.⁵¹ The electronic system is often close to a thermal ensemble but with a higher temperature than the lattice. During this final phase, lattice and electronic systems relax to thermal states with a common temperature. This final stage can exhibit macroscopic spatially dynamical features such as coherent phonons.⁵²

II Dynamical Friedel oscillations

1 Introduction to local quenches

This chapter addresses nonequilibrium dynamics after an impurity quench, i.e. the sudden potential change at a single lattice site. An impurity induces density modulations, which are peaked at the impurity site in equilibrium. This phenomenon is called Friedel oscillations after Jacques Friedel.⁵³ We expect the dynamical creation of similar density modulations in nonequilibrium. By comparing the equilibrium with the nonequilibrium situation, we extract the general features of this phenomenon. We encounter a nontrivial time evolution already for the noninteracting system. Thus, we only investigate a noninteracting, integrable model as interactions would only come into play at later time scales.

Similar quenches have recently been investigated in a series of publications by J. M. Zhang et al.^{54–56} They study the real-time behavior after an impurity quench in a one-dimensional tight-binding chain. Their numerical and analytic investigation shows cusps⁵⁶ and plateaus⁵⁵ in the dynamics of single-particle states, and the Fermi sea generates dynamic Friedel oscillations.⁵⁴ For a noninteracting system with impurity potential, the single-particle eigenstates were found to determine its nonequilibrium behavior.

We intend to generalize the impurity quench problem to a higher-dimensional setting. Our first choice fell on the Bethe lattice and Cayley tree because its symmetry enables us to solve this problem analytically. The infinite Bethe lattice is also important for fermions in high dimensions and dynamical mean-field theory.^{57–59} We find that the Hilbert space separates into states, which are either affected or not affected by the impurity. Consequently, we have to solve an effectively one-dimensional problem. Furthermore, the exact eigenstates for arbitrary lattices in the thermodynamic limit are known^{60,61} from the Lippmann-Schwinger equation. With all eigenstates at hand, we evaluate the impurity problem also on the square and the simple-cubic lattice.

First, we present shortly our noninteracting quench Hamiltonian and its initial ground state. Second, we explain how to compute the local density from the single particle states. Third, we introduce the Cayley tree and its limit, the Bethe lattice.⁶² After that, we explain how the symmetry of the Hamiltonian separates the Hilbert space into closed subspaces. By applying the Hamiltonian to any state of one subspace, the new states remains in the same subspace. Hence, our problem decomposes into separate lower-dimensional problems. Next, we apply an ansatz to generate all eigenstates of each

subspace. We focus on the shell-symmetric states as we can deduce all other eigenstates from them. If the impurity strength is larger than a critical value, a localized state emerges. For weaker impurities, all eigenstates are extended states.

In the second part, we introduce the Lippmann-Schwinger equation and deduce the single-particle eigenstates with impurity. If the local Green function is accessible, we can compute the eigenstates for an arbitrary lattice. The local Green function determines the emergence of the localized state. After checking this ansatz for the Bethe lattice, we evaluate the dynamics for the Bethe, the square, and the simple-cubic lattice.

In the third part, we show real-time dynamics results. We begin with the short-time dynamic of the single-particle states. We observe two qualitatively different regimes depending on the existence of the localized eigenstate. Next, the dynamics for the Fermi sea exhibit dynamical Friedel oscillation, which spread out with a fixed velocity. We will encounter our main result, when we compute the long-time limit. It relaxes to two physically different regimes: If no localized eigenstate exists, our observables relax to their thermal values. By contrast, if a localized state emerges, then the observable does not thermalize, and a GGE describes the long-time limit.

a) Impurity quench Hamiltonian

Now, we define the impurity quench Hamiltonian for our scenario,

$$\hat{H}_t = \begin{cases} \hat{H}_0 & \text{for } t < 0 \\ \hat{H}_0 + \hat{V} & \text{for } t \geq 0 \end{cases} .$$

The unperturbed, translationally invariant hopping Hamiltonian is the same as for the Hubbard Hamiltonian (I.1),

$$\hat{H}_0 = \sum_{\mathbf{k}} \epsilon_{\mathbf{k}} \hat{n}_{\mathbf{k}} .$$

In this chapter, we drop the spin index σ as the two spin species are uncorrelated. The second term in the quench Hamiltonian is the impurity operator, which acts on a site with index 0,

$$\hat{V} = V \hat{n}_0 .$$

For negative times, we have a translationally invariant system, hence the Bloch theorem gives us all single-particle $|\Phi_{\mathbf{k}}\rangle$ and N -particle $|\Phi_{\mathbf{k}_1 \dots \mathbf{k}_N}\rangle$ eigenstates,

$$|\Phi_{\mathbf{k}}\rangle = \hat{c}_{\mathbf{k}}^\dagger |\text{VAC}\rangle , \quad |\Phi_{\mathbf{k}_1 \dots \mathbf{k}_N}\rangle = \hat{c}_{\mathbf{k}_N}^\dagger \dots \hat{c}_{\mathbf{k}_1}^\dagger |\text{VAC}\rangle \quad \text{with} \quad \hat{c}_{\mathbf{k}}^\dagger = \sum_j e^{i\mathbf{k} \cdot \mathbf{R}_j} \hat{c}_j^\dagger .$$

II DYNAMICAL FRIEDEL OSCILLATIONS

Initially, our system shall start in the Fermi sea

$$|\text{FS}\rangle = \prod_{\epsilon_k < \epsilon_F} \hat{c}_k^\dagger |\text{VAC}\rangle .$$

There, every single-particle state below the Fermi energy ϵ_F is occupied. We choose to quench at time $t = 0$ as this simplifies the formalism. The initial state is an eigenstate of the prequench Hamiltonian. Therefore, the time evolution is trivial before the quench. After the quench, the propagator has the explicit form $e^{-it\hat{H}_t}$ as the Hamiltonian is constant. Here, we only consider a sudden quench. One can view more general switching protocols as preparing a time-evolved state, which relaxes at the end of the protocol. However, we focus on the translationally invariant ground state of the hopping Hamiltonian as the initial state.

b) Single-particle observable

A the main time-dependent observable we consider the site-resolved density

$$\langle \hat{n}_r \rangle_t = \langle \text{FS} | e^{it\hat{H}_t} \hat{n}_r e^{-it\hat{H}_t} | \text{FS} \rangle .$$

The Fermi sea is an eigenstate for negative times, and this density is then trivially constant. However, after the quench, the Hamiltonian is inhomogeneous, and the translationally invariant Fermi sea is no longer an eigenstate. Thus, the observables become time-dependent, and also site-dependent.

In general, our problem is the computation of a single-particle operator time evolved by a single-particle Hamiltonian. We deduce that our Heisenberg operator $e^{it\hat{H}_t} \hat{n}_r e^{-it\hat{H}_t}$ is also effectively a single-particle operator, due to two of its properties. The first is that the commutator of two single-particle operators remains a single-particle operator,

$$\left[\sum_{n,m} a_{nm} \hat{c}_n^\dagger \hat{c}_m, \sum_{p,q} b_{pq} \hat{c}_p^\dagger \hat{c}_q \right] = \sum_{n,m} \sum_p (a_{np} b_{pm} - b_{np} a_{pm}) \hat{c}_n^\dagger \hat{c}_m .$$

The second is that the exponential functions can be expressed as the commutator series

$$e^{it\hat{A}} \hat{B} e^{-it\hat{A}} = \sum_{l=0}^{\infty} \frac{(it)^l}{l!} \underbrace{[\hat{A}, \dots [\hat{A}, \hat{B}] \dots]}_{l \text{ times}} .$$

Then, the Heisenberg operator is a single-particle operator, and its most convenient form is

$$e^{it\hat{H}_t} \hat{n}_r e^{-it\hat{H}_t} = \sum_{\mathbf{k}_1, \mathbf{k}_2} \hat{c}_{\mathbf{k}_1}^\dagger \hat{c}_{\mathbf{k}_2} \langle \Phi_{\mathbf{k}_1} | e^{it\hat{H}_t} \hat{n}_r e^{-it\hat{H}_t} | \Phi_{\mathbf{k}_2} \rangle .$$

Here $|\Phi_{\mathbf{k}}\rangle$ is a single particle state with one particle with momentum \mathbf{k} . Applying the Fermi sea from both sides gives

$$\langle \hat{n}_r \rangle_t = \sum_{\epsilon_{\mathbf{k}} < \epsilon_F} \langle \Phi_{\mathbf{k}} | e^{it\hat{H}_t} \hat{n}_r e^{-it\hat{H}_t} | \Phi_{\mathbf{k}} \rangle = \sum_{\epsilon_{\mathbf{k}} < \epsilon_F} \left| \langle r | e^{-it\hat{H}_t} | \Phi_{\mathbf{k}} \rangle \right|^2. \quad (\text{II.1})$$

In order to evaluate our observable $\langle \hat{n}_r \rangle_t$, thus, it is sufficient to compute the overlap of the time-evolved single-particle states $e^{-it\hat{H}_t} |\Phi_{\mathbf{k}}\rangle$ with the local single-particle states $|r\rangle$.

2 Eigenstates of the Cayley tree

a) Introduction to the Cayley tree

We begin with the Cayley tree, which consist of a central site that is connected to Z other sites. These are the sites of the first ring. Each of these sites is further connected to Z sites. This generates a new ring with $(Z - 1)$ new sites per site in the previous ring. This generation of rings is iterated until the number of shells R is reached. All sites in ring R are connected only to the sites of the previous ring, and all other sites have Z connections. This gives a tree structure with N_r sites in ring r ,

$$N_0 = 1 , \quad N_r = ZK^{r-1} \quad (r \geq 1) \quad \text{with} \quad K = Z - 1 .$$

An example with coordination number $Z = 3$ and number of shells $R = 3$ is depicted in figure 3. We label each site of the Cayley tree with two integers, the first is the shell

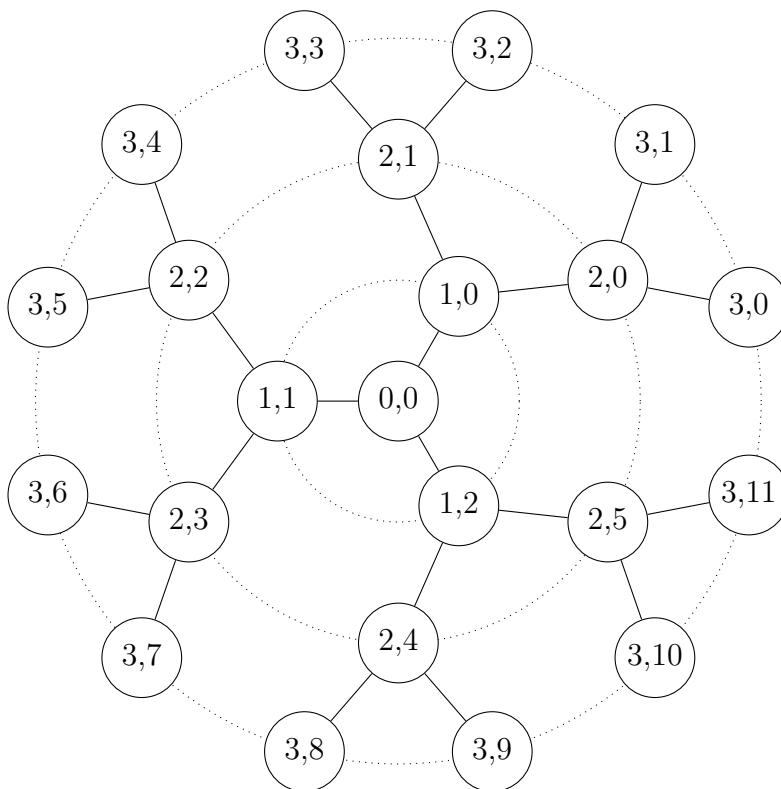


Figure 3: Cayley tree with $Z = 3$ and $R = 3$

2 EIGENSTATES OF THE CAYLEY TREE

number, and the second enumerates the sites in each shell. Hence, every site has a unique pair of numbers, and the state of a single occupied site is $|r, l\rangle$ with

$$0 \leq r \leq R, \quad 0 \leq l \leq N_r - 1.$$

In the limit of infinite shells, the Cayley tree is called Bethe lattice because then the approximation used by Bethe⁶² becomes exact. We use the tight-binding Hamiltonian and particles hop along the connections of the Cayley tree,

$$\hat{H}_0 = \frac{-1}{\sqrt{K}} \sum_{\langle(r,l),(r',l')\rangle} \hat{c}_{r,l}^\dagger \hat{c}_{r',l'}. \quad (\text{II.2})$$

The scaling of the hopping with $1/\sqrt{K}$ is necessary to get a nontrivial result in the limit $Z \rightarrow \infty$. For convenience, the scaled hopping amplitude is set to -1 . We position the impurity at the central site

$$\hat{V} = V \hat{c}_{0,0}^\dagger \hat{c}_{0,0}.$$

This impurity problem has an advantageous symmetry, which we exploit in the following section to separate the Hilbert space into closed subspaces. This means that by applying the Hamiltonian repeatedly, only states of the same subspace are generated. Hence, our higher-dimensional problem separates into several feasible lower-dimensional problems.

b) Separation of Hilbert space

We have a particular symmetry due to the role of the central site. Each site in a ring is equivalent to the others. Thus, applying the Hamiltonian to any shell-symmetric state generates only other shell-symmetric states.⁶³ Consequently, they form a closed subspace of the Hilbert space. We call the remaining states non-shell-symmetric states. The non-shell-symmetric states also form several enclosed subspaces with respect to the Hamiltonian.

Now, we explain how to find the closed subspaces. All sites of one ring are equally occupied in the shell-symmetric basis states.⁶³ We define them as

$$|r\rangle = |r_{000}\rangle = \frac{1}{\sqrt{N_r}} \sum_{l=0}^{N_r-1} |r, l\rangle. \quad (\text{II.3})$$

The first two indices in equation (II.3) refer to the original generating state, which is the central site $|0, 0\rangle$. The last index 0 indicates that no complex phase is added (compare

II DYNAMICAL FRIEDEL OSCILLATIONS

$|r_{n,l,k}\rangle$ below). using this basis, we can represent the Hamiltonian in a $(R+1) \times (R+1)$ matrix,

$$-\langle r|\hat{H}|r'\rangle \rightarrow \begin{pmatrix} -V & \sqrt{Z/K} & 0 & 0 & \cdots & 0 \\ \sqrt{Z/K} & 0 & 1 & 0 & & 0 \\ 0 & 1 & 0 & 1 & & \\ \vdots & & & & \ddots & \\ 0 & & & & 1 & 0 & 1 \\ 0 & & & & 0 & 1 & 0 \end{pmatrix}. \quad (\text{II.4})$$

We construct the eigenstates of matrix (II.4) in subsection c). Due to the symmetry of our nonequilibrium problem, the change in the local density is not affected by the non-shell-symmetric states and $\Delta\langle\hat{n}_{r,l}\rangle_t$ is completely captured by the change in the shell-symmetric basis states,

$$\Delta\langle\hat{n}_{r,l}\rangle_t = \frac{\Delta\langle\hat{n}_r\rangle_t}{N_r}. \quad (\text{II.5})$$

Next, we define auxiliary non-shell-symmetric states around the central site,

$$|0,0,k\rangle = \frac{1}{\sqrt{Z}} \sum_{m=0}^K e^{\frac{i2\pi km}{Z}} |1,m\rangle$$

with $1 \leq k \leq K$, and around other sites $|n,l\rangle$,

$$|n,l,k\rangle = \frac{1}{\sqrt{K}} \sum_{m=0}^{Z-2} e^{\frac{i2\pi km}{K}} |n+1,lK+m\rangle$$

with $1 \leq k \leq Z-2$, $1 \leq n \leq R-1$ and $0 \leq l \leq N_n-1$. Two effects determines the complex phases in these auxiliary states. First, when we apply an isotropic hopping Hamiltonian, contributions towards the center cancel each other. Thus, only hopping away from the center survives. Second, two auxiliary states around the same site with different k are orthogonal to each other. It is straightforward to see that applying the Hamiltonian repeatedly on an auxiliary state $|n,l,k\rangle$ generates $R-r$ states, which form a new closed subspace of the Hilbert space. These states live in the region between site $|n,l\rangle$ and the rim. Next, we choose the basis of these subspaces analogously to (II.3). Each basis state occupies only sites in one ring. The basis states are

$$\begin{aligned} |r_{00k}\rangle &= \sum_{m=0}^K \frac{e^{\frac{i2\pi km}{Z}}}{\sqrt{ZK^r}} \sum_{p=0}^{K^r-1} |1+r,mK^r+p\rangle, \\ |r_{nlk}\rangle &= \sum_{m=0}^{Z-2} \frac{e^{\frac{i2\pi km}{K}}}{\sqrt{K^{r+1}}} \sum_{p=0}^{K^r-1} |n+1+r,lK+mK^r+p\rangle. \end{aligned}$$

2 EIGENSTATES OF THE CAYLEY TREE

Now, we can represent the Hamiltonian by the $(R - n) \times (R - n)$ matrix

$$-\langle r_{nlk} | \hat{H} | r'_{nlk} \rangle \rightarrow \begin{pmatrix} 0 & 1 & 0 & \cdots & 0 \\ 1 & 0 & 1 & & 0 \\ \vdots & & \ddots & & \\ 0 & 1 & 0 & 1 & \\ 0 & 0 & 1 & 0 & \end{pmatrix}.$$

This matrix is equal to the matrix (II.4) if we set $V = 0$, $Z \rightarrow \infty$ and reduce the matrix size. Therefore, it is sufficient to focus on constructing the shell-symmetric eigenstates, and the non-shell-symmetric eigenstates follow directly. We emphasize that for any isotropic hopping Hamiltonian, this basis separates the Hilbert space into distinct subspaces. Only the matrix representation of the Hamiltonian changes accordingly. Additional impurities or anisotropic hopping will break the symmetry, and the Hilbert space would not separate necessarily. Our choice of the non-shell-symmetric basis states is not unique, and there exist different basis states with the same attributes. This is caused by the high degeneracy of the non-shell-symmetric eigenstates. Our new basis states are by construction orthonormal,

$$\langle r_{nlk} | r'_{n'l'k'} \rangle = \delta_{r,r'} \delta_{n,n'} \delta_{l,l'} \delta_{k,k'}.$$

Next, we count the basis states to show their completeness. The sum over the number

aux. state	$ 0, 0\rangle$	$ 0, 0, k\rangle$	$ n, l, k\rangle$
number of aux. states	1	K	$(Z - 2) \sum_{r=1}^{R-1} N_r$
number of states $ r\rangle_{nlk}$	$R + 1$	R	$R - r$

Table 1: Counting of orthonormal shell and non-shell-symmetric states

of new basis states from table 1 is equal to the number of sites in the Cayley tree,

$$1(R + 1) + KR + (Z - 2) \sum_{r=1}^{R-1} N_r (R - r) = \frac{ZK^R - 2}{Z - 2} = \sum_{r=0}^R N_r.$$

Hence, our basis is a complete single-particle basis, and we can fully represent the Hamiltonian in it. Our analysis is in agreement with previous work.⁶⁴⁻⁶⁷

II DYNAMICAL FRIEDEL OSCILLATIONS

c) Ansatz for eigenstates

Here, we solve the stationary Schrödinger equation

$$\hat{H}|\psi(z)\rangle = E|\psi(z)\rangle .$$

We generalize the ansatz used by Mahan⁶³ and van den Berg⁶⁸ for the shell-symmetric states and construct the eigenstates of matrix (II.4) with the general vector form

$$|\psi(z)\rangle = (f_0, f_1, \dots, f_R) .$$

First, we satisfy the periodic equations,

$$f_r E = f_{r-1} + f_{r+1} \quad \text{for } 2 \leq r \leq R-1 ,$$

by the ansatz,

$$f_r = z^r - \frac{y_V(z)}{z^r} \quad \text{for } 1 \leq r \leq R .$$

The energy is computed as

$$E = - \left(z + \frac{1}{z} \right) .$$

The first two equations fix $f_0 = \sqrt{K/Z}(1 - y_V(z))$ and

$$y_V(z) = \frac{\frac{z^2}{K} - Vz - 1}{\frac{1}{K} - Vz - z^2} .$$

The last equation gives $y_V(z) = z^{2(R+1)}$ and thus z has to satisfy the equation,

$$\left(z + \frac{1}{z} + V \right) \left(z^{R+1} - \frac{1}{z^{R+1}} \right) = \frac{Z}{K} \left(z^R - \frac{1}{z^R} \right) . \quad (\text{II.6})$$

The energy E is real and therefore, we have two different cases for z . In the first case, z is equal to $e^{i\varphi}$. In the second case, z is a real number. We restrict the intervals to $\varphi \in [0, \pi]$ and $z \in (-1, 1)$ because equation (II.6) is invariant by the substitution of z with z^{-1} . We obtain extended states for the complex values of z as the density $|f_r|^2$ oscillates with distance r . If z is real, then the wave function is exponentially localized $|f_r|^2 \leq 4z^{2r}$ and we call it bound or localized state.

In figure 4, we depict the eigenenergies depending on the attractive impurity strength. The impurity has a strong effect on the lowest eigenenergy, and the others get less

2 EIGENSTATES OF THE CAYLEY TREE

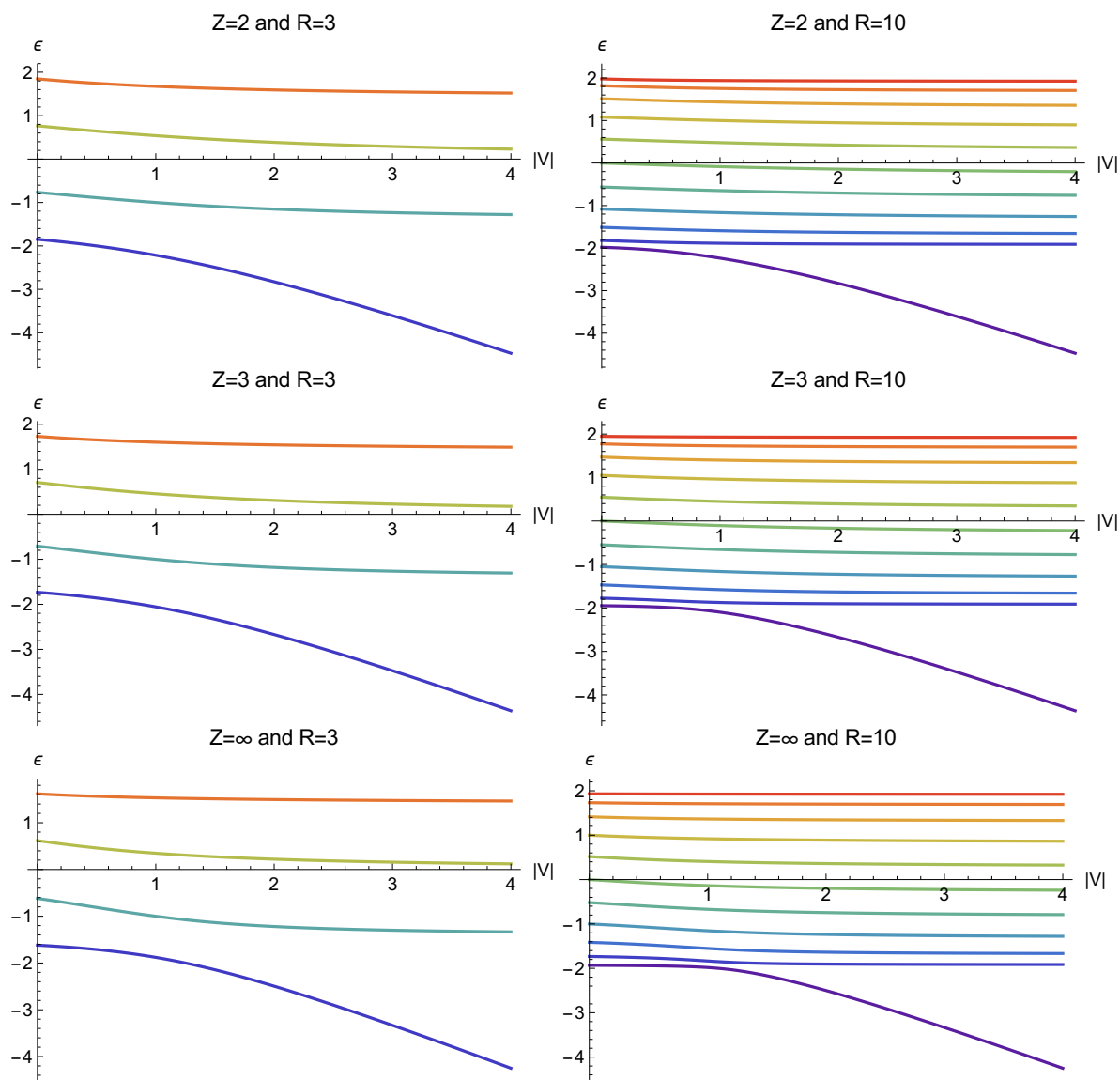


Figure 4: Discrete eigenenergies of the shell-symmetric states in the Cayley tree

affected. Their values decrease slightly for more attractive impurities. This decrease diminishes even more if we increase the number of shells R . The lowest state becomes the bound state, and its energy decreases in the order of the impurity strength. We obtain the corresponding eigenenergies for repulsive impurities by changing the sign of the eigenenergies in the plots of figure 4.

II DYNAMICAL FRIEDEL OSCILLATIONS

One particular effect is prominent in the diagram with $Z = \infty$ and $R = 10$: The lowest energy stays nearly constant up to $|V| \approx 1$, but then it significantly decreases. Next, we apply the limit $R \rightarrow \infty$, and then this feature becomes a kink. For $R \rightarrow \infty$ and

$$|V| \leq V_c = \frac{Z-2}{K} ,$$

equation (II.6) has $R+1$ different solutions of type $z = e^{i\varphi}$. For $|V| > V_c$, it has only R different solutions of this type and a localized state emerges. In both cases, the values of φ are evenly distributed in the interval $[0, \pi]$. In the limit $R \rightarrow \infty$, equation (II.6) simplifies for $z \in (-1, 1)$ to the quadratic equation,

$$\left(z + \frac{1}{z} + V \right) z = \frac{Z}{K} z^2 .$$

It has two solutions,

$$\begin{aligned} z_1 &= \left(\frac{V}{2} + \sqrt{\frac{V^2}{4} + \frac{1}{K}} \right) K > 0 , \\ z_2 &= \left(\frac{V}{2} - \sqrt{\frac{V^2}{4} + \frac{1}{K}} \right) K < 0 . \end{aligned} \tag{II.7}$$

For strong attractive impurities, $V < 0$ and $|V| > V_c$, we obtain $-1 < z_1 < 1$ and $z_2 < -1$. Analog for strong repulsive impurities, $V > 0$ and $|V| > V_c$, we obtain $z_1 > 1$ and $-1 < z_2 < 1$.

In summary, our ansatz captures all eigenstates of the Bethe lattice. We give their explicit form in the presence or absence of the impurity. We have $R+1$ extended shell-symmetric states without impurity ($V=0$),

$$\langle r | \phi(e^{i\varphi_j}) \rangle = s_r \left(e^{i\varphi_j} - \frac{y_0(e^{i\varphi_j})}{e^{ri\varphi_j}} \right) \quad \text{with} \quad s_r = \sqrt{1 - \frac{\delta_{r,0}}{Z}} = \begin{cases} \sqrt{K/Z} & \text{for } r=0 \\ 1 & \text{else} \end{cases} .$$

Furthermore, we have $R-n$ extended non-shell-symmetric eigenstates in each subspace. The subspaces are characterized by the three quantum numbers n , l and k ,

$$\langle r_{nlk} | \phi_{nlk}(e^{i\varphi_j}) \rangle = e^{i\varphi_j} - \frac{e^{-2i\varphi_j}}{e^{i\varphi_j}} .$$

The non-shell-symmetric eigenstates have the form of the shell-symmetric eigenstates with $Z \rightarrow \infty$ and $V = 0$ in their corresponding basis. Our findings for all eigenstates are in accordance with the analysis of the density of states by Yorikawa.⁶⁵ We mention that there the shell-symmetric states are called “linear chain eigenstates”, while “confinement states” correspond to our non-shell-symmetric eigenstates.

If the impurity is present, only the shell-symmetric eigenstates are affected and become

$$\langle r|\psi(z)\rangle = s_r \left(z^r - \frac{y_V(z)}{z^r} \right) .$$

For weak impurities $|V| < V_c$, we have $R + 1$ solutions with $z = e^{i\varphi_j}$. For strong impurities $|V| > V_c$ there are R solutions and one bound state solution $z = z_1$. Thus, an extended state deforms into a localized state. In the limit $R \rightarrow \infty$, the solutions φ_j are evenly spread in both cases and the sum over all φ_j becomes an integral,

$$\sum_j \frac{|\psi(e^{i\varphi_j})\rangle\langle\psi(e^{i\varphi_j})|}{\langle\psi(e^{i\varphi_j})|\psi(e^{i\varphi_j})\rangle} \xrightarrow{R \rightarrow \infty} \int_0^\pi \frac{d\varphi}{2\pi} |\psi(e^{i\varphi})\rangle\langle\psi(e^{i\varphi})| .$$

In conclusion, we expect two different regimes. For weak impurities $|V| < V_c$, the expectation values are computed by the integral over the extended states. For strong impurities $|V| > V_c$, they are computed by the integral plus the contribution of the localized state. For $Z = 2$, the critical impurity strength vanishes $V_c(Z = 2) = 0$. For every finite impurity strength, we are in the strong impurity regime.

If we want to generalize our ansatz to other finite lattices, the eigenstates still have the same form $|\psi(z)\rangle$, but equation (II.6) only has a finite set of solutions as in figure 4. In this work, we will not further investigate the finite-size effects of the Cayley tree. However, interesting recurrence effects^{54–56} are observed for the periodic chain, which we expect similarly for the Cayley tree.

d) Site-resolved initial density

In this subsection, we show that the density for the Fermi sea and the Bethe lattice is equal at every site. The density is site-independent for all fillings if the contribution of all eigenstates with respect to the angle φ are site-independent,

$$\langle \hat{n}_{r,l} \rangle_0 = \int_0^{\theta_F} \frac{d\varphi}{2\pi} \rho_{r,l}(\varphi) .$$

II DYNAMICAL FRIEDEL OSCILLATIONS

We have three different terms,

$$\rho_{r,l}(\varphi) = |\langle r, l | \phi(e^{i\varphi}) \rangle|^2 + \sum_{k_1=1}^{Z-1} |\langle r, l | \phi_{00k}(\varphi) \rangle|^2 + \sum_{r'=1}^{r-1} \sum_{k_2=1}^{Z-1} |\langle r, l | \phi_{r'l k}(\varphi) \rangle|^2.$$

The first is from the shell-symmetric states,

$$|\langle r, l | \phi(e^{i\varphi}) \rangle|^2 = \frac{1}{N_r} |\langle r | \phi(e^{i\varphi}) \rangle|^2.$$

The next is from the non-shell-symmetric states around the origin,

$$|\langle r, l | \phi_{00k}(\varphi) \rangle|^2 = \frac{K}{ZK^r} [|\langle r-1 | \phi(e^{i\varphi}) \rangle|^2]_{Z \rightarrow \infty}.$$

The last is from the non-shell-symmetric eigenstates around the sites $|r', l'\rangle$, which connect the origin with site $|r, l\rangle$,

$$|\langle r, l | \phi_{r'l k}(\varphi) \rangle|^2 = \frac{1}{K^{r-r'}} [|\langle r-1-r' | \phi(e^{i\varphi}) \rangle|^2]_{Z \rightarrow \infty}.$$

Inserting the density of a single eigenstate

$$|\langle r | \phi(e^{i\varphi}) \rangle|^2 = \left(1 - \frac{\delta_{0r}}{Z}\right) \left(1 - e^{i2r\varphi} \frac{\frac{e^{-i2\varphi}}{K} - 1}{\frac{1}{K} - e^{-i2\varphi}}\right) + \text{c.c.}$$

into the three contributions, we obtain after some simplifications,

$$\rho_{rl}(\varphi) = \frac{1 - e^{-i2\varphi}}{\frac{1}{K} - e^{-i2\varphi}} + \text{c.c.}$$

This is a site-independent result, which is the value at the central site $\rho_{00}(\varphi)$. This result holds also in the special case $r = 1$, where the third contribution vanishes. Consequently the equation,

$$\langle \hat{n}_{r,l} \rangle_0 = \langle \hat{n}_{0,0} \rangle_0 \equiv n(\theta_F),$$

holds for all fillings and arbitrary r and l . The filling function $n(\theta_F)$ is symmetric around half-filling

$$n(\theta_F) = 1 - n(\pi - \theta_F)$$

and its explicit form is

$$n(\theta_F) = \int_0^{\theta_F} \frac{d\varphi}{2\pi} ZK \frac{2 - 2 \cos(2\varphi)}{K^2 + 1 - 2K \cos(2\varphi)}$$

$$= \frac{Z\theta_F - (Z - 2) \left[\pi + \arctan \left(\frac{Z}{Z-2} \tan(\theta_F) \right) \right]}{2\pi} \Big|_{\theta_F > \frac{\pi}{2}}$$

In the two special cases $Z \rightarrow \infty$ and $Z = 2$, it further simplifies to

$$n(\theta_F) = \begin{cases} \frac{\theta_F - \cos(\theta_F) \sin(\theta_F)}{\pi} \Big|_{Z \rightarrow \infty} \\ \frac{\theta_F}{\pi} \Big|_{Z=2} \end{cases}$$

This function is depicted in figure 5.

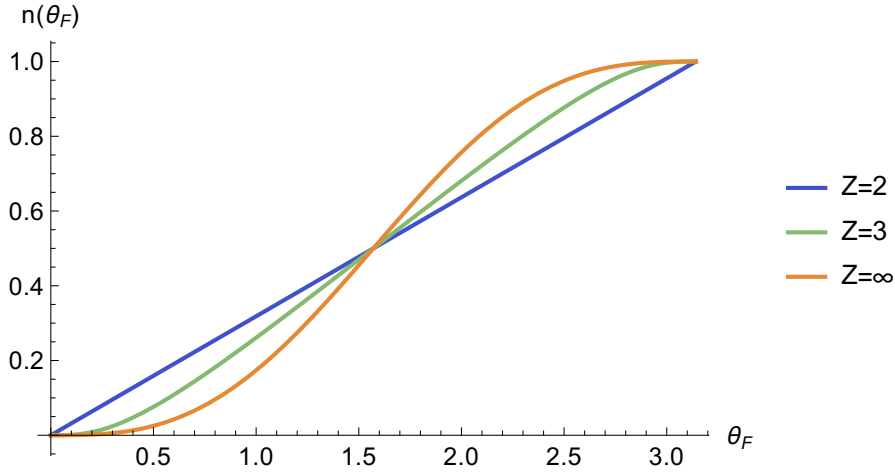


Figure 5: Filling as a function of θ_F for different coordination numbers Z

3 General lattices

a) Post-quench eigenstates

After the detailed study of the Cayley tree and Bethe lattice, we treat the impurity problem on an arbitrary lattice. During this subsection, we will deduce the general extended and localized single-particle eigenstates. We will assume a translationally invariant lattice in the thermodynamic limit. Generally, the Lippmann-Schwinger equation,⁶⁹

$$|\Psi_{\mathbf{k}}\rangle = |\Phi_{\mathbf{k}}\rangle + \left(\epsilon_{\mathbf{k}} + i\delta - \hat{H}_0\right)^{-1} \hat{V}|\Psi_{\mathbf{k}}\rangle, \quad (\text{II.8})$$

relates the extended eigenstates with perturbation $|\Psi_{\mathbf{k}}\rangle$ to the eigenstates without $|\Phi_{\mathbf{k}}\rangle$. First, we insert our impurity potential $\hat{V} = |0\rangle V \langle 0|$ as the perturbation, then apply the impurity state $\langle 0|$ from the left and solve for

$$\begin{aligned} g_{00}(z) &= \langle 0| \left(z - \hat{H}_0\right)^{-1} |0\rangle, \\ \langle 0|\Psi_{\mathbf{k}}\rangle &= \langle 0|\Phi_{\mathbf{k}}\rangle + V g_{00}(\epsilon_{\mathbf{k}} + i\delta) \langle 0|\Psi_{\mathbf{k}}\rangle, \\ \langle 0|\Psi_{\mathbf{k}}\rangle &= \frac{\langle 0|\Phi_{\mathbf{k}}\rangle}{1 - V g_{00}(\epsilon_{\mathbf{k}} + i\delta)}. \end{aligned}$$

We reinsert this into the Lippmann-Schwinger equation (II.8) and obtain

$$|\Psi_{\mathbf{k}}\rangle = |\Phi_{\mathbf{k}}\rangle + \frac{\left(\epsilon_{\mathbf{k}} + i\delta - \hat{H}_0\right)^{-1} |0\rangle V \langle 0|\Phi_{\mathbf{k}}\rangle}{1 - V g_{00}(\epsilon_{\mathbf{k}} + i\delta)}. \quad (\text{II.9})$$

Generally, the Lippmann-Schwinger equation (II.8) cannot be solved so trivially. The simplicity of our perturbation allows us to compute the new single-particle eigenstates.^{60,61} They are eigenstates of the post-quench Hamiltonian,

$$\begin{aligned} \left(\hat{H}_0 + \hat{V}\right) |\Psi_{\mathbf{k}}\rangle &= \epsilon_{\mathbf{k}} |\Phi_{\mathbf{k}}\rangle + \frac{\hat{H}_0 - \epsilon_{\mathbf{k}} - i\delta + \epsilon_{\mathbf{k}} + i\delta}{\epsilon_{\mathbf{k}} + i\delta - \hat{H}_0} \frac{|0\rangle V \langle 0|\Phi_{\mathbf{k}}\rangle}{1 - V g_{00}(\epsilon_{\mathbf{k}} + i\delta)} \\ &\quad + |0\rangle V \langle 0|\Phi_{\mathbf{k}}\rangle + \frac{g_{00}(\epsilon_{\mathbf{k}} + i\delta) |0\rangle V \langle 0|\Phi_{\mathbf{k}}\rangle}{1 - V g_{00}(\epsilon_{\mathbf{k}} + i\delta)} \\ &= \epsilon_{\mathbf{k}} |\Phi_{\mathbf{k}}\rangle + (\epsilon_{\mathbf{k}} + i\delta) \frac{\left(\epsilon_{\mathbf{k}} + i\delta - \hat{H}_0\right)^{-1} |0\rangle V \langle 0|\Phi_{\mathbf{k}}\rangle}{1 - V g_{00}(\epsilon_{\mathbf{k}} + i\delta)} \\ &= \epsilon_{\mathbf{k}} |\Psi_{\mathbf{k}}\rangle + O(\delta). \end{aligned}$$

The error vanishes for $\delta \rightarrow 0$. Only systems in the thermodynamic limit have a finite limit for $\delta \rightarrow 0$ and $\epsilon \rightarrow \epsilon_{\mathbf{k}}$,

$$\lim_{\delta \rightarrow 0} g_{00}(\epsilon + i\delta) = \Re\{g_{00}(\epsilon)\} - i \operatorname{sgn}(\delta)\pi\rho(\epsilon) .$$

This limit does not exist for systems with finite size. For finite lattices, the eigenenergies of $|\Psi_{\mathbf{k}}\rangle$ are shifted away from the eigenenergies of $|\Phi_{\mathbf{k}}\rangle$. We have seen examples for this shift for the Cayley tree in figure 4. Similarly, we construct a localized state,⁶⁰

$$|\Psi_{\text{loc}}\rangle = \frac{(E - \hat{H}_0)^{-1} |0\rangle}{\sqrt{\langle 0 | (E - \hat{H}_0)^{-2} |0\rangle}} .$$

We find that it is an eigenstate,

$$\begin{aligned} (\hat{H}_0 + \hat{V}) (E - \hat{H}_0)^{-1} |0\rangle &= |0\rangle V \langle 0 | (E - \hat{H}_0)^{-1} |0\rangle + \frac{\hat{H}_0 - E + E}{E - \hat{H}_0} |0\rangle \\ &= E (E - \hat{H}_0)^{-1} |0\rangle + |0\rangle (V g_{00}(E) - 1) , \end{aligned}$$

if its energy E fulfills the eigenvalue equation,

$$1 = V g_{00}(E) . \tag{II.10}$$

The Green function $g_{00}(E)$ is real for energies E outside the band and equation (II.10) can be solved. E lies below the band for attractive impurities and above for repulsive impurities.

If the eigenvalue equation (II.10) is fulfilled for an E , then there is one additional eigenstate. However, the number of eigenstates is equal in both cases. We indeed have a new localized state but also lost one extended state. In an infinite system, a missing extended state goes unnoticed in an extensive amount of states. On the other hand, if we compute the eigenstates of a finite system, then one eigenstate turns gradually into the localized state for strong impurities.

b) Shell-symmetric states

We will now investigate the generation of Friedel oscillations.⁵³ According to equation (II.1), we need the overlap of the states with local basis states. We have the single-particle eigenstates from the previous subsection. Furthermore, we need a proper local

II DYNAMICAL FRIEDEL OSCILLATIONS

single-particle basis. It has to capture the full effect of the impurity, but it should be as “few” states as possible. Our choice is the basis of nonorthogonal states

$$\hat{H}_0^r|0\rangle \text{ with } r \in \{0, \dots, R\}.$$

The parameter R corresponds to the radius in which we study the Friedel oscillations. We construct an orthonormal basis from that,

$$|r\rangle = \sum_{n=0}^r \alpha_n^{(r)} \hat{H}_0^n |0\rangle.$$

The coefficients $\alpha_n^{(r)}$ are computed by the Gram-Schmidt process starting from $r = 0$ ending with $r = R$. The states $|r\rangle$ are called shell-symmetric states. During the Gram-Schmidt process, only the moments

$$\langle 0 | \hat{H}_0^n | 0 \rangle = \int d\epsilon \rho(\epsilon) \epsilon^n = \bar{\epsilon}^n \quad (\text{II.11})$$

enter into the computation. The coefficients $\alpha_n^{(r)}$ depend only on the density of states $\rho(\epsilon)$ and not on the geometry of the system.

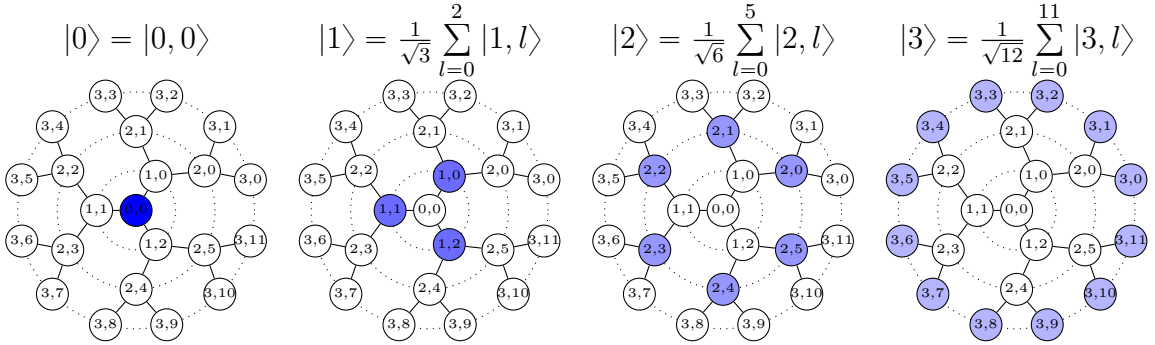


Figure 6: Shell-symmetric Bethe lattice states

We visualize two examples of shell-symmetric states to understand their distribution in real space. Our first example is the Bethe lattice in figure 6. There, the orthonormal states are uniformly occupied rings. We see that the density at each site decreases with increasing distance r . The intensity of the blue color indicates the density in the sketches.

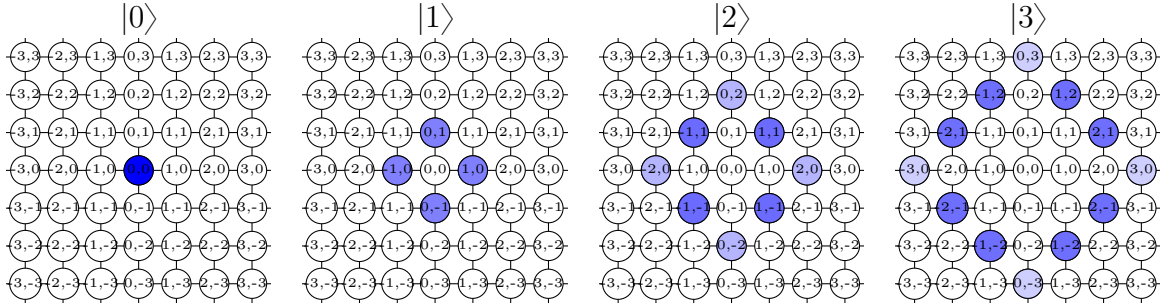


Figure 7: Shell-symmetric square lattice states

For the Bethe lattice, these shell-symmetric states are identical to the shell-symmetric basis states used in section 2. The second example is the square lattice in figure 7. These shell-symmetric states have a diamond form. Every site from one diamond has the same hopping distance towards the center. The hopping distance is the least number of necessary hops between two sites. For the square lattice, the hopping distance between sites (x_1, y_1) and (x_2, y_2) is $|x_1 - x_2| + |y_1 - y_2|$. As for the Bethe lattice, the density thins out away from the impurity. This thinning is stronger at the endpoints and weaker towards the middle of the edges.

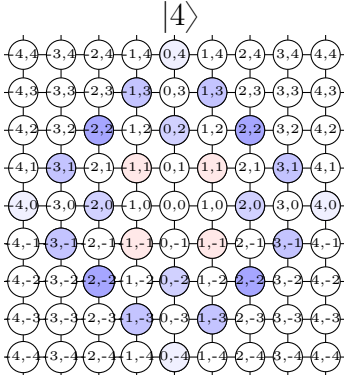


Figure 8: Shell-symmetric square lattice state with second diamond

A smaller second diamond appears for the square lattice states $|n\rangle$ with $n \geq 4$. It has a higher density at the endpoints and lower one at the middle, as shown in figure 8. The color change from blue to red indicates a sign change. Generally, the sign is ± 1 and not complex as the coefficients $\alpha_n^{(r)}$ are real.

II DYNAMICAL FRIEDEL OSCILLATIONS

This emergence of smaller diamonds is investigated in the upper plot of figure 9. The density of all sites with the same hopping distance to the center is summed up and plotted against the hopping distance. The even $|2m\rangle$ and uneven $|2m + 1\rangle$ shell-symmetric states are made out of m diamonds. The majority of the density is located at the most outer diamond, and it decreases for the diamonds towards the center.

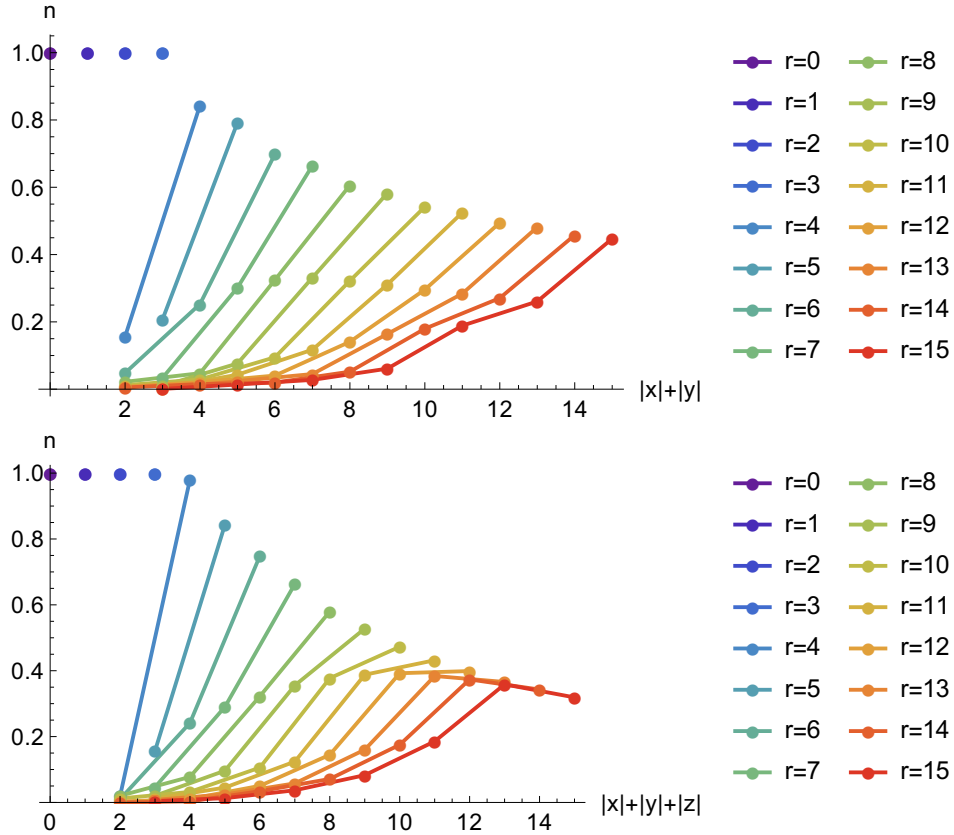


Figure 9: Density of shell-symmetric states for the square(top) and simple cubic(bottom) lattice

We apply the same analysis to the simple cubic lattice in the bottom plot of figure 9. The density of the first 4 states is at a single distance. For the higher states, it starts to spread. The majority of the density is at the furthest distances, but it spreads out more compared to the square lattice. The density maximum shifts to the second most outer diamond for the last two states with $r = 14, 15$. We expect this shift to further increase for larger r .

The shell-symmetric basis is not complete. Only the impurity site can be represented in it, whereas all other sites cannot. But the density change after the impurity quench is fully captured by it. This is due to the symmetry of our problem. The density of the orthogonal non-shell-symmetric states stays constant during our quench process. An arbitrary non-shell-symmetric state $|\text{NS}\rangle$ is orthogonal to the shell-symmetric basis states,

$$\langle \text{NS} | \hat{H}_0^n | 0 \rangle = 0 \quad \text{for } n \in \mathbb{N} .$$

Hence, the overlap of any non-shell-symmetric state with a time-dependent single-particle state $|\Phi_{\mathbf{k}}(t)\rangle$ is captured by the unperturbed Hamiltonian \hat{H}_0 ,

$$\langle \text{NS} | \Phi_{\mathbf{k}}(t) \rangle = \langle \text{NS} | e^{-it(\hat{H}_0 + \hat{V})} | \Phi_{\mathbf{k}} \rangle = \langle \text{NS} | e^{-it\hat{H}_0} | \Phi_{\mathbf{k}} \rangle = e^{-it\epsilon_{\mathbf{k}}} \langle \text{NS} | \Phi_{\mathbf{k}} \rangle .$$

We constructed the explicit form of these non-shell-symmetric states for the Cayley tree and Bethe lattice in section 2. We do not present the corresponding non-shell-symmetric states for other lattices. The impurity quench problem becomes one-dimensional if we represent it in the shell-symmetric states. This simplifies the analysis for higher-dimensional lattices.

c) Check for the Bethe lattice

In this subsection, we compute the eigenstates for the Bethe lattice from the Lippmann-Schwinger equation. They will be in accordance with the eigenstates from the finite Cayley tree in section 2. Hence, this subsection acts as a check for our method.

First, we need the local Green function⁷⁰

$$g_{00}(z) = \frac{2K}{(K-1)z + Z\sqrt{z^2 - 4}} \quad \text{with } \text{sgn}\left(\Im\sqrt{z^2 - 4}\right) = \text{sgn}(\Im z) \quad \text{and } \Re z > -2 .$$

We insert it into the eigenvalue equation (II.10) for the bound state. We assume the form $E = -(z_1 + z_1^{-1})$ for localized-state energy and place it into the Green function

$$1 = V g_{00}(-(z_1 + z_1^{-1})) \quad \xrightarrow{0 < z_1 < 1} \quad z_1 = \left(\frac{V}{2} + \sqrt{\frac{V^2}{4} + \frac{1}{K}} \right) K .$$

This is the same result as in (II.7). We note that the sign of the square root changes, because the Green function is antisymmetric in z . We need the Green function⁷⁰ from the central site to the shell-symmetric state $|r\rangle$,

$$\langle r | \left(z - \hat{H}_0 \right)^{-1} | 0 \rangle = g_{r0}(z) = g_{00}(z) \left(\frac{-2}{z + \sqrt{z^2 - 4}} \right)^r \sqrt{\frac{Z}{K}} s_r .$$

II DYNAMICAL FRIEDEL OSCILLATIONS

We obtain the identical behavior for the localized state

$$\langle r | \psi_{\text{loc}} \rangle \propto \left(\frac{-2}{-(z_1 + z_1^{-1}) - \sqrt{(z_1 + z_1^{-1})^2 - 4}} \right)^r s_r = z_1^r s_r .$$

The Green functions simplify for the continuous states,

$$g_{00} (-(e^{i\theta} + e^{-i\theta})) \stackrel{0 < \theta < \pi}{=} \frac{e^{i\theta}}{\frac{1}{K} - e^{i2\theta}} ,$$

$$\left(\frac{-2}{-(e^{i\theta} + e^{-i\theta}) - \sqrt{(e^{i\theta} + e^{-i\theta})^2 - 4}} \right)^r \stackrel{0 < \theta < \pi}{=} e^{-i\theta r} .$$

We insert this into equation (II.9) and recover the same eigenstate as in section 2,

$$\begin{aligned} \langle r | \psi(e^{i\theta}) \rangle &= \langle r | \phi(\theta) \rangle + \frac{g_{r0} (-(e^{i\theta} + e^{-i\theta})) V \langle 0 | \phi(\theta) \rangle}{1 - V g_{00} (-(e^{i\theta} + e^{-i\theta}))} \\ &= s_r (e^{ir\theta} - y_0(e^{i\theta})e^{-ir\theta}) + \frac{s_r e^{-ir\theta} V e^{i\theta} (1 - y_0(e^{i\theta}))}{\frac{1}{K} - e^{2i\theta} - V e^{i\theta}} \\ &= s_r \left(e^{ir\theta} - e^{-ir\theta} \underbrace{\frac{\frac{e^{2i\theta}}{K} - V e^{i\theta} - 1}{\frac{1}{K} - e^{2i\theta} - V e^{i\theta}}}_{= y_V(e^{i\theta})} \right) . \end{aligned}$$

We note that if we take the complex conjugated Green function, then our eigenstates would have the conjugated complex phases. Complex conjugation of the Green function corresponds to taking the limit to the real axis from the other side of the complex plane. In this subsection, we have found exactly the same eigenstates as in section 2. This confirms the eigenstates obtained from the Lippmann-Schwinger equation.

d) Critical impurity strength

In this subsection, we discuss the critical impurity strength V_c as it is a important property of this noninteracting system. It determines if an impurity generates a bound state. Our explicit results in section 4 crucially depend on the presence of the bound state. Hence, it is necessary to fully understand when the bound state is generated and which eigenenergy it receives. The critical impurity strength V_c is determined by the minimal ϵ_{min} and maximal ϵ_{max} band energies inserted into the eigenvalue equation (II.10),

$$\begin{aligned} \text{repulsive impurity: } & V > V_c ; \quad V_c = (g_{00}(\epsilon_{\text{max}} + \delta))^{-1} , \\ \text{attractive impurity: } & V < V_c ; \quad V_c = (g_{00}(\epsilon_{\text{min}} - \delta))^{-1} . \end{aligned} \tag{II.12}$$

We start with the tight-binding Hamiltonian on the hypercubic lattice. The hopping

dim	1	2	3	4	5	6	7	8	9	10
$ V_c $	0	0	1.98	3.22	4.32	5.37	6.40	7.42	8.43	9.44
$ E(V_c) $	1	2	3	4	5	6	7	8	9	10

Table 2: Critical impurity strength V_c for the tight-binding Hamiltonian on the hypercubic lattice

amplitude is set to -1 for all dimensions. We insert the local Green function,

$$g_{00}(z) = \int_0^\pi \frac{dk_1}{\pi} \cdots \int_0^\pi \frac{dk_{\text{dim}}}{\pi} \frac{1}{z + \cos(k_1) + \dots + \cos(k_{\text{dim}})},$$

and the band edges into equation (II.12). Then, we obtain the critical impurity strengths, which are depicted in table 2. In one and two dimensions, a localized state is generated

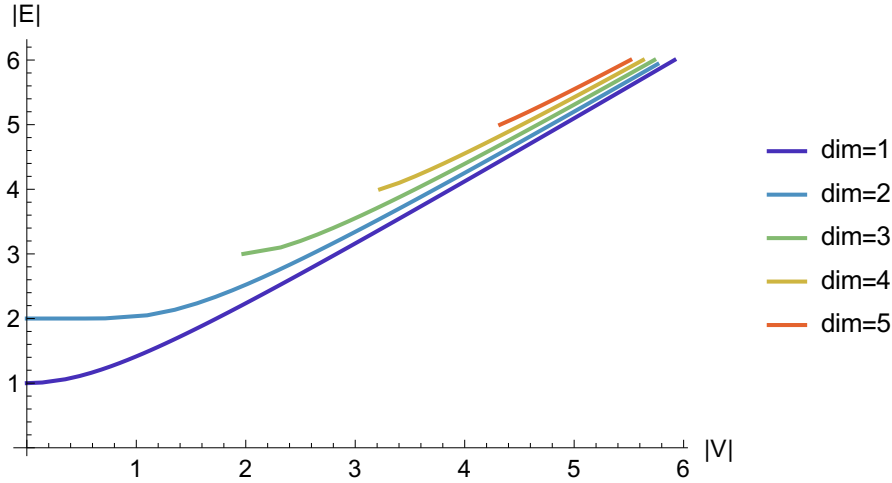


Figure 10: Eigenenergy E for varying impurity strength V and dimension on the hypercubic lattice

for any impurity. In higher dimensions, a certain threshold has to be overcome. The eigenenergy depends monotonously on the impurity strength as depicted in the plot of figure 10. It starts from the point $(|V_c|, |E(V_c)| = \text{dim})$ and then it converges to the identity $|E| = |V|$. To get a nontrivial limit in infinite dimensions, the hopping needs to

II DYNAMICAL FRIEDEL OSCILLATIONS

be scaled by $t \rightarrow t^*/\sqrt{\text{dim}}$.⁵⁷ Inserting the band edge into the scaled Green function gives ($t^* = -1$)

$$\begin{aligned}
g_{00}(\sqrt{\text{dim}}) &= \int_0^\pi \frac{dk_1}{\pi} \dots \int_0^\pi \frac{dk_{\text{dim}}}{\pi} \left(\sqrt{\text{dim}} + \frac{\cos(k_1)}{\sqrt{\text{dim}}} + \dots + \frac{\cos(k_{\text{dim}})}{\sqrt{\text{dim}}} \right)^{-1} \\
&= \frac{1}{\sqrt{\text{dim}}} \int_0^\pi \frac{dk_1}{\pi} \dots \int_0^\pi \frac{dk_{\text{dim}}}{\pi} \left(\sum_{n=1}^{\text{dim}} \frac{1 + \cos(k_n)}{\text{dim}} \right)^{-1} \\
&= \frac{1}{\sqrt{\text{dim}}} \int_0^\infty d\lambda \underbrace{\left(\int_0^\pi \frac{dk}{\pi} e^{-\frac{\lambda}{\text{dim}}(1+\cos(k))} \right)^{\text{dim}}}_{=1 - \frac{\lambda}{\text{dim}} + O(\frac{\lambda^2}{\text{dim}^2})} \\
&= \frac{1}{\sqrt{\text{dim}}} \int_0^\infty d\lambda e^{-\lambda} + O(\text{dim}^{-1}) = \frac{1}{\sqrt{\text{dim}}} + O(\text{dim}^{-1}) .
\end{aligned}$$

Therefore, the critical impurity strength is

$$|V_c| = \frac{1}{g_{00}(\sqrt{\text{dim}})} = \sqrt{\text{dim}} + O(1) .$$

$|V_c|$ diverges in the limit of infinite spatial dimensions for the tight-binding Hamiltonian, and therefore a single impurity does not induce a localized state. Generally, the local Green function $g_{00}(z)$ is solely determined by the density of states (d.o.s.). Any d.o.s. with finite bandwidth can be represented in infinite dimensions by a set of hopping amplitudes, although long-ranged hopping amplitudes are typically required.⁷¹

Next, we derive from the d.o.s. whether there is a finite V_c or not. The d.o.s. in one to three dimensions is diverse as depicted in figure 11. Because, V_c is computed by the Green function near the band edges, the particular behavior of $\rho(\epsilon)$ there has great influence on V_c . In one dimension $\rho(\epsilon)$ diverges, in two dimensions it becomes finite and in three dimensions it vanishes. It is easy to show that a finite d.o.s. at the band edge results in a logarithmic divergence,

$$g_{00}(\epsilon_{\min} - \delta) = - \int_0^{\epsilon_{\max} - \epsilon_{\min}} d\Delta \epsilon \frac{\rho(\epsilon_{\min} + \Delta \epsilon)}{\Delta \epsilon + \delta} = O(\log(\delta)) \quad \text{for } 0 < \rho(\epsilon) < \infty .$$

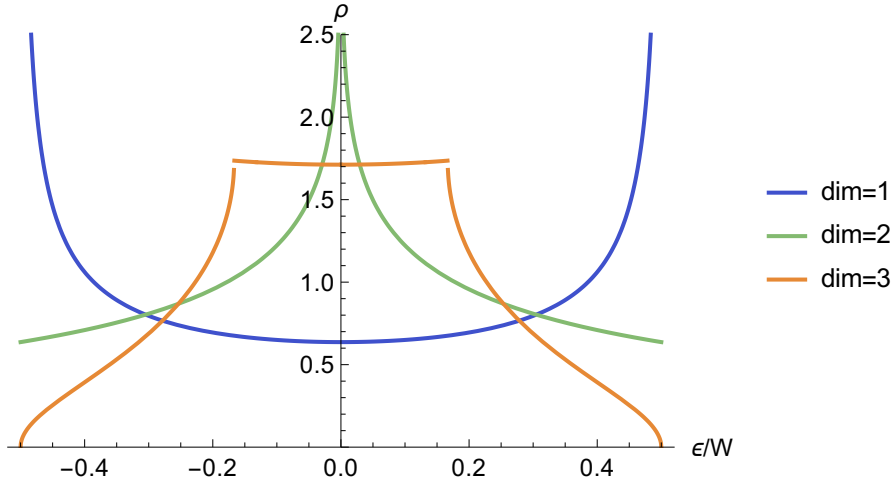


Figure 11: Density of states for the hypercubic lattice

This leads to a vanishing V_c with equation (II.12). We conclude that the d.o.s. needs to vanish at the bandedges to result in a finite V_c . We investigate only systems with a symmetric d.o.s., which gives the same critical impurity strength for attractive and repulsive impurities. For nonsymmetric d.o.s., we obtain distinct V_c for attractive and repulsive impurities. A finite V_c leads to two different post-quench regimes, which we investigate in the next section.

e) Evaluation and numerical procedure

We have all single-particle eigenstates and an appropriate basis. This enables us to evaluate our time-resolved observable. Inserting the shell-symmetric basis transforms our quantity from equation (II.1) to

$$\langle r | e^{-it(\hat{H}_0 + \hat{V})} | \Phi_{\mathbf{k}} \rangle = \sum_{n=0}^r \alpha_n^{(r)} \langle 0 | \hat{H}_0^n e^{-it(\hat{H}_0 + \hat{V})} | \Phi_{\mathbf{k}} \rangle .$$

The propagator $e^{-it(\hat{H}_0 + \hat{V})}$ will be replaced by the sum over all eigenstate projectors times their complex phases. The extended states always contribute, and the localized state contributes if the impurity is strong enough. We consider only single-band systems

II DYNAMICAL FRIEDEL OSCILLATIONS

and restrict ourselves to attractive impurities. The unitary time-evolution operator for our single-particle states becomes

$$\begin{aligned}\langle 0|\hat{H}_0^n e^{-it(\hat{H}_0+\hat{V})}|\Phi_{\mathbf{k}}\rangle &= \langle 0|\Phi_{\mathbf{k}}\rangle\Phi_n^{\text{loc}}(\epsilon_{\mathbf{k}}, t)\Theta(|V| - |V_c|) + \langle 0|\Phi_{\mathbf{k}}\rangle\Phi_n^{\text{ext}}(\epsilon_{\mathbf{k}}, t), \\ \langle 0|\Phi_{\mathbf{k}}\rangle\Phi_n^{\text{loc}}(\epsilon_{\mathbf{k}}, t) &= \langle 0|\hat{H}_0^n|\Psi_{\text{loc}}\rangle e^{-itE}\langle\Psi_{\text{loc}}|\Phi_{\mathbf{k}}\rangle, \\ \langle 0|\Phi_{\mathbf{k}}\rangle\Phi_n^{\text{ext}}(\epsilon_{\mathbf{k}}, t) &= \sum_{\mathbf{k}'}\langle 0|\hat{H}_0^n|\Psi_{\mathbf{k}'}\rangle e^{-it\epsilon_{\mathbf{k}}}\langle\Psi_{\mathbf{k}'}|\Phi_{\mathbf{k}}\rangle.\end{aligned}$$

Inserting the impurity eigenstates gives

$$\begin{aligned}\langle 0|\Phi_{\mathbf{k}}\rangle\Phi_n^{\text{loc}}(\epsilon_{\mathbf{k}}, t) &= \langle 0|\frac{\hat{H}_0^n}{E - \hat{H}_0}|0\rangle\frac{e^{-itE}\langle 0|\Phi_{\mathbf{k}}\rangle}{(E - \epsilon_{\mathbf{k}})\langle 0|(E - \hat{H}_0)^{-2}|0\rangle}, \\ \langle 0|\Phi_{\mathbf{k}}\rangle\Phi_n^{\text{ext}}(\epsilon_{\mathbf{k}}, t) &= \sum_{\mathbf{k}'}\langle 0|\Phi_{\mathbf{k}'}\rangle e^{-it\epsilon_{\mathbf{k}'}}\left(\epsilon_{\mathbf{k}'}^n + \frac{V\langle 0|\hat{H}_0^n(\epsilon_{\mathbf{k}'} + i\delta - \hat{H}_0)^{-1}|0\rangle}{1 - Vg_{00}(\epsilon_{\mathbf{k}'} + i\delta)}\right) \\ &\quad \times \left(\langle\Phi_{\mathbf{k}'}|\Phi_{\mathbf{k}}\rangle + \frac{V\langle\Phi_{\mathbf{k}'}|0\rangle\langle 0|\Phi_{\mathbf{k}}\rangle}{(1 - Vg_{00}(\epsilon_{\mathbf{k}'} - i\delta))(\epsilon_{\mathbf{k}'} - i\delta - \epsilon_{\mathbf{k}})}\right).\end{aligned}$$

First, the delta function $\langle\Phi_{\mathbf{k}'}|\Phi_{\mathbf{k}}\rangle$ with the sum over all \mathbf{k}' gives a term with constant amplitude in time. Next, we use

$$\sum_{\mathbf{k}'}|\langle 0|\Phi_{\mathbf{k}'}\rangle|^2 f(\epsilon_{\mathbf{k}'}) \longrightarrow \int d\epsilon \rho(\epsilon) f(\epsilon)$$

to turn the \mathbf{k}' summation into an energy integration

$$\Phi_n^{\text{loc}}(\epsilon_{\mathbf{k}}, t) = -\frac{g_n(E)e^{-itE}}{(E - \epsilon_{\mathbf{k}})g_0'(E)}, \quad g_n(z) = \langle 0|\hat{H}_0^n(z - \hat{H}_0)^{-1}|0\rangle, \quad (\text{II.13})$$

$$\begin{aligned}\Phi_n^{\text{ext}}(\epsilon_{\mathbf{k}}, t) &= e^{-it\epsilon_{\mathbf{k}}}\left(\epsilon_{\mathbf{k}}^n + \frac{g_n(\epsilon_{\mathbf{k}} + i\delta)V}{1 - Vg_0(\epsilon_{\mathbf{k}} + i\delta)}\right) \\ &\quad + V\int d\epsilon\frac{\rho(\epsilon)\epsilon^n e^{-it\epsilon}}{(1 - Vg_0(\epsilon + i\delta))(\epsilon - \epsilon_{\mathbf{k}} - i\delta)} \\ &\quad + V^2\int d\epsilon\frac{\rho(\epsilon)g_n(\epsilon - i\delta)e^{-it\epsilon}}{(1 - Vg_0(\epsilon + i\delta))(1 - Vg_0(\epsilon - i\delta))(\epsilon - \epsilon_{\mathbf{k}} - i\delta)}.\end{aligned} \quad (\text{II.14})$$

We derive the Green functions $g_n(z)$ for the shell-symmetric states from the local Green function $g_{00}(z) = g_0(z)$. We iterate the simple identity,

$$\frac{\epsilon^n}{z - \epsilon} = \frac{z\epsilon^{n-1}}{z - \epsilon} - \epsilon^{n-1},$$

and can compute these specific Green functions with the identity

$$g_n(z) = \int d\epsilon \frac{\rho(\epsilon)\epsilon^n}{z - \epsilon} = z^n g_0(z) - \sum_{m=0}^{n-1} \bar{\epsilon}^m z^{n-1-m}, \quad (\text{II.15})$$

where $\bar{\epsilon}^n$ are the moments from equation (II.11). Numerically, it is hard to compute an integration next to a pole. Thus, we remove the pole with a “dressed” time derivative,

$$e^{-it\epsilon_{\mathbf{k}}}\partial_t e^{it\epsilon_{\mathbf{k}}}\Phi_n^{\text{ext}}(\epsilon_{\mathbf{k}}, t) = -iV \int d\epsilon \frac{\rho(\epsilon)e^{-it\epsilon}}{1 - Vg_0(\epsilon + i\delta)} \left(\epsilon^n + \frac{Vg_n(\epsilon - i\delta)}{1 - Vg_0(\epsilon - i\delta)} \right). \quad (\text{II.16})$$

We then perform the time integration numerically. We obtain the expectation value for the Fermi sea by integrating over all occupied energies

$$\langle \hat{n}_r \rangle_t = \int_{\epsilon_{\min}}^{\epsilon_{\text{F}}} d\epsilon \rho(\epsilon) \left| \sum_{n=0}^r \alpha_n^{(r)} [\Phi_n^{\text{loc}}(\epsilon_{\mathbf{k}}, t)\Theta(|V| - |V_c|) + \Phi_n^{\text{ext}}(\epsilon_{\mathbf{k}}, t)] \right|^2. \quad (\text{II.17})$$

This is our complete evaluation procedure. If $g_0(\epsilon \pm i\delta)$ is analytically available, then we compute the energy integration in the right-hand side of equation (II.16) numerically. This has to be done for a set of times t_i and n . The times t_i have to span a fine grid as we time integrate it after multiplying it with $e^{it\epsilon_{\mathbf{k}}}$. The final step is to perform the energy integration in equation (II.17) numerically. Into the computation enters only the d.o.s. $\rho(\epsilon)$ and not the full information of the lattice. So we obtain identical results for two different lattices with the same d.o.s. . In the outlook subsection 6.a), we present the computational procedure in the single-site basis. The scheme can be applied to arbitrary lattices as long as the Green function is available.

4 Results for time-dependent quantities

This section is dedicated to our explicit results, and it is structured in the following. The transient behavior of single-particle states is discussed first. Then, we observe two distinct long-time regimes, which we analytically deduce. From that, we compute the Fermi-sea expectation values for the transient and the long-time limit. Next, we investigate the wave-front propagation followed by the subsection concerning the long-time Friedel oscillations. Finally, we will compare it to the thermal expectation value and obtain two physically different long-time regimes.

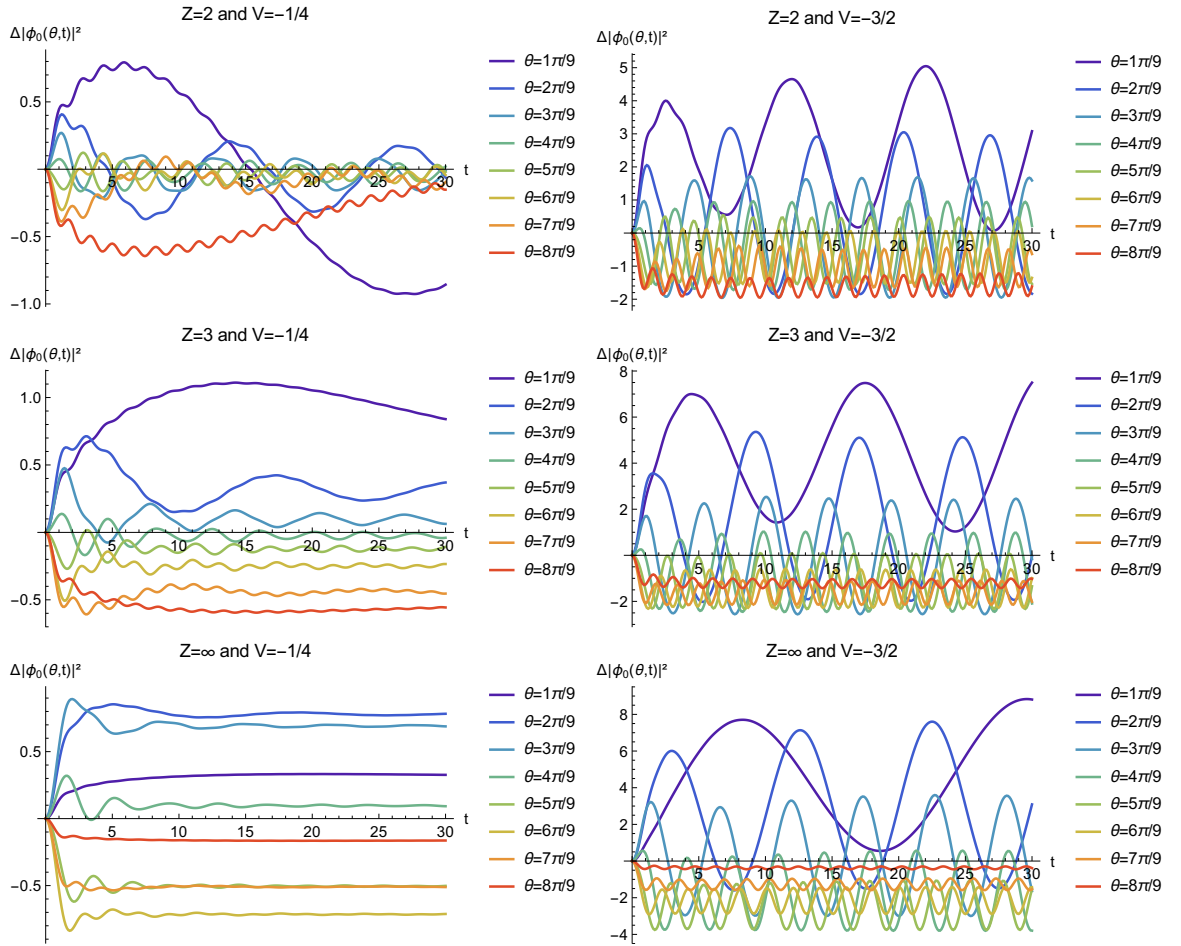


Figure 12: Time-dependent single-particle expectation values for the Bethe lattice

a) Single-particle expectation values

We begin with the density change caused by single occupied states

$$|\Phi_r(\epsilon_{\mathbf{k}}, t)|^2 = \left| \sum_{n=0}^r \alpha_n^{(r)} [\Phi_n^{\text{ext}}(\epsilon_{\mathbf{k}}, t) + \Theta(|V| - |V_c|) \Phi_n^{\text{loc}}(\epsilon_{\mathbf{k}}, t)] \right|^2.$$

Examples for the Bethe lattice are displayed in figure 12. Generally, we observe initial oscillations. They relax for the examples with $V = -\frac{1}{4}$ and $Z = 3, \infty$, which is the case $|V| < |V_c|$. We have the case $|V| > |V_c|$ in the four other plots, and the oscillations become steady. We conclude that the localized state is responsible for these undamped oscillations.

Next, we investigate the long-time behavior analytically. $\Phi_n^{\text{ext}}(\epsilon_{\mathbf{k}}, t)$ contains three terms, and two of them contain an explicit energy integration. We choose a new integration path in the lower complex plane. We have to handle the infinitesimal shift in the complex plane $\pm i\delta$ appropriately, which leads to the following result:

$$\begin{aligned} \Phi_n^{\text{ext}}(\epsilon_{\mathbf{k}}, t) = e^{-it\epsilon_{\mathbf{k}}} & \left(\epsilon_{\mathbf{k}}^n + \frac{g_n(\epsilon_{\mathbf{k}} + i\delta)V}{1 - Vg_0(\epsilon_{\mathbf{k}} + i\delta)} \right) + V \int_{L(d)} dz \frac{\rho(z)z^n e^{-itz}}{(1 - Vg_0(z))(z - \epsilon_{\mathbf{k}})} \\ & + V^2 \int_{L(d)} dz \frac{\rho(z)(g_n(z) + i2\pi\rho(z))e^{-itz}}{(1 - V(g_0(z) + i2\pi\rho(z)))(1 - Vg_0(z))(z - \epsilon_{\mathbf{k}})}. \end{aligned}$$

The integration path $L(d)$ is displayed in figure 13. The parameter d is a real, positive and finite number. Therefore, the path must go below the real axis. When we take the

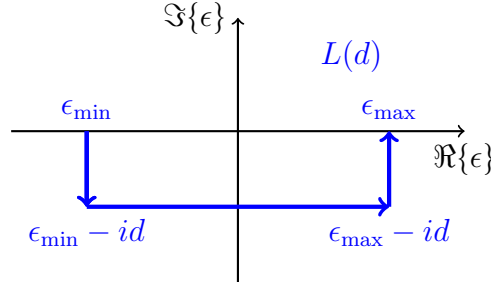


Figure 13: Complex integration path $L(d)$

II DYNAMICAL FRIEDEL OSCILLATIONS

limit $t \rightarrow \infty$, the two integration terms vanish due to e^{-itz} with $\text{Im}\{z\} < 0$. Generally, the integration over an integrable function with oscillating factor $e^{-it\epsilon}$ vanishes with t^{-1} ,

$$\int_{\epsilon_{\min}}^{\epsilon_{\max}} d\epsilon f(\epsilon) e^{-it\epsilon} \stackrel{\text{P.I.}}{=} i \left[f(\epsilon) \frac{e^{-it\epsilon}}{t} \right]_{\epsilon_{\min}}^{\epsilon_{\max}} - i \int_{\epsilon_{\min}}^{\epsilon_{\max}} d\epsilon f'(\epsilon) \frac{e^{-it\epsilon}}{t} = O(t^{-1}). \quad (\text{II.18})$$

It decays faster if $f(\epsilon_{\min}) = f(\epsilon_{\max}) = 0$. Replacing the contribution of the two integration terms with $O(t^{-1})$ results in

$$\Phi_r(\epsilon, t) = \sum_{n=0}^r \alpha_n^{(r)} \left[e^{-it\epsilon} \left(\epsilon^n + \frac{g_n(\epsilon + i\delta)V}{1 - Vg_0(\epsilon + i\delta)} \right) - \frac{\Theta(V_c - V)g_n(E)e^{-itE}}{(E - \epsilon)g'_0(E)} \right] + O(t^{-1}). \quad (\text{II.19})$$

If there is no localized state, then the expectation value relaxes to a constant value. Otherwise there are steady oscillations with frequency $\omega = (E - \epsilon_{\mathbf{k}})$. The qualitative behavior is determined by the case $|V| \lesseqgtr |V_c|$. The density change is an analytic function in its parameters even if we cross the point $|V| = |V_c|$. Hence, the relaxation time increases in the proximity of the critical impurity strength. The quantitative values strongly depend on the actual values of V and Z . There is a faster relaxation for $Z \rightarrow \infty$ than for $Z = 3$ and the same impurity strength because for $Z = 3$ we are closer to $|V_c|$. The oscillation frequency for the same θ decreases with increasing Z because the energy difference determines it. The energy of the extended states is determined by θ and is independent of Z , but the energy of the localized state decreases with increasing coordination number Z .

We evaluate the density change in the first three states for the square lattice in figure 14. The prolonged oscillations appear to be small for the weaker impurity $V = -\frac{1}{2}$. This implies that the bound-state contribution is small itself. The long-time oscillations are clearly visible for the stronger impurity $V = -\frac{3}{2}$. We expect relaxation on the simple cubic lattice in figure 15 as the dynamics are computed for $|V| < |V_c| = 1.98$. For $V = -\frac{1}{2}$ all single-particle values relax quickly and for $V = -\frac{3}{2}$ some values do not relax in the depicted time window ($t \leq 10$). Hence, we observe the increased relaxation duration for quenching closer to $|V_c|$.

4 RESULTS FOR TIME-DEPENDENT QUANTITIES

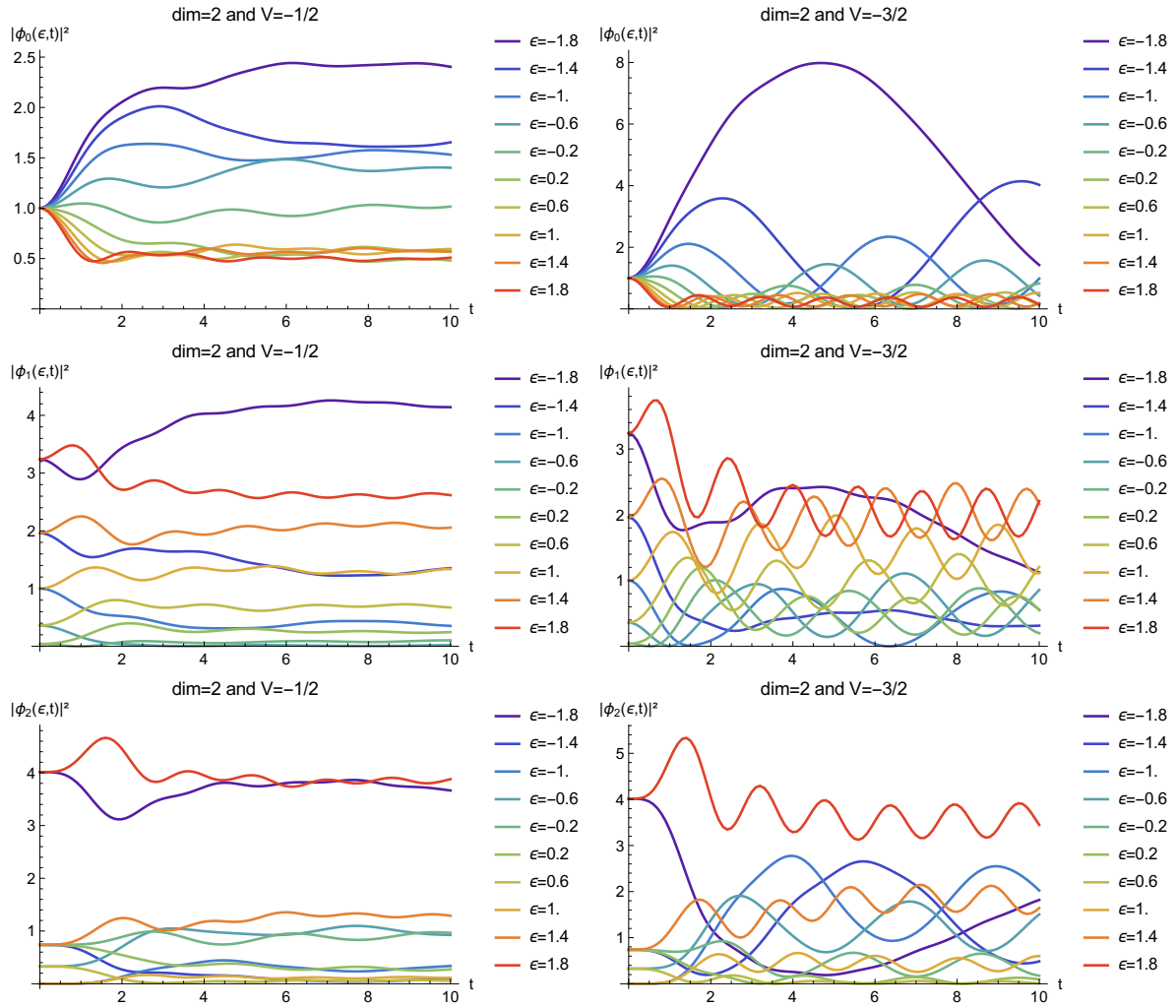


Figure 14: Short-time dynamics of the single-particle expectation values for the square lattice

II DYNAMICAL FRIEDEL OSCILLATIONS

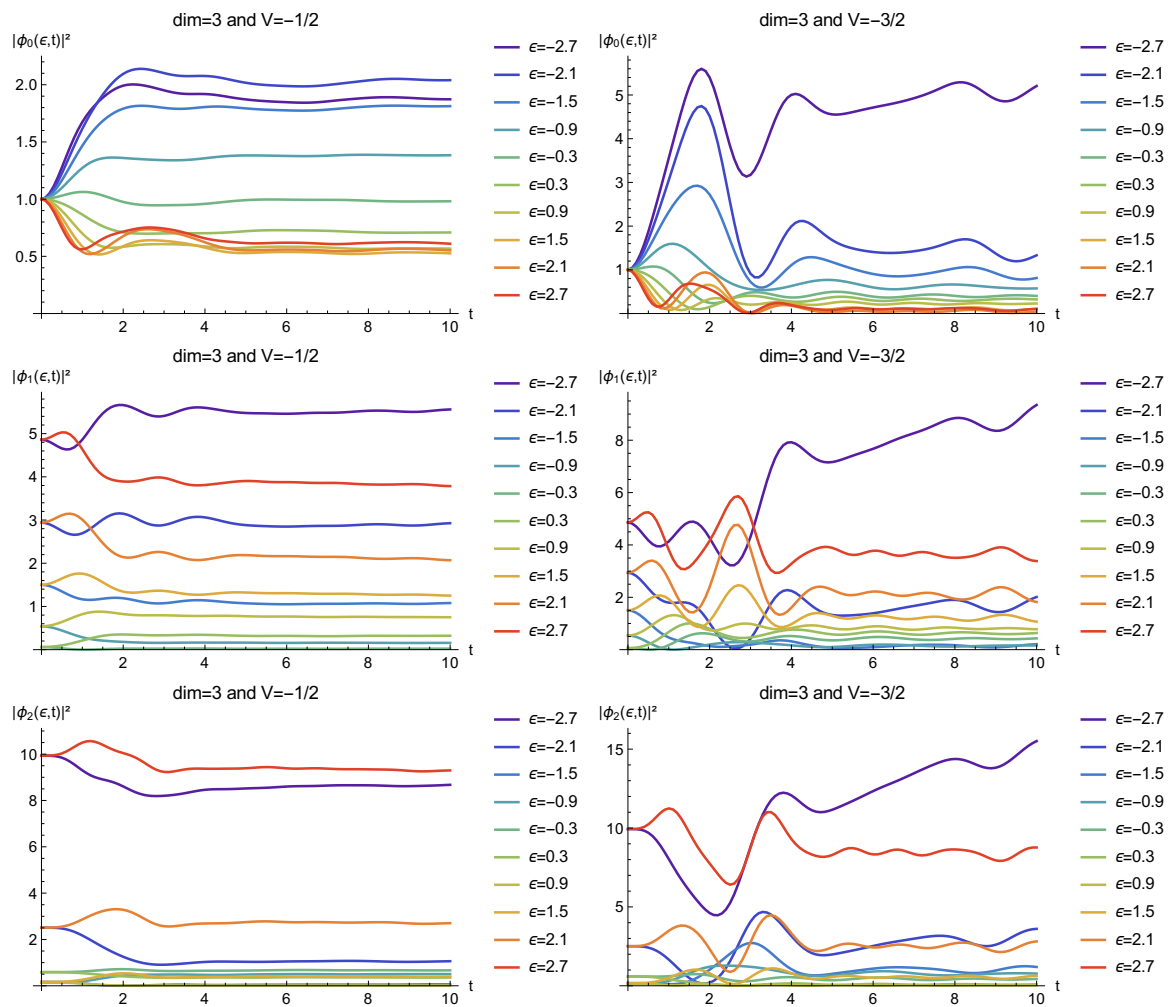


Figure 15: Short-time dynamics of the single-particle expectation values for the simple cubic lattice

b) Fermi-sea expectation values

Next, we examine the time-dependent expectation values for the Fermi sea. They are computed from the single-particle values as described in equation (II.17). Examples for the Bethe lattice are depicted in figure 16. The square and simple cubic lattice examples are shown in figure 17. We observe the same qualitative behavior in all plots that the density starts to oscillate and then relaxes. For the weak impurity case $|V| < |V_c|$, we expect this from the single-particle behavior in figure 12, 14 and 15.

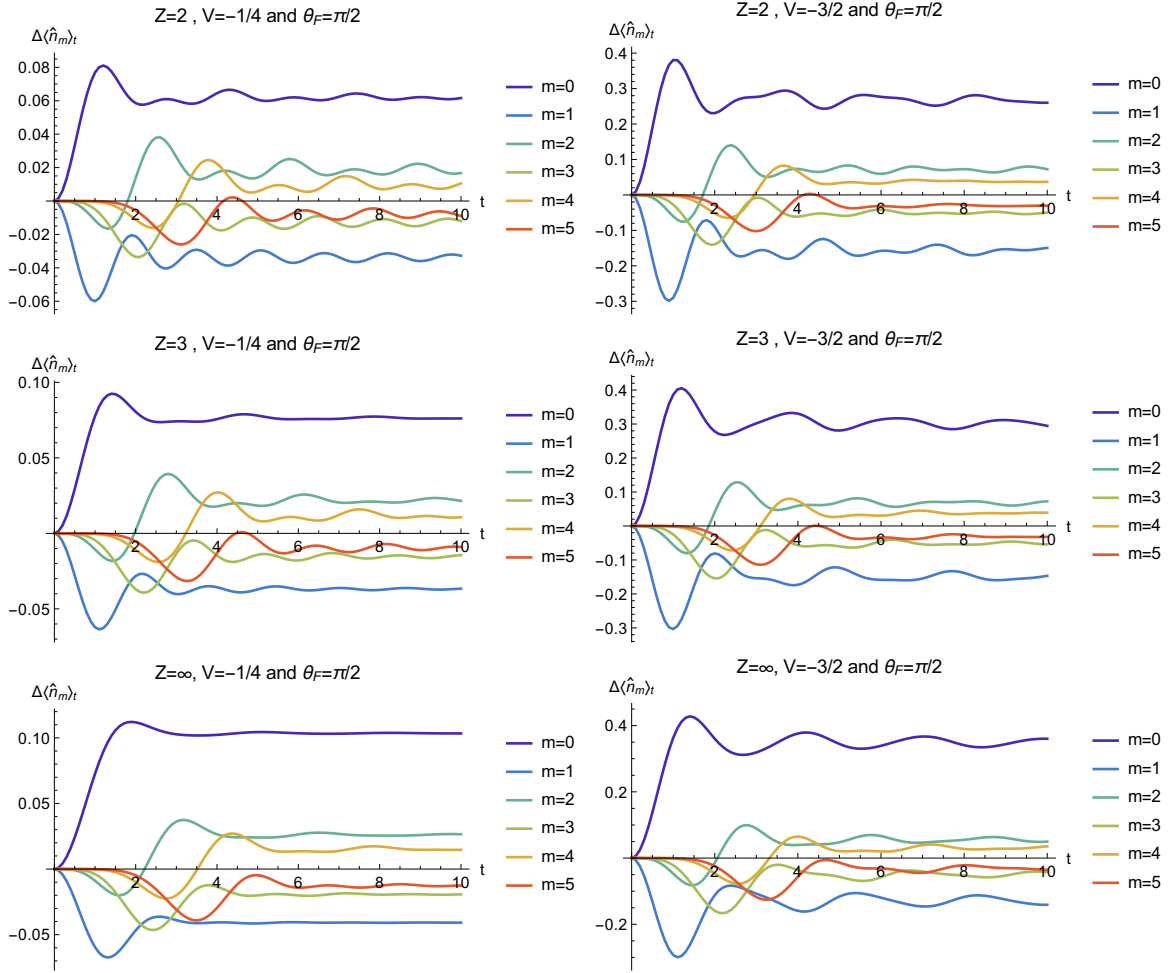


Figure 16: Time-dependent Fermi sea expectation values at half filling

The steady oscillations have different frequencies for $|V| > |V_c|$ and different $\epsilon_{\mathbf{k}}$. Thus,

II DYNAMICAL FRIEDEL OSCILLATIONS

the integration cancels them out in equation (II.17), which governs relaxation with $O(t^{-1})$ due to equation (II.18). Furthermore, we insert equation (II.19) and the long-time limit becomes

$$\begin{aligned} \langle \hat{n}_r \rangle_t = \int_{\epsilon_{\min}}^{\epsilon_F} d\epsilon \rho(\epsilon) & \left[\left| \sum_{n=0}^r \alpha_n^{(r)} \left(\epsilon^n + \frac{g_n(\epsilon + i\delta)V}{1 - Vg_0(\epsilon + i\delta)} \right) \right|^2 \right. \\ & \left. + \Theta(|V| - |V_c|) \left| \sum_{n=0}^r \alpha_n^{(r)} \frac{g_n(E)}{(E - \epsilon)g'_0(E)} \right|^2 \right] + O(t^{-1}) . \end{aligned}$$

We identify the first term as the density of the extended post-quench eigenstates $|\Psi_{\mathbf{k}}\rangle$ below the Fermi energy. The second term is the density of the bound state times its occupation at the quench,

$$\langle \hat{n}_r \rangle_t = \sum_{\epsilon_{\mathbf{k}} < \epsilon_F} |\langle r | \Psi_{\mathbf{k}} \rangle|^2 + \Theta(|V| - |V_c|) |\langle r | \Psi_{\text{loc}} \rangle|^2 \langle \hat{n}_{\text{loc}} \rangle_0 + O(t^{-1}) . \quad (\text{II.20})$$

We derived equation (II.20) for the shell-symmetric states $|r\rangle$, but it is also valid for any non shell-symmetric state $|\text{NS}\rangle$,

$$\langle \hat{n}_{\text{NS}} \rangle_t = \sum_{\epsilon_{\mathbf{k}} < \epsilon_F} \left| \underbrace{\langle \text{NS} | \Psi_{\mathbf{k}} \rangle}_{=\langle \text{NS} | \Phi_{\mathbf{k}} \rangle} \right|^2 + \Theta(|V| - |V_c|) \left| \underbrace{\langle \text{NS} | \Psi_{\text{loc}} \rangle}_{=0} \right|^2 \langle \hat{n}_{\text{loc}} \rangle_0 .$$

The eigenstates act as projectors, and therefore equation (II.20) is valid if we replace $|r\rangle$ with an arbitrary local state. The derivation of the long-time limit is one of the main results in this thesis and is further investigated in subsection d).

The examples in figure 16 and 17 are at half-filling. We observe three trends depending on the distance to the impurity m . First, the sign of the final density change alternates. Second, the absolute value of the relaxation plateau decreases. Third, the response time to the impurity increases with distance m . These decaying density oscillations with respect to m are Friedel oscillations. A light-cone effect governs their dynamic creation as we further analyze in the following subsection.

4 RESULTS FOR TIME-DEPENDENT QUANTITIES

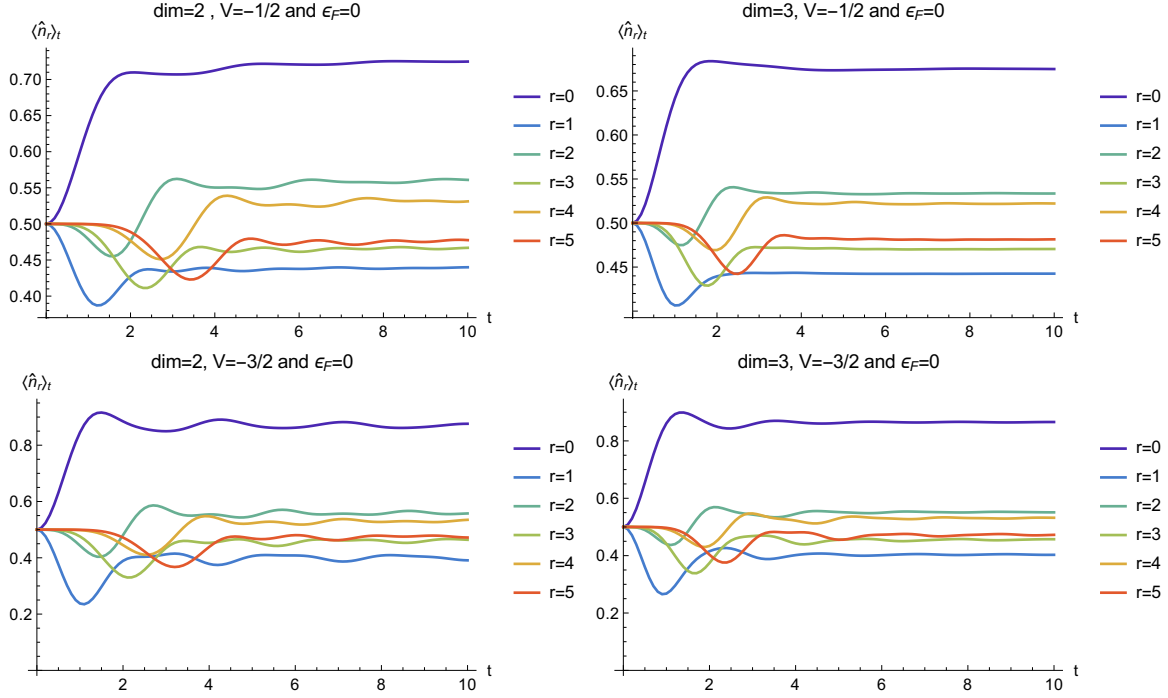


Figure 17: Short-time dynamics of the Fermi sea expectation values

c) Wave-front propagation

The on-site energy change at the quench disrupts the whole lattice, and this effect travels like a light cone by the hopping matrix. In figure 18, we depict the light-cone effect for the Bethe lattice by adding the distance to the normalized change. When the light cone reaches shell m , then the density starts its dynamic. This is no strict statement but more of a general trend. Spontaneously, we would connect the velocity of the cone v to the Fermi-velocity on the Bethe lattice,

$$v_F(\theta_F) = \left. \frac{\partial E(\theta)}{\partial \theta} \right|_{\theta=\theta_F} = 2 \sin(\theta_F) .$$

The light-cone velocity is independent of the filling in figure 18, and thus v is generally not equal to the Fermi velocity $v_F(\theta_F)$. All shell-symmetric states of the system are affected by the impurity quench and not only the states at the Fermi energy. Thus, the light cone should be connected to the maximum of the Fermi-velocities,

$$v = \max_{\theta_F} v_F(\theta_F) = 2 .$$

II DYNAMICAL FRIEDEL OSCILLATIONS

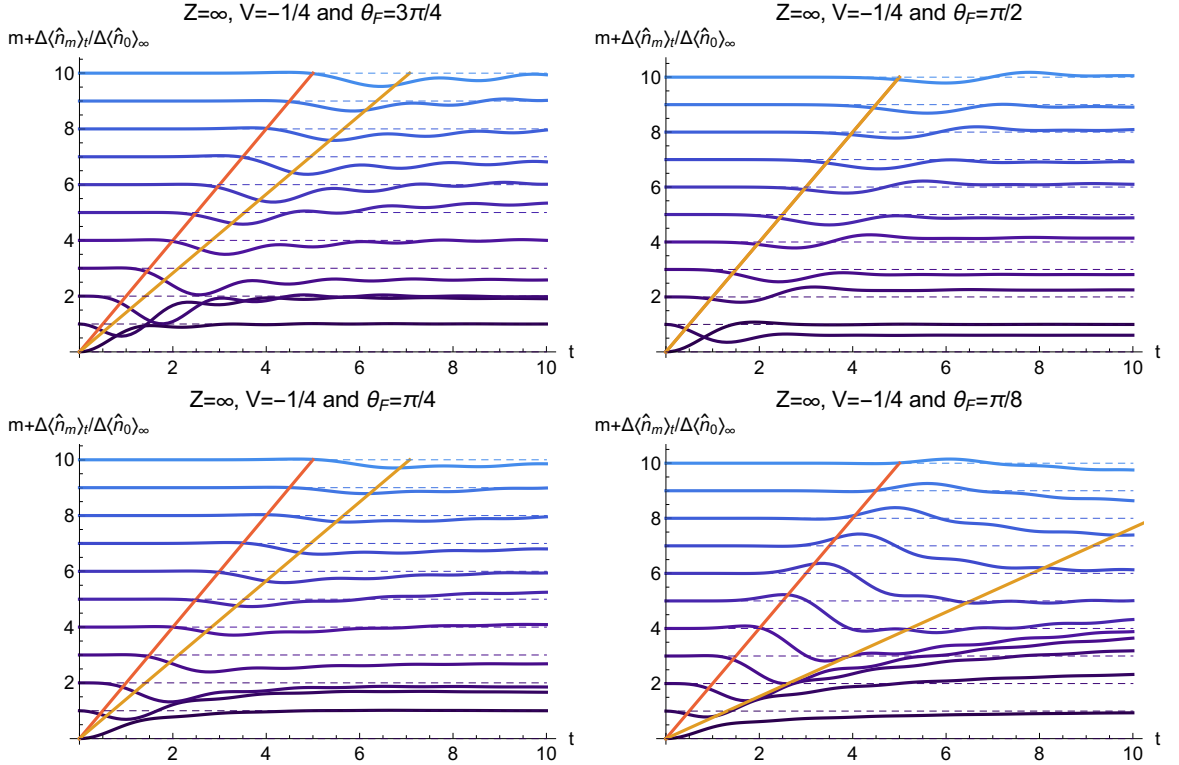


Figure 18: Propagation of the Friedel oscillations on the Bethe lattice. The orange line is the Fermi velocity and the red line the maximal Fermi velocity.

This statement is valid for the Bethe lattice, as we see in the four plots of figure 18. For the square lattice in figure 19, the slope of the light cone is ≈ 2 for all fillings. For the simple cubic lattice, the slope is 3 in figure 20. The Fermi velocity for the hypercubic lattice is

$$\mathbf{v}_F(\mathbf{k}) = \sum_{n=1}^d \mathbf{e}_n \sin(k_n) . \quad (\text{II.21})$$

Its maximum value for the square lattice is $\sqrt{2}$ and for the simple cubic $\sqrt{3}$. Consequently, the light-cone velocity in the shell-symmetric space is not equal to the maximum of the real-space Fermi velocities for these two lattices. We found in all lattices that the light-cone velocity is independent of the filling. Nevertheless, we were not able to find a congruent connection to the Fermi velocity. The light-cone velocity is equal to the half bandwidth in all examples. Probably, this statement is valid for our examples, but not in general.

4 RESULTS FOR TIME-DEPENDENT QUANTITIES

Equation (II.21) gives the Fermi velocity in real space, and we analyzed the cone velocity v in the space of shell-symmetric states. For the Bethe lattice, each shell-symmetric state occupies sites with a fixed distance to the central site. Thus, there is a unique definition of distance between a shell-symmetric state and the central site, and thus gives a clear value for the velocity. For the square or simple cubic lattice, on the other hand, the shell-symmetric states occupy various distances to the central site. Hence, the definition of the distance between two shell-symmetric states is not unique. Consequently, we should not connect the Fermi velocity in real space to the cone velocity for the shell-symmetric states. To predict the light cone in real space, we have to study our problem in the single-site basis. We suggest applying the computational scheme from the outlook subsection 6.a) to tackle this task.

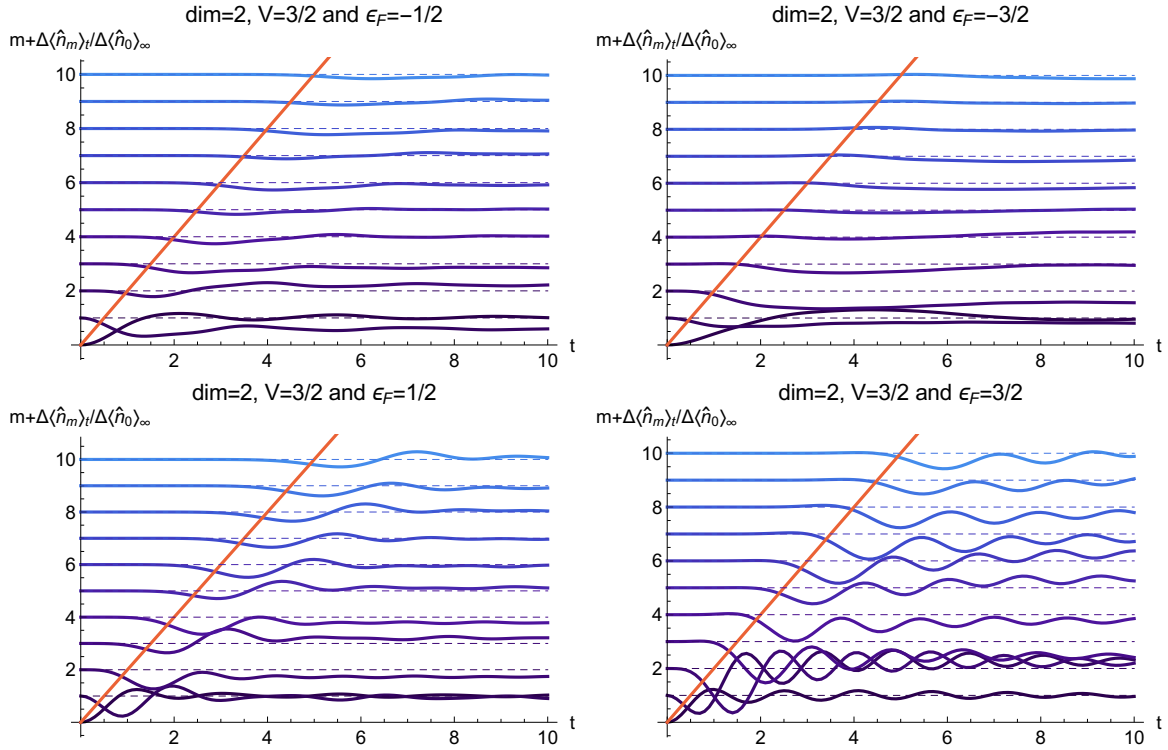


Figure 19: Propagation of the Friedel oscillations on the square lattice. The red line has a slope of 2

II DYNAMICAL FRIEDEL OSCILLATIONS

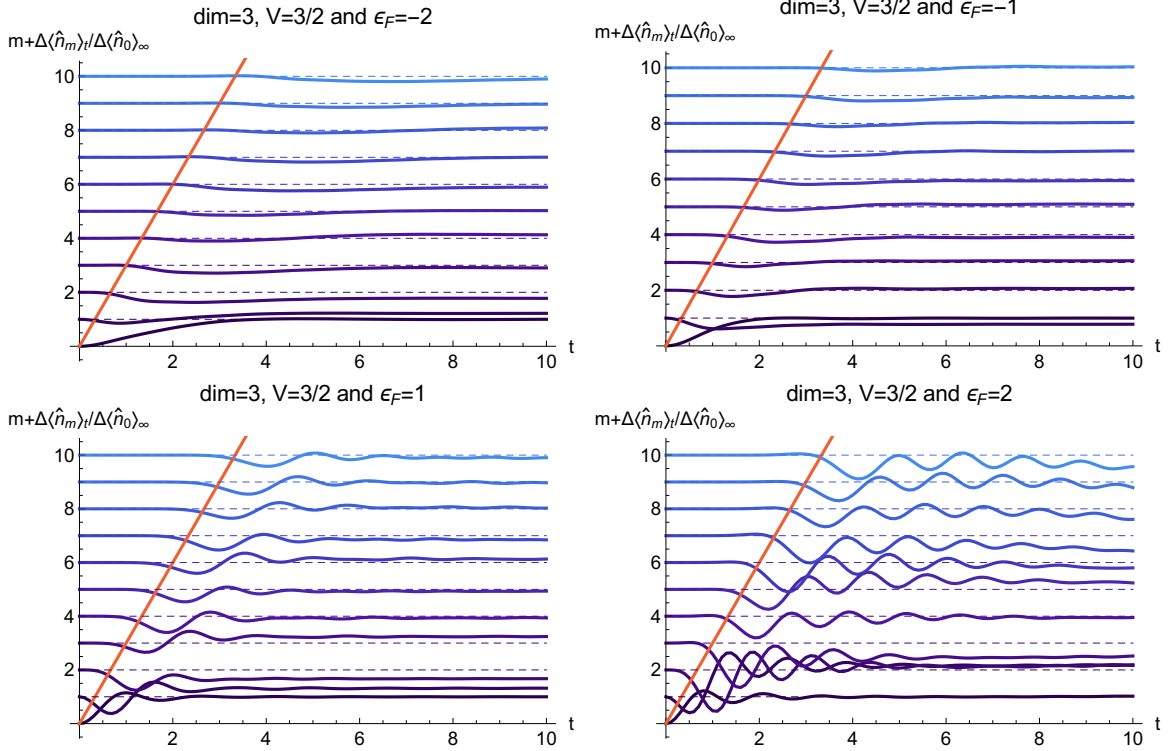


Figure 20: Propagation of the Friedel oscillations in the simple cubic lattice. The red line has a slope of 3

d) Steady-state Friedel oscillations

We learned that the Friedel oscillations relax to static values after the quench. We analyze in this section the details of this long-time limit. Its computation is easier than the real-time values because the numerical expensive terms vanish. At half-filling, the sign of density change alternates with r . We observed this already during the short-time section in figures 16 and 17. This change of the sign corresponds to the shortest possible oscillation length.

In figure 21 and 22, we see examples of long time solutions and observe that the oscillations' length strongly depends on the filling. The oscillation length increases away from half-filling and becomes quite smooth for nearly empty or nearly full bands. The power-law decay of the amplitude is similar in all examples. We conclude that the density change at the central site determines the scale of the whole Friedel oscillations. The density increase is two to three times greater in the plots on the right side than

4 RESULTS FOR TIME-DEPENDENT QUANTITIES

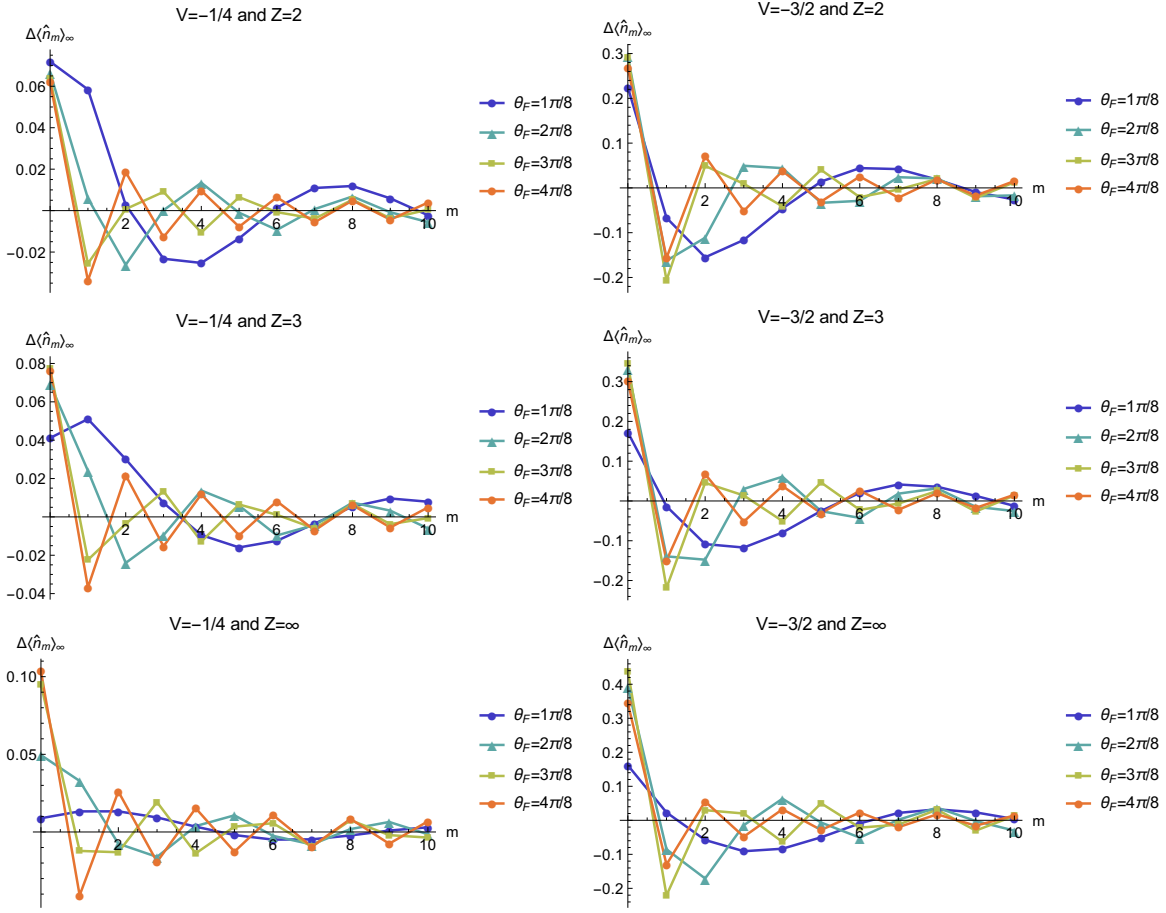


Figure 21: Friedel oscillations in the long-time limit for the Bethe lattice

those on the left side in figures 21 and 22. On the right side, we have strong impurities $V = -\frac{3}{2}$ and on the left weak ones $V = -\frac{1}{4}$ or $-\frac{1}{2}$. Thus, the impurity strength has a strong quantitative impact.

The impurity-site density varies with filling and impurity strength, as seen in figure 23. There arises a maximum for an intermediate impurity strength. It is more pronounced for low fillings, but its position is relatively independent of filling. To maximize the Friedel oscillations, we have to choose an intermediate impurity strength. Furthermore, the band should be at most half-filled for attractive impurities. Due to particle-hole symmetry, it should be at least half-filled for repulsive impurities. We note here that

II DYNAMICAL FRIEDEL OSCILLATIONS

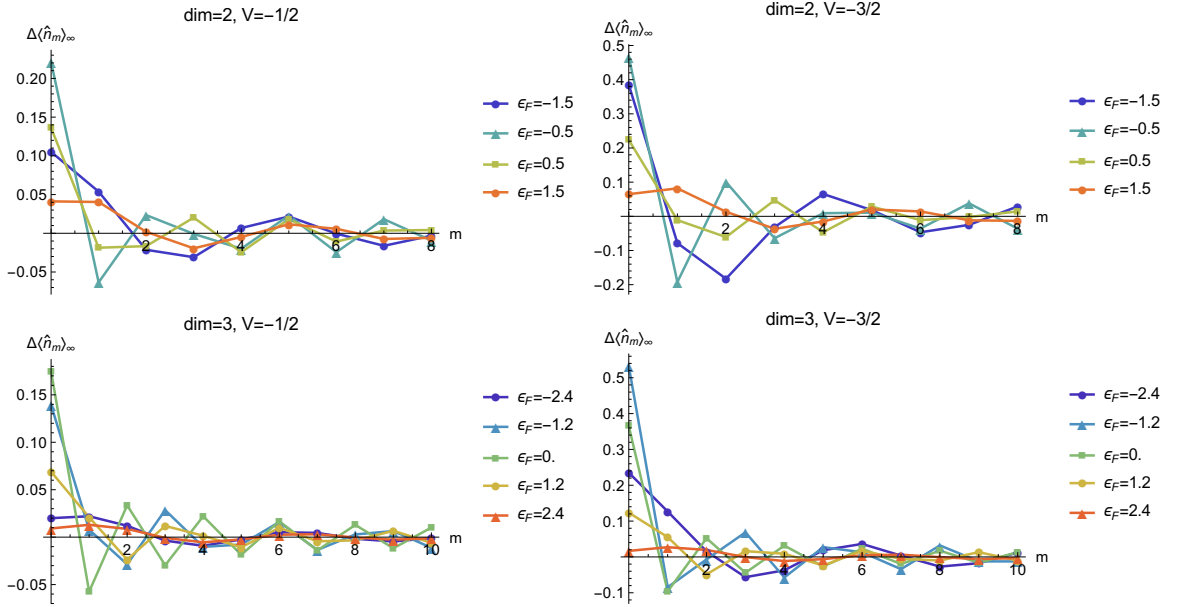


Figure 22: Friedel oscillations in the long-time limit for the square and simple cubic lattice

the long time-limit expectation value is not an analytic function at the point $|V| = |V_c|$. The expectation values converge differently in the two distinct regimes $|V| \lesssim |V_c|$.

e) Regular vs. generalized thermalization

On the one hand, we observe a decrease in density after a certain impurity strength in figure 23. But on the other hand, we expect increased density at the impurity site for more attractive impurities in the thermal expectation value. Thus, there is a qualitative deviation between the long-time limit and the thermal value.

Now, we calculate the corresponding thermal expectation value. The quench inserts energy in the scale $\sim V$, thus the average energy per site changes by $\sim V/L$. Therefore, we are still at zero temperature in the thermodynamic limit, and the thermal expectation value is computed for the many-particle ground state. All extended single-particle states below the Fermi-energy contribute. This is the same extended state contribution as in equation (II.20) for the long-time limit. If the impurity does not induce a localized state, then our observable relaxes to its thermal value. The localized state is occupied in the ground state for an attractive impurity as its energy is below the band. For a

4 RESULTS FOR TIME-DEPENDENT QUANTITIES

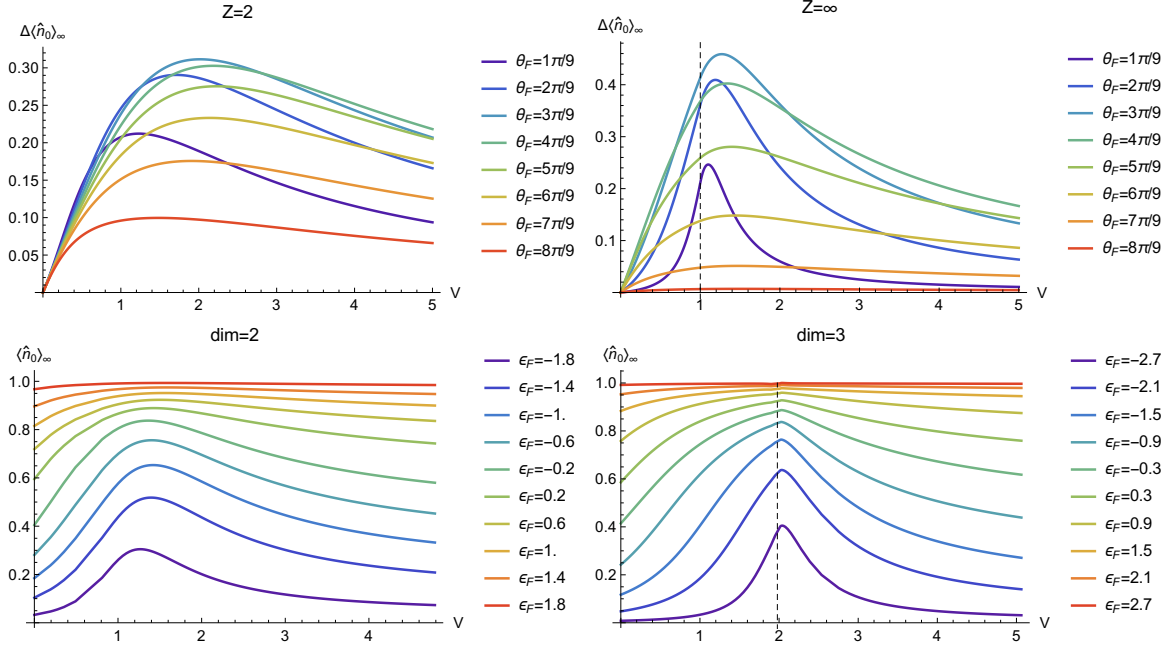


Figure 23: Impurity strength effect for different fillings

repulsive impurity, it is not occupied. Consequently, our observable does not thermalize for strong impurities $|V| > |V_c|$ because the bound state is always partially occupied in the long-time limit.

If no bound state exists, the diagonal ensemble expectation value, which captures the long-time limit, is equal to the ground state or thermal expectation value with $\beta \rightarrow \infty$. In the presence of a bound state, the thermal ensemble does not capture the correct values, and a generalized Gibbs ensemble (GGE)^{10–13} is necessary. The bound-state occupation number is an additional conserved quantity. Thus, the GGE is proportional to

$$\hat{\rho}_{\text{GGE}} \propto e^{-\beta \hat{H} - \mu \hat{N}} \times \begin{cases} 1 & |V| < |V_c| \\ \hat{n}_{z_1} \langle \text{FS} | \hat{n}_{z_1} | \text{FS} \rangle & |V| > |V_c| \end{cases} .$$

In many nonequilibrium problems of integrable models, generalized thermalization is observed.^{38,72} This means that the observables' long-time limit is captured by a GGE constructed from a set of conserved quantities. On the other hand, in most publications, finite systems are studied, in which the deviation decreases with the number of lattice sites L .^{12,13,38,72} We study our problem in the thermodynamic limit and an exact agreement of the long-time limit and the GGE prediction is possible and indeed observed here.

II DYNAMICAL FRIEDEL OSCILLATIONS

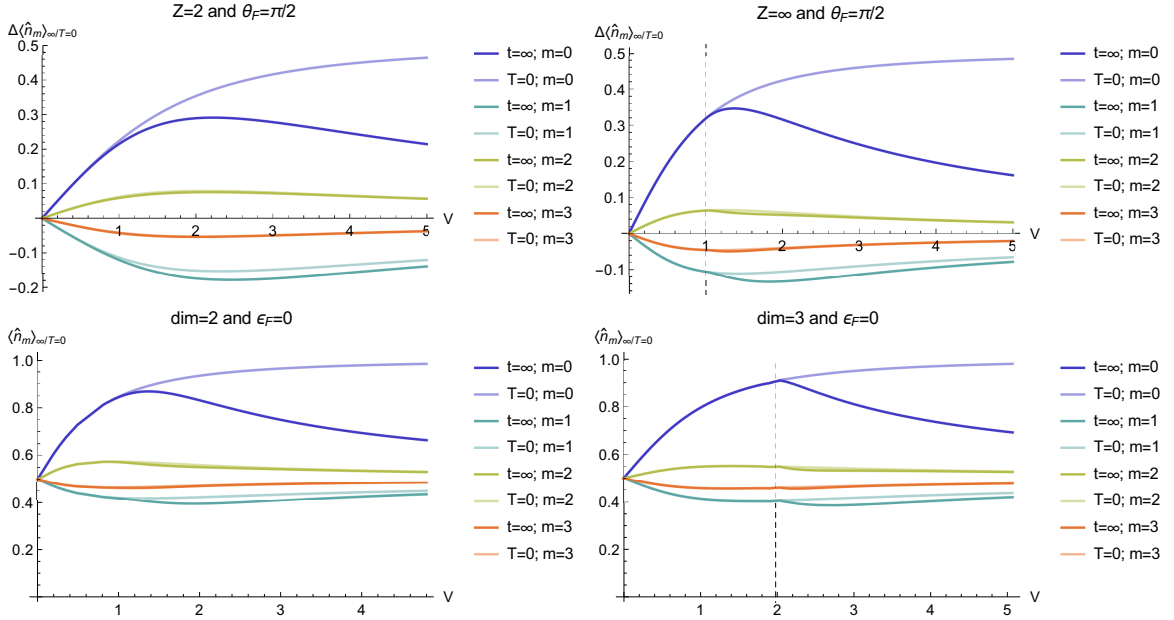


Figure 24: Comparison of long-time limit and thermal expectation value

The quantitative comparison of long-time limit and thermal value is plotted in figure 24. At the central site, the density increases monotonously for the thermal expectation value and peaks for the long-time limit at an intermediate impurity strength. For the sites in the vicinity of the impurity, we observe a similar trend that the density of the long-time limit is decreased compared to the thermal expectation value. This deviation decreases with distance to the central site. This phenomenon is inverted for repulsive impurities. The density of the long-time limit is higher than that of the thermal expectation value. Thus, the density after a strong repulsive impurity $V > V_c$ quench is higher in the long-time limit than in the ground state. We consider the regime $|V| < 1$ in the plots with $Z = 2$ and $\text{dim} = 2$ in figure 24. There the deviation between the thermal and long-time value is surprisingly small. We conclude that a weak impurity inducing a localized state lead to no exact thermalization, but we are close to it.

We study our problem in the shell-symmetric basis and not in the single-site basis. Thus, the density change depicted in all figures is only for the impurity site equal to an actual site. Our method can generally compute the values for the remaining sites. On the Bethe lattice, the conversion is simple. As equation (II.5) tells us, the density change at a single-site is smaller by a factor of N_r than the density change of the

4 RESULTS FOR TIME-DEPENDENT QUANTITIES

shell-symmetric state. For $Z = 2$, it is only a constant factor, but for $Z = 3$ this term grows exponentially with r , and for $Z \rightarrow \infty$, the local density change vanishes except for the central site. Hence, for $Z \geq 3$, the effect of Friedel oscillations on each site decrease exponentially, but the cumulative effect in a complete shell decays only with a power law.

On the square lattice and the simple-cubic lattice, the conversion is more evolved. First, the overlap of the investigated site $|\mathbf{i}\rangle$ with all shell-symmetric states $|r\rangle$ has to be computed. Second, we sum over the change in all shell-symmetric states to obtain the change on the site $|\mathbf{i}\rangle$,

$$\langle \mathbf{i} | \phi_k(t) \rangle - \langle \mathbf{i} | \phi_k(0) \rangle = \sum_r \langle \mathbf{i} | r \rangle (\langle r | \phi_k(t) \rangle - \langle r | \phi_k(0) \rangle) .$$

For the complete representation of site $|\mathbf{i}\rangle$, the non-shell-symmetric states are also required, but these are constant in time for our nonequilibrium problem.

In conclusion, we can observe two distinct long-time regimes after the quench. In the first case, when no localized state is generated, our observables relax to their thermal values. On the other hand, the localized state shifts the situation into the second case, and our observables relax to values derived from a GGE. Hence in our discussion of different systems, the most important question is whether a localized state is generated or not.

The GGE captures only the long-time limit for an extensive particles number as the Fermi sea. If we have a finite number of particles, then our observables oscillate like in figure 12, 14 and 15. We want to highlight that energy, particle, and bound state occupation conservation are enough to construct the correct GGE. This poses the question, under which circumstances the GGE after a local quench is computed from a few conserved quantities and not from an extensive amount. After global quenches, we generally need an extensive set of conserved quantities¹³ in an integrable system.

We return to our initial motivation to compare our results with the work of J. M. Zhang et al.⁵⁴⁻⁵⁶ First, we predict dynamical Friedel oscillations, which were observed for the chain,⁵⁴ for arbitrary lattices. Second, we also observe a density plateau after the quench.⁵⁵ We do not encounter the cusps in the single-particle states⁵⁶ because they first appear at the recurrence time, $t = R$ on the Bethe lattice. We cannot access this time scale because we first applied the limit $R \rightarrow \infty$. Thus, we are in the regime $t \ll R$ even if we take the limit $t \rightarrow \infty$. We do not observe the later plateaus⁵⁵ due to the same time-regime argument.

II DYNAMICAL FRIEDEL OSCILLATIONS

If we wanted to access this time scale, we would need to evaluate the finite Cayley tree instead of the Bethe lattice. One option is to tackle this task by constructing the exact eigenstates for finite Cayley trees. The other is to adapt our analytic evaluation to keep the times $t \sim R$ finite. Finally, it is more evolved to take the rim into account for the finite square and simple cubic lattice. There, the impurity quench destroys the symmetry of the system.

5 Summary for local quenches

We investigated the nonequilibrium dynamics after an on-site energy quench. The local density is our observable of choice. When only a single particle occupies the lattice, two very distinct regimes are observed. For weak impurities, the observables initially oscillate and then relax to constant values. For strong impurities, the oscillations become steady with constant amplitude and frequency. This emergence of a localized state is responsible for the two qualitatively different regimes. We only encounter the strong impurity regime for the special case of the chain ($Z = 2$) and the square lattice.

If the initial state is the Fermi sea, a many-particle state, then the qualitative behavior is similar in both regimes. Integrating over the different oscillation frequencies cancels them out, and relaxation occurs in both regimes. The impact of the impurity travels in a light cone through the lattice. The velocity of this cone is independent of filling. Therefore, the cone velocity is generally not equal to the Fermi velocity. Our investigation indicates that the velocity is equal to the maximum of all possible Fermi velocities. The physical reason is that the impurity affects all single-particle eigenstates and is not restricted to the states at the Fermi surface.

A comparison of the thermal and long-time expectation value still distinguishes the two regimes. In the weak-impurity regime, the local density thermalizes. However, the thermal and long-time expectation values differ from each other for strong impurities. We observe Friedel oscillation for the thermal and the time-dependent expectation values, and their oscillation length strongly depends on the filling. The Friedel oscillations inherit the thermalization for weak impurities and the lack of thermalization in presence of the bound state. We conclude that a single state outside the band inhibits thermalization for noninteracting systems, and the observables relax to a generalized Gibbs ensemble.^{10–13}

As discussed in the next chapter, self-consistent and time-dependent perturbation theory^{73,74} predicts thermalization of the occupation numbers for small interaction quenches. Thus, we also expect thermalization if we add a small interaction to our Hamiltonian. For weak impurities, the time scale of thermalization is the inverse bandwidth, because it happens already without interactions. For strong impurities, the interactions are necessary for thermalization, and thus the thermalization time scale will increase. Bertini et al.⁷⁵ developed a method to compute the relaxation dynamics of local observables for weakly interacting systems. They predict a relaxation time scale of $t = \tau/g$ for local observables. We expect thermalization of the local density in this

II DYNAMICAL FRIEDEL OSCILLATIONS

time scale $t = \tau/g$ by adding weak interactions. This scenario for thermalization in presence of a bound state would be worthwhile further investigate. In any case, weakly interacting systems with impurities are expected to thermalize on very distinct time scales for the two regimes of weak and strong impurities.

For our evaluations, we constructed all eigenstates for a single impurity potential in the thermodynamic limit. This is possible because the symmetry separates the Hilbert space into distinct subspaces with respect to the Hamiltonian. In the shell-symmetric basis $\hat{H}_0^n|0\rangle$, we have an effectively one-dimensional system. This is strictly true for the Cayley tree or in the thermodynamic limit for other lattices. The computation in the shell-symmetric basis requires only the density of states. Any density of states with finite bandwidth can be represented in infinite dimensions by a set of hopping amplitudes, although long-range hopping amplitudes are typically required.⁷¹ Thus, the dimensionality of the lattice is not apparent in the time evolution in the shell-symmetric states. With full information about the lattice, we can compute the time evolution for any site from the time evolution of the shell-symmetric states. In conclusion, this inhomogeneous problem was solved to a large extent here. However, in order to study the problem directly in the single-site basis, we need to generalize our evaluation procedure. This is done in the outlook subsection 6.a). A further generalization is necessary for the study of periodically driven or ramped impurities. We give a formal solution to this problem in outlook subsection 6.b) and verify it for the quench. Our method could also be used to compute additional quantities, e.g., correlation functions.⁷⁶

it is also possible to study finite size effects. We have the same eigenstates for a finite Cayley tree, but we must to compute the eigenvalues explicitly. For a large but finite Cayley tree, one could evaluate the overlap of states.⁷⁷ Due to the orthogonality catastrophe,⁷⁸ we expect it to vanish in the infinite size limit. Furthermore, we could then observe the reflection of the wavefront at the rim of the Cayley tree may be observed. This type of reflection is known to lead to cusps in the dynamics of single-particle states⁵⁶ and steps in the tight-binding chain's local density.⁵⁵ We expect analogous effects for the finite Cayley tree. For the square or simple cubic lattice, the computation of finite systems is more tedious because its surface destroys the advantageous symmetry.

6 Technical Outlook

a) Site-resolved computation

Here, we show an alternative way to derive our evaluation formulas (II.13) and (II.14). It will not depend on a particular basis and is applicable in the single-site basis. We start from

$$\Phi_{n,\mathbf{k}}(t) = \langle n | e^{-it(\hat{H}_0 + \hat{V})} | \Phi_{\mathbf{k}} \rangle$$

and apply the Laplace transformation

$$\begin{aligned} \mathcal{L}_{t \rightarrow x}(\Phi_{n,\mathbf{k}}(t)) &= \int_0^{\infty} dt e^{-tx} \langle n | e^{-it(\hat{H}_0 + \hat{V})} | \Phi_{\mathbf{k}} \rangle = i \langle n | \left(ix - \hat{H}_0 - \hat{V} \right)^{-1} | \Phi_{\mathbf{k}} \rangle \\ &= i \sum_l G_{nl}(ix) \langle l | \Phi_{\mathbf{k}} \rangle . \end{aligned}$$

Now, we obtained an expression based on the Green function with impurity

$$G_{nl}(z) = \langle n | \left(z - \hat{H}_0 - \hat{V} \right)^{-1} | l \rangle .$$

Next, we apply the cavity formula,

$$G_{nl}(z) = g_{nl}(z) + \frac{g_{n0}(z)Vg_{0l}(z)}{1 - Vg_{00}(z)} \quad \text{with} \quad g_{nl}(z) = \langle n | \left(z - \hat{H}_0 \right)^{-1} | l \rangle ,$$

and rewrite the Laplace transformed in terms of the Green function without impurity $g_{nm}(z)$,

$$\mathcal{L}_{t \rightarrow x}(\Phi_{n,\mathbf{k}}(t)) = i \frac{\langle n | \Phi_{\mathbf{k}} \rangle}{ix - \epsilon_{\mathbf{k}}} + \frac{ig_{n0}(ix)V\langle 0 | \Phi_{\mathbf{k}} \rangle}{(ix - \epsilon_{\mathbf{k}})(1 - Vg_{00}(ix))} .$$

For the inverse Laplace transformation, we utilize the Mellin's inverse formula,

$$\Phi_{n,\mathbf{k}}(t) = \mathcal{L}_{x \rightarrow t}^{-1}(\mathcal{L}_{t \rightarrow x}(\Phi_{n,\mathbf{k}}(t))) = \int_{-i\infty + \gamma}^{i\infty + \gamma} \frac{dx}{2\pi i} e^{xt} \mathcal{L}_{t \rightarrow x}(\Phi_{n,\mathbf{k}}(t)) . \quad (\text{II.22})$$

The parameter γ has to be chosen larger than the real parts of all poles. The poles of $G_{nl}(ix)$ lie all on the imaginary axis. Thus, $\gamma > 0$ is sufficient. We rotate the complex plane by substitution of the integration variable $x = -iz$. We choose the infinitesimal but positive number δ for γ and obtain

$$\Phi_{n,\mathbf{k}}(t) = - \int_{-\infty + i\delta}^{\infty + i\delta} \frac{dz}{2\pi i} e^{-izt} \left(\frac{\langle n | \Phi_{\mathbf{k}} \rangle}{z - \epsilon_{\mathbf{k}}} + \frac{g_{n0}(z)V\langle 0 | \Phi_{\mathbf{k}} \rangle}{(z - \epsilon_{\mathbf{k}})(1 - Vg_{00}(z))} \right) .$$

II DYNAMICAL FRIEDEL OSCILLATIONS

Next, we close the integration path by adding a half circle in the lower complex plane. Thus, we use the integration path L , which is depicted in figure 25. If the eigenvalue equation $1 = Vg_{00}(E)$ (II.10) is fulfilled, then an additional pole appears at $z = E$. The previous expression now splits into two terms,

$$\Phi_{n,\mathbf{k}}(t) = \theta(|V| - |V_c|)\Phi_{n,\mathbf{k}}^{\text{loc}}(t) + \Phi_{n,\mathbf{k}}^{\text{ext}}(t) .$$

The contribution of the localized state is computed by the residue theorem and gives

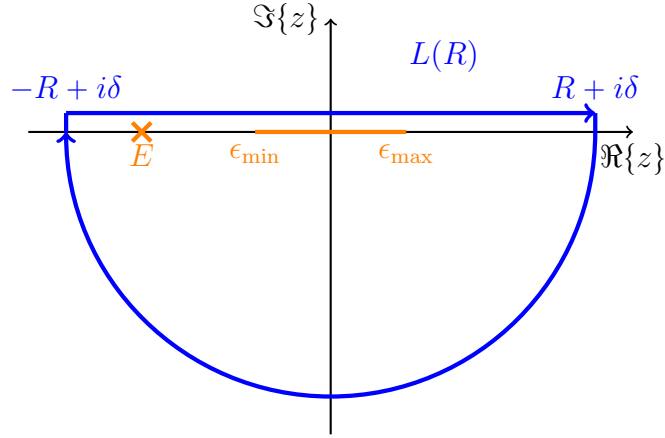


Figure 25: Complex integration path $L(R)$ to illustrate $L = \lim_{R \rightarrow \infty} L(R)$

the same term as in (II.13),

$$\begin{aligned} \Phi_{n,\mathbf{k}}^{\text{loc}}(t) &= \frac{\langle 0 | \Phi_{\mathbf{k}} \rangle V g_{n0}(E) e^{-itE}}{E - \epsilon_{\mathbf{k}}} \text{Res} \left(\frac{1}{1 - V g_{00}(z)}, E \right) \\ &= - \frac{\langle 0 | \Phi_{\mathbf{k}} \rangle g_{n0}(E) e^{-itE}}{(E - \epsilon_{\mathbf{k}}) g'_{00}(E)} . \end{aligned}$$

The branch cut along the band gives the extended states' contribution $\Phi_{n,\mathbf{k}}^{\text{ext}}(t)$. We compute it by integrating slightly above the band from left to right and slightly below the band from right to left,

$$\begin{aligned}
\Phi_{n,\mathbf{k}}^{\text{ext}}(t) &= \langle n|\Phi_{\mathbf{k}}\rangle e^{-it\epsilon_{\mathbf{k}}} - \int_{\epsilon_{\min}}^{\epsilon_{\max}} \frac{d\epsilon}{2\pi i} \sum_{s=\pm 1} \frac{s \langle 0|\Phi_{\mathbf{k}}\rangle e^{-it(\epsilon+is\delta)} V g_{n0}(\epsilon+is\delta)}{(1-Vg_{00}(\epsilon+is\delta))(\epsilon+is\delta-\epsilon_{\mathbf{k}})} \\
&= \left(\langle n|\Phi_{\mathbf{k}}\rangle + \frac{\langle 0|\Phi_{\mathbf{k}}\rangle g_{n0}(\epsilon_{\mathbf{k}}+i\delta)V}{1-Vg_{00}(\epsilon_{\mathbf{k}}+i\delta)} \right) e^{-it\epsilon_{\mathbf{k}}} \\
&\quad - \int_{\epsilon_{\min}}^{\epsilon_{\max}} \frac{d\epsilon}{2\pi i} \frac{\langle 0|\Phi_{\mathbf{k}}\rangle e^{-it\epsilon}}{(\epsilon-i\delta-\epsilon_{\mathbf{k}})} \left(\frac{Vg_{n0}(\epsilon+i\delta)}{1-Vg_{00}(\epsilon+i\delta)} - \frac{Vg_{n0}(\epsilon-i\delta)}{1-Vg_{00}(\epsilon-i\delta)} \right).
\end{aligned} \tag{II.23}$$

To obtain the second line from the first, we assumed $e^{-it(\epsilon\pm\delta)} = e^{-it\epsilon}$ and used the identity,

$$\int \frac{dx}{2\pi i} \frac{f(x)}{x+i\delta} = -f(0) + \int \frac{dx}{2\pi i} \frac{f(x)}{x-i\delta}.$$

When we insert our shell-symmetric basis $|n\rangle = \hat{H}_0^n|0\rangle$ and use the identities

$$g_{00}(\epsilon-i\delta) - g_{00}(\epsilon+i\delta) = 2\pi i\rho(\epsilon)$$

and (II.15), we recover the result from (II.14). Thus, this section is an additional check for our evaluation formula. The advantage of this derivation is that we do not assume specific $g_{nl}(z)$. Hence, we can insert arbitrary ones, e.g., the Green functions from any one single site to another single site. Therefore, we found a way to study our quench problem in an arbitrary single-particle basis.

II DYNAMICAL FRIEDEL OSCILLATIONS

To compute the density change at a specific site, we sum over all \mathbf{k} and have a problem of the general form,

$$\begin{aligned}
\langle \hat{n}_n \rangle_t &= \sum_{\epsilon_{\mathbf{k}} < \epsilon_F} |\langle n | \Phi_{\mathbf{k}} \rangle + \langle 0 | \Phi_{\mathbf{k}} \rangle f(\epsilon_{\mathbf{k}})|^2 \\
&= \sum_{\epsilon_{\mathbf{k}} < \epsilon_F} |\langle r | \Phi_{\mathbf{k}} \rangle|^2 + |\langle 0 | \Phi_{\mathbf{k}} \rangle f(\epsilon_{\mathbf{k}})|^2 + 2\Re \{ f(\epsilon_{\mathbf{k}}) \langle 0 | \Phi_{\mathbf{k}} \rangle \langle \Phi_{\mathbf{k}} | n \rangle \} \\
&= \int_{\epsilon_{\min}}^{\epsilon_F} d\epsilon \rho_{nn}(\epsilon) + \rho_{00}(\epsilon) |f(\epsilon)|^2 + 2\rho_{0n}(\epsilon) \Re \{ f(\epsilon) \} , \\
\rho_{nl}(\epsilon) &= \sum_{\mathbf{k}} \delta(\epsilon - \epsilon_{\mathbf{k}}) \langle n | \Phi_{\mathbf{k}} \rangle \langle \Phi_{\mathbf{k}} | l \rangle .
\end{aligned}$$

We require the site-dependent $\rho_{rl}(\epsilon)$ and obtain them from the imaginary part of the Green functions,

$$\begin{aligned}
\Im \{ g_{nl}(\epsilon - i\delta) \} &= \Im \left\{ \langle n | \frac{1}{\epsilon - i\delta - \hat{H}_0} | l \rangle \right\} \\
&= \sum_{\mathbf{k}} \Im \left\{ \frac{1}{\epsilon - i\delta - \epsilon_{\mathbf{k}}} \right\} \langle n | \Phi_{\mathbf{k}} \rangle \langle \Phi_{\mathbf{k}} | l \rangle \\
&= \pi \sum_{\mathbf{k}} \delta(\epsilon - \epsilon_{\mathbf{k}}) \langle r | \Phi_{\mathbf{k}} \rangle \langle \Phi_{\mathbf{k}} | l \rangle = \pi \rho_{nl}(\epsilon) .
\end{aligned}$$

If the Green functions $g_{rl}(z)$ are available, then we can compute the dynamic after an impurity quench in the corresponding single-particle basis. The single-site basis results are particularly suited for the study of the light-cone effect. Moreover, this procedure enables us to study the light-cone velocity in real space.

As an outlook, this method could be applied to the square lattice. There, the Green functions are analytically available,⁷⁹ and we can compute site-resolved dynamical Friedel oscillations. This allows us to study the cone velocity in different directions. First, the Fermi velocity in the diagonal direction is higher than in the direction of the lattice axis. Hence, we expect a higher velocity along the diagonal than along the lattice axis. The second feature, we intend to analyze is the Friedel oscillations. Their wavelength and decay rate should depend on the direction as well.

b) From quenched to ramped and driven impurities

Here, we give an outlook on how to compute the density modulations after continuously increasing the impurity strength. We obtain a formal solution (II.26), which leads to a

differential equation (II.27). At the end of this outlook section, we insert the quench as a ramp protocol, and the result is congruent with the previous section.

Formal solution

The ramp Hamiltonian is

$$\hat{H}(t) = \hat{H}_0 + f(t)\hat{V} \quad \text{with} \quad f(t < 0) = 0 .$$

We work in the shell-symmetric basis, and the quantities of interest are

$$\Phi_{n,\mathbf{k}}(t) = \langle 0 | \hat{H}_0^n \hat{U}(t) | \Phi_{\mathbf{k}} \rangle .$$

The differential equation for the propagator is

$$i \frac{\partial}{\partial t} \hat{U}(t) = (\hat{H}_0 + f(t)\hat{V}) \hat{U}(t) .$$

From that, we deduce coupled differential equations,

$$i \frac{\partial}{\partial t} \Phi_{n,\mathbf{k}}(t) = \Phi_{n+1,\mathbf{k}}(t) + f(t) V \overline{\epsilon^n} \Phi_{0,\mathbf{k}}(t) .$$

By induction, it is easy to show that

$$\Phi_{n,\mathbf{k}}(t) = \left(\left(i \frac{\partial}{\partial t} \right)^n - \sum_{m=0}^{n-1} \left(i \frac{\partial}{\partial t} \right)^{n-1-m} V f(t) \overline{\epsilon^m} \right) \Phi_{0,\mathbf{k}}(t) . \quad (\text{II.24})$$

Therefore, it is sufficient to compute $\Phi_{0,\mathbf{k}}(t)$ because all other $\Phi_{n,\mathbf{k}}(t)$ are easily derived from it. Next, we impose the boundary conditions that far away sites are not affected by the impurity. The state $\hat{H}_0^n |0\rangle$ captures the earliest impact for sites that are n hops away from the impurity. Hence, we choose the boundary condition as

$$\Phi_{n,\mathbf{k}}(t) = \langle 0 | \hat{H}_0^n e^{-it\hat{H}_0} | \Phi_{\mathbf{k}} \rangle = \epsilon_{\mathbf{k}}^n e^{-it\epsilon_{\mathbf{k}}} \langle 0 | \Phi_{\mathbf{k}} \rangle \quad \text{as} \quad n \rightarrow \infty \quad (\text{II.25})$$

Inserting the boundary condition (II.25) into (II.24) gives

$$\begin{aligned} \epsilon_{\mathbf{k}}^n e^{-it\epsilon_{\mathbf{k}}} \langle 0 | \Phi_{\mathbf{k}} \rangle &= \left(\left(i \frac{\partial}{\partial t} \right)^n - \sum_{m=0}^{n-1} \left(i \frac{\partial}{\partial t} \right)^{n-1-m} V f(t) \overline{\epsilon^m} \right) \Phi_{0,\mathbf{k}}(t) \quad \text{as} \quad n \rightarrow \infty , \\ e^{-it\epsilon_{\mathbf{k}}} \langle 0 | \Phi_{\mathbf{k}} \rangle &= \left(1 - \sum_{m=0}^{n-1} \left(i \frac{\partial}{\partial t} \right)^{-1-m} V f(t) \overline{\epsilon^m} \right) \Phi_{0,\mathbf{k}}(t) \quad \text{as} \quad n \rightarrow \infty . \end{aligned}$$

II DYNAMICAL FRIEDEL OSCILLATIONS

From the first to the second line, we integrated n times. When we take the limit $n \rightarrow \infty$, we obtain the local Green function,

$$e^{-it\epsilon_{\mathbf{k}}}\langle 0|\Phi_{\mathbf{k}}\rangle = \left(1 - g_{00}\left(i\frac{\partial}{\partial t}\right)Vf(t)\right)\Phi_{0,\mathbf{k}}(t).$$

Inverting this equation gives us a formal solution to a general local ramp problem,

$$\Phi_{0,\mathbf{k}}(t) = \left(1 - g_{00}\left(i\frac{\partial}{\partial t}\right)Vf(t)\right)^{-1} e^{-it\epsilon_{\mathbf{k}}}\langle 0|\Phi_{\mathbf{k}}\rangle. \quad (\text{II.26})$$

Differential equation

We derive a differential equation from the formal solution (II.26). First, we multiply our quantity by the inverse complex phase,

$$\tilde{\Phi}_{0,\mathbf{k}}(t) = e^{it\epsilon_{\mathbf{k}}}\Phi_{0,\mathbf{k}}(t).$$

Then the $\epsilon_{\mathbf{k}}$ terms cancel each other when we apply the time derivative

$$\frac{\partial}{\partial t}\tilde{\Phi}_{0,\mathbf{k}}(t) = e^{it\epsilon_{\mathbf{k}}}\left[\frac{\partial}{\partial t}\left(1 - g_{00}\left(i\frac{\partial}{\partial t}\right)Vf(t)\right)^{-1}\right]e^{-it\epsilon_{\mathbf{k}}}\langle 0|\Phi_{\mathbf{k}}\rangle.$$

The time derivative of the operator is computed as

$$\begin{aligned} & \frac{\partial}{\partial t}\left(1 - g_{00}\left(i\frac{\partial}{\partial t}\right)Vf(t)\right)^{-1} \\ &= \sum_{m=0}^{\infty}\frac{\partial}{\partial t}\left(g_{00}\left(i\frac{\partial}{\partial t}\right)Vf(t)\right)^m \\ &= \sum_{m=1}^{\infty}\sum_{l=0}^{m-1}\left(g_{00}\left(i\frac{\partial}{\partial t}\right)Vf(t)\right)^{m-1-l}g_{00}\left(i\frac{\partial}{\partial t}\right)Vf'(t)\left(g_{00}\left(i\frac{\partial}{\partial t}\right)Vf(t)\right)^l \\ &= \sum_{m=0}^{\infty}\left(g_{00}\left(i\frac{\partial}{\partial t}\right)Vf(t)\right)^m g_{00}\left(i\frac{\partial}{\partial t}\right)Vf'(t)\sum_{l=0}^{\infty}\left(g_{00}\left(i\frac{\partial}{\partial t}\right)Vf(t)\right)^l \\ &= \left(1 - g_{00}\left(i\frac{\partial}{\partial t}\right)Vf(t)\right)^{-1} g_{00}\left(i\frac{\partial}{\partial t}\right)Vf'(t)\left(1 - g_{00}\left(i\frac{\partial}{\partial t}\right)Vf(t)\right)^{-1}. \end{aligned}$$

We insert it back into the previous equation and obtain the differential equation,

$$\frac{\partial}{\partial t}\tilde{\Phi}_{0,\mathbf{k}}(t) = e^{it\epsilon_{\mathbf{k}}}\left(1 - g_{00}\left(i\frac{\partial}{\partial t}\right)Vf(t)\right)^{-1} g_{00}\left(i\frac{\partial}{\partial t}\right)Vf'(t)e^{-it\epsilon_{\mathbf{k}}}\tilde{\Phi}_{0,\mathbf{k}}(t). \quad (\text{II.27})$$

Evaluation for quench protocol

Now, we test the formal expression (II.26) by inserting the step function as the ramping protocol into equation (II.27). The integration gives

$$\begin{aligned} \tilde{\Phi}_{0,\mathbf{k}}(t) - \tilde{\Phi}_{0,\mathbf{k}}(0^-) &= \int_{0^-}^t d\tau e^{i\tau\epsilon_{\mathbf{k}}} \left(1 - g_{00} \left(i \frac{\partial}{\partial \tau} \right) V f(\tau) \right)^{-1} \\ &\quad g_{00} \left(i \frac{\partial}{\partial \tau} \right) V f'(\tau) e^{-i\tau\epsilon_{\mathbf{k}}} \tilde{\Phi}_{0,\mathbf{k}}(\tau) . \end{aligned} \quad (\text{II.28})$$

We insert on the right-hand side the identity of the delta function,

$$f'(\tau) = \delta(\tau) = \int_{-\infty}^{\infty} \frac{d\omega}{2\pi} e^{-i\tau\omega} .$$

For the quench, we can apply the approximations

$$\tilde{\Phi}_{0,\mathbf{k}}(\tau) \approx \tilde{\Phi}_{0,\mathbf{k}}(0^-) = \langle 0 | \Phi_{\mathbf{k}} \rangle , \quad f(\tau) \approx f(\tau > 0) = 1 .$$

If we shift ω away from the real axis, we can evaluate the derivatives and integration with respect to τ in equation (II.28). We have to shift ω into the upper half of the complex plane because then all poles are below the integration path,

$$\tilde{\Phi}_{0,\mathbf{k}}(t) - \tilde{\Phi}_{0,\mathbf{k}}(0^-) = \langle 0 | \Phi_{\mathbf{k}} \rangle \int_{-\infty+i\delta}^{\infty+i\delta} \frac{d\omega}{2\pi} \frac{e^{-it\omega} - 1}{-i\omega} \frac{g_{00}(\omega + \epsilon_{\mathbf{k}})V}{1 - g_{00}(\omega + \epsilon_{\mathbf{k}})V} .$$

If we shift ω into the lower half of the complex plane, we obtain a trivial result. The final step is to substitute $\omega = z - \epsilon_{\mathbf{k}}$, and we recover the result from the Laplace transformation method (II.22).

This check confirms the validity of equations (II.26) and (II.27). The next step would be developing a numerical procedure that computes the density due to an impurity, which is continuously switched on or periodically driven.

III Prethermalization induced by weak interactions

1 Introduction to the perturbative expansion

In this chapter, we start again from a translationally invariant system, but now the perturbation is spatially homogeneous. Therefore, local interactions induce nontrivial dynamics in the system as the hopping Hamiltonian is diagonal in reciprocal space. In particular, we investigate two scenarios for driving of a correlated electron system. The first one is interaction-driven and the second one is hopping-amplitudes-driven. In both cases, all expectation values have trivial dynamics for the noninteracting state. We will include the interactions perturbatively and the hopping terms nonperturbatively to describe the prethermal regime.

Möckel and Kehrein established a method to capture the dynamics after a weak interaction quench^{73,80} and applied it to the Hubbard model in infinite spatial dimensions. It predicts a nonthermal steady state for intermediate times, which is called the prethermal state. Later on, quasiparticle scattering governed by the Boltzmann equation^{45–47} sets in, and a thermal distribution forms. We note that prethermalization can also be understood on statistical grounds.⁸¹ Here, we address several open questions concerning the prethermal steady state. While the prethermal state is a general feature and is expected in most models, there exist counterexamples, e.g., the one- and two-dimensional Hubbard model,^{82,83} which does not relax to a steady state for individual momentum occupation numbers.

We tackle several model-independent questions in section 2. The first one is the development of a general method. The initial approach was a leading-order interaction expansion for continuous unitary transformations.^{73,80} The same result was reproduced by evaluating Keldysh-Green's function diagrams⁸⁴ and by a single canonical transformation.⁸⁵ The fundamental concept in these approaches is an expansion in interaction strength. We apply the interaction representation in subsection a) and obtain the expression directly for arbitrary models, protocols, and observables. We evaluate the first finite correction term and assign the observables into two categories. The observables from the first category have a finite first-order correction. The first-order term of the other category vanishes, and we thus compute the second-order term. The fundamental difference between the two classes of observables is the number of convolutions in time: First-order observables have one time convolution, and second-order observables have two. This adds a memory effect to the second-order observables. Second, we construct constants of motions for an interacting system from the adiabatic theorem.^{86–88} We

1 INTRODUCTION TO THE PERTURBATIVE EXPANSION

build a generalized Gibbs ensemble (GGE),¹⁰⁻¹³ which describes the prethermalization plateau⁸⁵ after arbitrary driving.

We investigate interaction-driven problems in section 3, which are in particular quenches,^{73,80} ramps,⁸⁴ and periodic drives.⁸⁹ We define in subsection a) an effective nonequilibrium protocol with prior adiabatic switching⁸⁶⁻⁸⁸ to include initial interacting states. We evaluate the general terms for first- and second-order observables. We choose the Hubbard model with infinite spatial dimension as our example model and compute its expectation values in subsection b). The first investigated phenomenon is crossing points in a transients as discussed in subsection c). The next one is the relaxation behavior in subsection d). This is followed by the subsection concerning ramps e) as they bridge the gap between adiabatic switching and quenching. The final subsection f) covers periodic drives. Our findings in section 3 reproduce the results of previous work^{73,80,84,85,89} and are more comprehensive in certain aspects.

The last and largest section 4 covers the prethermal dynamics after an electric field pulse. It shows that an electric field pulse induces a prethermal steady state in weakly interacting systems. Peierls' substitution captures the external field, and therefore we have a hopping amplitude-driven process. The methods of the previous sections need to be adapted to this case. Generally, the computation becomes more cumbersome, but our method includes all orders in electric field strength and is still perturbative in interaction strength. The results indicate which order in interaction and field strength is sufficient to capture the prethermal state.

In summary, this chapter predicts a generalization of previous approaches to describe the prethermal state. Our method works for arbitrary time protocols and arbitrary interacting initial states, leading to new applications of which some are discussed here.

2 General expansion in interaction strength

a) Formal time integration

We first derive formal expressions for time-dependent observables. These steps are similar in both following parts, but we use different representations. The interaction representation will give us equations (III.5) and (III.7), which describe the prethermal regime. These two formulas will be the main result of this subsection.

Schrödinger representation

We will express a Heisenberg operator in a commutator series. The time evolution of a state is captured by the time evolution operator $\hat{U}(t)$. It has the initial condition $\hat{U}(0) = 1$ and the differential equation ($\hbar = 1$)

$$\frac{d}{dt}\hat{U}(t) = -i\hat{H}(t)\hat{U}(t) .$$

Hence, we can write the Heisenberg equation of motion as

$$\frac{d}{dt}\hat{U}^\dagger(t)\hat{A}\hat{U}(t) = \hat{U}^\dagger(t) \left[i\hat{H}(t), \hat{A} \right] \hat{U}(t) .$$

We integrate the differential equation and obtain

$$\hat{U}^\dagger(t)\hat{A}\hat{U}(t) = \hat{A} + \int_0^t dt_1 \hat{U}^\dagger(t_1) \left[i\hat{H}(t_1), \hat{A} \right] \hat{U}(t_1) . \quad (\text{III.1})$$

This integral equation (III.1) is valid for every operator \hat{A} . Therefore, \hat{A} is allowed to be dependent on a parameter or a set of parameters. Thus, we can replace \hat{A} by the right-hand side of equation (III.1) and receive

$$\hat{U}^\dagger(t)\hat{A}\hat{U}(t) = \hat{A} + i \int_0^t dt_1 \left[\hat{H}(t_1), \hat{A} \right] + i^2 \int_0^t dt_1 \int_0^{t_1} dt_2 \hat{U}^\dagger(t_2) \left[\hat{H}(t_2), \left[\hat{H}(t_1), \hat{A} \right] \right] \hat{U}(t_2) .$$

The operator $[\hat{H}(t_n), \dots [\hat{H}(t_1), \hat{A}] \dots]$ depends on n parameters and we iterate equation (III.1) N times and obtain

$$\begin{aligned} \hat{U}^\dagger(t) \hat{A} \hat{U}(t) &= \sum_{n=0}^N (i)^n \int_0^t dt_1 \dots \int_0^{t_{n-1}} dt_n [\hat{H}(t_n), \dots [\hat{H}(t_1), \hat{A}] \dots] \\ &+ (i)^{N+1} \int_0^t dt_1 \dots \int_0^{t_N} dt_{N+1} \hat{U}^\dagger(t_{N+1}) [\hat{H}(t_{N+1}), \dots [\hat{H}(t_1), \hat{A}] \dots] \hat{U}(t_{N+1}) . \end{aligned}$$

If $\hat{H}(t)$ is bounded such that the last term vanishes for $N \rightarrow \infty$, this becomes

$$\hat{U}^\dagger(t) \hat{A} \hat{U}(t) = \sum_{n=0}^{\infty} (i)^n \int_0^t dt_1 \dots \int_0^{t_{n-1}} dt_n [\hat{H}(t_n), \dots [\hat{H}(t_1), \hat{A}] \dots] . \quad (\text{III.2})$$

Equation (III.2) is a series representation for an arbitrary Heisenberg operator. If we apply the initial state from both sides, we obtain the time-dependent expectation value as a series expansion.

Dirac representation

If our Hamiltonian consists out of an exactly solvable part $\hat{H}_0(t)$ and a perturbation $g\hat{H}_1(t)$, then we can apply the Dirac or interaction representation. Every operator is dressed by the time-evolution operator with respect to $\hat{H}_0(t)$,

$$\hat{O}_I(t) = \hat{U}_0^\dagger(t) \hat{O} \hat{U}_0(t) .$$

Thus, we are now interested in the transformation,

$$\hat{S}(t) = \hat{U}_0^\dagger(t) \hat{U}(t) .$$

Its differential equation is

$$\frac{d}{dt} \hat{S}(t) = -ig \hat{H}_{1,I}(t) \hat{S}(t) .$$

The equation of motion for dressing with $\hat{S}(t)$ from left and $\hat{S}^\dagger(t)$ from right is

$$\begin{aligned} \frac{d}{dt} \hat{S}^\dagger(t) \hat{A} \hat{S}(t) &= \hat{S}^\dagger(t) [ig \hat{H}_{1,I}(t), \hat{A}] \hat{S}(t) , \\ \hat{S}^\dagger(t) \hat{A} \hat{S}(t) &= \hat{A} + \int_0^t d\tau \hat{S}^\dagger(\tau) [ig \hat{H}_{1,I}(\tau), \hat{A}] \hat{S}(\tau) . \end{aligned} \quad (\text{III.3})$$

III PRETHERMALIZATION INDUCED BY WEAK INTERACTIONS

Analogously to the previous part, we obtain the series expansion by iterating equation (III.3). To obtain the Heisenberg operator, we replace \hat{A} with $\hat{A}_I(t)$. Consequently, the result for the series expansion is

$$\hat{S}^\dagger(t)\hat{A}_I(t)\hat{S}(t) = \sum_{n=0}^{\infty} (ig)^n \int_0^t dt_1 \dots \int_0^{t_{n-1}} dt_n \left[\hat{H}_{1,I}(t_n), \dots \left[\hat{H}_{1,I}(t_1), \hat{A}_I(t) \right] \dots \right]. \quad (\text{III.4})$$

We have found with equation (III.4) an explicit series expansion in the perturbation strength g for an arbitrary Heisenberg operator.

Now, we generalize the second-order expansion for the interaction quench^{73,80,85} to arbitrary time protocols. We assume that the initial state $|\Psi_0\rangle$ is an eigenstate of $\hat{H}_0(s)$ and observable \hat{a} . Furthermore, these two operators shall commute for all times, $[\hat{a}, \hat{H}_0(s)] = 0$. Then, the first-order term vanishes and the second-order term is the first finite correction,

$$\langle \hat{a} \rangle_t = \langle \hat{a} \rangle_0 - g^2 \int_0^t dt_1 \int_0^{t_1} dt_2 \langle \left[\hat{H}_{1,I}(t_2), \left[\hat{H}_{1,I}(t_1), \hat{a} \right] \right] \rangle_0 + O(g^3). \quad (\text{III.5})$$

Equation (III.5) is the prethermalization formula for an arbitrary time protocol and is one of the main results in this dissertation. In sections 3 and 4, we present explicit results for various nonequilibrium protocols in the Hubbard model. If the Hamiltonian stays constant after a certain point in time, then the Fourier transformed of the double commutator is useful. Thus, we define

$$\begin{aligned} J_{\hat{a}}(\epsilon) &= - \int_{-\infty}^{\infty} \frac{d\tau}{2\pi} e^{-i\tau\epsilon} \langle \Psi_0 | \left[\hat{V}, \left[e^{i\tau\hat{H}_0} \hat{V} e^{-i\tau\hat{H}_0}, \hat{a} \right] \right] | \Psi_0 \rangle \\ &= 2\Re \left\{ \langle \Psi_0 | \left[\hat{V}, \hat{a} \right] \delta(\hat{H}_0 - E_0 - \epsilon) \hat{V} | \Psi_0 \rangle \right\} \\ &= \sum_n |V_{0n}|^2 (a_n - a_0) 2\delta(E_n - E_0 - \epsilon). \end{aligned} \quad (\text{III.6})$$

We use the abbreviation $\langle \Psi_n | \hat{V} | \Psi_m \rangle = V_{nm}$ and the eigenvalues $\hat{a}|\Psi_n\rangle = a_n|\Psi_n\rangle$ and $\hat{H}_0|\Psi_n\rangle = E_n|\Psi_n\rangle$. The $\langle \Psi_0 | \left[\hat{V}, \left[\hat{V}_I(\tau), \hat{a} \right] \right] | \Psi_0 \rangle$ is real and symmetric in τ , therefore $J_{\hat{a}}(\epsilon)$ is real and symmetric in ϵ . In subsection 3.b), we compute $J_{\hat{a}}(\epsilon)$ for the half-filled Hubbard model with infinite spatial dimensions. We will utilize $J_{\hat{a}}(\epsilon)$ in subsection c) and in section 3.

If an operator \hat{A} does not commute with $\hat{H}_0(s)$, then the first order survives, and the leading order result is

$$\langle \hat{A} \rangle_t = \langle \hat{A}(t) \rangle_0 + g i \underbrace{\int_0^t dt_1 \langle [\hat{H}_{1,I}(t_1), \hat{A}_I(t)] \rangle_0}_{=\Delta A^{(1)}} + O(g^2). \quad (\text{III.7})$$

Observables with expectation values as for \hat{A} are called first-order observables and for \hat{a} are called second-order observables. Examples for second-order observables are kinetic energy and mode occupation numbers in the Hubbard model. The first-order observable of interest will be the double occupation. We can also Fourier transform the single commutator ($A_{nm} = \langle \Psi_n | \hat{A} | \Psi_m \rangle$),

$$\begin{aligned} \tilde{J}_{\hat{A}}(\epsilon) &= \int_{-\infty}^{\infty} \frac{d\tau}{2\pi} e^{-i\tau\epsilon} \langle [e^{i\tau\hat{H}_0} \hat{V} e^{-i\tau\hat{H}_0}, \hat{A}] \rangle_0 \\ &= \langle \Psi_0 | \left(\hat{V} \delta(E_0 - \hat{H}_0 - \epsilon) \hat{A} - \hat{A} \delta(\hat{H}_0 - E_0 - \epsilon) \hat{V} \right) | \Psi_0 \rangle \\ &= \sum_n \delta(E_n - E_0 - \epsilon) V_{0n} A_{n0} - \delta(E_0 - E_n - \epsilon) A_{0n} V_{n0}. \end{aligned} \quad (\text{III.8})$$

We now exploit this to predict the long-time limit for first-order observables. If there exists a long-time limit, then it is equal to the long-time average. Our Hamiltonian shall be constant after time t_{fin} . First, we split the time integral into the two parts of a time-dependent and a time-independent Hamiltonian,

$$\begin{aligned} \lim_{t \rightarrow \infty} \Delta A^{(1)}(t) &= \lim_{T \rightarrow \infty} \int_{t_{\text{fin}}}^T \frac{dt}{T} \Delta A^{(1)}(t) \\ &= \lim_{T \rightarrow \infty} \int_{t_{\text{fin}}}^T \frac{dt}{T} i \left(\int_{t_{\text{fin}}}^t d\tau + \int_0^{t_{\text{fin}}} d\tau \right) \langle [\hat{H}_{1,I}(\tau), \hat{A}_I(t)] \rangle_0. \end{aligned}$$

The time-averaging makes $\hat{A}_I(t)$ diagonal for $0 < \tau < t_{\text{fin}}$, in analogy to the diagonal ensemble in equation (I.3). The initial state is an eigenstate of $\langle \Psi_n | \hat{A}_{\text{diag}} | \Psi_m \rangle = \delta_{nm} A_{nn}$

III PRETHERMALIZATION INDUCED BY WEAK INTERACTIONS

and thus the expectation value of the single commutator vanishes. Therefore, the long-time limit is

$$\begin{aligned} \lim_{t \rightarrow \infty} \Delta A^{(1)}(t) &= \int d\epsilon \tilde{J}_{\hat{A}}(\epsilon) \lim_{T \rightarrow \infty} \int_{t_{\text{fin}}}^T \frac{dt}{T} i \int_{t_{\text{fin}}}^t d\tau e^{i(t-\tau)\epsilon} + i \int_0^{t_{\text{fin}}} d\tau \underbrace{\langle [\hat{H}_{1,I}(\tau), \hat{A}_{\text{diag},I}(t_{\text{fin}})] \rangle}_0 \\ &= \int d\epsilon \frac{\tilde{J}_{\hat{A}}(\epsilon)}{-\epsilon} . \end{aligned} \quad (\text{III.9})$$

The long-time limit of the first-order observables depends solely on the initial state and the final Hamiltonian. Therefore, it is independent of the explicit nonequilibrium protocol due to equation (III.9). The long-time limit for the second-order observables will be captured by a generalized Gibbs ensemble, as we show in subsection c).

The series expansion for propagator $\hat{U}(t)$,²⁷ $\hat{S}(t)$ ⁹⁰ and density matrix $\hat{\rho}(t) = \hat{U}(t)\hat{\rho}\hat{U}^\dagger(t)$ ⁹¹ are derived in several quantum mechanics textbooks,

$$\begin{aligned} \hat{U}(t) &= \sum_{n=0}^{\infty} (-i)^n \int_0^t dt_1 \dots \int_0^{t_{n-1}} dt_n \hat{H}(t_1), \dots \hat{H}(t_n) , \\ \hat{S}(t) &= \sum_{n=0}^{\infty} (-ig)^n \int_0^t dt_1 \dots \int_0^{t_{n-1}} dt_n \hat{H}_{1,I}(t_1) \dots \hat{H}_{1,I}(t_n) , \\ \hat{\rho}(t) &= \sum_{n=0}^{\infty} (-i)^n \int_0^t dt_1 \dots \int_0^{t_{n-1}} dt_n [\hat{H}(t_1), \dots [\hat{H}(t_n), \hat{\rho}] \dots] \\ &= \sum_{n=0}^{\infty} (-ig)^n \int_0^t dt_1 \dots \int_0^{t_{n-1}} dt_n [\hat{H}_{1,I}(t_1), \dots [\hat{H}_{1,I}(t_n), \hat{\rho}] \dots] . \end{aligned}$$

We deduced expansions (III.2) and (III.4) because they are used rarely in the literature.⁹² If we expand expectation values up to a certain order in g , we always obtain the same terms independent of whether we use the series expansion for propagator, density matrix, or Heisenberg operator. Secular terms, which grow in time, appear in the perturbative expansion of $\hat{U}(t)$ or $\hat{S}(t)$, but experience shows that the Heisenberg operator usually does not contain such terms.⁹³

It is common practice to express the propagators with time-ordering operators. The

2 GENERAL EXPANSION IN INTERACTION STRENGTH

time-ordering operators interchange the positions of the operators $\hat{H}(t_i)$ depending on their time.

$$\begin{aligned}
 T_{>} : \text{ greater time more to the left} & \quad \Rightarrow \quad \hat{U}(t) = T_{>} e^{-i \int_0^t d\tau \hat{H}(\tau)} \\
 T_{<} : \text{ lesser time more to the left} & \quad \Rightarrow \quad \hat{U}^\dagger(t) = T_{<} e^{i \int_0^t d\tau \hat{H}(\tau)}
 \end{aligned}$$

If we define two appropriate time-ordering operators, then we can reveal that the series expansions for $\hat{U}(t)$, $\hat{\rho}(t)$ and $\hat{U}^\dagger(t)\hat{A}\hat{U}(t)$ are congruent to each other. Let us first define

$$\begin{aligned}
 T_{\geq}^{(\hat{\rho})} : \text{ lesser time closer to } \hat{\rho} \\
 T_{\leq}^{(\hat{A})} : \text{ greater time closer to } \hat{A}
 \end{aligned}$$

The following computational steps are then straightforward,

$$\begin{aligned}
 \hat{U}^\dagger(t)\hat{A}\hat{U}(t) &= \sum_{n=0}^{\infty} (i)^n \int_0^t dt_1 \dots \int_0^{t_{n-1}} dt_n \left[\hat{H}(t_n), \dots \left[\hat{H}(t_1), \hat{A} \right] \dots \right] \\
 &= \sum_{n=0}^{\infty} \frac{(i)^n}{n!} \int_0^t dt_1 \dots \int_0^t dt_n T_{\leq}^{(\hat{A})} \left[\hat{H}(t_n), \dots \left[\hat{H}(t_1), \hat{A} \right] \dots \right] \\
 &= T_{\leq}^{(\hat{A})} e^{i \int_0^t d\tau \hat{H}(\tau)} \hat{A} e^{-i \int_0^t d\tau \hat{H}(\tau)} \\
 &= \left(T_{<} e^{i \int_0^t d\tau \hat{H}(\tau)} \right) \hat{A} \left(T_{>} e^{-i \int_0^t d\tau \hat{H}(\tau)} \right).
 \end{aligned}$$

We apply the same procedure to

$$\begin{aligned}
 \hat{\rho}(t) &= \sum_{n=0}^{\infty} \frac{(-i)^n}{n!} \int_0^t dt_1 \dots \int_0^t dt_n T_{\geq}^{(\hat{\rho})} \left[\hat{H}(t_1), \dots \left[\hat{H}(t_n), \hat{\rho} \right] \dots \right] \\
 &= T_{\geq}^{(\hat{\rho})} e^{-i \int_0^t d\tau \hat{H}(\tau)} \hat{\rho} e^{i \int_0^t d\tau \hat{H}(\tau)} \\
 &= \left(T_{>} e^{-i \int_0^t d\tau \hat{H}(\tau)} \right) \hat{\rho} \left(T_{<} e^{i \int_0^t d\tau \hat{H}(\tau)} \right).
 \end{aligned}$$

Hence, the series expansion in $\hat{H}(\tau)$ for $\hat{U}^\dagger(t)\hat{A}\hat{U}(t)$ match each other closely. We note that the steps are identical for the expansion in g if the time-ordering operators act upon $\hat{H}_{I,1}(\tau)$ instead of $\hat{H}(\tau)$.

b) Construction of constants of motion

The prethermalization plateau after a weak interaction quench is described by a generalized Gibbs ensemble⁸⁵ (GGE). Here, we present a straightforward way to construct the corresponding constants of motion for this GGE. The noninteracting initial Hamiltonian \hat{H}_0 shall have constants of motion \hat{I}_α . They commute with \hat{H}_0 and can be represented in the eigenbasis $\{|\Psi_n\rangle\}$ of \hat{H}_0 ,

$$\left[\hat{I}_\alpha, \hat{H}_0\right] = 0 \quad \Rightarrow \quad \hat{I}_\alpha = \sum_n |\Psi_n\rangle I_{\alpha,n} \langle\Psi_n| .$$

To generate a constant of motion \tilde{I}_α for the fully-interacting Hamiltonian $\hat{H} = \hat{H}_0 + g\hat{V}$, we replace the eigenstates $\{|\Psi_n\rangle\}$ with the eigenstates $\{|\tilde{\Psi}_n\rangle\}$ of \hat{H} ,

$$\tilde{I}_\alpha = \sum_n |\tilde{\Psi}_n\rangle I_{\alpha,n} \langle\tilde{\Psi}_n| \quad \Rightarrow \quad \left[\tilde{I}_\alpha, \hat{H}\right] = 0 .$$

The adiabatic transformation is the self-suggesting choice to transform eigenstates of one Hamiltonian to the eigenstates of another Hamiltonian. Here, we choose it as

$$\hat{R}_{\text{ad}} = T_{>} \exp\left\{-i \int_0^\infty d\tau (\hat{H}_0 + g\hat{V}e^{-\tau\delta})\right\} .$$

The interaction is changed infinitesimal slowly if we take the limit $\delta \rightarrow 0^+$. The adiabatic theorem in quantum mechanics^{86–88} states for admissible Hamiltonians that

$$\hat{R}_{\text{ad}}|\tilde{\Psi}_n\rangle = |\Psi_n\rangle e^{i\phi_n} , \quad |\tilde{\Psi}_n\rangle = \hat{R}_{\text{ad}}^\dagger|\Psi_n\rangle e^{i\phi_n} .$$

We assume that the adiabatic theorem is applicable. Thus, the dressed operators are the desired constants of motion,

$$\tilde{I}_\alpha = \hat{R}_{\text{ad}}^\dagger \hat{I}_\alpha \hat{R}_{\text{ad}} = \sum_n |\tilde{\Psi}_n\rangle I_{\alpha,n} \langle\tilde{\Psi}_n| .$$

When formula (III.5) is applied, the \tilde{I}_α are directly expanded in interaction strength,

$$\hat{R}_{\text{ad}}^\dagger \hat{I}_\alpha \hat{R}_{\text{ad}} = \sum_{n=0}^{\infty} (ig)^n \int_0^\infty d\tau_1 \dots \int_0^{\tau_{n-1}} d\tau_n \left[\hat{V}_I(\tau_n) e^{-\delta\tau_n}, \dots \left[\hat{V}_I(\tau_1) e^{-\delta\tau_1}, \hat{I}_\alpha \right] \dots \right] .$$

The definition is $\hat{V}_I(t) = e^{it\hat{H}_0} \hat{V} e^{-it\hat{H}_0}$ as the initial time of the effective Hamiltonian is zero. We insert $\{|\Psi_n\rangle\}$, the eigenbasis of \hat{H}_0 , to evaluate the expansion to second order.

We neglect the terms $O(g^3)$ to simplify the equations. The computational steps are straightforward for the off-diagonal elements,

$$\begin{aligned}
 \langle \Psi_n | \tilde{I}_\alpha | \Psi_m \rangle &\stackrel{n \neq m}{=} ig \int_0^\infty d\tau \langle \Psi_n | e^{-\delta\tau} [\hat{V}_I(\tau), \hat{I}_\alpha] | \Psi_m \rangle \\
 &\quad - g^2 \int_0^\infty d\tau_1 \int_0^{\tau_1} d\tau_2 e^{-\delta(\tau_1+\tau_2)} \langle \Psi_n | [\hat{V}_I(\tau_2), [\hat{V}_I(\tau_1), \hat{I}_\alpha]] | \Psi_m \rangle \\
 &= ig V_{nm} (I_{\alpha,m} - I_{\alpha,n}) \int_0^\infty d\tau e^{(-\delta+i(E_n-E_m))\tau} - g^2 \sum_l V_{nl} V_{lm} \int_0^\infty d\tau_1 \int_0^{\tau_1} d\tau_2 e^{-\delta(\tau_1+\tau_2)} \\
 &\quad \times (e^{i\tau_2(E_n-E_l)+i\tau_1(E_l-E_m)} (I_{\alpha,m} - I_{\alpha,l}) + e^{i\tau_1(E_n-E_l)+i\tau_2(E_l-E_m)} (I_{\alpha,n} - I_{\alpha,l})) \\
 &= g \frac{V_{nm}(I_{\alpha,n} - I_{\alpha,m})}{E_n - E_m} + g^2 \sum_{l \neq n} \frac{V_{nl} V_{lm} (I_{\alpha,n} - I_{\alpha,l})}{(E_n - E_m)(E_n - E_l)} - g^2 \sum_{l \neq m} \frac{V_{nl} V_{lm} (I_{\alpha,l} - I_{\alpha,m})}{(E_n - E_m)(E_l - E_m)},
 \end{aligned}$$

and the diagonal elements,

$$\begin{aligned}
 \langle \Psi_n | \tilde{I}_\alpha | \Psi_n \rangle &= I_{\alpha,n} - g^2 \int_0^\infty d\tau_1 \int_0^{\tau_1} d\tau_2 e^{-\delta(\tau_1+\tau_2)} \langle \Psi_n | [\hat{V}_I(\tau_2), [\hat{V}_I(\tau_1), \hat{I}_\alpha]] | \Psi_n \rangle \\
 &= I_{\alpha,n} - g^2 \sum_l V_{nl} V_{ln} (I_{\alpha,n} - I_{\alpha,l}) \int_0^\infty d\tau_1 \int_0^{\tau_1} d\tau_2 e^{-\delta(\tau_1+\tau_2)} 2 \cos((\tau_1 - \tau_2)(E_n - E_l)) \\
 &= I_{\alpha,n} + g^2 \sum_{l \neq n} \frac{V_{nl} V_{ln} (I_{\alpha,l} - I_{\alpha,n})}{(E_l - E_n)^2}.
 \end{aligned}$$

We assume nondegenerate eigenenergies E_n and use the abbreviations $I_{\alpha,n} = \langle \Psi_n | \hat{I}_\alpha | \Psi_n \rangle$ and $V_{nm} = \langle \Psi_n | \hat{V} | \Psi_m \rangle$. This expansion to second order gives the same operators as found by Kollar, Wolf and Eckstein.⁸⁵ We also need $\hat{R}_{\text{ad}} \hat{I}_\alpha \hat{R}_{\text{ad}}^\dagger$ in the next subsection and evaluate it by slowly switching the interaction on,

$$\hat{R}_{\text{ad}} \hat{I}_\alpha \hat{R}_{\text{ad}}^\dagger = \sum_{n=0}^{\infty} (ig)^n \int_{-\infty}^0 d\tau_1 \dots \int_{-\infty}^{\tau_{n-1}} d\tau_n [\hat{V}_I(\tau_n) e^{\delta\tau_n}, \dots [\hat{V}_I(\tau_1) e^{\delta\tau_1}, \hat{I}_\alpha] \dots].$$

c) Generalized Gibbs ensemble of the prethermal steady state

We now construct a GGE from our constants of motions and show that it captures the prethermalization plateau after an arbitrary nonequilibrium protocol. We start from a noninteracting state. The protocol takes place from initial time t_{ini} to final time t_{fin} and the Hamiltonian is constant afterwards,

$$\hat{H}_0(t) = \sum_{\alpha} \epsilon_{\alpha}(t) \hat{I}_{\alpha} \quad , \quad \epsilon_{\alpha}(t) = \begin{cases} \epsilon_{\alpha} & \text{for } t < t_{\text{ini}} \\ \epsilon_{\alpha} + \delta\epsilon_{\alpha}(t) & \text{for } t_{\text{ini}} \leq t \leq t_{\text{fin}} \\ \epsilon_{\alpha} & \text{for } t_{\text{fin}} < t \end{cases} \quad ,$$

$$\hat{H}_1(t) = \begin{cases} 0 & \text{for } t < t_{\text{ini}} \\ \hat{H}_1(t) & \text{for } t_{\text{ini}} \leq t \leq t_{\text{fin}} \\ \hat{V} & \text{for } t_{\text{fin}} < t \end{cases} \quad .$$

We assume that $[\hat{I}_{\alpha}, \hat{I}_{\beta}] = 0$ and therefore $[\tilde{I}_{\alpha}, \tilde{I}_{\beta}] = 0$. The statistical ensemble of the GGE^{10–13} is defined as

$$\tilde{\rho}_G = \frac{\prod_{\alpha} e^{-\lambda_{\alpha} \tilde{I}_{\alpha}}}{\text{Tr} \left\{ \prod_{\beta} e^{-\lambda_{\beta} \tilde{I}_{\beta}} \right\}} \quad . \quad (\text{III.10})$$

The constants λ_{α} are fixed by the conditions,

$$\text{Tr} \{ \tilde{I}_{\alpha} \tilde{\rho}_G \} = \langle \tilde{I}_{\alpha} \rangle_{t_{\text{fin}}} \quad .$$

We have defined the GGE and show in the rest of this subsection that this GGE governs the prethermal plateau. This means that the long-time limit of $\langle \hat{I}_{\alpha} \rangle_t$ is equal to the GGE prediction in second order,

$$\lim_{t \rightarrow \infty} \langle \hat{I}_{\alpha} \rangle_t = \text{Tr} \{ \hat{I}_{\alpha} \tilde{\rho}_G \} + O(g^3) \quad . \quad (\text{III.11})$$

The noninteracting Hamiltonian has the same set of eigenstates for all times. Therefore, the time-ordering operator in $\hat{U}_0(t)$ can be omitted,

$$\hat{U}_0(t) = T_{>} \exp \left\{ -i \int_{t_{\text{ini}}}^t d\tau \hat{H}_0(\tau) \right\} = \exp \left\{ -i \int_{t_{\text{ini}}}^t d\tau \hat{H}_0(\tau) \right\} \quad .$$

2 GENERAL EXPANSION IN INTERACTION STRENGTH

The initial state shall be an eigenstate of $\hat{H}_0(t)$, so the prethermalization equation (III.5) is applicable. The Hamiltonian becomes time-independent after t_{fin} , and we shift the interaction dressing to time t_{fin} , so $\hat{H}_{1,I}(t)$ has an advantageous form afterwards,

$$\hat{H}_{1,I}(t) = \begin{cases} 0 & \text{for } t < t_{\text{ini}} \\ \hat{H}_{1,I}(t) = \hat{U}_0(t_{\text{fin}})\hat{U}_0^\dagger(t)\hat{H}_1(t)\hat{U}_0(t)\hat{U}_0^\dagger(t_{\text{fin}}) & \text{for } t_{\text{ini}} \leq t \leq t_{\text{fin}} \\ \hat{V}_I(t) = e^{i\hat{H}_0(t-t_{\text{fin}})}\hat{V}e^{-i\hat{H}_0(t-t_{\text{fin}})} & \text{for } t_{\text{fin}} < t \end{cases} .$$

This shift does not affect the initial state, as it is an eigenstate of $\hat{H}_0(t)$, or the observables \hat{I}_α , as they commute with $\hat{H}_0(t)$.

If the long-time limit exists, then it is equal to the long-time average. We apply the prethermalization equation (III.5) and the long-time average splits into three terms for second order,

$$\begin{aligned} \overline{\langle \hat{I}_\alpha \rangle} &= \lim_{T \rightarrow \infty} \int_{t_{\text{fin}}}^T \frac{dt}{T} \langle \hat{I}_\alpha \rangle_t \\ &= \langle \hat{I}_\alpha \rangle_{t_{\text{ini}}} + g^2 (\Delta_{\alpha,1} + \Delta_{\alpha,2} + \Delta_{\alpha,3}) + O(g^3) , \end{aligned} \quad (\text{III.12})$$

$$\Delta_{\alpha,1} = - \lim_{T \rightarrow \infty} \int_{t_{\text{fin}}}^T \frac{dt}{T} \int_{t_{\text{fin}}}^t d\tau_1 \int_{t_{\text{fin}}}^{\tau_1} d\tau_2 \langle [\hat{V}_I(\tau_2), [\hat{V}_I(\tau_1), \hat{I}_\alpha]] \rangle_{t_{\text{ini}}} ,$$

$$\Delta_{\alpha,2} = - \lim_{T \rightarrow \infty} \int_{t_{\text{fin}}}^T \frac{dt}{T} \int_{t_{\text{fin}}}^t d\tau_1 \int_{t_{\text{ini}}}^{t_{\text{fin}}} d\tau_2 \langle [\hat{H}_{1,I}(\tau_2), [\hat{V}_I(\tau_1), \hat{I}_\alpha]] \rangle_{t_{\text{ini}}} ,$$

$$\Delta_{\alpha,3} = - \int_{t_{\text{ini}}}^{t_{\text{fin}}} d\tau_1 \int_{t_{\text{ini}}}^{\tau_1} d\tau_2 \langle [\hat{H}_{1,I}(\tau_2), [\hat{H}_{1,I}(\tau_1), \hat{I}_\alpha]] \rangle_{t_{\text{ini}}} .$$

The $\Delta_{\alpha,1}$ corresponds to the quench, which will be discussed in section 3, and results in

$$\Delta_{\alpha,1} = \int d\epsilon J_{I_\alpha}(\epsilon) \lim_{T \rightarrow \infty} \int_{t_{\text{fin}}}^T \frac{dt}{T} \int_{t_{\text{fin}}}^t d\tau_1 \int_{t_{\text{fin}}}^{\tau_1} d\tau_2 \cos(\epsilon(\tau_1 - \tau_2)) = \int d\epsilon \frac{J_{I_\alpha}(\epsilon)}{\epsilon^2} .$$

This term and can be expressed as an integral over $J_{I_\alpha}(\epsilon)$ because the Hamiltonian is constant. $\Delta_{\alpha,2}$ in equation (III.12) is a mixture of nonequilibrium protocol and the

III PRETHERMALIZATION INDUCED BY WEAK INTERACTIONS

long-time evolution. $\Delta_{\alpha,3}$ describes the nonequilibrium protocol from t_{ini} to t_{fin} .

Next, we compute the GGE prediction. We assume that the expectation values with respect to the initial state are equal to that of a statistical ensemble $\hat{\rho}_{\text{ini}}$. Therefore, the zeroth order of the GGE is equal to $\hat{\rho}_{\text{ini}}$,

$$\langle \hat{O} \rangle_{t_{\text{ini}}} = \text{Tr}\{\hat{O}\hat{\rho}_{\text{ini}}\} \quad \text{and} \quad \tilde{\rho}_G = \hat{\rho}_{\text{ini}} + O(g) . \quad (\text{III.13})$$

Both assumptions are valid if we compute the expectation values by Wick's theorem. We further use the transformed ensemble $\hat{\rho}_G$, which we relate with our assumption (III.13) to the initial ensemble $\hat{\rho}_{\text{ini}}$,

$$\hat{\rho}_G = \hat{R}_{\text{ad}}\tilde{\rho}_G\hat{R}_{\text{ad}}^\dagger = \frac{\prod_{\alpha} e^{-\lambda_{\alpha}\tilde{I}_{\alpha}}}{\text{Tr}\left\{\prod_{\beta} e^{-\lambda_{\beta}\hat{I}_{\beta}}\right\}} = \hat{\rho}_{\text{ini}} + O(g) .$$

The statistical prediction of the GGE is

$$\begin{aligned} \text{Tr}\{\hat{I}_{\alpha}\tilde{\rho}_G\} &= \text{Tr}\{\hat{R}_{\text{ad}}\hat{I}_{\alpha}\hat{R}_{\text{ad}}^\dagger\hat{\rho}_G\} \\ &= \text{Tr}\{\hat{I}_{\alpha}\hat{\rho}_G\} + \text{Tr}\left\{\left(\hat{R}_{\text{ad}}\hat{I}_{\alpha}\hat{R}_{\text{ad}}^\dagger - \hat{I}_{\alpha}\right)\hat{\rho}_G\right\} . \end{aligned}$$

The first term becomes

$$\text{Tr}\{\hat{I}_{\alpha}\hat{\rho}_G\} = \text{Tr}\{\tilde{I}_{\alpha}\tilde{\rho}_G\} = \langle \tilde{I}_{\alpha} \rangle_{t_{\text{fin}}} .$$

The zeroth order vanishes trivially in the second term $\text{Tr}\{(\hat{R}_{\text{ad}}\hat{I}_{\alpha}\hat{R}_{\text{ad}}^\dagger - \hat{I}_{\alpha})\hat{\rho}_G\}$. $\hat{\rho}_G$ is diagonal in the eigenbasis of \hat{I}_{α} and the first-order correction is computed by a single

commutator. Thus, the first order in g vanishes as well. Consequently replacing $\hat{\rho}_G$ with $\hat{\rho}_{\text{ini}}$ gives an error of $O(g^3)$,

$$\begin{aligned}
 & \text{Tr}\left\{\left(\hat{R}_{\text{ad}}\hat{I}_\alpha\hat{R}_{\text{ad}}^\dagger - \hat{I}_\alpha\right)\hat{\rho}_G\right\} \\
 &= \sum_{n=1}^{\infty}(-ig)^n \int_{t_{\text{fin}}}^{\infty} d\tau_1 \dots \int_{t_{\text{fin}}}^{\tau_{n-1}} d\tau_n \text{Tr}\left\{\left[\hat{V}_I(\tau_n)e^{\delta\tau_n}, \dots \left[\hat{V}_I(\tau_1)e^{\delta\tau_1}, \hat{I}_\alpha\right] \dots\right]\hat{\rho}_G\right\} \\
 &= \sum_{n=2}^{\infty}(-ig)^n \int_{t_{\text{fin}}}^{\infty} d\tau_1 \dots \int_{t_{\text{fin}}}^{\tau_{n-1}} d\tau_n \text{Tr}\left\{\left[\hat{V}_I(\tau_n)e^{\delta\tau_n}, \dots \left[\hat{V}_I(\tau_1)e^{\delta\tau_1}, \hat{I}_\alpha\right] \dots\right]\hat{\rho}_G\right\} \\
 &= (-ig)^2 \int_{t_{\text{fin}}}^{\infty} d\tau_1 \int_{t_{\text{fin}}}^{\tau_1} d\tau_2 \text{Tr}\left\{\left[\hat{V}_I(\tau_2)e^{\delta\tau_2}, \left[\hat{V}_I(\tau_1)e^{\delta\tau_1}, \hat{I}_\alpha\right]\right]\hat{\rho}_{\text{ini}}\right\} + O(g^3) \\
 &= \text{Tr}\left\{\left(\hat{R}_{\text{ad}}\hat{I}_\alpha\hat{R}_{\text{ad}}^\dagger - \hat{I}_\alpha\right)\hat{\rho}_{\text{ini}}\right\} + O(g^3) .
 \end{aligned}$$

The GGE prediction up to second order is equal to

$$\text{Tr}\{\hat{I}_\alpha\tilde{\rho}_G\} = \langle\tilde{I}_\alpha\rangle_{t_{\text{fin}}} + \langle\left(\hat{R}_{\text{ad}}\hat{I}_\alpha\hat{R}_{\text{ad}}^\dagger - \hat{I}_\alpha\right)\rangle_{t_{\text{ini}}} + O(g^3) .$$

We have an explicit expansion in interaction strength g for the two terms on the right-hand side. The expectation value of the constants of motions at t_{fin} has three second-order terms,

$$\begin{aligned}
 \langle\tilde{I}_\alpha\rangle_{t_{\text{fin}}} &= \langle\hat{U}^\dagger(t_{\text{fin}})\hat{R}_{\text{ad}}^\dagger\hat{I}_\alpha\hat{R}_{\text{ad}}\hat{U}(t_{\text{fin}})\rangle_{t_{\text{ini}}} \\
 &= \langle\hat{I}_\alpha\rangle_{t_{\text{ini}}} + g^2\left(\tilde{\Delta}_{\alpha,1} + \tilde{\Delta}_{\alpha,2} + \tilde{\Delta}_{\alpha,3}\right) + O(g^3) , \tag{III.14} \\
 \tilde{\Delta}_{\alpha,1} &= - \int_{t_{\text{fin}}}^{\infty} d\tau_1 \int_{t_{\text{fin}}}^{\tau_1} d\tau_2 \langle\left[\hat{V}_I(\tau_2)e^{-\delta\tau_2}, \left[\hat{V}_I(\tau_1)e^{-\delta\tau_1}, \hat{I}_\alpha\right]\right]\rangle_{t_{\text{ini}}} , \\
 \tilde{\Delta}_{\alpha,2} &= - \int_{t_{\text{fin}}}^{\infty} d\tau_1 \int_{t_{\text{ini}}}^{t_{\text{fin}}} d\tau_2 \langle\left[\hat{H}_{1,I}(\tau_2), \left[\hat{V}_I(\tau_1)e^{-\delta\tau_1}, \hat{I}_\alpha\right]\right]\rangle_{t_{\text{ini}}} , \\
 \tilde{\Delta}_{\alpha,3} &= - \int_{t_{\text{ini}}}^{t_{\text{fin}}} d\tau_1 \int_{t_{\text{ini}}}^{\tau_1} d\tau_2 \langle\left[\hat{H}_{1,I}(\tau_2), \left[\hat{H}_{1,I}(\tau_1), \hat{I}_\alpha\right]\right]\rangle_{t_{\text{ini}}} .
 \end{aligned}$$

III PRETHERMALIZATION INDUCED BY WEAK INTERACTIONS

The last term of equation (III.14) is equal to the last term from the long-time average in equation (III.12), $\tilde{\Delta}_{\alpha,3} = \Delta_{\alpha,3}$. We obtain $\tilde{\Delta}_{\alpha,2} = \Delta_{\alpha,2}$ after explicit integration over τ_1 and insertion of the eigenbasis of \hat{H}_0 ,

$$\begin{aligned} \lim_{T \rightarrow \infty} \int_{t_{\text{fin}}}^T \frac{dt}{T} \int_{t_{\text{fin}}}^t d\tau_1 [\hat{V}_I(\tau_1), \hat{I}_\alpha] &= \sum_{n,m} \frac{|\Psi_n\rangle V_{nm} (I_{\alpha,n} - I_{\alpha,m}) \langle \Psi_m|}{i(E_n - E_m)} \\ &= \int_{t_{\text{fin}}}^{\infty} d\tau_1 [\hat{V}_I(\tau_1) e^{-\delta\tau_1}, \hat{I}_\alpha] . \end{aligned}$$

The term $\tilde{\Delta}_{\alpha,1}$ of equation (III.14) is half the value of $\Delta_{\alpha,1}$,

$$\tilde{\Delta}_{\alpha,1} = \int d\epsilon J_{I_\alpha}(\epsilon) \int_{t_{\text{fin}}}^{\infty} d\tau_1 \int_{t_{\text{fin}}}^{\tau_1} d\tau_2 e^{-\delta\tau_2} e^{-\delta\tau_1} \cos(\epsilon(\tau_1 - \tau_2)) = \int d\epsilon \frac{J_{I_\alpha}(\epsilon)}{2\epsilon^2} .$$

The remaining term is equal to half the value of $\Delta_{\alpha,1}$ as well,

$$\begin{aligned} \langle (\hat{R}_{\text{ad}} \hat{I}_\alpha \hat{R}_{\text{ad}}^\dagger - \hat{I}_\alpha) \rangle_{t_{\text{ini}}} &= (-ig)^2 \int_{-\infty}^{t_{\text{fin}}} d\tau_1 \int_{-\infty}^{\tau_1} d\tau_2 e^{\delta\tau_1} e^{\delta\tau_2} \langle [\hat{V}_I(\tau_2), [\hat{V}_I(\tau_1), \hat{I}_\alpha]] \rangle_{t_{\text{ini}}} + O(g^3) \\ &= g^2 \int d\epsilon J_{I_\alpha}(\epsilon) \int_{-\infty}^{t_{\text{fin}}} d\tau_1 \int_{-\infty}^{\tau_1} d\tau_2 e^{\delta\tau_2} e^{\delta\tau_1} \cos(\epsilon(\tau_1 - \tau_2)) + O(g^3) \\ &= g^2 \int d\epsilon \frac{J_{I_\alpha}(\epsilon)}{2\epsilon^2} + O(g^3) . \end{aligned}$$

Consequently, the sum of all second-order terms is equal on both sides of equation (III.11),

$$\begin{aligned} \overline{\langle \hat{I}_\alpha \rangle} &= \langle \tilde{I}_\alpha \rangle_{t_{\text{fin}}} + \langle (\hat{R}_{\text{ad}} \hat{I}_\alpha \hat{R}_{\text{ad}}^\dagger - \hat{I}_\alpha) \rangle_{t_{\text{ini}}} + O(g^3) \\ &= \text{Tr}\{\hat{I}_\alpha \tilde{\rho}_G\} + O(g^3) . \end{aligned}$$

In summary, we have proven equation (III.11). We achieved this by evaluating all terms to second-order that arise from the series expansion. We handled the adiabatic transformation as the time-evolution with an appropriate time-dependent Hamiltonian. Hence, we have generalized the GGE prediction from the quench⁸⁵ to arbitrary protocols.

2 GENERAL EXPANSION IN INTERACTION STRENGTH

Our derivation even includes weakly interacting initial states generated by adiabatic switching from the noninteracting states. We will further explain this in subsection 3.a). While several steps in our derivation are inspired by reference,⁸⁵ the formal construction of constants of motion is more general and can be computed to arbitrary orders. One open question is whether the long-time limit is equal to the GGE in $O(g^3)$ or higher.

The central message from this subsection is that the prethermal plateau of first-order and second-order are fundamentally different. For first-order observables, the plateau value depends solely on the final Hamiltonian as we learned in equation (III.9). Thus, there is no memory of the nonequilibrium protocol. Contrarily, for second-order observables, the GGE and plateau values are sensitive to the specific protocol. In subsection 3.e), we will compute interaction ramps and the plateau values are fine-tuned by the ramp duration. In section 4, the initial and final Hamiltonian are identical, nevertheless, the hopping-amplitude drive generates prethermal steady values in the occupation probabilities.

3 Interaction quenches, ramps and periodic drives

In this section, we will develop and apply a method to compute the prethermal regime for weak time-dependent interactions. In particular, we investigate quenches,^{73,80} ramps,⁸⁴ and periodic drives⁸⁹ for the Hubbard model with infinite spatial dimensions. First, we define an effective Hamiltonian and evaluate the general terms in subsection a). Next, we compute the necessary expressions for the Hubbard model b), which become feasible in infinite dimensions. In subsection c), we discuss crossing points in transients of first-order observables. After that, we study the relaxation behavior to the prethermal plateau in subsection d). In subsection e), we explore the influence of ramping duration and ramping smoothness on the prethermal plateau. In the last subsection f), we analyze periodic interaction drives, which exhibit two qualitatively different regimes.⁸⁹

a) Effective model and general method

First, we define an effective Hamiltonian, which enables us to start from an uncorrelated initial state. For this effective Hamiltonian, we evaluate equations (III.5) and (III.7) for general models with help of the Fourier transformed from equations (III.6) and (III.8). We treat the first- and second-order observables independently and will obtain the expressions from equations (III.15) and (III.16), which will be the main results of this subsection.

The noninteracting Hamiltonian \hat{H}_0 shall be time-independent, and the interaction has a time-dependent factor. In section 4, the noninteracting Hamiltonian will become time-dependent as well. We can write the ramp Hamiltonian as

$$\hat{H}(t) = \hat{H}_0 + \hat{V} \begin{cases} g_0 & t \leq 0 \\ g_0 + \Delta g f(t) & t > 0 \end{cases} .$$

Our initial state $|\Psi\rangle$ is an eigenstate of the Hamiltonian at $t \leq 0$. We assume that the initial interacting state $|\Psi\rangle$ can be generated from a noninteracting state $|\Psi_0\rangle$ by adiabatic switching,⁸⁶⁻⁸⁸ where $|\Psi_0\rangle$ is the corresponding eigenstate of \hat{H}_0 . We thus replace our original problem of an interacting state with an auxiliary problem. In the auxiliary problem, we start from the noninteracting state $|\Psi_0\rangle$ ramp adiabatically and then apply the nonequilibrium protocol. The auxiliary Hamiltonian is

$$\hat{H}_{\text{eff}}(t) = \hat{H}_0 + \hat{V}g(t) \quad \text{with} \quad g(t) = \begin{cases} g_0 e^{t\delta} & t \leq 0 \\ g_0 + \Delta g f(t) & t > 0 \end{cases}$$

We have to take the limit $\delta \rightarrow 0^+$ for adiabatic switching. Now, we can apply the perturbative expansion for first- and second-order observables. We compute two limits

that of initial time to minus infinity, and that of $\delta \rightarrow 0^+$ and will perform them analytically. The general procedure is to first analytically evaluate all terms without ramping function $f(t)$. Then, we will combine the terms for negative and positive times to a single expression and avoid the numerical computation of both limits.

First-order observables

We enter the auxiliary Hamiltonian into equation (III.7) and replace the expectation value of the commutator with its Fourier transformed,

$$\begin{aligned} \langle \hat{A} \rangle_t &= \langle \hat{A} \rangle_0 + i \int_{-\infty}^t d\tau g(\tau) \langle [\hat{V}_I(\tau), \hat{A}_I(t)] \rangle_0 + O(g^2) \\ &= \langle \hat{A} \rangle_0 + \int d\epsilon \tilde{J}_{\hat{A}}(\epsilon) \underbrace{\int_{-\infty}^t d\tau g(\tau) e^{i(t-\tau)\epsilon}}_{=g\varphi^{(1)}(t,\epsilon)} + O(g^2) . \end{aligned}$$

The Fourier transformed $\tilde{J}_{\hat{A}}(\epsilon)$ was defined in equation (III.8). Next, we compute the time integration by splitting the time integration into positive and negative times,

$$\begin{aligned} g\varphi^{(1)}(t, \epsilon) &= \int_{-\infty}^t d\tau g(\tau) e^{i(t-\tau)\epsilon} \\ &= \int_{-\infty}^0 d\tau g_0 e^{\delta\tau} e^{i(t-\tau)\epsilon} + \int_0^t d\tau (g_0 + \Delta g f(\tau)) e^{i(t-\tau)\epsilon} \\ &= g_0 \frac{i}{\epsilon} + \Delta g \int_0^t d\tau f(\tau) e^{i(t-\tau)\epsilon} . \end{aligned}$$

III PRETHERMALIZATION INDUCED BY WEAK INTERACTIONS

When we combine the term from the adiabatic ramp with the g_0 -term for positive times, we obtain a time-independent term, which is equal to the value at the end of the adiabatic ramp. The result is

$$\begin{aligned} \langle \hat{A} \rangle_t &= \langle \hat{A} \rangle_0 + g_0 \Delta A_{\text{ad}}^{(1)} + \Delta g \Delta A_{\text{ramp}}^{(1)}(t) + O(g^2) \quad (\text{III.15}) \\ \Delta A_{\text{ad}}^{(1)} &= i \int_{-\infty}^0 d\tau e^{\tau\delta} \langle [\hat{V}_I(\tau), \hat{A}] \rangle_0 = \int d\epsilon \frac{\tilde{J}_{\hat{A}}(\epsilon)}{-\epsilon} \\ \Delta A_{\text{ramp}}^{(1)}(t) &= i \int_0^t d\tau f(\tau) \langle [\hat{V}_I(\tau), \hat{A}_I(t)] \rangle_0 = \int d\epsilon \tilde{J}_{\hat{A}}(\epsilon) i \int_0^t d\tau f(\tau) e^{i(t-\tau)\epsilon} . \end{aligned}$$

We note that expectation values for the first-order observables are computed perturbatively as the adiabatic value plus the ramp of $\Delta g f(t)$.

Second-order observables

The first-order term vanishes for the second-order observables \hat{a} . Therefore, we apply equation (III.5) with the Fourier transformed $J_{\hat{a}}(\epsilon)$ from equation (III.6). The result is

$$\begin{aligned} \langle \hat{a} \rangle_t &= \langle \hat{a} \rangle_0 - \int_{-\infty}^t d\tau_1 \int_{-\infty}^{\tau_1} d\tau_2 g(\tau_1) g(\tau_2) \langle [\hat{V}_I(\tau_2), [\hat{V}_I(\tau_1), \hat{a}_I(t)]] \rangle_0 + O(g^3) \\ &= \langle \hat{a} \rangle_0 + \underbrace{\int d\epsilon J_{\hat{a}}(\epsilon) \int_{-\infty}^t d\tau_1 \int_{-\infty}^{\tau_1} d\tau_2 g(\tau_1) g(\tau_2) \cos(\epsilon(\tau_1 - \tau_2))}_{=g^2\varphi^{(2)}(t,\epsilon)} + O(g^3) , \\ g^2\varphi^{(2)}(t,\epsilon) &= \int_{-\infty}^0 d\tau_1 \int_{-\infty}^{\tau_1} d\tau_2 g_0 e^{\delta\tau_1} g_0 e^{\delta\tau_2} \cos((\tau_1 - \tau_2)\epsilon) \\ &\quad + \int_0^t d\tau_1 (g_0 + \Delta g f(\tau_1)) \int_{-\infty}^0 d\tau_2 g_0 e^{\delta\tau_2} \cos((\tau_1 - \tau_2)\epsilon) \\ &\quad + \int_0^t d\tau_1 (g_0 + \Delta g f(\tau_1)) \int_0^{\tau_1} d\tau_2 (g_0 + \Delta g f(\tau_2)) \cos((\tau_1 - \tau_2)\epsilon) . \end{aligned}$$

3 INTERACTION QUENCHES, RAMPS AND PERIODIC DRIVES

Next, we use the identity,

$$0 = \int_{-\infty}^0 d\tau_2 e^{\delta\tau_2} \cos((\tau_1 - \tau_2)\epsilon) + \int_0^{\tau_1} d\tau_2 \cos((\tau_1 - \tau_2)\epsilon) ,$$

allowing us to simplify,

$$g^2 \varphi^{(2)}(t, \epsilon) = \frac{g_0^2}{2\epsilon^2} + \int_0^t d\tau_1 (g_0 + \Delta g f(\tau_1)) \int_0^{\tau_1} d\tau_2 \Delta g f(\tau_2) \cos((\tau_1 - \tau_2)\epsilon) .$$

The final result has three second-order terms,

$$\begin{aligned} \langle \hat{a} \rangle_t &= \langle \hat{a} \rangle_0 + g_0^2 \Delta a_{\text{ad}}^{(2)} + g_0 \Delta g \Delta a_{\text{mix}}^{(2)}(t) + \Delta g^2 \Delta a_{\text{ramp}}^{(2)}(t) + O(g^3) , \quad (\text{III.16}) \\ \Delta a_{\text{ad}}^{(2)} &= - \int_{-\infty}^0 d\tau_1 \int_{-\infty}^{\tau_1} d\tau_2 e^{\delta\tau_1} e^{\delta\tau_2} \langle [\hat{V}_I(\tau_2), [\hat{V}_I(\tau_1), \hat{a}]] \rangle_0 = \int d\epsilon \frac{J_{\hat{a}}(\epsilon)}{2\epsilon^2} , \\ \Delta a_{\text{mix}}^{(2)}(t) &= - \int_0^t d\tau_1 \int_0^{\tau_1} d\tau_2 f(\tau_2) \langle [\hat{V}_I(\tau_2), [\hat{V}_I(\tau_1), \hat{a}]] \rangle_0 \\ &= \int d\epsilon J_{\hat{a}}(\epsilon) \int_0^t d\tau_1 \int_0^{\tau_1} d\tau_2 f(\tau_2) \cos(\epsilon(\tau_1 - \tau_2)) , \\ \Delta a_{\text{ramp}}^{(2)}(t) &= - \int_0^t d\tau_1 f(\tau_1) \int_0^{\tau_1} d\tau_2 f(\tau_2) \langle [\hat{V}_I(\tau_2), [\hat{V}_I(\tau_1), \hat{a}]] \rangle_0 \\ &= \int d\epsilon J_{\hat{a}}(\epsilon) \int_0^t d\tau_1 \int_0^{\tau_1} d\tau_2 f(\tau_1) f(\tau_2) \cos(\epsilon(\tau_1 - \tau_2)) . \end{aligned}$$

The first term corresponds to the adiabatic correction. The third corresponds to the ramp from $g = 0$ to $g = \Delta g$, and the second is a new mixing term. The ramp and the mixing term are related to one another by

$$f(t) \frac{\partial \Delta a_{\text{mix}}^{(2)}(t)}{\partial t} = \frac{\partial \Delta a_{\text{ramp}}^{(2)}(t)}{\partial t} .$$

For the first-order observables, we have a simple linear combination of adiabatic and nonequilibrium terms. Thus, they do not affect each other. For second-order observables

III PRETHERMALIZATION INDUCED BY WEAK INTERACTIONS

however, the mixing term emerges, initially interacting and noninteracting states have a qualitatively different dynamics. The physical interpretation is that the second-order observables are more sensitive to the history of the nonequilibrium process than the first-order observables. Finally, we note that the adiabatic corrections $A_{\text{ad}}^{(1)}$ and $\Delta a_{\text{ad}}^{(2)}$ are equal to corresponding terms from the time-independent Rayleigh-Schrödinger perturbation theory,^{94–96}

$$\begin{aligned} |\Psi_{\text{RS}}\rangle &= |\Psi_0\rangle + g_0 \sum_{n \neq 0} \frac{|\Psi_n\rangle V_{n0}}{E_n - E_0} + O(g_0^2) , \\ g_0 A_{\text{ad}}^{(1)} &= \langle \Psi_{\text{RS}} | \hat{A} | \Psi_{\text{RS}} \rangle - \langle \Psi_0 | \hat{A} | \Psi_0 \rangle + O(g_0^2) , \\ g_0^2 a_{\text{ad}}^{(2)} &= \langle \Psi_{\text{RS}} | \hat{a} | \Psi_{\text{RS}} \rangle - \langle \Psi_0 | \hat{a} | \Psi_0 \rangle + O(g_0^3) . \end{aligned}$$

b) Hubbard model in infinite spatial dimensions

We compute the commutator expectation values for the Hubbard model in this subsection. We begin with the evaluation of an expectation value of two two-body interaction operators,

$$\langle [\hat{V}^{(1)}, \hat{V}^{(2)}] \rangle_0 \quad \text{with} \quad \hat{V}^{(i)} = \sum_{\alpha, \beta, \gamma, \delta} V_{\alpha\beta\gamma\delta}^{(i)} \hat{c}_\alpha^\dagger \hat{c}_\beta^\dagger \hat{c}_\gamma \hat{c}_\delta .$$

The state is uncorrelated with $\langle \hat{c}_\alpha^\dagger \hat{c}_\beta \rangle_0 = \delta_{\alpha\beta} \langle \hat{n}_\alpha \rangle_0$. According to Wick's theorem,^{26, 27, 90} all possible two-particle contractions contribute. We assume a state with a fixed particle number. Hence, contractions of two annihilation or two creation operators vanish. We assume next that if two indices of $V_{\alpha\beta\gamma\delta}^{(i)}$ are identical, then it vanishes or the other two indices are identical as well. The physical interpretation of this assumption is that if one particle is not scattered, the other one is not scattered as well. Thus assumption is fulfilled e.g. for a translationally invariant interaction term.⁴⁵ When two c -operators from the same interaction term are contracted together, then the initial state is an eigenstate of the remainder of this interaction. Due to the commutator, we then obtain zero. Thus, the terms containing contraction of two c -operators from the same interaction are not contributing. Under these assumptions, the term simplifies to

$$\begin{aligned} &V_{\alpha\beta\gamma\delta}^{(1)} V_{\alpha'\beta'\gamma'\delta'}^{(2)} \langle [\hat{c}_\alpha^\dagger \hat{c}_\beta^\dagger \hat{c}_\gamma \hat{c}_\delta, \hat{c}_{\alpha'}^\dagger \hat{c}_{\beta'}^\dagger \hat{c}_{\gamma'} \hat{c}_{\delta'}] \rangle_0 \\ &= V_{\alpha\beta\gamma\delta}^{(1)} V_{\alpha'\beta'\gamma'\delta'}^{(2)} \left(\langle \hat{c}_\alpha^\dagger \hat{c}_\beta^\dagger \hat{c}_{\gamma'} \hat{c}_{\delta'} \rangle_0 \langle \hat{c}_\gamma \hat{c}_\delta \hat{c}_{\alpha'}^\dagger \hat{c}_{\beta'}^\dagger \rangle_0 - \langle \hat{c}_{\alpha'}^\dagger \hat{c}_{\beta'}^\dagger \hat{c}_\gamma \hat{c}_\delta \rangle_0 \langle \hat{c}_{\gamma'} \hat{c}_{\delta'} \hat{c}_\alpha^\dagger \hat{c}_\beta^\dagger \rangle_0 \right) . \end{aligned}$$

3 INTERACTION QUENCHES, RAMPS AND PERIODIC DRIVES

The expectation value is

$$\begin{aligned}
\langle [\hat{V}^{(1)}, \hat{V}^{(2)}] \rangle_0 &= \sum_{\substack{\alpha, \beta, \gamma, \delta, \\ \alpha', \beta', \gamma', \delta'}} V_{\alpha\beta\gamma\delta}^{(1)} V_{\alpha'\beta'\gamma'\delta'}^{(2)} (\delta_{\alpha\delta'} \delta_{\beta\gamma'} - \delta_{\alpha\gamma'} \delta_{\beta\delta'}) (\delta_{\gamma\beta'} \delta_{\delta\alpha'} - \delta_{\gamma\alpha'} \delta_{\delta\beta'}) \\
&\quad \times \left(\langle \hat{n}_\alpha \rangle_0 \langle \hat{n}_\beta \rangle_0 (1 - \langle \hat{n}_\gamma \rangle_0) (1 - \langle \hat{n}_\delta \rangle_0) \right. \\
&\quad \left. - \langle \hat{n}_\gamma \rangle_0 \langle \hat{n}_\delta \rangle_0 (1 - \langle \hat{n}_\alpha \rangle_0) (1 - \langle \hat{n}_\beta \rangle_0) \right) \\
&= \sum_{\alpha, \beta, \gamma, \delta} V_{\alpha\beta\gamma\delta}^{(1)} \left(V_{\delta\gamma\beta\alpha}^{(2)} - V_{\gamma\delta\beta\alpha}^{(2)} - V_{\delta\gamma\alpha\beta}^{(2)} + V_{\gamma\delta\alpha\beta}^{(2)} \right) \\
&\quad \times \left(\langle \hat{n}_\alpha \rangle_0 \langle \hat{n}_\beta \rangle_0 (1 - \langle \hat{n}_\gamma \rangle_0) (1 - \langle \hat{n}_\delta \rangle_0) \right. \\
&\quad \left. - \langle \hat{n}_\gamma \rangle_0 \langle \hat{n}_\delta \rangle_0 (1 - \langle \hat{n}_\alpha \rangle_0) (1 - \langle \hat{n}_\beta \rangle_0) \right).
\end{aligned}$$

The sign changes when we commute the two creation operators or the two annihilation operators of one interaction. Thus, the coefficients $V_{\alpha\beta\gamma\delta}^{(i)}$ have to respect the symmetry

$$V_{\alpha\beta\gamma\delta}^{(i)} = -V_{\beta\alpha\gamma\delta}^{(i)} = -V_{\alpha\beta\delta\gamma}^{(i)} = V_{\beta\alpha\delta\gamma}^{(i)}.$$

This further simplifies our expectation value to

$$\langle [\hat{V}^{(1)}, \hat{V}^{(2)}] \rangle_0 = 4 \sum_{\alpha, \beta, \gamma, \delta} V_{\alpha\beta\gamma\delta}^{(1)} V_{\delta\gamma\beta\alpha}^{(2)} \left(\langle \hat{n}_\alpha \rangle_0 \langle \hat{n}_\beta \rangle_0 (1 - \langle \hat{n}_\gamma \rangle_0) (1 - \langle \hat{n}_\delta \rangle_0) \right. \\
\left. - \langle \hat{n}_\gamma \rangle_0 \langle \hat{n}_\delta \rangle_0 (1 - \langle \hat{n}_\alpha \rangle_0) (1 - \langle \hat{n}_\beta \rangle_0) \right).$$

In the subsection 6.a), we explicitly consider the interactions

$$\hat{V}^{(1)} \rightarrow \hat{V} \quad \text{and} \quad \hat{V}^{(2)} \rightarrow \left[e^{it\hat{H}_0} \hat{V} e^{-it\hat{H}_0}, \hat{n}_\nu \right] \quad \text{with} \quad \hat{H}_0 = \sum_{\alpha} \epsilon_{\alpha} \hat{n}_{\alpha} \quad \text{and} \quad \hat{V} = \hat{V}^{\dagger}.$$

This leads to

$$V_{\alpha\beta\gamma\delta}^{(1)} \rightarrow V_{\alpha\beta\gamma\delta}, \quad V_{\alpha\beta\gamma\delta}^{(2)} \rightarrow V_{\alpha\beta\gamma\delta} e^{it(\epsilon_{\alpha} + \epsilon_{\beta} - \epsilon_{\gamma} - \epsilon_{\delta})} (\delta_{\nu\delta} + \delta_{\nu\gamma} - \delta_{\nu\beta} - \delta_{\nu\alpha})$$

and results in

$$\begin{aligned}
&\langle [\hat{V}, [e^{it\hat{H}_0} \hat{V} e^{-it\hat{H}_0}, \hat{n}_\nu]] \rangle_0 \\
&= 4 \sum_{\alpha, \beta, \gamma, \delta} |V_{\alpha\beta\gamma\delta}|^2 e^{it(\epsilon_{\alpha} + \epsilon_{\beta} - \epsilon_{\gamma} - \epsilon_{\delta})} (\delta_{\nu\delta} + \delta_{\nu\gamma} - \delta_{\nu\beta} - \delta_{\nu\alpha}) \\
&\quad \times \left(\langle \hat{n}_\alpha \rangle_0 \langle \hat{n}_\beta \rangle_0 (1 - \langle \hat{n}_\gamma \rangle_0) (1 - \langle \hat{n}_\delta \rangle_0) - \langle \hat{n}_\gamma \rangle_0 \langle \hat{n}_\delta \rangle_0 (1 - \langle \hat{n}_\alpha \rangle_0) (1 - \langle \hat{n}_\beta \rangle_0) \right) \\
&= 16 \sum_{\beta, \gamma, \delta} |V_{\nu\beta\gamma\delta}|^2 \cos(t(\epsilon_{\nu} + \epsilon_{\beta} - \epsilon_{\gamma} - \epsilon_{\delta})) \left(\langle \hat{n}_\nu \rangle_0 \langle \hat{n}_\beta \rangle_0 (1 - \langle \hat{n}_\gamma \rangle_0) (1 - \langle \hat{n}_\delta \rangle_0) \right. \\
&\quad \left. - \langle \hat{n}_\gamma \rangle_0 \langle \hat{n}_\delta \rangle_0 (1 - \langle \hat{n}_\nu \rangle_0) (1 - \langle \hat{n}_\beta \rangle_0) \right).
\end{aligned}$$

III PRETHERMALIZATION INDUCED BY WEAK INTERACTIONS

In section 3, we focus on the Hubbard model, and the interaction is the double occupation

$$\nu \rightarrow \sigma \mathbf{k} \quad \Longrightarrow \quad V_{\nu\beta\gamma\delta} \rightarrow \frac{\Delta_{\mathbf{k}+\mathbf{k}_1+\mathbf{k}_2+\mathbf{k}_3}}{4L^2} \delta_{\sigma\sigma_3} \delta_{\sigma_1\sigma_2} (1 - \delta_{\sigma\sigma_1}) .$$

Therefore, the expectation value is

$$\begin{aligned} & \left\langle \left[\hat{D}, \left[e^{it\hat{H}_0} \hat{D} e^{-it\hat{H}_0}, \hat{n}_{\sigma\mathbf{k}} \right] \right] \right\rangle_0 \\ &= 2 \sum_{\mathbf{k}_1, \mathbf{k}_2, \mathbf{k}_3} \frac{\Delta_{\mathbf{k}+\mathbf{k}_1+\mathbf{k}_2+\mathbf{k}_3}}{L^2} \cos(t(\epsilon_{\mathbf{k}} + \epsilon_{\mathbf{k}_1} - \epsilon_{\mathbf{k}_2} - \epsilon_{\mathbf{k}_3})) \\ & \quad \times \left(\langle \hat{n}_{\sigma\mathbf{k}} \rangle_0 \langle \hat{n}_{\bar{\sigma}\mathbf{k}_1} \rangle_0 (1 - \langle \hat{n}_{\bar{\sigma}\mathbf{k}_2} \rangle_0) (1 - \langle \hat{n}_{\sigma\mathbf{k}_3} \rangle_0) \right. \\ & \quad \left. - \langle \hat{n}_{\bar{\sigma}\mathbf{k}_2} \rangle_0 \langle \hat{n}_{\sigma\mathbf{k}_3} \rangle_0 (1 - \langle \hat{n}_{\sigma\mathbf{k}} \rangle_0) (1 - \langle \hat{n}_{\bar{\sigma}\mathbf{k}_1} \rangle_0) \right) \\ &= 2\Re \sum_i F_{\bar{\sigma}}^+(\mathbf{R}_i, t) F_{\bar{\sigma}}^-(\mathbf{R}_i, t) \left(f_{\sigma\mathbf{k}}^+(\mathbf{R}_i, t) F_{\sigma}^-(\mathbf{R}_i, t) - f_{\sigma\mathbf{k}}^-(\mathbf{R}_i, t) F_{\sigma}^+(\mathbf{R}_i, t) \right) . \end{aligned}$$

We use the abbreviations

$$\begin{aligned} f_{\sigma\mathbf{k}}^+(\mathbf{R}_i, t) &= e^{-i(\mathbf{R}_i \cdot \mathbf{k} + t\epsilon_{\mathbf{k}})} \langle \hat{n}_{\sigma\mathbf{k}} \rangle_0 , \\ f_{\sigma\mathbf{k}}^-(\mathbf{R}_i, t) &= e^{i(\mathbf{R}_i \cdot \mathbf{k} + t\epsilon_{\mathbf{k}})} (1 - \langle \hat{n}_{\sigma\mathbf{k}} \rangle_0) , \\ F_{\sigma}^{\pm}(\mathbf{R}_i, t) &= \frac{1}{L} \sum_{\mathbf{k}} f_{\sigma\mathbf{k}}^{\pm}(\mathbf{R}_i, t) . \end{aligned}$$

The expressions for the kinetic energy and double occupation, we deduce as

$$\begin{aligned} \left\langle \left[\hat{D}, \left[\hat{D}_I(t), \hat{H}_0 \right] \right] \right\rangle_0 &= \sum_{\sigma\mathbf{k}} \epsilon_{\mathbf{k}} \left\langle \left[\hat{D}, \left[\hat{D}_I(t), \hat{n}_{\sigma\mathbf{k}} \right] \right] \right\rangle_0 \\ &= 2\Re \sum_{i\sigma} F_{\bar{\sigma}}^+(\mathbf{R}_i, t) F_{\bar{\sigma}}^-(\mathbf{R}_i, t) \left(F_{\sigma}^-(\mathbf{R}_i, t) i \frac{\partial}{\partial t} F_{\sigma}^+(\mathbf{R}_i, t) \right. \\ & \quad \left. - F_{\sigma}^+(\mathbf{R}_i, t) (-i) \frac{\partial}{\partial t} F_{\sigma}^-(\mathbf{R}_i, t) \right) \\ &= 2\Re \sum_i i \frac{\partial}{\partial t} F_{\bar{\sigma}}^+(\mathbf{R}_i, t) F_{\bar{\sigma}}^-(\mathbf{R}_i, t) F_{\sigma}^-(\mathbf{R}_i, t) F_{\sigma}^+(\mathbf{R}_i, t) , \\ i \left\langle \left[\hat{D}, \hat{D}_I(t) \right] \right\rangle_0 &= \int_0^t d\tau \left\langle \left[\hat{D}, \left[\hat{D}_I(\tau), \hat{H}_0 \right] \right] \right\rangle_0 \\ &= 2\Re \sum_i i F_{\bar{\sigma}}^+(\mathbf{R}_i, t) F_{\bar{\sigma}}^-(\mathbf{R}_i, t) F_{\sigma}^-(\mathbf{R}_i, t) F_{\sigma}^+(\mathbf{R}_i, t) . \end{aligned}$$

3 INTERACTION QUENCHES, RAMPS AND PERIODIC DRIVES

The numerical summation over all lattice sites i is challenging. This issue simplifies in the limit of infinite spatial dimensions.⁵⁷ The lattice sum of the functions $F_\sigma^\pm(\mathbf{R}_i, t)$ is bounded by

$$\sum_i |F_\sigma^\pm(\mathbf{R}_i, t)|^2 = F_\sigma^\pm(\mathbf{0}, 0) \leq 1 .$$

The function $F_\sigma^\pm(\mathbf{R}_i, t)$ has the same value for each lattice point in the same symmetry group. Hence, its absolute value is bounded by the number of lattice points z_i in the symmetry group of \mathbf{R}_i ,

$$|F_\sigma^\pm(\mathbf{R}_i, t)| \leq \frac{1}{\sqrt{z_i}} .$$

Only $\mathbf{R}_i = \mathbf{0}$ has a finite contribution in the limit of infinite spatial dimensions,⁵⁷ as z_i goes to infinity for infinite dimension and all other symmetry groups. We consider a paramagnetic state $F_\sigma^\pm(\mathbf{R}_i, t) = F_\sigma^\pm(\mathbf{R}_i, t)$ with a symmetric density of states (d.o.s.) $\rho(\epsilon) = \rho(-\epsilon)$ at half filling $\epsilon_F = 0$,

$$F_\sigma^\pm(\mathbf{R}_i, t) \rightarrow \delta_{0, \mathbf{R}_i} F(t) \quad \text{with} \quad F(t) = \int_{-W/2}^0 d\epsilon \rho(\epsilon) e^{-it\epsilon} .$$

In particular, we investigate the constant, the semielliptic, and the Gaussian d.o.s. . The corresponding functions $F(t)$ are found in table 3. For our main quantities discontinuity

d.o.s.	constant	semielliptic	Gaussian
$\rho(\epsilon)$	$\frac{\Theta(1-\epsilon^2)}{2}$	$\frac{2}{\pi}\Theta(1-\epsilon^2)\sqrt{1-\epsilon^2}$	$\frac{e^{-\epsilon^2}}{\sqrt{\pi}}$
$F(t)$	$\frac{\sin(t) + i(\cos(t) - 1)}{t}$	$\frac{J_1(t) - iH_1(t)}{t}$	$\frac{e^{-t^2/4}}{2} - \frac{i}{\sqrt{\pi}}D_+(t/2)$

Table 3: Functions $F(t)$ from different densities of states

at the Fermi surface, kinetic energy, and double occupation, we use the abbreviations

$$\begin{aligned} \Delta n(t) &= 1 + U^2 \Delta n^{(2)}(t) + O(U^3) , \\ \langle \hat{H}_0 \rangle_t &= E_0 + U^2 E_{\text{kin}}^{(2)}(t) + O(U^3) , \\ \langle \hat{D} \rangle_t &= \frac{1}{4} + U \Delta D^{(1)}(t) + O(U^2) . \end{aligned}$$

III PRETHERMALIZATION INDUCED BY WEAK INTERACTIONS

Evaluation of $J_{\hat{a}}(\epsilon)$ and $\tilde{J}_{\hat{D}}(\epsilon)$

We compute now the functions $J_{\hat{a}}(\epsilon)$ for the half-filled Hubbard model in infinite spatial dimensions. They are symmetric, $J_{\hat{a}}(\epsilon) = J_{\hat{a}}(-\epsilon)$, and have the form

$$J_{\hat{n}_{\sigma\mathbf{k}}}(\epsilon) = J_{\epsilon_{\mathbf{k}}}(\epsilon) \stackrel{\epsilon_{\mathbf{k}} > 0}{=} \int_{-\infty}^{\infty} \frac{dt}{2\pi} e^{-it\epsilon} 2\Re \left\{ e^{it\epsilon_{\mathbf{k}}} F(t)^3 \right\} \stackrel{\epsilon \geq 0}{=} \begin{cases} \alpha_3(\epsilon - \epsilon_{\mathbf{k}}) & \text{for } \epsilon > \epsilon_{\mathbf{k}} \\ 0 & \text{for } \epsilon < \epsilon_{\mathbf{k}} \end{cases} ,$$

$$J_{\hat{H}_0}(\epsilon) = - \int_{-\infty}^{\infty} \frac{dt}{2\pi} e^{-it\epsilon} 2\Re \left\{ i \frac{\partial}{\partial t} F(t)^4 \right\} = |\epsilon| \alpha_4(|\epsilon|) , \quad \tilde{J}_{\hat{D}}(\epsilon) = \text{sgn}(\epsilon) \alpha_4(|\epsilon|) ,$$

$$\alpha_n(\epsilon) = \int_0^{W/2} d\epsilon_1 \dots \int_0^{W/2} d\epsilon_n \rho(\epsilon_1) \dots \rho(\epsilon_n) \delta(\epsilon_1 + \dots + \epsilon_n - \epsilon) = \int_{-\infty}^{\infty} \frac{dt}{2\pi} e^{-it\epsilon} F(t)^n .$$

The remaining functions $\alpha_3(\epsilon)$ and $\alpha_4(\epsilon)$ are piecewise analytic in intervals of the half bandwidth $\frac{W}{2}$,

$$\alpha_n(\epsilon) = \begin{cases} 0 & \text{for } \epsilon < 0 \\ \alpha_{n,1}(\epsilon) & \text{for } 0 < \epsilon < \frac{W}{2} \\ \alpha_{n,2}(\epsilon) & \text{for } \frac{W}{2} < \epsilon < W \\ \vdots & \vdots \\ \alpha_{n,n}(\epsilon) & \text{for } \frac{W(n-1)}{2} < \epsilon < \frac{Wn}{2} \\ 0 & \text{for } \frac{Wn}{2} < \epsilon \end{cases} .$$

We compute them recursively as

$$\alpha_{n+1,m}(\epsilon) = \int_0^{\epsilon - \frac{m-1}{2}W} d\epsilon_1 \rho(\epsilon_1) \alpha_{n,m}(\epsilon - \epsilon_1) + \int_{\epsilon - \frac{m-1}{2}W}^{W/2} d\epsilon_1 \rho(\epsilon_1) \alpha_{n,m-1}(\epsilon - \epsilon_1) ,$$

$$\alpha_{1,1}(\epsilon) = \rho(\epsilon) , \quad \alpha_{n,0}(\epsilon) = \alpha_{n,n+1}(\epsilon) = 0 .$$

If the d.o.s. is a poly in ϵ , then the analytic evaluation of $\alpha_3(\epsilon)$ and $\alpha_4(\epsilon)$ is straight-forward. The real-time dynamics can be computed analytically as long as the ramping

3 INTERACTION QUENCHES, RAMPS AND PERIODIC DRIVES

functions are not too complicated. Examples for $f(t)$ are given in subsection e). We obtain for the constant density of states (d.o.s.) with $\rho(\epsilon) = 1/2$ and $W = 2$,

$$\begin{aligned}\alpha_{3,1}(\epsilon) &= \frac{\epsilon^2}{16}, \\ \alpha_{3,2}(\epsilon) &= -\frac{\epsilon^2}{8} + \frac{3\epsilon}{8} - \frac{3}{16}, \\ \alpha_{3,3}(\epsilon) &= \frac{\epsilon^2}{16} - \frac{3\epsilon}{8} + \frac{9}{16}, \\ \alpha_{4,1}(\epsilon) &= \frac{\epsilon^3}{96}, \\ \alpha_{4,2}(\epsilon) &= -\frac{\epsilon^3}{32} + \frac{\epsilon^2}{8} - \frac{\epsilon}{8} + \frac{1}{24}, \\ \alpha_{4,3}(\epsilon) &= \frac{\epsilon^3}{32} - \frac{\epsilon^2}{4} + \frac{5\epsilon}{8} - \frac{11}{24}, \\ \alpha_{4,4}(\epsilon) &= -\frac{\epsilon^3}{96} + \frac{\epsilon^2}{8} - \frac{\epsilon}{2} + \frac{2}{3}.\end{aligned}$$

We perform the integrations numerically for more complicated cases, e.g., semielliptic, Gaussian or next-neighbor hopping on the square lattice. We display the results of $\alpha_3(\epsilon)$

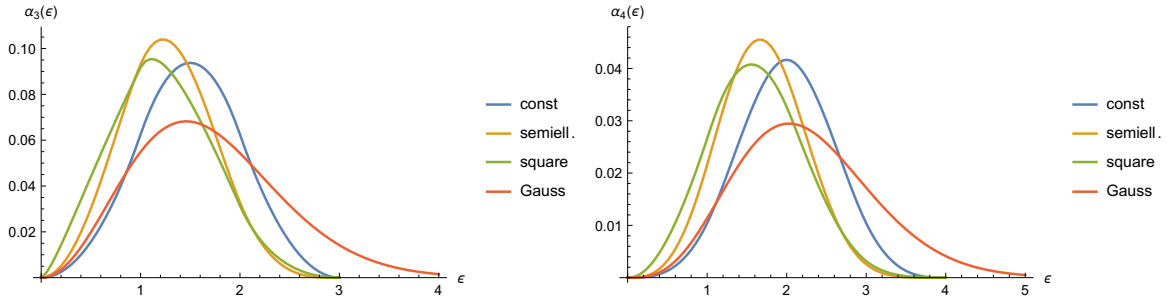


Figure 26: $\alpha_3(\epsilon)$ and $\alpha_4(\epsilon)$ for various d.o.s.

and $\alpha_4(\epsilon)$ for these d.o.s. and a bandwidth of $W = 2$ in figure 26. In all cases, the functions are qualitatively similar. They rise from zero up to a maximum and decrease after that. For a finite bandwidth, these functions vanish as expected at $\epsilon = 3$ or $\epsilon = 4$. by contrast, they are finite for the Gaussian d.o.s. for all finite ϵ . The functions $\alpha_3(\epsilon)$ and $\alpha_4(\epsilon)$ for the constant d.o.s. are symmetric, while otherwise the peak is shifted to the left.

III PRETHERMALIZATION INDUCED BY WEAK INTERACTIONS

Next, we analyze the small- ϵ behavior as it determines the convergence of the equilibrium correction $\int d\epsilon \frac{J_a(\epsilon)}{2\epsilon^2}$. If $\rho(0)$ is finite, we obtain

$$\alpha_n(\epsilon) = \frac{\epsilon^{n-1}}{(n-1)!} \rho(0)^n + O(\epsilon^n) .$$

The square lattice d.o.s. has a logarithmic divergence around $\epsilon = 0$ and therefore the functions grow faster for small ϵ ,

$$\rho(\epsilon) = c \log(\epsilon) + O(1) \quad \Rightarrow \quad \alpha_n(\epsilon) = \frac{\epsilon^{n-1} c^n}{(n-1)!} \log(\epsilon)^n + O(\epsilon^{n-1} \log(\epsilon)^{n-1}) .$$

The small ϵ contribution to the integral $\int d\epsilon \frac{J_a(\epsilon)}{2\epsilon^2}$ is finite in both cases. Finally, we analyze the Gaussian d.o.s., for which we use an special integration technique as discussed next.

Integration technique for the Gaussian d.o.s.

We compute the functions $\alpha_n(\epsilon)$ for the Gaussian d.o.s. as

$$\begin{aligned} \alpha_n(\epsilon) &= \int_{-\infty}^{\infty} \frac{dt}{2\pi} e^{-it\epsilon} \int_0^{\infty} d\epsilon_1 \dots \int_0^{\infty} d\epsilon_n \frac{e^{\sum_{l=1}^n it\epsilon_l - \epsilon_l^2}}{\sqrt{\pi^n}} \\ &= \frac{\epsilon^{n-1}}{\sqrt{\pi^n}} \int_0^{\infty} dx_1 \dots \int_0^{\infty} dx_n e^{-\epsilon^2 \sum_{l=0}^n x_l^2} \delta(1 - \sum_{l=0}^n x_l) \\ &= \int_{1/n}^1 db a_n(b) \frac{\epsilon^{n-1} e^{-b\epsilon^2}}{\sqrt{\pi^n}} . \end{aligned}$$

The functions $a_n(b)$ are strictly positive and have the definition

$$a_n(b) = \int_0^{\infty} dx_1 \dots \int_0^{\infty} dx_n \delta(1 - \sum_{i=1}^n x_i) \delta(b - \sum_{j=1}^n x_j^2) . \quad (\text{III.17})$$

The functions $a_3(b)$ and $a_4(b)$ are evaluated analytically in appendix 1. Due to the geometry of the higher-dimensional sphere, the functions $a_n(b)$ are non-zero only in the interval $(\frac{1}{n}, 1)$. We compute the real-time functions by Fourier transformation

$$\begin{aligned} F(t)^n &= \int_{-\infty}^{\infty} d\epsilon e^{it\epsilon} \alpha_n(\epsilon) = \int_{1/n}^1 db \frac{a_n(b)}{\sqrt{\pi^n}} \int_{-\infty}^{\infty} d\epsilon e^{it\epsilon} \alpha_n(\epsilon) \epsilon^{n-1} e^{-b\epsilon^2} \\ &= \int_{1/n}^1 db \frac{a_n(b)}{\sqrt{b\pi^{n-1}}} \left(-i \frac{\partial}{\partial t}\right)^{n-1} e^{-\frac{t^2}{4b}}. \end{aligned}$$

This technique enables us to analytically compute the time integrations in some cases. An example will be given in subsection d).

Now, we have access to all the $J_{\hat{a}}(\epsilon)$ and $\tilde{J}_{\hat{A}}(\epsilon)$ for our numerical evaluation. In the next subsections c) to f), we will compute the transients for the expectation values of double occupation, kinetic energy and mode occupation numbers. The procedure works as following: We insert $J_{\hat{a}}(\epsilon)$ and $\tilde{J}_{\hat{A}}(\epsilon)$ from this subsection into equation (III.15) or (III.16) and perform the integration over ϵ analytically or numerically.

c) Nonequilibrium crossing points

We compute the dynamics of a time-dependent first-order observable. We start from initial states of varying interaction strength g_0 and ramp to a fixed final interaction strength g_1 . We compare the dynamic with respect to the various initial states. Equation (III.15) predicts for interaction ramps and in particular quenches that the time-dependent expectation value is computed as the adiabatic term plus the dynamical term with respect to the noninteracting state,

$$\langle \hat{A} \rangle_t = \langle \hat{A} \rangle_0 + g_0 \Delta A_{\text{ad}}^{(1)} + (g_1 - g_0) \Delta A_{\text{ramp}}^{(1)}(t) + O(g^2).$$

We assume the existence of times t^* at which

$$\Delta A_{\text{ad}}^{(1)} = \Delta A_{\text{ramp}}^{(1)}(t^*). \quad (\text{III.18})$$

Then equation (III.15) is independent of g_0

$$\langle \hat{A} \rangle_{t^*} = \langle \hat{A} \rangle_0 + g_1 \Delta A_{\text{ad}}^{(1)} + O(g^2).$$

Therefore, any two lines of $\langle \hat{A} \rangle_t$ with identical g_1 and different g_0 cross at time t^* and we call it nonequilibrium crossing point. We emphasize that t^* strongly depends on

III PRETHERMALIZATION INDUCED BY WEAK INTERACTIONS

the chosen observable \hat{A} , ramp function $f(t)$ and the model under investigation. No finite time t^* may exist or several such times. One particular solution for t^* is the long-time limit because of equation (III.9). Hence, the crossing point has the value of the prethermalization plateau. If perturbation theory is applicable, then crossing points are predicted for every quench or ramp with fixed final interaction strength. Thus, crossing points are a very general nonequilibrium phenomenon.

We were informed by F. Maislinger and H. G. Evertz that they had observed an crossing point in the double occupation for different Hubbard interaction quenches in infinite dimensions.⁹⁷ In their nonequilibrium DMFT calculations, the lines of $\langle \hat{D} \rangle_t$ cross at time $t \approx 0.5$ for fixed U_1 and variable U_0 and a semielliptical d.o.s. with bandwidth 4. We now show that our perturbative method explains the origin of this crossing point and compare the nonequilibrium DMFT data of the reference⁹⁷ with our method. First, we apply the first-order formula (III.15) to the quench with $f(t > 0) = 1$. Second, we insert the half-filled Hubbard model in infinite spatial dimensions and evaluate the perturbative expression,

$$\begin{aligned} \langle \hat{D} \rangle_t &= \frac{1}{4} + U_0 \Delta D_{\text{ad}}^{(1)} + (U_1 - U_0) \Delta D_{\text{qu}}^{(1)}(t) + O(U^2) , \\ \Delta D_{\text{qu}}^{(1)}(t) &= \int_0^t d\tau 2\Re \{ iF(\tau)^4 \} , \quad \Delta D_{\text{ad}}^{(1)} = \Delta D_{\text{qu}}^{(1)}(\infty) , \end{aligned} \quad (\text{III.19})$$

with $F(t)$ given in table 3. Examples are depicted in figure 27 for various d.o.s. with bandwidth $W = 4$. In all cases, we observe at least one crossing point at a finite time t^* , and the values are listed in table 4. Moreover, we obtain similar values for t_1^* and $\Delta D_{\text{qu}}^{(1)}(\infty)$ for all tested d.o.s., thus this point is an almost universal feature comparable to the high-temperature crossing point of the specific heat in the Hubbard model.⁹⁸

d.o.s.	constant	semielliptic	Gaussian	square lattice
t_1^*	0.438075	0.526404	0.59826	0.589538
t_2^*	1.32381	1.64790		
$\Delta D_{\text{qu}}^{(1)}(\infty)$	-0.034831	-0.0417323	-0.0466286	-0.0463528

Table 4: Perturbative crossing-point values for the double occupation

The plot in the right upper corner of figure 27 corresponds to the DMFT calculations. Our results describe one crossing point at $t^* \approx 0.53$ and a second one at $t^* \approx 1.65$. The

3 INTERACTION QUENCHES, RAMPS AND PERIODIC DRIVES

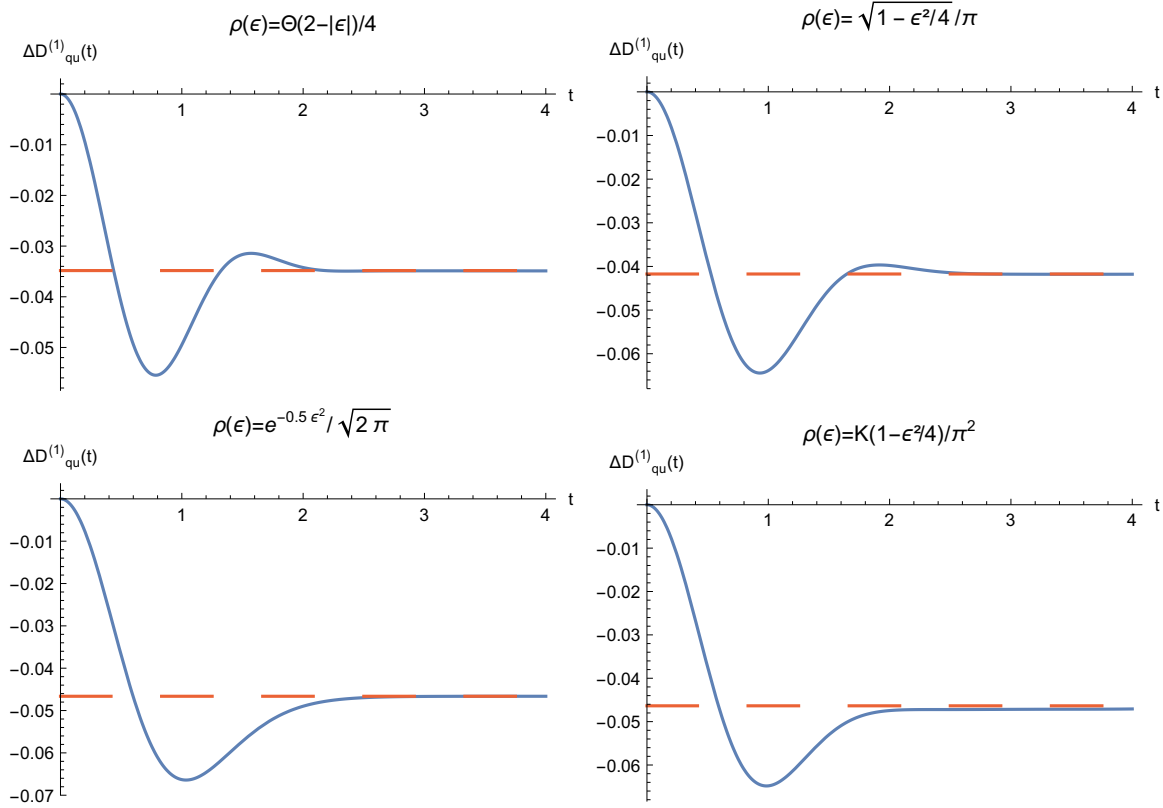


Figure 27: Perturbation theory for constant, semielliptic, Gaussian and square lattice d.o.s.

error of the perturbation theory is $O(U_0^2)$ at $t = 0$, and it further grows in time with $O((U_1 - U_0)^2 t^2)$. Therefore, large enough times becomes inaccessible in this method even for very weak quenches. Hence, we expect a significantly larger error at time $t^* \approx 1.65$ than at $t^* \approx 0.53$.

We compare the results of DMFT and the perturbation theory in figure 28. Initially, the difference is minimal ($U_0 \leq 2$) and increases with time as expected. The error remains small for small $U_1 \approx 0.5$ in the depicted times. The error increases at a much greater rate for larger U_1 . The perturbation theory is in good agreement with the numerical data for times $t \lesssim 0.5$ and thus explains the first observed crossing point. The right column of figure 28 shows close-up views of the crossing regions. The DMFT lines lie further to the right than the corresponding perturbative lines. Hence, the DMFT crossing region is shifted slightly to later times compared to the narrow crossing point

III PRETHERMALIZATION INDUCED BY WEAK INTERACTIONS

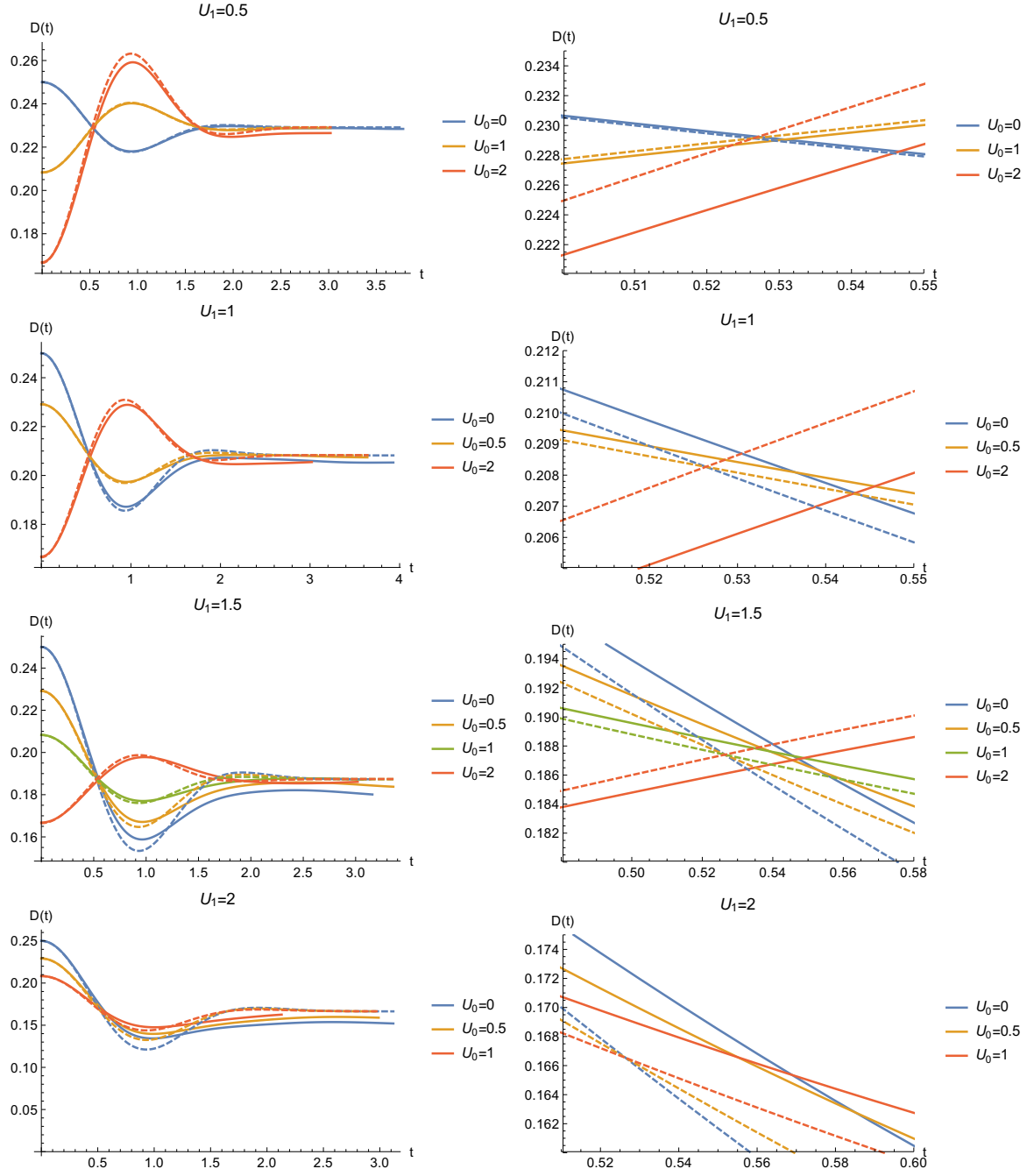


Figure 28: Double occupation after an interaction quench from U_0 to U_1 . Solid lines: nonequilibrium DMFT data.⁹⁷ Dashed lines: perturbative results from equation (III.19)

3 INTERACTION QUENCHES, RAMPS AND PERIODIC DRIVES

of perturbation theory at $t^* = 0.526404$.

A close-up view of the second crossing point at $t^* \approx 1.65$ is shown in figure 29. The perturbative prediction is in good agreement for $U_1 = 0.5$, but not for $U_1 = 1$ in which case the crossing region occurs at $t \approx 1.75$. This is significantly later than the perturbative value $t^* = 1.64790$. The crossing region's time window increases in the $U_1 = 0.5$ case from a sharp $\Delta t^* \approx 0.546 - 0.530 = 0.016$ around the first crossing point to a broader $\Delta t^* \approx 1.69 - 1.61 = 0.08$ around the second one. The broadening indicates a stronger deviation from perturbation theory. The deviation induces a breakdown of the second crossing region for $U_1 \geq 1$ as neighboring lines do not intersect with each other, e.g., the lines of $U_0 = 0$ and $U_0 = 0.5$ for $U_1 = 1$ in figure 29.

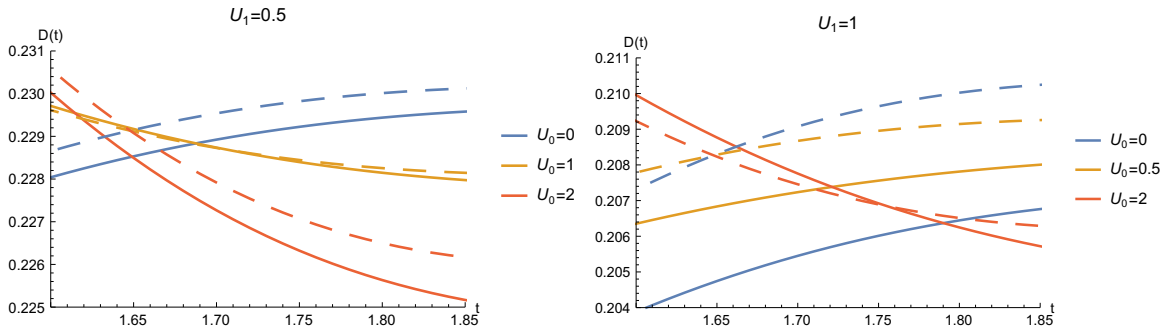


Figure 29: Close-up view on second crossing point. Solid lines: nonequilibrium DMFT data.⁹⁷ Dashed lines: perturbative results from equation (III.19)

To analyze these crossing points systematically we now ask, which d.o.s. induces a second crossing point within our method. We use the parameterized symmetric d.o.s. from reference⁹⁹ for this investigation,

$$\rho_n(\epsilon) = \frac{n+1}{4n} \left(1 - \left| \frac{\epsilon}{2} \right|^n \right).$$

More spectral density is distributed at the center of the band for small n , and increasing n distributes it more evenly, as seen on the left side of figure 30. The corresponding $\tilde{J}_D(\epsilon)$ are depicted on the right side of figure 30. Their peaks grow and shift to smaller ϵ for smaller n .

The time evolution in figure 31 exhibit no second crossing point for $n = 1$ and it emerges for $n \geq 2$. The crossing times are listed in table 5, and they shift to earlier times with

III PRETHERMALIZATION INDUCED BY WEAK INTERACTIONS

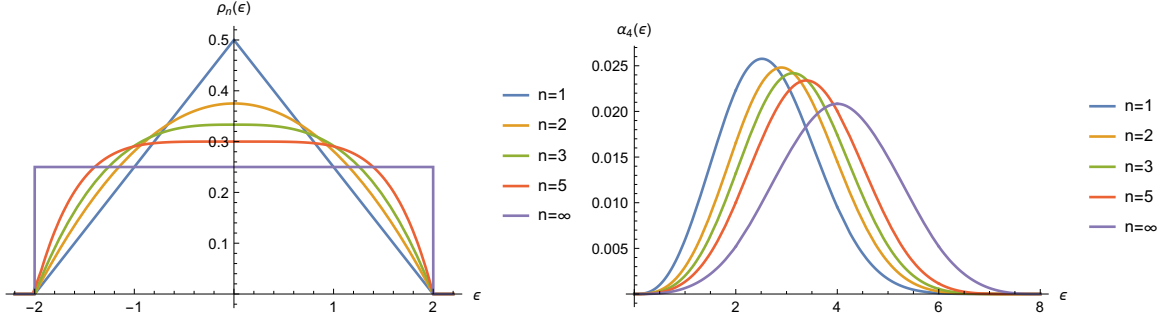


Figure 30: Parameterized d.o.s. (left) and corresponding $\alpha_4(\epsilon) = \tilde{J}_D(\epsilon)$ (right)

increasing n , which makes them sharper in nonperturbative calculations. We found three d.o.s. - triangle ($n = 1$), Gaussian, and square lattice - with a single crossing point: Their common feature is a more pronounced density peak. The flatter densities exhibit a second crossing point. Therefore, the existence of a second crossing point is a criterion for whether a d.o.s. is mostly flat or peaked. We note that similar conclusions can be drawn from the crossing point in the local spectral function as it reveals details of the noninteracting d.o.s. at its band edges.⁹⁹

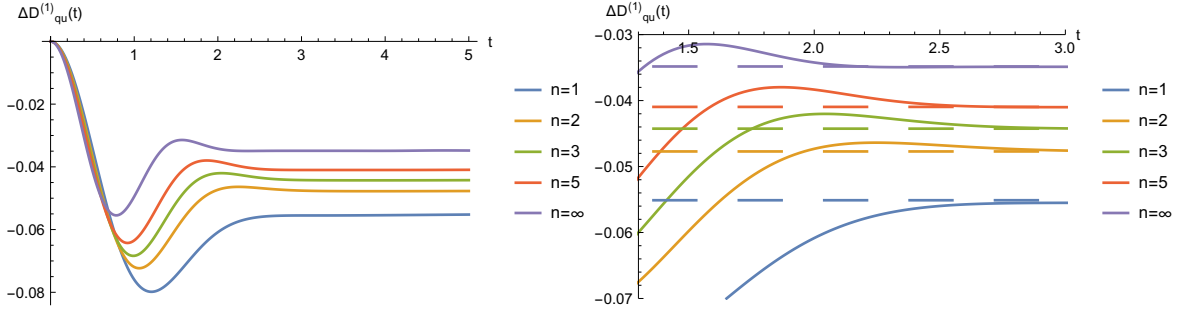


Figure 31: Perturbation theory for $\rho_n(\epsilon)$ with close-up view (right) and long-time limit as dotted lines

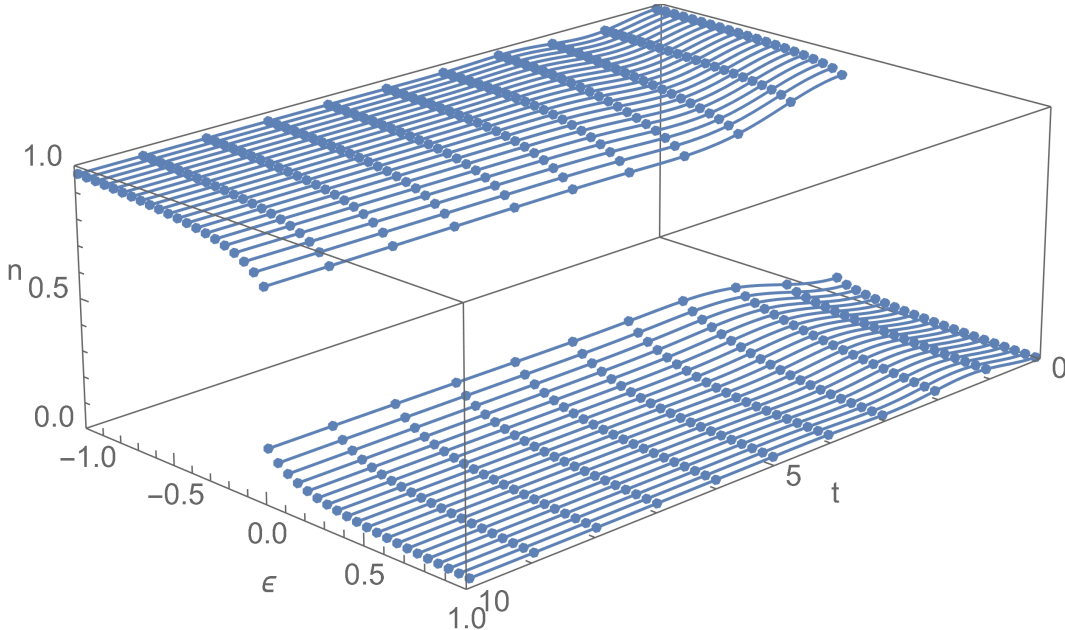
In summary, perturbation theory predicts crossing points for first-order observables and different initial but fixed final Hamiltonian. The comparison with nonequilibrium DMFT shows that earlier crossing times t^* and weaker interactions U_1 increase the sharpness of the crossing region. The deviation from perturbation theory shifts and broadens the crossing regions. Crossing points are called isosbestic points and are a generic feature if a linear approximation is applicable.¹⁰⁰

n	1	2	3	5	∞
t_1^*	0.700995	0.603257	0.558392	0.51594	0.438075
t_2^*		1.96021	1.75271	1.58609	1.32381
$\Delta D_{\text{qu}}^{(1)}(\infty)$	-0.0551087	-0.0477122	-0.044257	-0.0409581	-0.034831

 Table 5: Perturbative crossing-point values for the double occupation and $\rho_n(\epsilon)$

d) Relaxation after interaction quenches

In this subsection, we apply our method to the occupation numbers after the quench in the Hubbard model in infinite spatial dimensions. We discuss general features and show one explicit example in figures 32. In infinite dimensions, the occupation probability $\langle \hat{n}_{\sigma\mathbf{k}} \rangle_t$ depends only on the energy $\epsilon_{\mathbf{k}}$. We thus find the same general behavior of $\langle \hat{n}_{\sigma\mathbf{k}} \rangle_t$ for all density of states (d.o.s.). In particular, the states below the Fermi surface get depopulated, and the states above it are filled, while the total number of particles is conserved. The increase or decrease is not monotonous but is overlaid with oscillations. The dynamics are more pronounced for the states closer to the Fermi surface and less for the states towards the band edges.


 Figure 32: Quench from $U_0 = 1$ to $U_1 = 1.5$ with semielliptic d.o.s. within our method

III PRETHERMALIZATION INDUCED BY WEAK INTERACTIONS

Next, we investigate the relaxation behavior to the plateau value. We restrict our investigation to quenches. There the mix-term becomes equal to the ramp-term for second-order observables and we label it quench-term,

$$f(t > 0) = 1 \Rightarrow \Delta a_{\text{mix}}^{(2)}(t) = \Delta a_{\text{ramp}}^{(2)}(t) = \Delta a_{\text{qu}}^{(2)}(t) .$$

It is thus sufficient to study the relaxation to the prethermalization plateau for this quench-term. First, we evaluate the general form and obtain three contributions,

$$\begin{aligned} \Delta a_{\text{qu}}^{(2)}(t) &= \int_{-\infty}^{\infty} d\epsilon J_{\hat{a}}(\epsilon) \int_0^t dt_1 \int_0^{t_1} dt_2 e^{i(\epsilon+i\delta)(t_1-t_2)} \\ &= \int_{-\infty+i\delta}^{\infty+i\delta} d\epsilon J_{\hat{a}}(\epsilon) \left(\frac{1 - e^{i\epsilon t}}{\epsilon^2} + \frac{it}{\epsilon} \right) . \end{aligned}$$

The last term is linear in time t but it vanishes due to $J_{\hat{a}}(\epsilon) = J_{\hat{a}}(-\epsilon)$ and $J_{\hat{a}}(\epsilon = 0) = 0$,

$$\Delta a_{\text{qu}}^{(2)}(t) = \int_{-\infty}^{\infty} d\epsilon J_{\hat{a}}(\epsilon) \frac{1 - \cos(\epsilon t)}{\epsilon^2} .$$

The linear term can survive for periodically driven systems. The first term is time-independent and gives the plateau value. The cosine function describes oscillations, which are averaged out in the long-time limit. In figure 33, we display one numerical example for the jump at the Fermi energy. A close-up view on the plateau value reveals smaller damped oscillations. Next, we derive the long-time relaxations, and it governs these smaller oscillations. The long-time behavior of our observables is determined by the functions $F_{\sigma}^{\pm}(t)$. For a finite bandwidth, we partially integrate them to expand in powers of inverse time t^{-1} ,

$$\begin{aligned} F_{\sigma}^{+}(t) &= \int_{\epsilon_{\text{min}}}^{\epsilon_{\text{F}}} \rho_{\sigma}(\epsilon) e^{it\epsilon} d\epsilon \\ &= \left[\frac{e^{-it\epsilon} \rho_{\sigma}(\epsilon)}{-it} \right]_{\epsilon_{\text{F}}}^{\epsilon_{\text{max}}} - \left[\frac{e^{-it\epsilon} \rho'_{\sigma}(\epsilon)}{(-it)^2} \right]_{\epsilon_{\text{F}}}^{\epsilon_{\text{max}}} + O(t^{-3}) . \end{aligned}$$

The expansion for $F_{\sigma}^{-}(t)$ works analogously. When we evaluate an occupation number, we integrate a product of three functions of type $F_{\sigma}^{\pm}(t)$ over time t . The integration

3 INTERACTION QUENCHES, RAMPS AND PERIODIC DRIVES

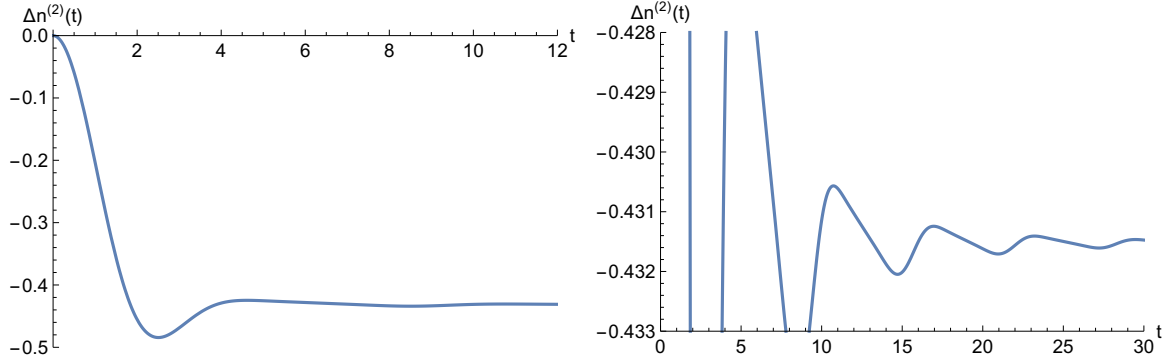


Figure 33: Closeup view on damped oscillations in the discontinuity of the Fermi surface after an interaction quench with constant d.o.s.

does not alter the power law t^{-3} as it is multiplied by an oscillatory function. Thus, our occupation numbers relax with t^{-3} or faster. The discontinuity at the Fermi surface can relax with t^{-2} as oscillation frequencies cancel each other out. We evaluate the long-time behavior of the discontinuity at the Fermi surface and the kinetic energy for the semielliptic d.o.s. ,

$$\Delta n^{(2)}(t) - \Delta n^{(2)}(\infty) = \frac{2^{9/2}3 \cos(t + \frac{1}{4}\pi)}{t^{7/2}\pi^{5/2}} + O(t^{-4}) ,$$

$$E_{\text{kin}}^{(2)}(t) - E_{\text{kin}}^{(2)}(\infty) = \frac{2^{9/2}}{t^{9/2}\pi^{7/2}} \sin(t - \frac{3\pi}{4}) + O(t^{-5}) ,$$

and the constant d.o.s. ,

$$\Delta n^{(2)}(t) - \Delta n^{(2)}(\infty) = -\frac{3 \sin(t) - \frac{3}{4} \sin(2t) + \frac{1}{9} \sin(3t)}{2t^3} + O(t^{-4}) ,$$

$$E_{\text{kin}}^{(2)}(t) - E_{\text{kin}}^{(2)}(\infty) = \frac{4\cos(t) - 3 \cos(2t) + \frac{4}{3} \cos(3t) - \frac{1}{4} \cos(4t)}{16t^4} + O(t^{-5}) .$$

The semielliptic d.o.s. relaxes faster because its d.o.s. vanishes at the band edges. The noninteger power law stems from the infinite derivative at the band edges. We compute an envelope function from our large-time expansion, and it encloses the oscillations perfectly on intermediate times, as seen in figure 34. This method of computing the relaxation behavior can be applied analogously to ramps. We expect the same power-law decay as for the quench but with altered oscillations and amplitude.

The relaxation of the double occupation is exactly the negative of the kinetic energy due to energy conservation. The double occupation oscillates around its plateau

III PRETHERMALIZATION INDUCED BY WEAK INTERACTIONS

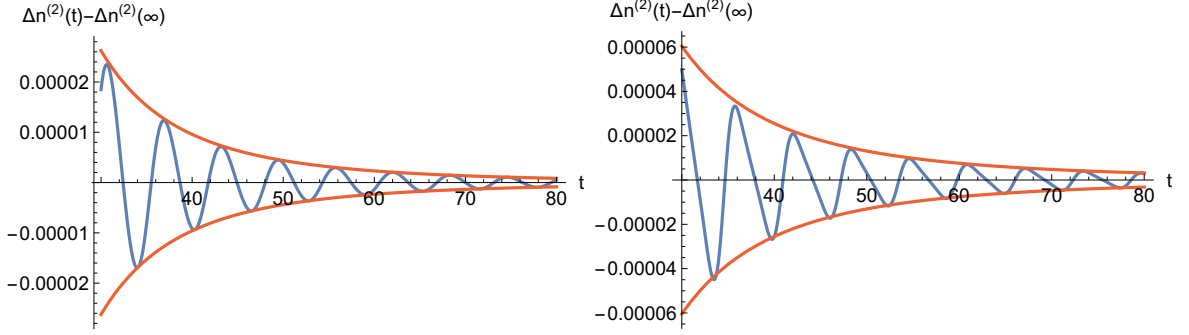


Figure 34: Enveloping the long-time behavior after an interaction quench with semielliptic (right) or constant (left) d.o.s.

value for the constant and semielliptic d.o.s. . Thus our method predicts infinitely many crossing points with $\Delta D^{(1)}(t^*) = \Delta D_{\text{ad}}^{(1)}$ for these two d.o.s. .

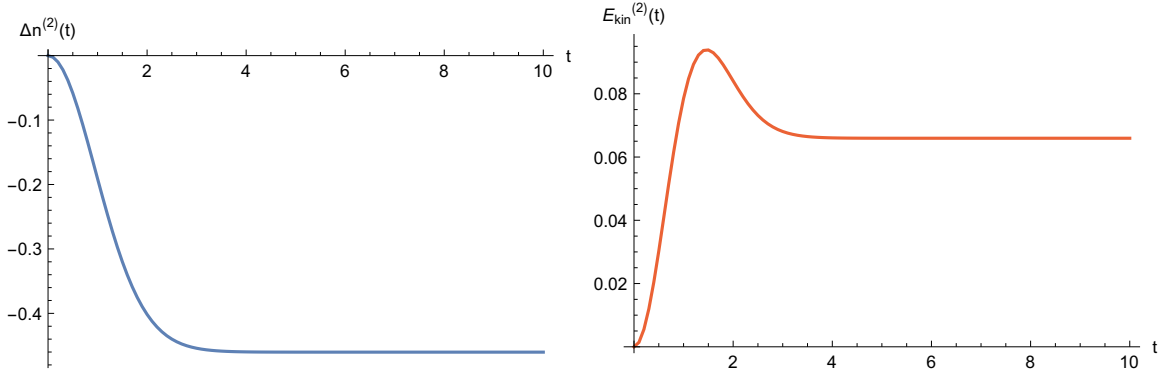


Figure 35: Fermi gap (left) and kinetic energy (right) after an interaction quench for the Gaussian d.o.s.

For the Gaussian d.o.s. , we can compute the two main observables analytically and obtain for the quench,

$$\Delta n^{(2)}(t) = \int_{\frac{1}{3}}^1 db a_3(b) 2 \frac{e^{-\frac{t^2}{4b}} - 1}{\pi \sqrt{b}} , \quad E_{\text{kin}}^{(2)}(t) = \int_{\frac{1}{4}}^1 db a_4(b) \frac{2b + (t^2 - 2b)e^{-\frac{t^2}{4b}}}{4\sqrt{\pi^3 b^5}} . \quad (\text{III.20})$$

One feature is that the discontinuity at the Fermi surface is a strictly decreasing function. The two functions are plotted in figure 35. They decrease Gaussian for large times and

thus much faster than for a d.o.s. with finite bandwidth. Moreover, this Gaussian decay causes a much smoother dynamic than the power-law decay for a d.o.s. with finite bandwidth.

In conclusion, we predict relaxation to the prethermal plateau in two stages. First, the large initial oscillations quickly relax, and then small oscillations prevail on intermediate times as they are weakly damped for certain d.o.s. . For example the Gaussian d.o.s. does not exhibit this second stage of relaxation.

e) Ramps: Crossover from quench to adiabatic regime

In this subsection, we examine interaction ramps during a finite time interval T . They thus lie in between the adiabatic ramp and the quench. There will be initial oscillations comparable to the quench for short ramping times, but the observables change monotonously if the ramping times are long enough. The example in figure 36 exhibits no oscillations as the ramping is slow, $T = 10$.

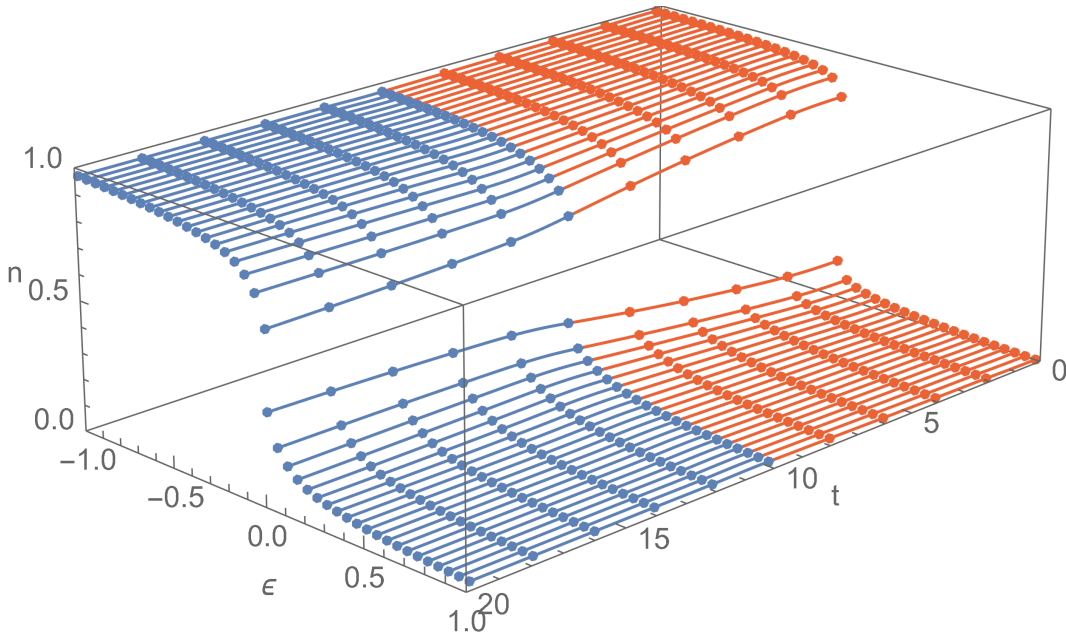


Figure 36: Linear ramp from $U_0 = 1$ to $U_1 = 1.5$ over $T = 10$ with square lattice d.o.s. within our method

The main objective of this subsection is to compare of the plateau values after various

III PRETHERMALIZATION INDUCED BY WEAK INTERACTIONS

ramps for second-order observables. The plateau value after the quench is exactly twice the value of the adiabatic ramp^{73,80,85} for all second-order observables. Therefore, we expect that the plateau values lie in between for all finite ramps. By contrast, the plateau value of the first-order observables is independent of ramping function and ramping time.

The ramping functions start at $t = 0$ with $f(0) = 0$ and stop at $t = T$ with $f(t \geq T) = 1$. We consider a class of smooth activation functions $S_n(x)$ for our ramping protocol. They are widely used in programming^{101–104} for small n . They have the definition¹⁰⁵

$$S_n(x) = x^{n+1} \sum_{m=0}^n \binom{n+m}{m} \binom{2n+1}{n-m} (-x)^m. \quad (\text{III.21})$$

They are the Hermite interpolation between the points $(0, 0)$ and $(1, 1)$ with vanishing first $n - 1$ derivatives at both points. Our ramping functions are displayed in figure 37 and defined as

$$f_n(t) = \begin{cases} 0 & \text{for } t < 0 \\ S_n\left(\frac{t}{T}\right) & \text{for } 0 < t < T \\ 1 & \text{for } T \leq t \end{cases}. \quad (\text{III.22})$$

The plateau values are computed from the $J_a(\epsilon)$ and the specific ramping protocol $f(t)$.

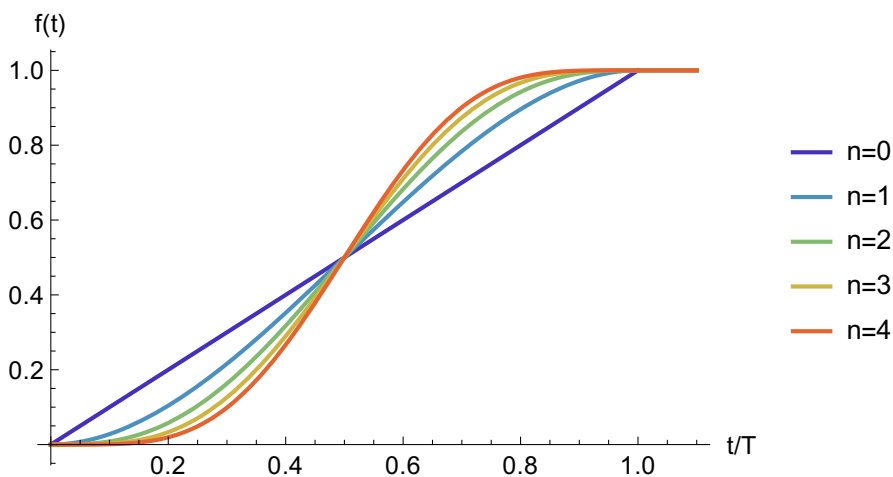


Figure 37: Ramping functions from equations (III.21) and (III.22)

3 INTERACTION QUENCHES, RAMPS AND PERIODIC DRIVES

First, we evaluate the general time evolution for the ramping protocol $f(t)$. Next, we take the long-time average,

$$\begin{aligned} \Delta a_{\text{ramp}}^{(2)}(t \rightarrow \infty) &= \lim_{\tau \rightarrow \infty} \int_0^\tau \frac{dt}{\tau} \Delta a_{\text{ramp}}^{(2)}(t) = \int d\epsilon J_{\hat{a}}(\epsilon) h_{\text{ramp}}(\epsilon) , \\ h_{\text{ramp}}(\epsilon) &= \lim_{\tau \rightarrow \infty} \int_0^\tau \frac{dt}{\tau} \left(\int_0^T d\tau_1 \int_0^{\tau_1} d\tau_2 f(\tau_2) \cos((\tau_1 - \tau_2)\epsilon) \right. \\ &\quad \left. + \int_T^t d\tau_1 \int_0^T d\tau_2 f(\tau_2) \cos((\tau_1 - \tau_2)\epsilon) + \int_T^t d\tau_1 \int_T^{\tau_1} d\tau_2 \cos((\tau_1 - \tau_2)\epsilon) \right) . \end{aligned}$$

For the quench ($h_{\text{qu}}(\epsilon) = \frac{1}{\epsilon^2}$) and the adiabatic switching ($h_{\text{ad}}(\epsilon) = \frac{1}{2\epsilon^2}$), the functions $h_{\text{ramp}}(\epsilon)$ are known. For the linear ramp, we have,

$$h_{\text{lin. ramp}}(\epsilon) = \frac{1}{2\epsilon^2} + \frac{1 - \cos(T\epsilon)}{\epsilon^4 T^2} \quad \text{with} \quad f(t) = f_0(t) .$$

In the limits $T \rightarrow 0$ and $T \rightarrow \infty$, thus gives the correct functions for quench and adiabatic switching. The prethermalization plateau values for kinetic energy and discontinuity at the Fermi surface are depicted in figure 38. We computed the values for various ramps and observe the monotonic decrease from the quench to the adiabatic case. Generally, the kinetic energy approaches the adiabatic limit faster than the discontinuity. Surprisingly, the adiabatic limit is reached at later times for smoother ramps. Our explanation for this phenomenon is that increasing smoothness n results in a higher peak slope of the ramping functions. A higher slope corresponds to a more abrupt procedure, which brings us closer to the quench.

The behavior for the occupation numbers is shown in figure 39. The states closer to the Fermi surface are more strongly affected than the states towards the band edges. A smoother ramp leads to reaching the adiabatic limit at longer ramping times. Up to

III PRETHERMALIZATION INDUCED BY WEAK INTERACTIONS

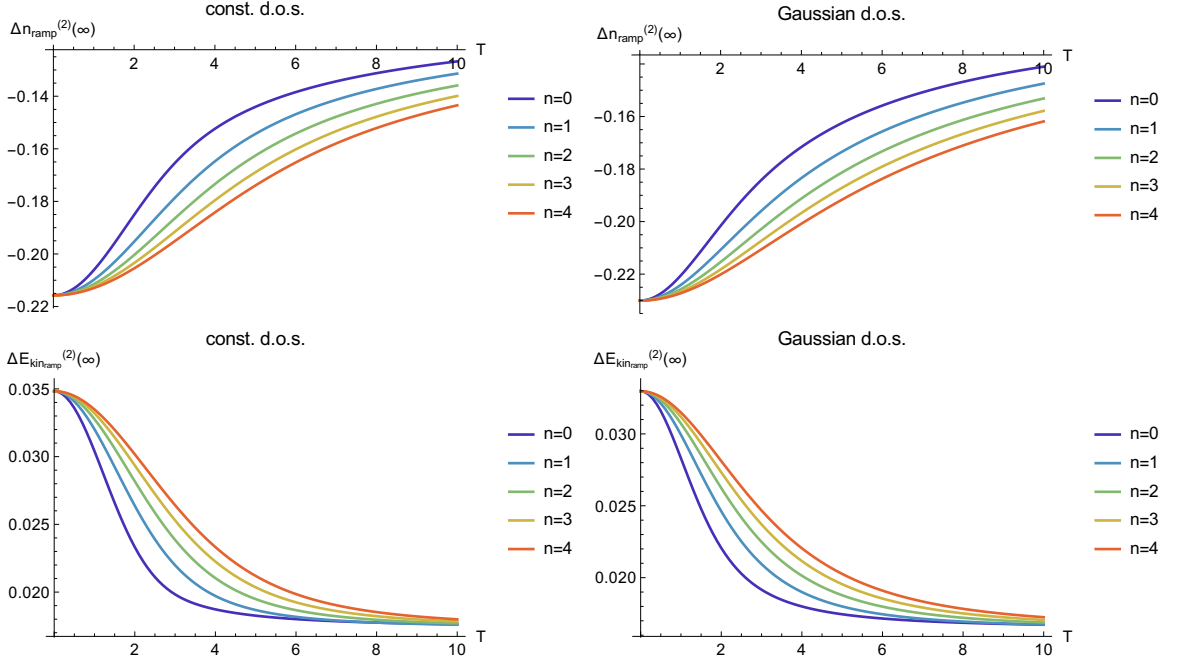


Figure 38: Prethermalization plateau of kinetic energy (bottom) and discontinuity at ϵ_F (top)

now, we have investigated the ramp term. Next, we take the mixing term into account for initially interacting states. Its general value is computed as

$$\begin{aligned}
 \Delta a_{\text{mix}}^{(2)}(t > T) &= \int d\epsilon J_{\hat{a}}(\epsilon) \left(\int_0^T d\tau_1 \int_0^{\tau_1} d\tau_2 f(\tau_2) \cos((\tau_1 - \tau_2)\epsilon) \right. \\
 &\quad \left. + \int_T^t d\tau_1 \int_0^T d\tau_2 f(\tau_2) \cos((\tau_1 - \tau_2)\epsilon) + \int_T^t d\tau_1 \int_T^{\tau_1} d\tau_2 \cos((\tau_1 - \tau_2)\epsilon) \right) \\
 &= \Delta a_{\text{qu}}^{(2)}(t - T) + \int d\epsilon J_{\hat{a}}(\epsilon) \int_0^T d\tau_2 f(\tau_2) \frac{\sin((t - \tau_2)\epsilon)}{\epsilon}.
 \end{aligned}$$

When we take the long-time average, only the quench term remains

$$\lim_{\tau \rightarrow \infty} \int_0^{\tau} \frac{dt}{\tau} \Delta a_{\text{mix}}^{(2)}(t) = \Delta a_{\text{qu}}^{(2)}(t \rightarrow \infty) = 2\Delta a_{\text{ad}}^{(2)}.$$

3 INTERACTION QUENCHES, RAMPS AND PERIODIC DRIVES

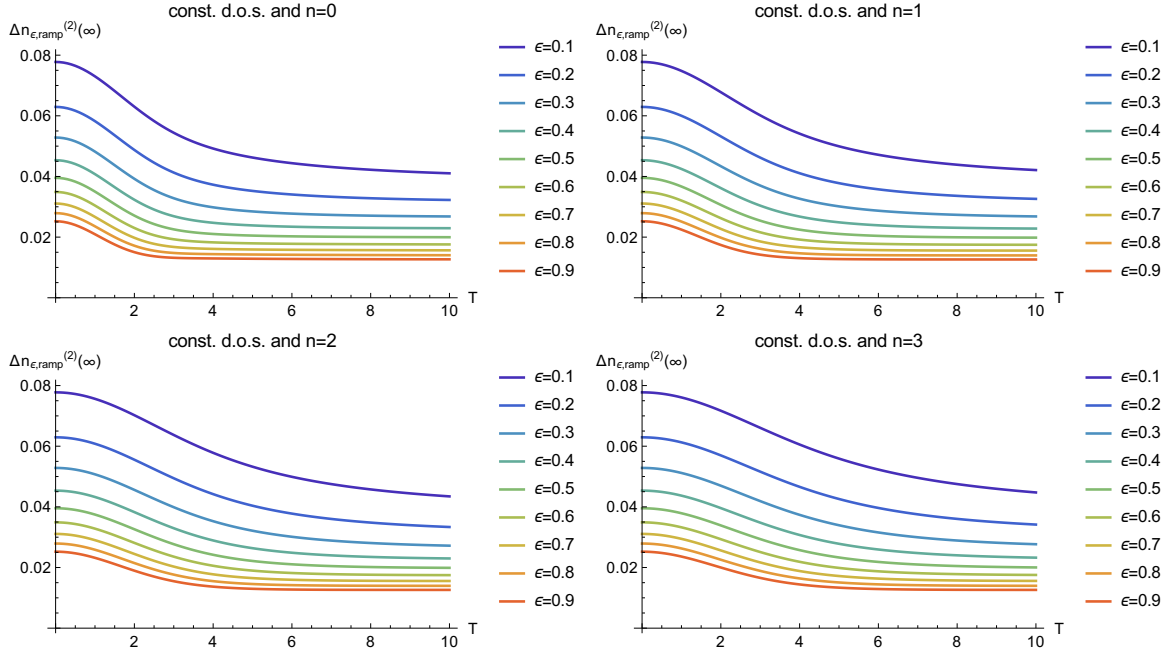


Figure 39: Prethermalization plateau for various occupation numbers above ϵ_F

Thus, the long-time limit of the mixing term is independent of the ramping protocol. This is a feature of a first-order observable. For the quench, the mixing and ramp term are identical and have the same long-time limit. Furthermore, we expect the same value for adiabatically ramping directly to $g_0 + \Delta g$ and ramping adiabatically there in two steps. For a two-step adiabatic ramp, we have proven that

$$(g_0 + \Delta g)^2 \Delta a_{\text{ad}}^{(2)} = g_0^2 \Delta a_{\text{ad}}^{(2)} + g_0 \Delta g \underbrace{\Delta a_{\text{mix}}^{(2)}(\infty)}_{=2\Delta a_{\text{ad}}^{(2)}} + (\Delta g)^2 \underbrace{\Delta a_{\text{ramp}}^{(2)}(\infty)}_{=\Delta a_{\text{ad}}^{(2)}} .$$

In summary, ramps fall in between quench and adiabatic value.⁸⁴ Some observables, i.e., kinetic energy, converge faster to the adiabatic limit than others, i.e., the discontinuity at the Fermi surface. The deviation from the prethermal plateau to the ground state is not affected by initial interactions.

f) Periodically driven system

Periodic, high-frequency driving can engineer interesting effective Hamiltonians which are very distinct from their equilibrium counterparts.¹⁰⁶ This new line of research is termed “Floquet engineering” and has motivated new interest in periodically driven systems.

III PRETHERMALIZATION INDUCED BY WEAK INTERACTIONS

Here, we investigate a periodically driven interaction $f(t) = (1 - \cos(\omega t))/2$ with our method. This scenario was computed at stroboscopic times with Floquet analysis and the quench equations by reference.⁸⁹ Within our framework, it is straightforward to evaluate it at arbitrary times.

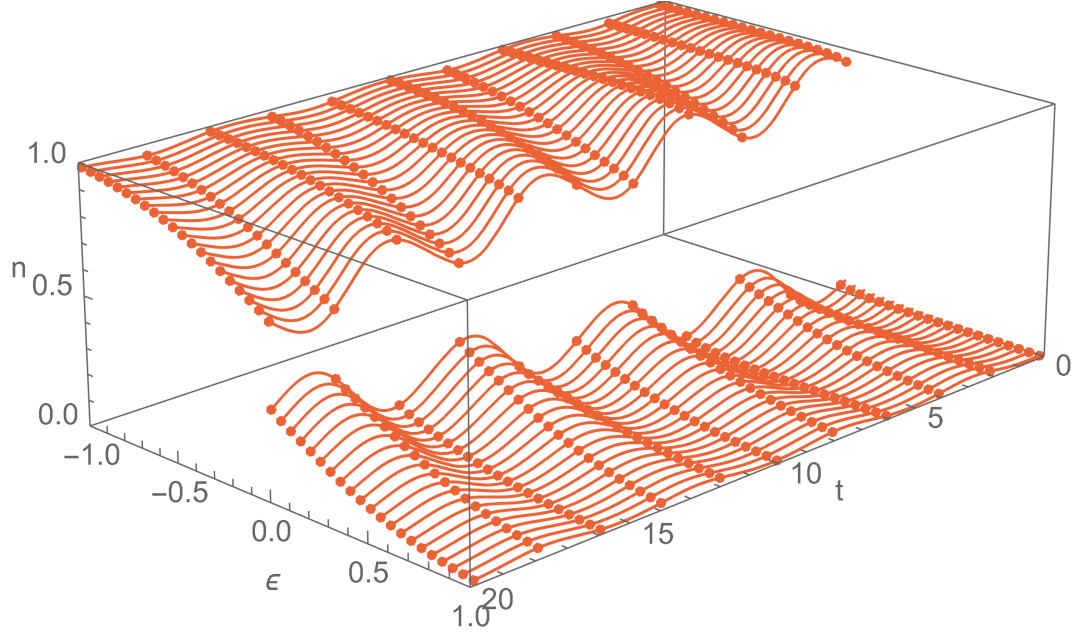


Figure 40: Periodic drive between $U_0 = 1$ and $U_1 = 1.5$ with $T = 5$, $\omega = \frac{2\pi}{T}$ and constant d.o.s. within our method

An example is depicted in figure 40. We observe the driving frequency in the time-dependent occupation probabilities. The Fermi gap shrinks further after each period in this example. We deduce this behavior by evaluating the general form of the ramp term,

$$\Delta a_{\text{ramp}}^{(2)}(t) = \int_{-\infty}^{\infty} d\epsilon J_{\hat{a}}(\epsilon) \int_0^t d\tau_1 \frac{1 - \cos(\omega\tau_1)}{2} \int_0^{\tau_1} d\tau_2 \frac{1 - \cos(\omega\tau_2)}{2} e^{i(\epsilon+i\delta)(\tau_1-\tau_2)} .$$

3 INTERACTION QUENCHES, RAMPS AND PERIODIC DRIVES

We perform the time integration analytically and obtain

$$\begin{aligned}
\Delta a_{\text{ramp}}^{(2)}(t) = & \int_{-\infty+i\delta}^{\infty+i\delta} d\epsilon J_{\hat{a}}(\epsilon) \frac{3\epsilon^4 - 3\epsilon^2\omega^2 + 4\omega^4}{16(\epsilon^3 - \epsilon\omega^2)^2} + \int_{-\infty+i\delta}^{\infty+i\delta} d\epsilon J_{\hat{a}}(\epsilon) \frac{it(3\epsilon^2 - 2\omega^2)}{8\epsilon(\epsilon^2 - \omega^2)} \\
& - \left(\cos(\omega t) - \frac{\cos(2\omega t)}{4} \right) \int_{-\infty+i\delta}^{\infty+i\delta} d\epsilon \frac{J_{\hat{a}}(\epsilon)}{4\epsilon^2 - 4\omega^2} \\
& - \int_{-\infty+i\delta}^{\infty+i\delta} d\epsilon J_{\hat{a}}(\epsilon) \left(\frac{i \sin(\omega t) (2\epsilon^2 - \omega^2)}{4\epsilon\omega(\epsilon^2 - \omega^2)} - \frac{i\epsilon \sin(2\omega t)}{16\epsilon^2\omega - 16\omega^3} \right) \\
& - \int_{-\infty+i\delta}^{\infty+i\delta} d\epsilon J_{\hat{a}}(\epsilon) \frac{\omega^2 e^{i\epsilon t} (\epsilon^2 \cos(t\omega) - \epsilon^2 - i\epsilon\omega \sin(t\omega) + \omega^2)}{4(\epsilon^3 - \epsilon\omega^2)^2} .
\end{aligned}$$

The last term vanishes in the long-time limit due to the factor $e^{i\epsilon t}$, while the other terms prevail for large times. The first term gives a plateau, the second term is linear, and the remaining terms cause oscillations with frequency ω or 2ω .

We evaluate the linear-in-time term by replacing the integration above the real axis by a delta function plus a principal value integral,

$$\int_{-\infty+i\delta}^{\infty+i\delta} dx \frac{f(x)}{x} = -i\pi f(0) + P \int_{-\infty}^{\infty} dx \frac{f(x)}{x} .$$

Due to the symmetry $J_{\hat{a}}(\epsilon) = J_{\hat{a}}(-\epsilon)$, the principal value integral results in zero and only the delta terms contribute. As for the quench, we have $J_{\hat{a}}(\epsilon = 0) = 0$ and $J_{\hat{a}}(\epsilon) = J_{\hat{a}}(-\epsilon)$, thus the linear term gives

$$\int_{-\infty+i\delta}^{\infty+i\delta} d\epsilon J_{\hat{a}}(\epsilon) \frac{it(3\epsilon^2 - 2\omega^2)}{8(\epsilon^3 - \epsilon\omega^2)} = \frac{t\pi J_{\hat{a}}(\omega)}{8} .$$

III PRETHERMALIZATION INDUCED BY WEAK INTERACTIONS

For the sine term we also find that the delta function contributes and that the principal value integral vanishes. The simplified expression is then

$$\begin{aligned} \Delta a_{\text{ramp}}^{(2)}(t) &= \frac{\pi J_{\hat{a}}(\omega)}{4} \left(\frac{t}{2} - \frac{\sin(\omega t)}{\omega} + \frac{\sin(2\omega t)}{4\omega} \right) \\ &+ \int_{-\infty}^{\infty} d\epsilon \frac{J_{\hat{a}}(\epsilon)}{4(\epsilon^2 - \omega^2)} \left[\frac{3\epsilon^4 - 3\epsilon^2\omega^2 + 4\omega^4}{4\epsilon^2(\epsilon^2 - \omega^2)} - \left(\cos(\omega t) - \frac{\cos(2\omega t)}{4} \right) \right] \\ &- \int_{-\infty}^{\infty} d\epsilon J_{\hat{a}}(\epsilon) \frac{\omega^2 \cos(\epsilon t) (\epsilon^2 \cos(t\omega) - \epsilon^2 + \omega^2) + \omega^2 \epsilon \sin(\epsilon t) \sin(t\omega)}{4(\epsilon^3 - \epsilon\omega^2)^2}. \end{aligned}$$

We recover the result from reference,⁸⁹ when we insert the stroboscopic times $t_m = \frac{2\pi m}{\omega}$,

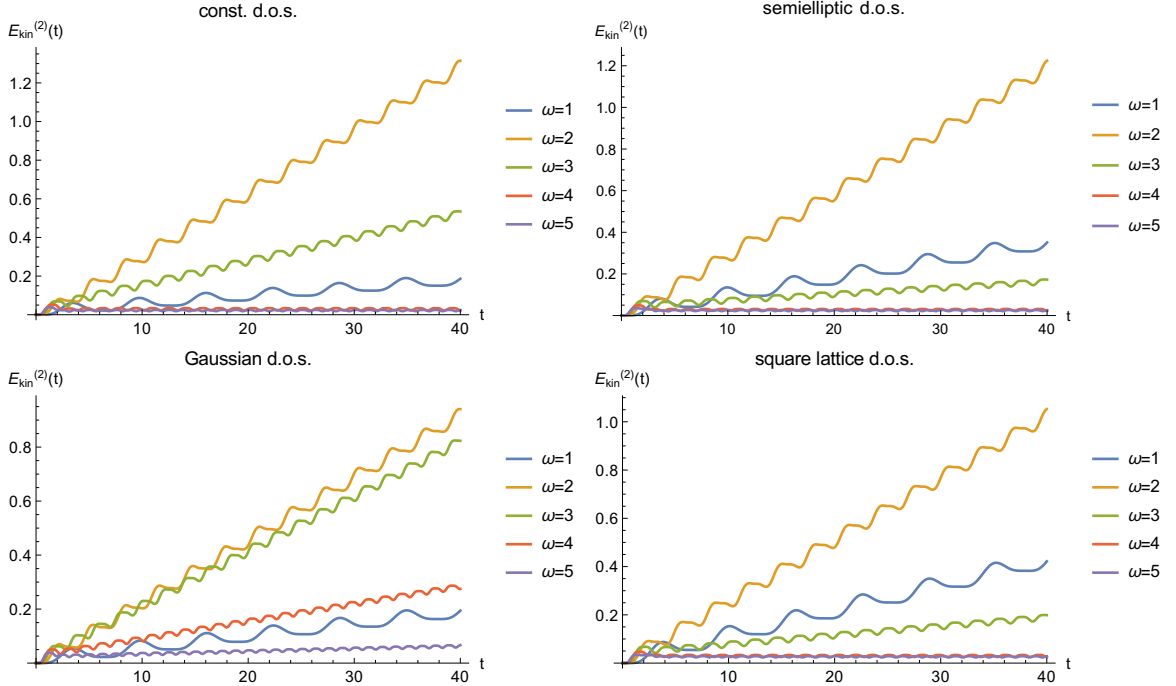


Figure 41: Energy increases due to periodic driving for various d.o.s.

$$\Delta a_{\text{ramp}}^{(2)}(t_m) = \frac{t_m \pi J_{\hat{a}}(\omega)}{8} + \int_{-\infty}^{\infty} d\epsilon J_{\hat{a}}(\epsilon) \frac{\omega^4 (1 - \cos(\epsilon t_m))}{4(\epsilon^3 - \epsilon\omega^2)^2}.$$

3 INTERACTION QUENCHES, RAMPS AND PERIODIC DRIVES

Next, we analyze the linear term as it heats the system. The growth rate of the linear-in-time term is $\frac{\pi}{8}J_{\hat{a}}(\omega)$. We choose the kinetic energy as an observable because it captures the essential energy increase. The double occupation contributes to the energy as well, but it does not have a linear term. Only if the linear term vanishes for all occupation numbers, then it vanishes for the kinetic energy as well. We observe the linear growth for $\omega < 2W = 4$ for all d.o.s. in figure 41. The Gaussian d.o.s. does not have finite bandwidth, and thus it exhibits linear growth for any driving frequency. The heating rate strongly depends on the frequency, and we depict the corresponding $J_{\hat{H}_0}(\omega)$ in figure 42. Each $J_{\hat{H}_0}(\epsilon)$ peaks at the value ω^* , which is determined by

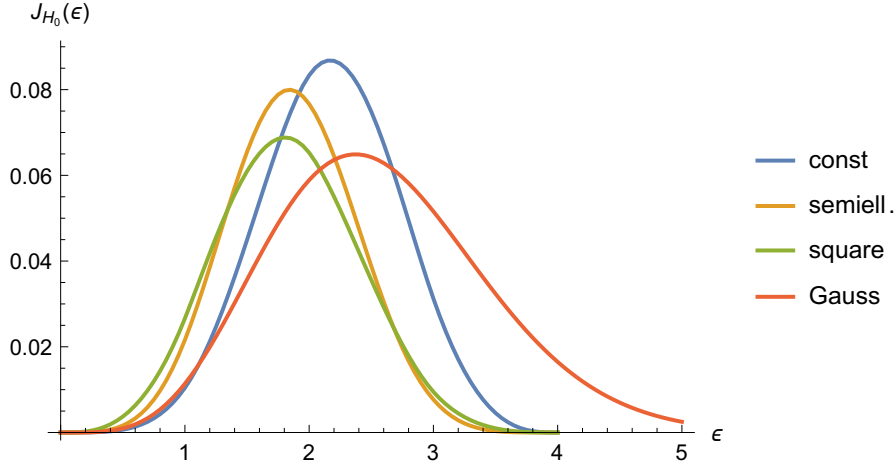


Figure 42: Term responsible for linear heating

$$\left. \frac{\partial J_{\hat{H}_0}(\omega)}{\partial \omega} \right|_{\omega^*} = 0 \quad \text{and} \quad J_{\hat{H}_0}(\omega) = |\omega| \alpha_4(|\omega|) .$$

The peak values are listed in table 6. The peak appears around $\omega^* \approx W = 2$ for all

d.o.s.	constant	semielliptic	Gaussian	square lattice
ω^*	2.16908	1.84212	2.37397	1.80793
$J_{\hat{H}_0}(\omega^*)$	0.0868304	0.0799781	0.0649045	0.0688302

Table 6: Optimal heating frequency for various d.o.s.

example d.o.s. . Hence, we conclude that driving with $\omega \approx W$ will always lead to rapid heating independent of the specific d.o.s. .

III PRETHERMALIZATION INDUCED BY WEAK INTERACTIONS

The linear term for the occupation numbers stems from $J_{\epsilon_k}(\omega) = \text{sgn}(\epsilon_k)\alpha_3(\omega - |\epsilon_k|)$ and the function $\alpha_3(\epsilon)$ is finite in the interval $(0, 3W/2)$. Therefore, we have four different regimes for the linear terms of the occupation numbers. First, all linear term vanishes for fast driving with $\omega \geq 2W$. Second, states at the band edges with $|\epsilon_k| > \omega - 3W/2$ show linear growth for $2W > \omega \geq 3W/2$. An example is depicted on the left side of figure 43. The growth rate increases closer to the band edges. Third, all occupation numbers are linear for $3 > \omega > W/2$. Fourth, states towards the Fermi surface with $|\epsilon_k| < \omega$ are linear for slow driving $W/2 \geq \omega > 0$. An example is depicted on the right side of the figure 43, where the growth rate increase for states closer to the Fermi surface as the function $\alpha_3(\epsilon)$ is monotonously increasing in the interval $(0, W/2)$.

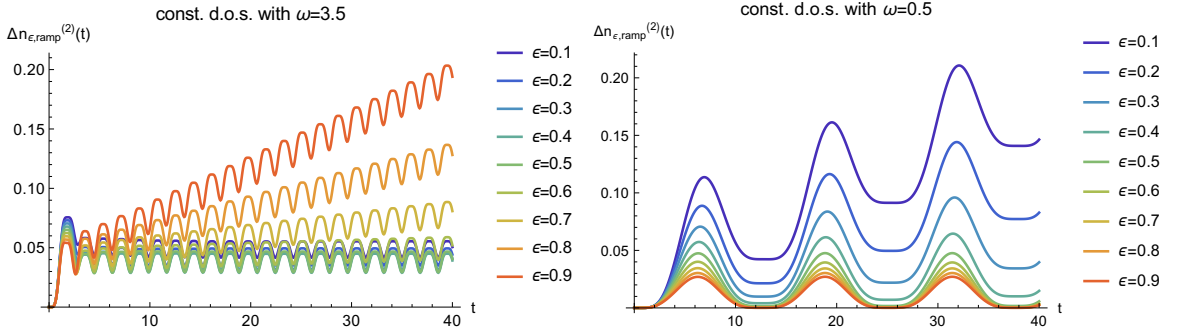


Figure 43: Ramp term of occupation numbers for periodic driving

If we start from an interacting state, then the mixing term contributes as well,

$$\begin{aligned}
 \Delta a_{\text{mix}}^{(2)}(t) &= \int_{-\infty}^{\infty} d\epsilon J_{\hat{a}}(\epsilon) \int_0^t d\tau_1 \int_0^{\tau_2} d\tau_2 \frac{1 - \cos(\omega\tau_2)}{2} e^{i(\epsilon+i\delta)(\tau_1-\tau_2)} \\
 &= \int_{-\infty+i\delta}^{\infty+i\delta} d\epsilon \frac{J_{\hat{a}}(\epsilon)}{2\epsilon^2} + \int_{-\infty+i\delta}^{\infty+i\delta} d\epsilon J_{\hat{a}}(\epsilon) \frac{it}{2\epsilon} - \int_{-\infty+i\delta}^{\infty+i\delta} d\epsilon J_{\hat{a}}(\epsilon) \frac{i\epsilon \sin(t\omega) + \omega \cos(t\omega)}{2\omega(\epsilon^2 - \omega^2)} \\
 &\quad + \int_{-\infty+i\delta}^{\infty+i\delta} d\epsilon J_{\hat{a}}(\epsilon) \frac{e^{it\epsilon\omega^2}}{2\epsilon^2(\epsilon^2 - \omega^2)} \\
 &= -\frac{\pi J_{\hat{a}}(\omega) \sin(t\omega)}{2\omega} + \int_{-\infty}^{\infty} d\epsilon J_{\hat{a}}(\epsilon) \left(\frac{1}{2\epsilon^2} - \frac{\cos(t\omega)}{2(\epsilon^2 - \omega^2)} + \frac{\cos(t\epsilon)\omega^2}{2\epsilon^2(\epsilon^2 - \omega^2)} \right).
 \end{aligned}$$

3 INTERACTION QUENCHES, RAMPS AND PERIODIC DRIVES

The linear contribution of the mixing term vanishes, and the plateau term is independent of the driving frequency. Thus, initial interactions do not affect the linear heating. However, the plateau value and the oscillations are altered by initial interactions.

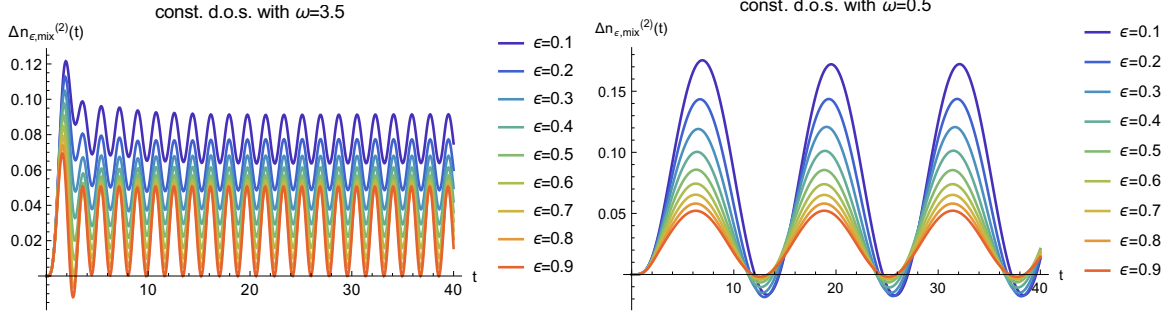


Figure 44: Mixing term of occupation numbers for periodic driving

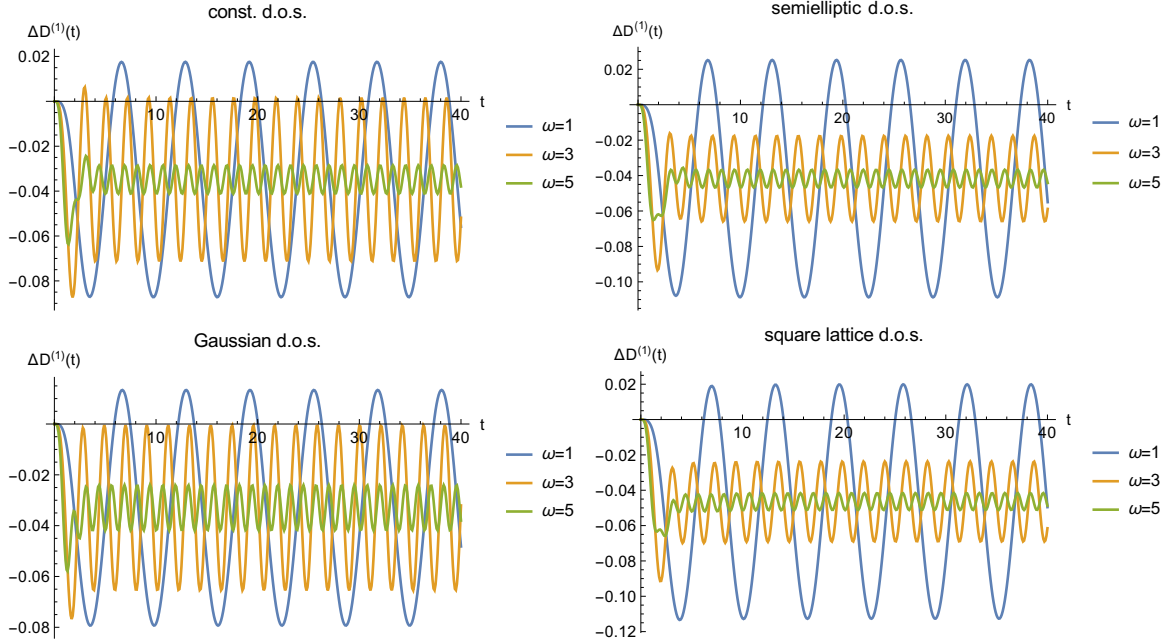


Figure 45: Double occupation change due to periodic driving for various d.o.s.

The mixing term rapidly relaxes to steady oscillations around a plateau value in figure 44. The ramp term for the occupation numbers with $\epsilon > 0$ is always positive, but the

III PRETHERMALIZATION INDUCED BY WEAK INTERACTIONS

mixing term can be negative. The occupation numbers are restricted to non-negative values and therefore the second-order corrections obey the inequality,

$$g^2 \Delta n_\epsilon^{(2)}(t) = g_0^2 \Delta n_{\epsilon,\text{ad}}^{(2)} + g_0 \Delta g \Delta n_{\epsilon,\text{mix}}^{(2)}(t) + \Delta g^2 \Delta n_{\epsilon,\text{ramp}}^{(2)}(t) > 0 \quad \text{for } \epsilon > 0 .$$

The double occupation oscillates around a constant value, as seen in figure 45. This value is independent of the driving frequency ω and corresponds to a ramp to the mean interaction strength. Thus, the mixing term and the first-order observable have similar qualitative behavior. This indicates that the mixing term is similar to a first-order observable.

In conclusion, the linear heating⁸⁹ is not affected by initial interactions or the double occupation. Furthermore, our method reveals more details of the dynamic as it is not restricted to stroboscopic times.

4 Photoinduced prethermalization

In the previous section, the dynamics were induced by a time-dependent interaction. Here, the interaction remains constant, but the hopping Hamiltonian become time-dependent. This is a new class of problem, and in particular, the weakly interacting system will be hit by a short homogeneous electric field pulse.

As the noninteracting Hamiltonian commutes with itself at different times, the occupation numbers are time-independent in the absence of interactions. Observables such as kinetic energy and current thus have trivial dynamics in this case. The prethermalization dynamics are therefore generated due to the time-independent interactions, and we compute them by applying equations (III.5) and (III.7).

Our perturbative method operates on the time scale of the inverse hopping amplitude. Consequently, we can compute the prethermalization regime if the end of the pulse lies within this time window. However, the pulse must not extend into the thermalization time scale, determined by inverse interaction strength. The derivation of the thermalization time scale is discussed in the outlook subsection 6.a). Some tools from the previous sections are not applicable here, making the evaluation more tedious. Some results will be quite technical and specific to the chosen model. Our main goal is to show that an electric field pulse will generate a prethermal state in a weakly interacting system and to characterize this state.

This section is structured as follows. First, we evaluate equations (III.5) and (III.7) with time-dependent single-particle energies. Second, we describe a homogeneous time-dependent tight-binding Hamiltonian, using the We achieve this by applying the Peierls substitution. Third, we evaluate the expectation values for the Hubbard model with infinite dimensions. We present all resulting terms explicitly for this model and compute the resulting values for two shapes of pulses. We will find that observables are linear or quadratic in electric field strength. We will also observe that the prethermal plateau is linear in pulse duration. We find that it is necessary to expand at least to second order in interaction and electric field strength to capture the prethermal state. Linear response theory always predicts a return to the initial state. Here, we compute the conductivity in linear response theory, which relates the external to the internal electric field.¹⁰⁷ Next, we evaluate the change in conductivity after a pump pulse. Our method predicts the same conductivity for the prethermal plateau as in a thermal state with the corresponding energy. Therefore, a probe pulse with a momentum resolution would be needed to observe the prethermal state. Finally, the prethermal momentum

III PRETHERMALIZATION INDUCED BY WEAK INTERACTIONS

distribution turns out to be well approximated by a universal scaling law for long pulses. We propose pumping near the Drude peak frequency to generate a pronounced and long-lived nonthermal state.

a) Hamiltonian with homogeneous electric field

Here, we introduce our effective Hamiltonian in order to evaluate equations (III.5) and (III.7) in the next subsection. As in section 3, we switch on the interactions adiabatically to generate the interacting state. Our auxiliary time-dependent Hamiltonian consists out of three contributions. The first is the noninteracting time-independent hopping Hamiltonian \hat{H}_0 . The second is the change in the hopping Hamiltonian caused by the electric field $\delta\hat{H}_0(t)$, which vanishes before and after the pulse. The last part is the adiabatically ramped interaction, which generates the initially interacting state,

$$\hat{H}(t) = \hat{H}_0 + \delta\hat{H}_0(t) + g f(t)\hat{V} \quad \text{with} \quad f(t) = \begin{cases} e^{\delta t} & \text{for } t < 0 \\ 1 & \text{for } t \geq 0 \end{cases}$$

with $\delta \rightarrow 0^+$. Our auxiliary initial state is a noninteracting eigenstate

$$|\Psi(t = -\infty)\rangle = |\Psi_0\rangle \quad \text{with} \quad \left(\hat{H}_0 + \delta\hat{H}_0(t)\right)|\Psi_0\rangle = E_0(t)|\Psi_0\rangle. \quad (\text{III.23})$$

The electric field is homogeneous. Therefore, the Hamiltonian $\hat{H}_0 + \delta\hat{H}_0(t)$ is transitional invariant during the pulse, and the initial state stays an eigenstate. It will be the Fermi sea for the explicit computation as in the previous section. Furthermore, the hopping Hamiltonian commutes with itself at different times,

$$\left[\hat{H}_0 + \delta\hat{H}_0(t), \hat{H}_0 + \delta\hat{H}_0(t')\right] = 0. \quad (\text{III.24})$$

The assumption in equation (III.24) is valid if the electric field acts uniformly. This allows us to apply equation (III.5) and the time ordering in $\hat{U}_0(t)$ can be omitted,

$$\hat{U}_0(t_1, t_2) = T_{>} \exp \left\{ -i \int_{t_2}^{t_1} d\tau \hat{H}_0 + \delta\hat{H}_0(\tau) \right\} = \sum_m |\Psi_m\rangle \langle \Psi_m| e^{-i \int_{t_2}^{t_1} d\tau E_m(\tau)}.$$

Here, $\{|\Psi_m\rangle\}$ are the eigenstates of \hat{H}_0 . The technical difference compared to section 3 is that the noninteracting eigenenergies are now time-dependent.

b) General method

Next, we insert our auxiliary Hamiltonian into equations (III.5) and (III.7). We insert the eigenbasis $\{|\Psi_m\rangle\}$ of \hat{H}_0 and separate the expectation value into a time-independent contribution and a time-dependent contribution $\varphi_m^{(j)}(t)$. The next step is to bring these $\varphi_m^{(j)}(t)$ into a usable form for the three regimes: adiabatic ramp, during and after the pulse. The procedure is similar to section 3. However, we cannot use the $J_{\hat{a}}(\epsilon)$ and $\tilde{J}_{\hat{A}}(\epsilon)$ because this requires time-independent eigenenergies E_m .

We compute the second-order observables with equation (III.5),

$$\langle \hat{a} \rangle_t = \langle \hat{a} \rangle_0 + g^2 (-1) \underbrace{\int_{-\infty}^t dt_1 \int_{-\infty}^{t_1} dt_2 \langle [\hat{H}_{1,I}(t_2), [\hat{H}_{1,I}(t_1), \hat{a}]] \rangle_0}_{=\Delta a^{(2)}(t)} + O(g^3) .$$

We insert the operator $\hat{H}_{1,I}(t) = f(t)\hat{V}_I(t)$ and rewrite the expectation value as

$$\begin{aligned} & \langle [\hat{V}_I(t_2), [\hat{V}_I(t_1), \hat{a}]] \rangle_0 \\ &= \langle \hat{V}U_0^\dagger(t_1, t_2) [\hat{V}, \hat{a}] U_0(t_1, t_2) \rangle_0 - \langle U_0^\dagger(t_1, t_2) [\hat{V}, \hat{a}] U_0(t_1, t_2) \hat{V} \rangle_0 \\ &= \langle \hat{V}U_0^\dagger(t_1, t_2) [\hat{V}, \hat{a}] U_0(t_1, t_2) \rangle_0 - \langle \hat{V}U_0^\dagger(t_1, t_2) [\hat{a}, \hat{V}] U_0(t_1, t_2) \rangle_0^* \\ &= 2\text{Re} \left\{ \langle \hat{V}U_0^\dagger(t_1, t_2) [\hat{V}, \hat{a}] U_0(t_1, t_2) \rangle_0 \right\} \\ &= - \sum_m e^{i \int_{t_2}^{t_1} d\tau \Delta E_m(\tau)} |V_{0m}|^2 \Delta a_m + \text{c.c.} . \end{aligned} \quad (\text{III.25})$$

Let us abbreviate the differences of eigenenergies $\Delta E_m(\tau) = E_m(\tau) - E_0(\tau)$ and eigenvalues $\Delta a_m = a_m - a_0$. We identify then the time-dependent contributions $\varphi_m^{(2)}(t)$ in

$$\Delta a^{(2)}(t) = \sum_m |V_{0m}|^2 \Delta a_m \underbrace{\int_{-\infty}^t dt_1 \int_{-\infty}^{t_1} dt_2 f(t_1) f(t_2) e^{i \int_{t_2}^{t_1} d\tau \Delta E_m(\tau)}}_{=\varphi_m^{(2)}(t)} + \text{c.c.} . \quad (\text{III.26})$$

III PRETHERMALIZATION INDUCED BY WEAK INTERACTIONS

We proceed as for the first-order observables and apply equation (III.7),

$$\langle \hat{A} \rangle_t = \langle \hat{A} \rangle_0 + g i \underbrace{\int_0^t dt_1 \langle [\hat{H}_{1,I}(t_1), \hat{A}_I(t)] \rangle_0}_{=\Delta A^{(1)}(t)} + O(g^2) .$$

Next, we rewrite the expectation value,

$$\begin{aligned} i \langle [\hat{V}_I(t_1), \hat{A}_I(t)] \rangle_0 &= i \langle \hat{V} U_0^\dagger(t, t_1) \hat{A} U_0(t, t_1) \rangle_0 - i \langle U_0^\dagger(t, t_1) \hat{A} U_0(t, t_1) \hat{V} \rangle_0 \\ &= i \langle \hat{V} U_0^\dagger(t, t_1) \hat{A} U_0(t, t_1) \rangle_0 - i \langle \hat{V} U_0^\dagger(t, t_1) \hat{A} U_0(t, t_1) \rangle_0^* \\ &= 2 \operatorname{Re} \left\{ i \langle \hat{V} U_0^\dagger(t, t_1) \hat{A} U_0(t, t_1) \rangle_0 \right\} \\ &= \sum_m i e^{i \int_{t_1}^t d\tau \Delta E_m(\tau)} V_{0m} A_{m0} + \text{c.c.} , \end{aligned} \quad (\text{III.27})$$

and identify the time-dependent term $\varphi_m^{(1)}(t)$ for the first-order observables,

$$\Delta A^{(1)}(t) = \sum_m V_{0m} A_{m0} \underbrace{\int_{-\infty}^t dt_1 i f(t_1) e^{i \int_{t_1}^t d\tau \Delta E_m(\tau)}}_{=\varphi_m^{(1)}(t)} + \text{c.c.} . \quad (\text{III.28})$$

We then convert the convolutions in $\varphi_m^{(1)}(t)$ and $\varphi_m^{(2)}(t)$ from equations (III.28) and (III.26) into usable forms. We distinguish three regimes: adiabatic ramp, during and after the pulse.

Adiabatic ramp

The adiabatic ramp gives the same contributions as the time-independent Rayleigh-Schrödinger perturbation theory,⁹⁴⁻⁹⁶

$$\varphi_m^{(1)}(t=0) = i \int_{-\infty}^0 dt_1 f(t_1) e^{it_1 \Delta E_m} \xrightarrow{\delta \rightarrow 0} \frac{-1}{\Delta E_m} , \quad (\text{III.29})$$

$$\varphi_m^{(2)}(t=0) = 2 \int_{-\infty}^0 dt_1 \int_{-\infty}^{t_1} dt_2 f(t_1) f(t_2) \cos((t_1 - t_2) \Delta E_m) \xrightarrow{\delta \rightarrow 0} \frac{1}{\Delta E_m^2} . \quad (\text{III.30})$$

We already encountered this in section 3.

During the pulse

The noninteracting energies become time-dependent during the electric field pulse, $t \geq 0$. We separate the time-dependent contribution $\delta E_m(t)$ from the time-independent difference, $\Delta E_m(t) = \Delta E_m + \delta E_m(t)$ with $\Delta E_m(t < 0) = \Delta E_m$. We transform the expressions of $\varphi_m^{(1)}(t)$ and $\varphi_m^{(2)}(t)$ into two parts. The first gives the contribution of the adiabatic ramp and the second captures the field excitations. For the first-order observables, we split the time integration at the end of the ramp ($t = 0$)

$$\begin{aligned} \varphi_m^{(1)}(t) &= i \int_{-\infty}^t dt_1 f(t_1) e^{i(t-t_1)\Delta E_m} \exp \left(i \int_{t_1}^t d\tau \delta E_m(\tau) \right) \\ &= i \int_{-\infty}^0 dt_1 f(t_1) e^{i(t-t_1)\Delta E_m} + i \int_0^t dt_1 e^{i(t-t_1)\Delta E_m} \exp \left(i \int_{t_1}^t d\tau \delta E_m(\tau) \right). \end{aligned}$$

The first term, we evaluate in the adiabatic limit and represent it as a time-independent value plus an integral,

$$i \int_{-\infty}^0 dt_1 f(t_1) e^{i(t-t_1)\Delta E_m} \xrightarrow{\delta \rightarrow 0} \frac{-e^{it\Delta E_m}}{\Delta E_m} = \frac{-1}{\Delta E_m} - i \int_0^t dt_1 e^{i(t-t_1)\Delta E_m}.$$

Consequently, we have separated $\varphi_m^{(1)}(t)$ into an time-independent and time-dependent contribution,

$$\varphi_m^{(1)}(t) = \frac{-1}{\Delta E_m} + i \int_0^t dt_1 e^{i(t-t_1)\Delta E_m} \left[\exp \left(i \int_{t_1}^t d\tau \delta E_m(\tau) \right) - 1 \right]. \quad (\text{III.31})$$

If there is no field, we have $\delta E_m(t) = 0$, and only the term from the adiabatic switching survives. This behavior is expected because the instantaneous state is an exact eigenstate of our Hamiltonian,^{86–88} and the observables are constant in time. The evaluation is more

III PRETHERMALIZATION INDUCED BY WEAK INTERACTIONS

advanced for the second-order observables with two time convolutions. We compute the ramp for $t_2 < t_1 < 0$ and obtain

$$\begin{aligned}\varphi_m^{(2)}(t) &= 2\Re \int_{-\infty}^t dt_1 \int_{-\infty}^{t_1} dt_2 f(t_1) f(t_2) \exp\left(i \int_{t_2}^{t_1} dt' (\Delta E_m + \delta E_m(t'))\right) \\ &= \frac{1}{\Delta E_m^2} + 2\Re \int_0^t dt_1 \exp\left(i \int_0^{t_1} dt' (\Delta E_m + \delta E_m(t'))\right) \\ &\quad \times \left\{ \int_0^{t_1} dt_2 \exp\left(-i \int_0^{t_2} dt' (\Delta E_m + \delta E_m(t'))\right) + \int_{-\infty}^0 dt_2 f(t_2) e^{-i\Delta E_m t_2} \right\}.\end{aligned}$$

Next, we apply partial integration on the term in the curly braces,

$$\begin{aligned}\int_0^{t_1} dt_2 \exp\left(-i \int_0^{t_2} dt' (\Delta E_m + \delta E_m(t'))\right) &\stackrel{\text{P.I.}}{=} \frac{i}{\Delta E_m} \left[\exp\left(-i \int_0^{t_1} dt' (\Delta E_m + \delta E_m(t'))\right) - 1 \right. \\ &\quad \left. + i \int_0^{t_1} dt_2 \delta E_m(t_2) \exp\left(-i \int_0^{t_2} dt' (\Delta E_m + \delta E_m(t'))\right) \right].\end{aligned}$$

The first term does not contribute as it is fully imaginary when multiplied by the factor in front of the braces. The second term cancels out with

$$\int_{-\infty}^0 dt_2 f(t_2) e^{-i\Delta E_m t_2} \xrightarrow{\delta \rightarrow 0} \frac{i}{\Delta E_m}.$$

Therefore, solely the third term remains in the final form,

$$\varphi_m^{(2)}(t) = \frac{1}{\Delta E_m^2} - 2\Re \int_0^t dt_1 \int_0^{t_1} dt_2 \exp\left(i \int_{t_2}^{t_1} dt' (\Delta E_m + \delta E_m(t'))\right) \frac{\delta E_m(t_2)}{\Delta E_m}. \quad (\text{III.32})$$

Equation (III.32) satisfies the check with $\delta E_m(t) = 0$ as well. We note that equations (III.31) and (III.32) can be converted into other forms, but the presented forms are best suited to our scenario.

After the pulse

The pulse stops at time t_{fin} and $\delta E_m(t > t_{\text{fin}}) = 0$. The integrand vanishes after the pulse in equation (III.31), and we restrict the integration to the pulse duration,

$$\varphi_m^{(1)}(t) = \frac{-1}{\Delta E_m} + ie^{it\Delta E_m} \int_0^{t_{\text{fin}}} dt_1 e^{-it_1\Delta E_m} \left[\exp \left(i \int_{t_1}^{t_{\text{fin}}} d\tau \delta E_m(\tau) \right) - 1 \right]. \quad (\text{III.33})$$

If we assume that the ΔE_m are continuously spread, then the second term vanishes for large times t . Integrating a smooth function in ΔE_m times $e^{it\Delta E_m}$ generally results in a t^{-1} decay, which is explained in equation (II.18). Thus, the interaction energy and other first-order observables relax to their values prior to the pulse.

Next, we compute the contribution of the second-order observables after the pulse,

$$\begin{aligned} \varphi_m^{(2)}(t) - \varphi_m^{(2)}(t_{\text{fin}}) &= \\ &= -2\Re \int_{t_{\text{fin}}}^t dt_1 \int_0^{t_1} dt_2 \exp \left(i \int_{t_2}^{t_1} dt' (\Delta E_m + \delta E_m(t')) \right) \frac{\delta E_m(t_2)}{\Delta E_m} \\ &= -2\Re \int_{t_{\text{fin}}}^t dt_1 e^{i(t_1 - t_{\text{fin}})\Delta E_m} \int_0^{t_{\text{fin}}} dt_2 \exp \left(i \int_{t_2}^{t_{\text{fin}}} dt' (\Delta E_m + \delta E_m(t')) \right) \frac{\delta E_m(t_2)}{\Delta E_m} \\ &= 2\Re \frac{1 - e^{i(t - t_{\text{fin}})\Delta E_m}}{i\Delta E_m} \int_0^{t_{\text{fin}}} dt_2 \exp \left(i \int_{t_2}^{t_{\text{fin}}} dt' (\Delta E_m + \delta E_m(t')) \right) \frac{\delta E_m(t_2)}{\Delta E_m}. \end{aligned} \quad (\text{III.34})$$

The second term of this expression goes to zero for large times due to $e^{it\Delta E_m}$. Thus, the prethermalization plateau is computed as the first term plus the value at the end of the pulse.

In this subsection, we reformulated all terms of interest. They are time-independent if no electric field is applied. We performed all limits, i.e. $\delta \rightarrow 0^+$ and $t_1, t_2 \rightarrow -\infty$. In the next subsection, we construct the explicit time-dependent eigenenergies in our model.

c) Electric field pulse on the hypercubic lattice

Here, we briefly review the formalism used by V. Turkowski and J. K. Freericks¹⁰⁸ to capture an external electric field by a free Hamiltonian in infinite dimensions. An

III PRETHERMALIZATION INDUCED BY WEAK INTERACTIONS

electromagnetic field is described by a scalar potential $\Phi(\mathbf{r}, t)$ and a vector potential $\mathbf{A}(\mathbf{r}, t)$,

$$\mathbf{E}(\mathbf{r}, t) = -\nabla\Phi(\mathbf{r}, t) - \frac{1}{c} \frac{\partial \mathbf{A}(\mathbf{r}, t)}{\partial t} .$$

Next, the Landau gauge is applied where $\Phi(\mathbf{r}, t) = 0$ and the electric field is fully captured by the vector potential. We note that the electric field $\mathbf{E}(\mathbf{r}, t)$ inside the solid is not equal to the external excitation field.¹⁰⁷ The Peierls substitution¹⁰⁹ is used to describe the internal electric field by modifying the hopping amplitudes,

$$t_{ij} \rightarrow t_{ij} \exp\left(-i \frac{e}{\hbar c} \int_{\mathbf{R}_i}^{\mathbf{R}_j} d\mathbf{r} \cdot \mathbf{A}(\mathbf{r}, t)\right) .$$

The electric field is time-dependent but shall have no spatial dependence. This setup is called dipole approximation, and it is adequate if the applied field varies slowly on the atomic scale, which is the case for optical frequencies.¹⁴ The electromagnetic field does not satisfy Maxwell's equations, which is a drawback of the dipole approximation. The Peierls substitution requires a slowly varying magnetic field,¹¹⁰ which is true for the dipole approximation as the magnetic field vanishes.

We will consider the limit of infinite dimensions, for which the hopping needs to be scaled as $t \rightarrow t^*/\sqrt{2d}$.⁵⁷ Adding the vector potential to the nearest-neighbor hopping Hamiltonian in d dimension on the hypercubic lattice gives

$$\hat{H}_0 + \delta\hat{H}_0(t) = \sum_{\sigma, \mathbf{k}} \epsilon(\mathbf{k} - \frac{ea}{\hbar c} \mathbf{A}(t)) \hat{n}_{\sigma \mathbf{k}} \quad \text{with} \quad \epsilon(\mathbf{k}) = -\frac{t^*}{\sqrt{d}} \sum_{j=1}^d \cos(k_j) . \quad (\text{III.35})$$

The current is the main observable and is computed as¹⁴

$$\hat{j}_\alpha = -c \frac{\partial \left(\hat{H}_0 + \delta\hat{H}_0(t) \right)}{\partial A_\alpha(t)} = \frac{eat^*}{\hbar\sqrt{d}} \sum_{\sigma, \mathbf{k}} \sin(k_\alpha - \frac{ea}{\hbar c} A_\alpha(t)) \hat{n}_{\sigma \mathbf{k}} .$$

We use the trick from reference¹⁰⁸ to simplify the situation and set the field direction in $\mathbf{e}_A = (1, 1, \dots, 1)$ and $c \equiv 1, \frac{e a}{\hbar} \equiv 1$. Consequently, the time-dependent dispersion simplifies to

$$\begin{aligned} \epsilon_{\mathbf{k}} + \delta\epsilon_{\mathbf{k}}(t) &\equiv \epsilon(\mathbf{k} - \mathbf{A}(t)) = -\frac{t^*}{\sqrt{d}} \sum_{j=1}^d \cos(k_j - A(t)) \\ &= \cos(A(t))\epsilon_{\mathbf{k}} + \sin(A(t))\bar{\epsilon}_{\mathbf{k}} \quad \text{with} \quad \bar{\epsilon}_{\mathbf{k}} = -\frac{t^*}{\sqrt{d}} \sum_{j=1}^d \sin(k_j) . \end{aligned}$$

$\bar{\epsilon}_{\mathbf{k}}$ quantifies how antiparallel \mathbf{k} is to \mathbf{e}_A , $-\mathbf{k} \cdot \mathbf{e}_A \sim \bar{\epsilon}_{\mathbf{k}}$. The time-dependent Hamiltonian has the compact form

$$\hat{H}_0 + \delta\hat{H}_0(t) = \hat{H}_0 \cos(A(t)) + \hat{H}_0 \sin(A(t)) \quad \text{with} \quad \hat{H}_0 = \sum_{\sigma, \mathbf{k}} \bar{\epsilon}_{\mathbf{k}} \hat{n}_{\sigma \mathbf{k}} . \quad (\text{III.36})$$

The noninteracting Hamiltonian $\hat{H}_0 + \delta\hat{H}_0(t)$ consists of two time-independent operators \hat{H}_0 and \hat{H}_0 with time-dependent factors. The two main observables, current and kinetic energy, are computed as

$$\begin{aligned} j &\equiv \langle \hat{\mathbf{j}} \cdot \mathbf{e}_A \rangle_t = \cos(A(t)) \langle \hat{H}_0 \rangle_t + \sin(A(t)) \langle \hat{H}_0 \rangle_t , \\ E_{\text{kin}} &\equiv \langle \hat{H}_0 + \delta\hat{H}_0(t) \rangle_t = \cos(A(t)) \langle \hat{H}_0 \rangle_t + \sin(A(t)) \langle \hat{H}_0 \rangle_t . \end{aligned}$$

For our discussion, we compute the expectation values of \hat{H}_0 and \hat{H}_0 as well. This Hamiltonian concerning contains the essential aspects of a real electric field pulse., but nevertheless allows us to construct a computational scheme, as discussed in the next subsection.

d) Hubbard model with infinite spatial dimensions

In the previous subsection, we discussed the details of the hopping Hamiltonian including the electric field. Here, we explain the computational procedure for the expectation values of the Hubbard model with infinite spatial dimensions. First, we recall the results from subsection 3.b) and extend them to the field-pulse in the diagonal direction. Second, we present all expressions in a list of explicit expressions. Last, we explain a computation technique, which enables us to extract numerical values from the expressions.

We use the time-dependent Hamiltonian from equation (III.36) in a Hubbard model with

III PRETHERMALIZATION INDUCED BY WEAK INTERACTIONS

time-independent interaction U . The expectation values for the occupation numbers were derived in subsection 3.b). We replace

$$\begin{aligned} t\hat{H}_0 &\longrightarrow \int d\tau \hat{H}_0 + \delta\hat{H}_0(\tau) = \tau_1\hat{H}_0 + \tau_2\hat{\bar{H}}_0, \\ \tau_1 &= \int d\tau \cos(A(\tau)), \quad \tau_2 = \int d\tau \sin(A(\tau)), \\ \hat{D}_I(\tau_1, \tau_2) &= e^{i(\tau_1\hat{H}_0 + \tau_2\hat{\bar{H}}_0)} \hat{D} e^{-i(\tau_1\hat{H}_0 + \tau_2\hat{\bar{H}}_0)}. \end{aligned}$$

This leads to the replacement $F_\sigma^\pm(\mathbf{R}, t) \rightarrow F_\sigma^\pm(\mathbf{R}, \tau_1, \tau_2)$ for the Hubbard model,

$$\begin{aligned} f_{\sigma\mathbf{k}}^+(\mathbf{R}_i, \tau_1, \tau_2) &= e^{-i(\mathbf{R}_i \cdot \mathbf{k} + \tau_1 \epsilon_{\mathbf{k}} + \tau_2 \bar{\epsilon}_{\mathbf{k}})} \langle \hat{n}_{\sigma\mathbf{k}} \rangle_0, \\ f_{\sigma\mathbf{k}}^-(\mathbf{R}_i, \tau_1, \tau_2) &= e^{i(\mathbf{R}_i \cdot \mathbf{k} + \tau_1 \epsilon_{\mathbf{k}} + \tau_2 \bar{\epsilon}_{\mathbf{k}})} (1 - \langle \hat{n}_{\sigma\mathbf{k}} \rangle_0), \\ F_\sigma^\pm(\mathbf{R}_i, \tau_1, \tau_2) &= \frac{1}{L} \sum_{\mathbf{k}} f_{\sigma\mathbf{k}}^\pm(\mathbf{R}_i, \tau_1, \tau_2). \end{aligned}$$

The expectation values are identical to subsection 3.b),

$$\begin{aligned} \langle [\hat{D}, [\hat{D}_I(\tau_1, \tau_2), \hat{n}_{\sigma\mathbf{k}}]] \rangle_0 &= 2\Re \sum_{i,s=\pm} s f_{\sigma\mathbf{k}}^s(\mathbf{R}_i, \tau_1, \tau_2) F_\sigma^{-s}(\mathbf{R}_i, \tau_1, \tau_2) \prod_{\lambda=\pm} F_\sigma^\lambda(\mathbf{R}_i, \tau_1, \tau_2), \\ i \langle [\hat{D}, \hat{D}_I(\tau_1, \tau_2)] \rangle_0 &= 2\Re i \sum_i \prod_{\lambda=\pm} F_\sigma^\lambda(\mathbf{R}_i, \tau_1, \tau_2) F_\sigma^\lambda(\mathbf{R}_i, \tau_1, \tau_2), \\ \langle [\hat{D}, [\hat{D}_I(\tau_1, \tau_2), \hat{H}_0]] \rangle_0 &= \frac{\partial}{\partial \tau_1} i \langle [\hat{D}, \hat{D}_I(\tau_1, \tau_2)] \rangle_0, \\ \langle [\hat{D}, [\hat{D}_I(\tau_1, \tau_2), \hat{\bar{H}}_0]] \rangle_0 &= \frac{\partial}{\partial \tau_2} i \langle [\hat{D}, \hat{D}_I(\tau_1, \tau_2)] \rangle_0. \end{aligned}$$

$\mathbf{R}_i = \mathbf{0}$ is the only finite contribution in infinite dimensions,⁵⁷ and the problem simplifies to

$$\begin{aligned} F_\sigma^\pm(\tau_1, \tau_2, \mathbf{R}) &\xrightarrow{d \rightarrow \infty} \delta_{\mathbf{R}, \mathbf{0}} F_\sigma^\pm(\tau_1, \tau_2), \\ F_\sigma^\pm(\tau_1, \tau_2) &= \int d\epsilon \int d\bar{\epsilon} \rho(\epsilon, \bar{\epsilon}) e^{\mp i(\tau_1 \epsilon + \tau_2 \bar{\epsilon})} \begin{cases} \langle \hat{n}_{\sigma\epsilon\bar{\epsilon}} \rangle_0 & \text{for } + \\ (1 - \langle \hat{n}_{\sigma\epsilon\bar{\epsilon}} \rangle_0) & \text{for } - \end{cases}, \\ \rho(\epsilon, \bar{\epsilon}) &= \sum_{\mathbf{k}} \delta(\epsilon - \epsilon_{\mathbf{k}}) \delta(\bar{\epsilon} - \bar{\epsilon}_{\mathbf{k}}). \end{aligned}$$

V. Turkowski and J. K. Freericks¹⁰⁸ computed $\rho(\epsilon, \bar{\epsilon})$ for the tight-binding Hamiltonian. They used the method developed by Müller-Hartmann,^{111–113} which utilizes the Fourier transform,

$$\begin{aligned}
 \int_{-\infty}^{\infty} d\epsilon \int_{-\infty}^{\infty} d\bar{\epsilon} \rho(\epsilon, \bar{\epsilon}) e^{it_1\epsilon + it_2\bar{\epsilon}} &= \int_{-\pi}^{\pi} \frac{dk_1}{2\pi} \dots \int_{-\pi}^{\pi} \frac{dk_d}{2\pi} e^{it_1\epsilon_{\mathbf{k}} + it_2\bar{\epsilon}_{\mathbf{k}}} \\
 &= \left(\int_{-\pi}^{\pi} \frac{dk}{2\pi} e^{\frac{it^*}{\sqrt{d}}(-t_1 \cos(k) + t_2 \sin(k))} \right)^d \\
 &= \left(1 - \frac{t_1^2 + t_2^2}{4d} + O(d^{-\frac{3}{2}}) \right)^d \xrightarrow{d \rightarrow \infty} e^{-\frac{t_1^2 + t_2^2}{4}}, \\
 \Rightarrow \rho(\epsilon, \bar{\epsilon}) &= \int_{-\infty}^{\infty} \frac{dt_1}{2\pi} \int_{-\infty}^{\infty} \frac{dt_2}{2\pi} e^{-it_1\epsilon - it_2\bar{\epsilon}} e^{-\frac{t_1^2 + t_2^2}{4}} = \frac{e^{-\epsilon^2 - \bar{\epsilon}^2}}{\pi}.
 \end{aligned}$$

We choose the paramagnetic Fermi sea $\langle \hat{n}_{\sigma\mathbf{k}} \rangle_0 = \langle \hat{n}_{\bar{\sigma}\mathbf{k}} \rangle_0 = \Theta(\epsilon_F - \epsilon_{\mathbf{k}})$ at half-filling, $\epsilon_F = 0$, as auxiliary the initial state. Then, the functions $F_{\sigma}^{\pm}(\tau_1, \tau_2)$ become identical,

$$\begin{aligned}
 F(\tau_1, \tau_2) &= F_{\sigma}^{+}(\tau_1, \tau_2) = F_{\bar{\sigma}}^{+}(\tau_1, \tau_2) = F_{\sigma}^{-}(\tau_1, \tau_2) = F_{\bar{\sigma}}^{-}(\tau_1, \tau_2) \\
 &= \int_0^{\infty} d\epsilon \frac{e^{-\epsilon^2 + i\epsilon\tau_1}}{\sqrt{\pi}} \int_{-\infty}^{\infty} d\bar{\epsilon} \frac{e^{-\bar{\epsilon}^2 + i\bar{\epsilon}\tau_2}}{\sqrt{\pi}}.
 \end{aligned}$$

List of explicit expressions

We now obtain the final expressions that need to be evaluated. We have to sum according to (III.26) and (III.28) with $\langle \Psi_n | \hat{D} | \Psi_m \rangle = D_{nm}$,

$$D^{(1)}(t) = \sum_m |D_{0m}|^2 \varphi_m^{(1)}(t) + \text{c.c.}, \quad n_{\sigma\mathbf{k}}^{(2)}(t) = \sum_m |D_{0m}|^2 \Delta n_{\sigma\mathbf{k},m} \varphi_m^{(2)}(t).$$

We insert $\varphi_m^{(1)}(t)$ as written in equations (III.29), (III.31) and (III.33). For $\varphi_m^{(2)}(t)$, we use the expressions from (III.30), (III.32) and (III.34). The effect of the electric field is captured by

$$\delta E_m(t_2) = \Delta E_m (\cos(A(t_2)) - 1) + \Delta \bar{E}_m \sin(A(t_2)).$$

Next, we replace the factors ΔE_m and $\Delta \bar{E}_m$ with differentiations,

$$(\Delta E_m)^{n_1} (\Delta \bar{E}_m)^{n_2} e^{i\tau_1 \Delta E_m + i\tau_2 \Delta \bar{E}_m} = \left(\frac{\partial}{\partial i\tau_1} \right)^{n_1} \left(\frac{\partial}{\partial i\tau_2} \right)^{n_2} e^{i\tau_1 \Delta E_m + i\tau_2 \Delta \bar{E}_m}.$$

III PRETHERMALIZATION INDUCED BY WEAK INTERACTIONS

We have thus reformulated $\varphi_m^{(1)}(t)$ and $\varphi_m^{(2)}(t)$ in terms of $e^{i\tau_1\Delta E_m+i\tau_2\Delta\bar{E}_m}$ and operations on it, which are independent of m . Thus, we execute the sum over m and insert the expectation values for the double occupation in infinite dimension,

$$\sum_m i e^{i\tau_1\Delta E_m+i\tau_2\Delta\bar{E}_m} |D_{0m}|^2 + \text{c.c.} = i \langle [\hat{D}, \hat{D}_I(\tau_1, \tau_2)] \rangle_0 \xrightarrow{d \rightarrow \infty} 2\Re i F(\tau_1, \tau_2)^4 ,$$

and the occupation numbers ($\epsilon_k > 0$),

$$\begin{aligned} - \sum_m e^{i\tau_1\Delta E_m+i\tau_2\Delta\bar{E}_m} |D_{0m}|^2 \Delta n_{\sigma\mathbf{k},m} + \text{c.c.} &= \langle [\hat{D}, [\hat{D}_I(\tau_1, \tau_2), \hat{n}_{\sigma\mathbf{k}}]] \rangle_0 \\ &\xrightarrow{d \rightarrow \infty} -2\Re e^{i\epsilon_k\tau_1+i\bar{\epsilon}_k\tau_2} F(\tau_1, \tau_2)^3 . \end{aligned}$$

We use the abbreviations

$$\begin{aligned} \partial E(t_2) &= (\cos(A(t_2)) - 1) \frac{\partial}{\partial i\tau_1} + \sin(A(t_2)) \frac{\partial}{\partial i\tau_2} , \\ \tau_1(t_1, t_2) &= \int_{t_2}^{t_1} d\tau \cos(A(\tau)) , \quad \tau_2(t_1, t_2) = \int_{t_2}^{t_1} d\tau \sin(A(\tau)) , \end{aligned} \quad (\text{III.37})$$

and the results for the double occupation are

$$D^{(1)}(0) = -2\Re \left(\frac{\partial}{\partial i\tau_1} \right)^{-1} F(\tau_1, 0)^4 \Big|_{\tau_1=0} , \quad \Delta D^{(1)}(t) = D^{(1)}(t) - D^{(1)}(0) , \quad (\text{III.38})$$

$$\Delta D^{(1)}(t) \stackrel{t \geq 0}{=} 2\Re i \int_0^t dt_1 F(\tau_1(t, t_1), \tau_2(t, t_1))^4 - F(t - t_1, 0)^4 , \quad (\text{III.39})$$

$$\Delta D^{(1)}(t) \stackrel{t > t_{\text{fin}}}{=} 2\Re i \int_0^{t_{\text{fin}}} dt_1 F(t - t_{\text{fin}} + \tau_1(t_{\text{fin}}, t_1), \tau_2(t_{\text{fin}}, t_1))^4 - F(t - t_1, 0)^4 . \quad (\text{III.40})$$

We drop the spin index as our system is paramagnetic. The vector \mathbf{k} occurs only in the two energies $\epsilon_{\mathbf{k}}$ and $\bar{\epsilon}_{\mathbf{k}}$. Therefore, we rename $\langle \hat{n}_{\sigma\mathbf{k}} \rangle_t \rightarrow \langle \hat{n}_{\epsilon_{\mathbf{k}}\bar{\epsilon}_{\mathbf{k}}} \rangle_t$ and the resulting terms above the Fermi surface ($\epsilon > 0$) are

$$n_{\epsilon\bar{\epsilon}}^{(2)}(0) = \Re \left(\frac{\partial}{\partial i\tau_1} \right)^{-2} e^{i\tau_1\epsilon} F(\tau_1, 0)^3 \Big|_{\tau_1=0}, \quad \Delta n_{\epsilon\bar{\epsilon}}^{(2)}(t) = n_{\epsilon\bar{\epsilon}}^{(2)}(t) - n_{\epsilon\bar{\epsilon}}^{(2)}(0), \quad (\text{III.41})$$

$$\Delta n_{\epsilon\bar{\epsilon}}^{(2)}(t) \stackrel{t>0}{=} - \int_0^t dt_1 \int_0^{t_1} dt_2 2\Re \left(\frac{\partial}{\partial i\tau_1} \right)^{-1} \partial E(t_2) e^{i\tau_1\epsilon + i\tau_2\bar{\epsilon}} F(\tau_1, \tau_2)^3 \Big|_{\substack{\tau_1 = \tau_1(t_1, t_2) \\ \tau_2 = \tau_2(t_1, t_2)}}, \quad (\text{III.42})$$

$$\begin{aligned} \Delta n_{\epsilon\bar{\epsilon}}^{(2)}(t) \stackrel{t>t_{\text{fin}}}{=} \Delta n_{\epsilon\bar{\epsilon}}^{(2)}(t_{\text{fin}}) - \int_0^{t_{\text{fin}}} dt_2 2\Re \left(\frac{\partial}{\partial i\tau_1} \right)^{-2} i\partial E(t_2) e^{i\tau_1\epsilon + i\tau_2\bar{\epsilon}} F(\tau_1, \tau_2)^3 \Big|_{\substack{\tau_1 = \tau_1(t_{\text{fin}}, t_2) \\ \tau_2 = \tau_2(t_{\text{fin}}, t_2)}} \\ + \int_0^{t_{\text{fin}}} dt_2 2\Re \left(\frac{\partial}{\partial i\tau_1} \right)^{-2} i\partial E(t_2) e^{i\tau_1\epsilon + i\tau_2\bar{\epsilon}} F(\tau_1, \tau_2)^3 \Big|_{\substack{\tau_1 = t - t_{\text{fin}} + \tau_1(t_{\text{fin}}, t_2) \\ \tau_2 = \tau_2(t_{\text{fin}}, t_2)}}. \end{aligned} \quad (\text{III.43})$$

Below the Fermi surface ($\epsilon_{\mathbf{k}} < 0$), the sign of the corrections changes and $\epsilon_{\mathbf{k}}$ is replaced by its absolute value, $n_{\epsilon\bar{\epsilon}}^{(2)}(t) = -n_{-\epsilon\bar{\epsilon}}^{(2)}(t)$, due to particle-hole symmetry at half-filling. The terms for \hat{H}_0 and $\hat{\bar{H}}_0$ are computed analogously and we replace

$$\begin{aligned} e^{i\tau_1\epsilon + i\tau_2\bar{\epsilon}} F(\tau_1, \tau_2)^3 &\longrightarrow \frac{\partial}{\partial i\tau_1} F(\tau_1, \tau_2)^4 \quad \text{for } \hat{H}_0, \\ e^{i\tau_1\epsilon + i\tau_2\bar{\epsilon}} F(\tau_1, \tau_2)^3 &\longrightarrow \frac{\partial}{\partial i\tau_2} F(\tau_1, \tau_2)^4 \quad \text{for } \hat{\bar{H}}_0 \end{aligned}$$

in equations (III.41), (III.42) and (III.43). The next step is to replace

$$\left(\frac{\partial}{\partial i\tau_1} \right)^{n_1} \left(\frac{\partial}{\partial i\tau_2} \right)^{n_2} e^{i\tau_1\epsilon + i\tau_2\bar{\epsilon}} F(\tau_1, \tau_2)^3 \quad \text{and} \quad \left(\frac{\partial}{\partial i\tau_1} \right)^{n_1} \left(\frac{\partial}{\partial i\tau_2} \right)^{n_2} F(\tau_1, \tau_2)^4 \quad (\text{III.44})$$

with numerically feasible terms. In our explicit terms, n_1 and n_2 take the integer values $n_1 \in \{-2, -1, 0, 1\}$ and $n_2 \in \{0, 1, 2\}$. If n_i takes positive values, then we only need to differentiate, but we have to integrate with the appropriate boundary conditions for negative values. We will avoid the integration with a special computation technique, which we explain in the following.

Computation technique for integrations

In equation (III.44), we have to integrate if $n_1 \leq -1$. Here, we provide a method to avoid this integration. We apply the transformation

$$\begin{aligned}
 F(\tau_1, \tau_2)^m &= \left(\int_{-\infty}^{\infty} d\bar{\epsilon} \frac{e^{-\bar{\epsilon}^2 + i\bar{\epsilon}\tau_2}}{\sqrt{\pi}} \right)^m \left(\int_0^{\infty} d\epsilon_1 \dots \int_0^{\infty} d\epsilon_m \frac{e^{-\sum_{l=1}^m \epsilon_l^2 + i\epsilon_l \tau_1}}{\sqrt{\pi^m}} \right) \\
 &= e^{-\frac{m\tau_2^2}{4}} \int_0^{\infty} d\epsilon_0 \frac{e^{i\tau_1 \epsilon_0}}{\sqrt{\pi^m}} \int_0^{\infty} d\epsilon_1 \dots \int_0^{\infty} d\epsilon_m \delta(\epsilon_0 - \sum_{l=1}^m \epsilon_l) e^{-\sum_{l=1}^m \epsilon_l^2} \\
 &= e^{-\frac{m\tau_2^2}{4}} \int_0^{\infty} d\epsilon_0 \frac{e^{i\tau_1 \epsilon_0}}{\sqrt{\pi^m}} \epsilon_0^{m-1} \int_0^{\infty} dx_1 \dots \int_0^{\infty} dx_m \delta(1 - \sum_{l=1}^m x_l) e^{-\epsilon_0^2 \sum_{l=1}^m x_l^2}.
 \end{aligned}$$

Now, we integrate $m - 1$ times and obtain

$$\begin{aligned}
 \left(\frac{\partial}{\partial i\tau_1} \right)^{1-m} F(\tau_1, \tau_2)^m &= e^{-\frac{m\tau_2^2}{4}} \int_0^{\infty} db \int_0^{\infty} d\epsilon_0 \frac{e^{i\tau_1 \epsilon_0 - b\epsilon_0^2}}{\sqrt{\pi^m}} a_m(b) \\
 &= e^{-\frac{m\tau_2^2}{4}} \int_{\frac{1}{m}}^1 db \frac{a_m(b)}{\sqrt{b\pi^m}} \left(\frac{\sqrt{\pi}}{2} e^{-\frac{\tau_1^2}{4b}} + i D_+ \left(\frac{\tau_1}{2\sqrt{b}} \right) \right), \quad (\text{III.45}) \\
 a_n(b) &= \int_0^{\infty} dx_1 \dots \int_0^{\infty} dx_n \delta(1 - \sum_{i=1}^n x_i) \delta(b - \sum_{j=1}^n x_j^2).
 \end{aligned}$$

We encountered the functions $a_n(b)$ in subsection 3.b) and the computation of $a_3(b)$ and $a_4(b)$ is done in appendix 1. We are avoiding the integrations because $m - 1 + n_1 \geq 0$ with $m \in \{3, 4\}$. One drawback is that the integration over b has to be done numerically. The procedure for the occupation numbers away from the Fermi surface works analogously. There, we also have to integrate over ϵ_0 numerically. The term of interest for $\epsilon > 0$ is

$$\begin{aligned}
 e^{i\tau_1 \epsilon} F(\tau_1, \tau_2)^3 &= e^{-\frac{3\tau_2^2}{4}} \int_{\epsilon}^{\infty} d\epsilon_0 \frac{e^{i\tau_1 \epsilon}}{\sqrt{\pi^3}} \int_0^{\infty} d\epsilon_1 \int_0^{\infty} d\epsilon_2 \int_0^{\infty} d\epsilon_3 \delta(\epsilon_0 - \epsilon - \epsilon_1 - \epsilon_2 - \epsilon_3) e^{-\epsilon_1^2 - \epsilon_2^2 - \epsilon_3^2} \\
 &= e^{-\frac{3\tau_2^2}{4}} \int_{\epsilon}^{\infty} d\epsilon_0 \epsilon_0^2 \int_0^{\infty} db \frac{e^{i\tau_1 \epsilon - b\epsilon_0^2}}{\sqrt{\pi^3}} a_3 \left(\frac{b}{(1 - \frac{\epsilon}{\epsilon_0})^2} \right).
 \end{aligned}$$

The function $a_3(b)$ is nonzero only between $\frac{1}{3}$ and 1, hence we restrict our integration region. We integrate twice and scale b to obtain

$$\left(\frac{\partial}{\partial i\tau_1}\right)^{-2} e^{i\tau_1\epsilon} F(\tau_1, \tau_2)^3 = e^{-\frac{3\tau_2^2}{4}} \int_{\frac{1}{3}}^1 db a_3(b) \int_{\epsilon}^{\infty} d\epsilon_0 \left(1 - \frac{\epsilon}{\epsilon_0}\right)^2 \frac{e^{i\tau_1\epsilon_0 - b\epsilon_0^2}}{\sqrt{\pi^3}}. \quad (\text{III.46})$$

We recover the previous result in the limit $\epsilon \rightarrow 0$. Now, we have covered all aspects of the numerical procedure. We insert the numerical feasible terms from equations (III.45) and (III.46) into equations (III.38) to (III.43). We compute the derivatives with respect to τ_1 and τ_2 analytically. We need to find suitable exact or approximate forms for $\tau_1(t_1, t_2)$ and $\tau_2(t_1, t_2)$ depending on $A(t)$. Then, we numerically integrate over b , t_1 and t_2 . For the occupation numbers away from the Fermi energy, we integrate numerically over ϵ_0 as well.

e) Numerical results

We now present our numerical results for nonperturbative electric fields. First, we introduce the pulse protocols and discuss the trivial dynamics of the noninteracting terms of kinetic energy and current,

$$\begin{aligned} E_{\text{kin}}(t) &= E_{\text{kin}}^{(0)}(t) + U^2 E_{\text{kin}}^{(2)}(t) + O(U^3), & E_{\text{kin}}^{(0)}(t) &= \langle \hat{H}_0 \rangle_0 \cos(A(t)), \\ j(t) &= j^{(0)}(t) + U^2 j^{(2)}(t) + O(U^3), & j^{(0)}(t) &= \langle \hat{H}_0 \rangle_0 \sin(A(t)). \end{aligned}$$

The operators of double occupation and occupation numbers are time-independent in the Schrödinger picture, and their expectation values are therefore static on the noninteracting level. Therefore, our main interest is the correction terms in interaction strength.

Two classes of pulses and their noninteracting contribution

We have two different classes of internal electric field pulses. The first class is “simple” oscillations with constant amplitude, which have the index one,

$$\begin{aligned} E_1(t) &= E \sin\left(\frac{2\pi t}{T}\right) \Theta(mT - t)\Theta(t), \\ A_1(t) &= -\frac{ET}{\pi} \sin\left(\frac{\pi t}{T}\right)^2 \Theta(mT - t)\Theta(t). \end{aligned} \quad (\text{III.47})$$

III PRETHERMALIZATION INDUCED BY WEAK INTERACTIONS

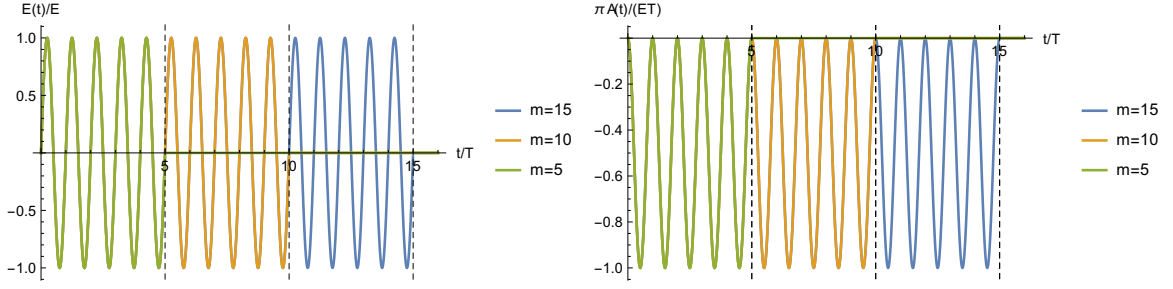


Figure 46: Normalized “simple” electric field (left) and vector potential (right)

For longer pulses, only additional oscillations are appended, and the shape is not affected. The second shape is more “realistic” and has an enveloping function,

$$E_2(t) = E \sin\left(\frac{2\pi t}{T}\right) \sin\left(\frac{\pi t}{mT}\right) \Theta(mT - t)\Theta(t) ,$$

$$A_2(t) = \frac{EmT}{2\pi} \left(\frac{\sin\left(\frac{\pi(m-2)t}{mT}\right)}{m-2} - \frac{\sin\left(\frac{\pi(m+2)t}{mT}\right)}{m+2} \right) \Theta(mT - t)\Theta(t) . \quad (\text{III.48})$$

The amplitude changes more slowly for a greater number of oscillations. Examples are

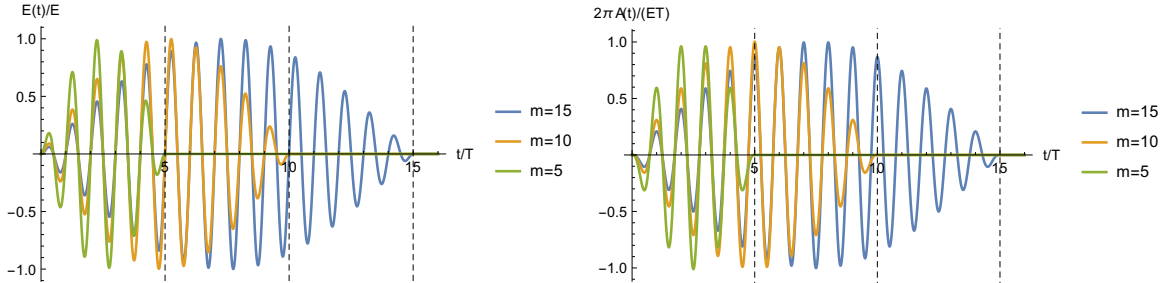


Figure 47: Normalized “realistic” electric field (left) and vector potential (right)

depicted in figure 46 for index 1 and in figure 47 for index 2. $E_i(t)$ and $A_i(t)$ vanish after $t_{\text{fin}} = Tm$ for both pulses. The vertical dotted lines indicate $t_{\text{fin}} = Tm$ in the following plots. T is the duration of one oscillation and m is the number of oscillations. It is important that $A_i(t > t_{\text{fin}}) = 0$, because then the Hamiltonian before and after the pulse are identical.

The zeroth-order term of the kinetic energy $E_{\text{kin}}^{(0)}(t)$ and current $j^{(0)}(t)$ is shown in

4 PHOTOINDUCED PRETHERMALIZATION

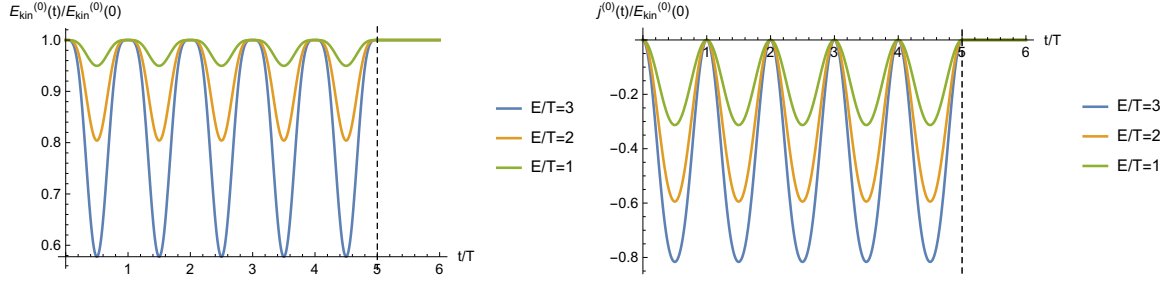


Figure 48: Normalized kinetic energy (left) and current (right) for “simple” pulse $m = 5$

figures 48 and 49. During the pulse, their qualitative behavior is very similar to the corresponding $A_i(t)$ even for high amplitudes ($E/T > 1$). The scaling with the field strength E is approximately linear for the current and quadratic for the kinetic energy. This scaling behavior stems from the expansions for small amplitudes E .

After the pulse, they have the same values as before. The explanation for this is simple. The noninteracting state is for all times an eigenstate of Hamiltonian $\hat{H}_0 + \delta\hat{H}_0(t)$. Hence, its time evolution is trivial, and the dynamics of the observables stem from the explicit time-dependence of the operators, which are given in equation (III.36). With this statement, we close the discussion of the purely noninteracting results and advance to the corrections in interaction strength.

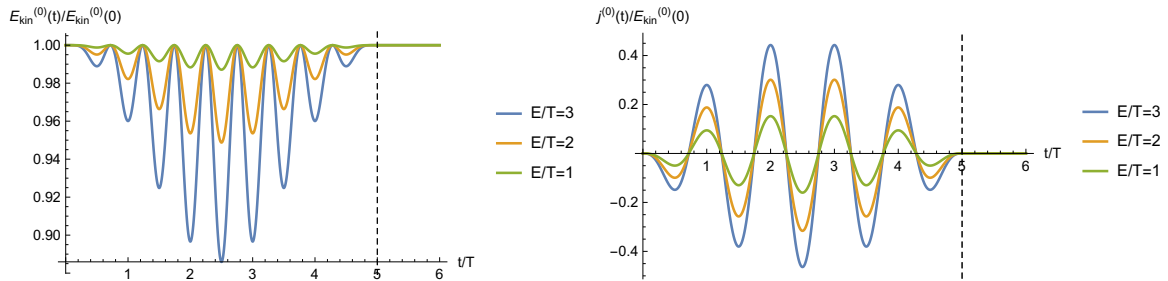


Figure 49: Normalized kinetic energy (left) and current (right) for “realistic” pulse $m = 5$

Prethermalization results

We focus on the corrections in interaction strength beginning with results for the double occupation in figure 50. It scales quadratically with the field strength E , and the qualitative behavior is affected for fields above $E > 2$. The general shape of the curve is

III PRETHERMALIZATION INDUCED BY WEAK INTERACTIONS

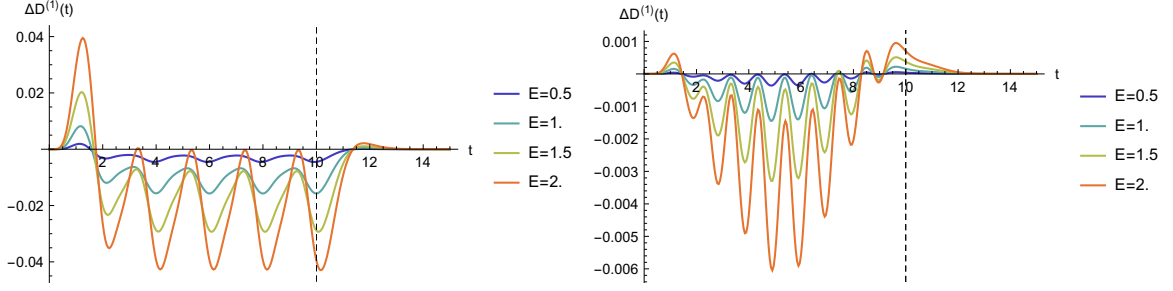


Figure 50: Double occupation for “simple” (left) and ”realistic” (right) pulse with $T = 2$ and $m = 5$

similar to $-A_i(t)$ with a slight shift in time and short excursions to positive values at the start and after the pulse. As a first-order observable, it relaxes to its initial value.

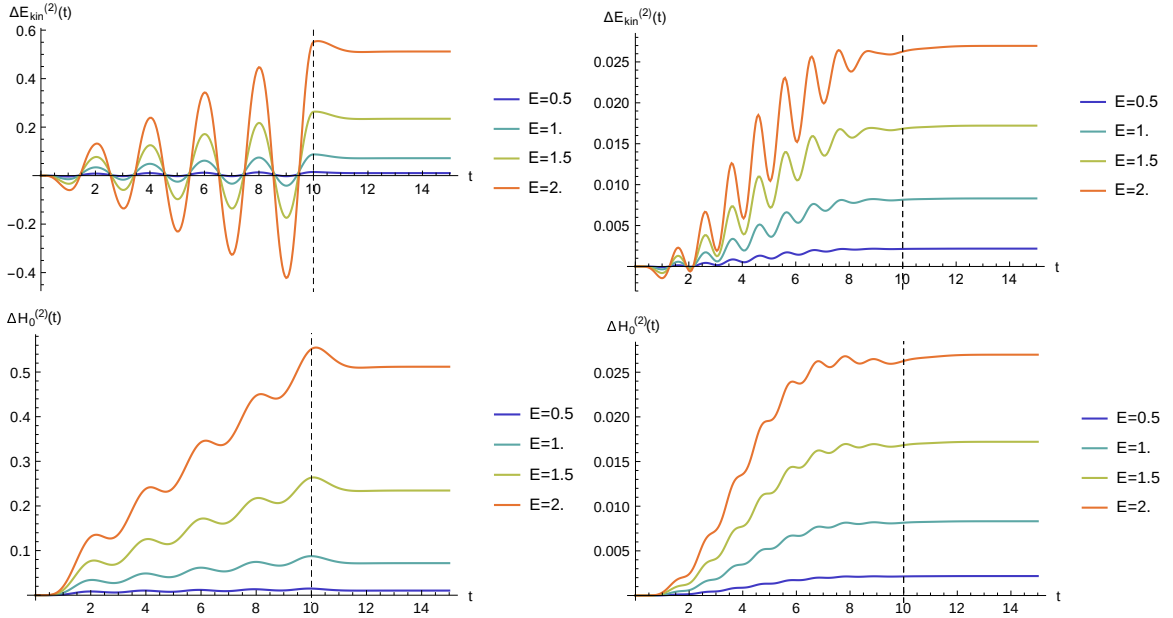


Figure 51: Kinetic energy (top) and $\langle \hat{H}_0 \rangle_t^{(2)}$ (bottom) for “simple” (left) and “realistic” (right) pulse with $T = 2$ and $m = 5$

We see the change of kinetic energy and the unperturbed Hamiltonian \hat{H}_0 in figure 51. They relax to a finite prethermalization plateau, as they are second-order observables. The kinetic energy has stronger oscillations during the pulse, while \hat{H}_0 is more steady.

4 PHOTOINDUCED PRETHERMALIZATION

These two observables become identical after the pulse. The field strength E scales these two observables quadratically.

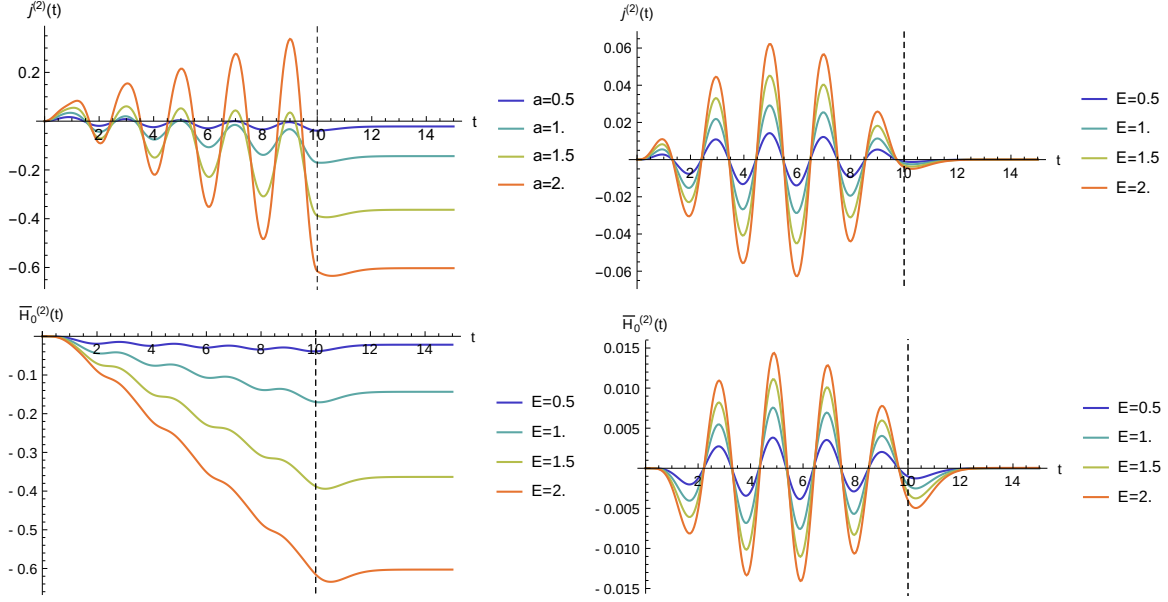


Figure 52: Current (top) and $\langle \hat{H}_0 \rangle_t^{(2)}$ (bottom) for “simple” (left) and “realistic” (right) pulse with $T = 2$ and $m = 5$

The current j and \hat{H}_0 are displayed in figure 52. The “simple” pulse on the left-hand side exhibit different features than the “realistic” pulse on the right-hand side. We clearly observe the prethermalization plateau in the left-hand plots for the “simple” pulse. The plateau value on the right-hand side vanishes. This distinction still holds if we further vary the parameters E , T , and m . We conclude that the current’s prethermalization plateau vanishes for an enveloped pulse. This leads to the question under which general circumstances the prethermalization plateau vanishes. The current and \hat{H}_0 oscillate similarly, and both scale linear in E for the enveloped pulse in figure 52. The scaling with E is not linear for the “simple” pulse.

Another difference between “simple” and “realistic” pulses becomes visible in the occupation numbers in figure 53. The “simple” pulse affects occupation numbers with higher $\bar{\epsilon}$ more. For the realistic pulse, we observe the opposite effect that the occupation numbers with higher $\bar{\epsilon}$ are less affected. For both pulses, the states at the Fermi surface are affected the most, and the influence decreases away from it.

III PRETHERMALIZATION INDUCED BY WEAK INTERACTIONS

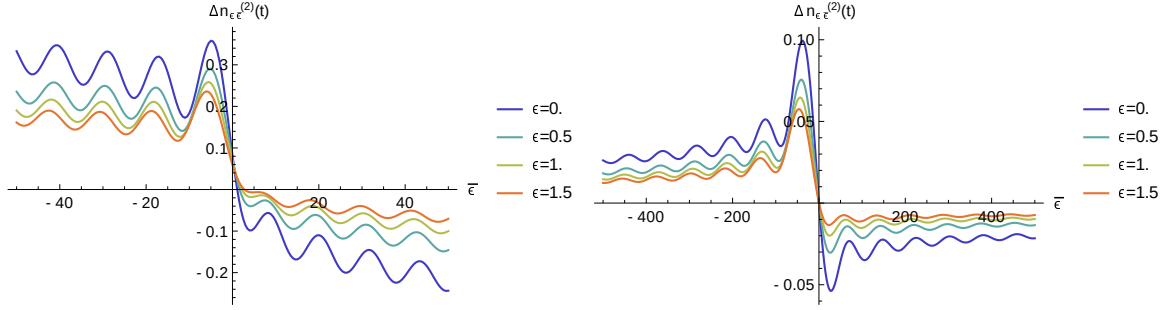


Figure 53: Change in the occupation numbers at time $t = 1$ for $E = 2$ and $T = 2$ for “simple” (left) and “realistic” (right) pulse shape

The amplitude E scales the result in our examples and has very little influence on the qualitative form. Of course, this is not valid anymore for $E > 2$. However, these values belong to extremely intense fields and are omitted here. Hence, our next step is to expand in E for weak electric fields. This simplifies the discussion of the results as the parameter space is reduced.

f) Expansion in field strength

We learned in the previous subsection that the numerical terms are dominated by the linear or quadratic term in electric field strength. We extract those terms by expanding for weak fields. The electric field strength E enters through function $A(t)$. We expand $\langle \hat{D} \rangle_t$ and $\langle \hat{H}_0 \rangle_t$ to $O(A^2)$ because the first order vanishes and for $\langle \hat{H}_0 \rangle_t$ to $O(A)$. For the occupations numbers $\langle \hat{n}_{\epsilon\bar{\epsilon}} \rangle_t$, we compute the first- and second-order terms in $A(t)$. We start by expanding the abbreviations from equation (III.37),

$$\tau_1(t_1, t_2) = t_1 - t_2 - \int_{t_2}^{t_1} d\tau \frac{A(\tau)^2}{2} + O(A^4), \quad \tau_2(t_1, t_2) = \int_{t_2}^{t_1} d\tau A(\tau) + O(A^3).$$

Consequently, we expand the integrand of the double occupation as

$$\begin{aligned} & 2\Re i \left(F(\tau_1(t, t_1), \tau_2(t, t_1))^4 - F(t - t_1, 0)^4 \right) \\ &= - \left[\int_{t_2}^{t_1} d\tau A(\tau)^2 \frac{\partial}{\partial \tau_1} + 2 \left(\int_{t_2}^{t_1} d\tau A(\tau) \right)^2 \right] \Re i F(\tau_1, 0)^4 \Big|_{\tau_1=t_1-t_2} + O(A^3). \end{aligned}$$

In an analogous manner, we obtain for the occupation numbers:

$$\begin{aligned}
 & \partial E(t_2) e^{i\tau_1 \epsilon + i\tau_2 \bar{\epsilon}} F(\tau_1, \tau_2)^3 \Big|_{\substack{\tau_1 = \tau_1(t_1, t_2) \\ \tau_2 = \tau_2(t_1, t_2)}} \\
 &= \left(\frac{A(t_2)^2}{2} \frac{\partial}{\partial i\tau_1} + A(t_2) \frac{\partial}{\partial i\tau_2} \right) e^{i\tau_1 \epsilon + i\tau_2 \bar{\epsilon}} F(\tau_1, \tau_2)^3 \Big|_{\substack{\tau_1 = t_1 - t_2 \\ \tau_2 = \int_{t_2}^{t_1} d\tau A(\tau)}} + O(A^3) \\
 &= \frac{A(t_2)^2}{2} \frac{\partial}{\partial i\tau_1} e^{i\tau_1 \epsilon} F(\tau_1, 0)^3 \Big|_{\tau_1 = t_1 - t_2} \\
 &\quad + A(t_2) \left(\bar{\epsilon} + \frac{3}{2} i\tau_2 \right) e^{i\tau_1 \epsilon + i\tau_2 \bar{\epsilon} - \frac{3}{4} \tau_2^2} F(\tau_1, 0)^3 \Big|_{\substack{\tau_1 = t_1 - t_2 \\ \tau_2 = \int_{t_2}^{t_1} d\tau A(\tau)}} + O(A^3) \\
 &= \frac{A(t_2)^2}{2} \frac{\partial}{\partial i\tau_1} e^{i\tau_1 \epsilon} F(\tau_1, 0)^3 \Big|_{\tau_1 = t_1 - t_2} + A(t_2) \bar{\epsilon} e^{i\tau_1 \epsilon} F(\tau_1, 0)^3 \Big|_{\tau_1 = t_1 - t_2} \\
 &\quad + A(t_2) \int_{t_2}^{t_1} d\tau A(\tau) i \left(\bar{\epsilon}^2 + \frac{3}{2} \right) e^{i\tau_1 \epsilon} F(\tau_1, 0)^3 \Big|_{\tau_1 = t_1 - t_2} + O(A^3) . \quad (\text{III.49})
 \end{aligned}$$

We obtain the expansions for $\langle \hat{H}_0 \rangle_t$ and $\langle \hat{\bar{H}}_0 \rangle_t$ by integrating over equation (III.49) times ϵ or $\bar{\epsilon}$. The linear term vanishes in $\langle \hat{H}_0 \rangle_t$ and the result is

$$\begin{aligned}
 & 2\Re \partial E(t_2) F(\tau_1, \tau_2)^4 \Big|_{\substack{\tau_1 = \tau_1(t_1, t_2) \\ \tau_2 = \tau_2(t_1, t_2)}} \\
 &= A(t_2) \left(-A(t_2) \frac{\partial}{\partial \tau_1} + 4 \int_{t_2}^{t_1} d\tau A(\tau) \right) \Re i F(\tau_1, 0)^4 \Big|_{\tau_1 = t_1 - t_2} + O(A^3) .
 \end{aligned}$$

The quadratic terms vanishes in $\langle \hat{\bar{H}}_0 \rangle_t$ and we obtain

$$\partial E(t_2) \frac{\partial}{\partial i\tau_2} F(\tau_1, \tau_2)^4 \Big|_{\substack{\tau_1 = \tau_1(t_1, t_2) \\ \tau_2 = \tau_2(t_1, t_2)}} = 2A(t_2) F(\tau_1, 0)^4 \Big|_{\tau_1 = t_1 - t_2} + O(A^3) .$$

We insert the expansions back into equations (III.39), (III.40), (III.42) and (III.43). We use the pulse shapes from equations (III.47) and (III.48) in our following results.

Prethermalization results

Now, we present the numerical results for the expansion in field strength. The second inte-

III PRETHERMALIZATION INDUCED BY WEAK INTERACTIONS

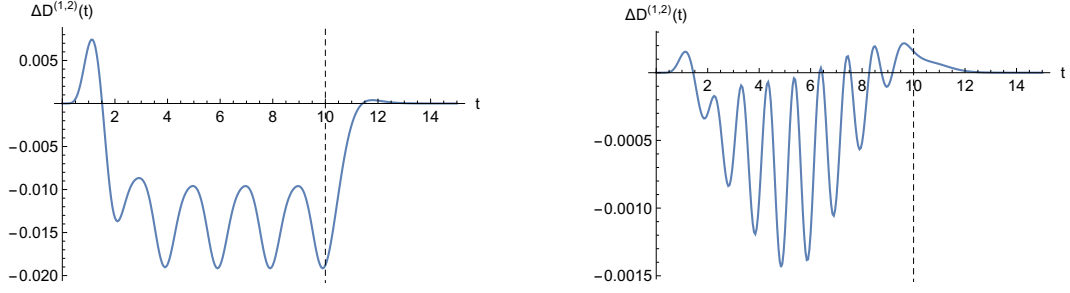


Figure 54: Double occupation term for “simple” (left) and “realistic” (right) pulse shape with $T = 2$ and $m = 5$

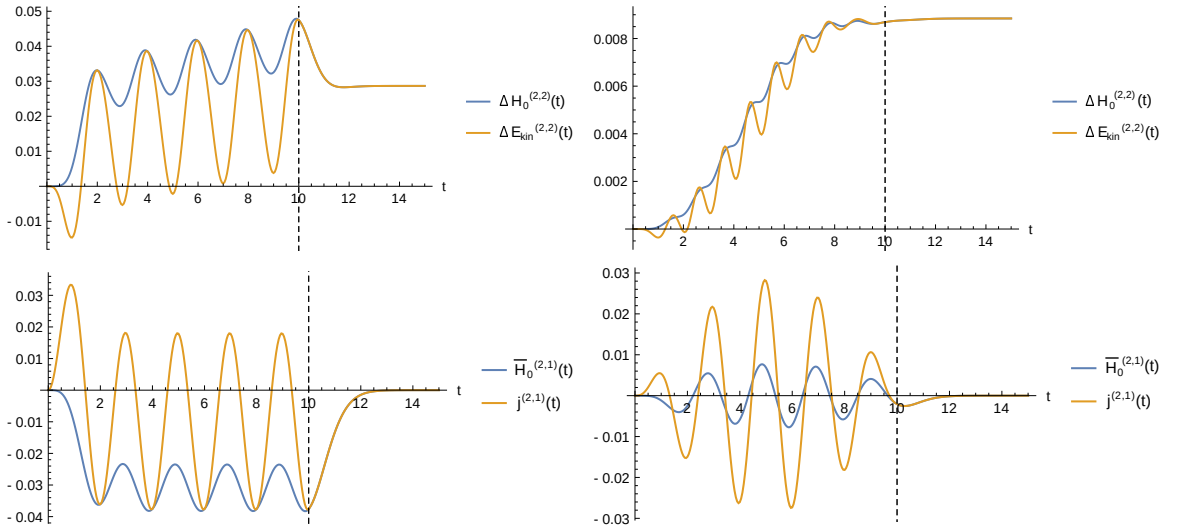


Figure 55: Second-order terms for “simple” (left) and “realistic” (right) pulse shape with $T = 2$ and $m = 5$

ger of the exponent denotes the order in field strength, $A^{(n)}(t) = E^m A^{(n,m)}(t) + O(E^{m+1})$. The double occupation term has the exponent $(1, 2)$, and therefore, it scales linearly in interaction strength U and quadratic in field strength E . The expansion term in figure 54 has the same features as the nonperturbative term in figure 50. Thus, the expansion is accurate for the double occupation.

Next, we compare the expansion for the second-order observables in figure 55 with figures 51 and 52. The plots for the enveloped pulse are in good agreement. However, some features for the “simple” pulse are lost in the expansion. The current and \widehat{H}_0

4 PHOTOINDUCED PRETHERMALIZATION

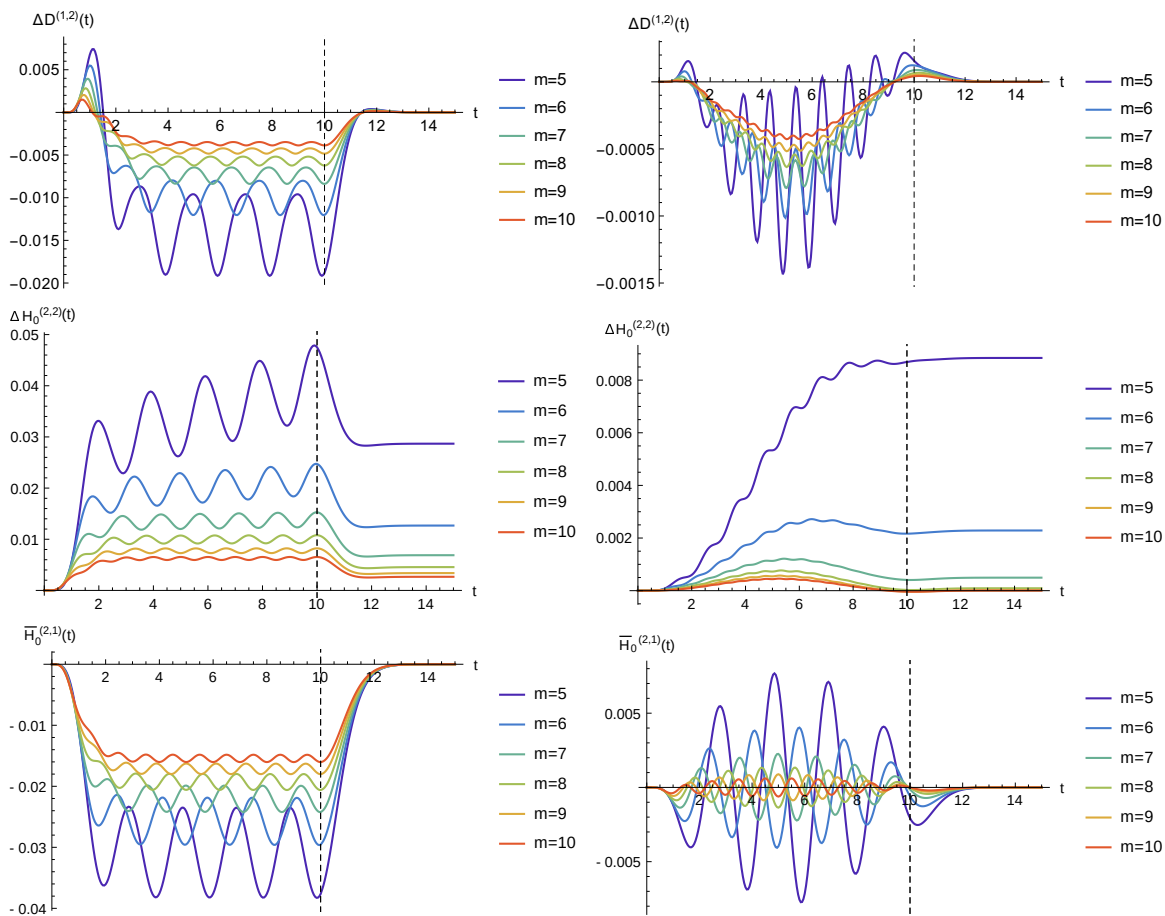


Figure 56: Double occupation (top), \hat{H}_0 (middle) and $\hat{\bar{H}}_0$ (bottom) with varying pulse oscillations m for “simple” (left) and “realistic” (right) pulse shape

III PRETHERMALIZATION INDUCED BY WEAK INTERACTIONS

have no prethermalization plateau for the expansion. Furthermore, the kinetic energy oscillates into negative values in figure 51, but has positive values for all times in the expansion. Hence, these two effects originate from higher-order contributions. The first one is the prethermalization plateau for the current, and the second one are negative kinetic-energy corrections.

Now, we keep the pulse duration constant and vary the number of oscillations in figure 56. We do not display current and kinetic energy because they can be computed from \hat{H}_0 and $\hat{\tilde{H}}_0$. The impact generally increases for lower frequency. This means that the oscillations are more pronounced in the observables, and the plateau values increase. Especially the kinetic-energy plateau after the pulse, which is identical to the plateau of \hat{H}_0 , increases for lower frequency. The plateaus for current and $\hat{\tilde{H}}_0$ vanish after the pulse.

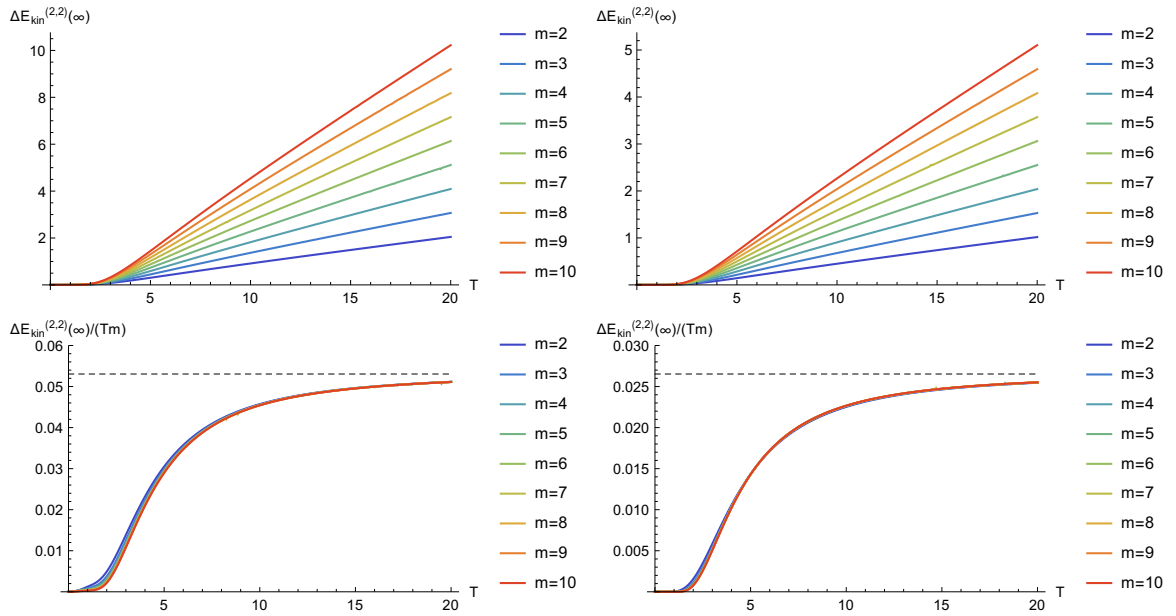


Figure 57: Plateau value of kinetic energy (top) and scaled (bottom) with varying pulse oscillations m and periods T for “simple” (left) and “realistic” (right) pulse shape

In the following, we examine the prethermalization plateau of the kinetic energy in more detail. We display the plateau value against the period duration T for various periods m in the top plots of figure 57. The plateau value increase for lower frequencies, and the increase becomes linear for $T \geq 6$. Furthermore, longer wave trains increase the plateau.

The lines are evenly spread, which indicates linearity in m .

We rescale the kinetic energy by the pulse duration Tm in the bottom plots of figure 57. All ten lines collapse to a single line. The collapse is nearly perfect for the “realistic” pulse, and slight deviations are observed for the “simple” pulse. The limit $T \rightarrow \infty$ is a finite value for the scaled kinetic energy. The plateau value of the kinetic energy is a complicated function concerning frequency and pulse shape. However, it scales linearly with duration and quadratically with field strength. For low-frequency pulses, it scales linearly with T as well. The absorbed energy of the system is equal to the plateau value of the kinetic energy within our method as the double occupation returns to its initial value.

The scaling of the prethermal plateau with mTE^2 is the main result of this section and will be further investigated in subsection i). There, we will compute prethermal plateau in response to an external electric field pulse. For this, we require the conductivity in linear response theory to relate the internal to the external electric field.

g) Linear response

The established method to study the effect of a weak electric field is the linear response theory.^{27,60,90} First, we shortly introduce linear response theory and then compute the conductivity. Finally, inserting the conductivity into the Maxwell equations will give us the relation between the external and the internal electric field.

Generally, a time-independent Hamiltonian \hat{H} is perturbed by a time-dependent external field $F(t)$. We expand to the first order in this field $F(t)$. The operator $\hat{\chi}$ couples the field to the Hamiltonian

$$\hat{H}_t = \hat{H} + \hat{\chi}F(t) .$$

This needs to be generalized for a spatially varying field,

$$\hat{H}_t = \hat{H} + \sum_r \hat{\chi}_r F_r(t) .$$

The first-order term is computed for any observable \hat{O} by

$$\delta\langle\hat{O}\rangle_t = \langle\hat{O}\rangle_t - \langle\hat{O}\rangle_0 = \int_0^t d\tau F(\tau) \langle [i(\hat{\chi})_H(\tau), (\hat{O})_H(t)] \rangle_0 + O(F^2) .$$

III PRETHERMALIZATION INDUCED BY WEAK INTERACTIONS

The operators are in the Heisenberg picture with respect to \hat{H} . We start from an eigenstate at time $t = 0$ and thus the expectation value of the commutator depends on the time difference. We define a response function $\phi_{\hat{O}}(t - \tau)$,

$$\langle [i\hat{\chi}(\tau), \hat{O}(t)] \rangle_0 = \langle [i\hat{\chi}, \hat{O}(t - \tau)] \rangle_0 = \phi_{\hat{O}}(t - \tau) .$$

This method has a general advantage. The response function is an equilibrium property of the system together with $\hat{\chi}$ and \hat{O} . We do not compute the time-dependence of $\langle \hat{O} \rangle_t$ for different pulses, but we investigate the pulse independent $\phi_{\hat{O}}(t - \tau)$. If we apply the Laplace transformation, then the convolution becomes a multiplication,

$$\mathcal{L}_{t \rightarrow z}(\delta \langle \hat{O} \rangle_t) = \mathcal{L}_{t \rightarrow z}(F(t)) \mathcal{L}_{t \rightarrow z}(\phi_{\hat{O}}(t)) .$$

Conductivity

The electric field does not enter the Hamiltonian directly. Instead, the vector potential $\mathbf{A}(\mathbf{r}, t)$ shifts the momenta of the electrons. We use Landau gauge $\mathbf{E}(\mathbf{r}, t) = -c^{-1} \partial_t \mathbf{A}(\mathbf{r}, t)$. We drop the spatial dependence of $\mathbf{A}(\mathbf{r}, t)$ as we focus on the dipole approximation, which assumes a spatially homogeneous field. The general perturbation in the dipole approximation is

$$\delta \hat{H}_0(t) = \sum_{\sigma, \mathbf{k}} \left[\epsilon(\mathbf{k} - \frac{ea}{\hbar c} \mathbf{A}(t)) - \epsilon(\mathbf{k}) \right] \hat{n}_{\sigma \mathbf{k}} .$$

Expansion to $O(A^2)$ with $\mathbf{A}(t) = \mathbf{e}_A A(t)$ gives,

$$\begin{aligned} \delta \hat{H}_0(t) &= -\frac{ea}{\hbar c} A(t) \hat{H}_0^{(1)} + \frac{e^2 a^2}{2\hbar^2 c^2} A(t)^2 \hat{H}_0^{(2)} + O(A^3) , \\ \hat{H}_0^{(n)} &= \sum_{\sigma, \mathbf{k}} \epsilon^{(n)}(\mathbf{k}) \hat{n}_{\sigma \mathbf{k}} , \quad \epsilon^{(n)}(\mathbf{k}) = \left. \frac{\partial^n \epsilon(\mathbf{k} + \mathbf{e}_A x)}{\partial x^n} \right|_{x=0} . \end{aligned}$$

The current operator is

$$\hat{j}(t) = -c \frac{\partial \hat{H}(t)}{\partial A(t)} = -c \frac{\partial \delta \hat{H}_0(t)}{\partial A(t)} = \frac{ea}{\hbar} \hat{H}_0^{(1)} - \frac{e^2 a^2}{\hbar^2 c} A(t) \hat{H}_0^{(2)} + O(A^2) .$$

The expectation value of $\hat{H}_0^{(1)}$ is usually zero, and the one of $\hat{H}_0^{(2)}$ is finite without an electric field. Therefore, the current is linear in $A(t)$ and is computed in linear response theory as

$$\langle \hat{j} \rangle_t = -\frac{e^2 a^2}{\hbar^2 c} A(t) \langle \hat{H}_0^{(2)} \rangle_t - i \int_{t_{\text{ini}}}^t d\tau \frac{e^2 a^2}{\hbar^2 c} A(\tau) \langle [\left(\hat{H}_0^{(1)} \right)_{\hat{H}}(\tau), \left(\hat{H}_0^{(1)} \right)_{\hat{H}}(t)] \rangle_{t_{\text{ini}}} + O(A^2) .$$

4 PHOTOINDUCED PRETHERMALIZATION

Every observable is expressed as the convolution of the electric field, $E(t) = -c^{-1}\partial_t A(t)$, with the response function. This defines the response function. The response function of the current is the conductivity $\sigma \equiv \phi_j$ and its two parts are called diamagnetic and paramagnetic conductivity,¹¹⁴

$$\begin{aligned} \langle \hat{j} \rangle_t &= \int_{t_{\text{ini}}}^t d\tau E(\tau) \sigma(t, \tau) + O(E^2) , \\ \sigma(t, \tau) &= \sigma^{\text{dia}}(t) + \sigma^{\text{pm}}(t, \tau) , \quad \sigma^{\text{dia}}(t) = \frac{e^2 a^2}{\hbar^2} \langle \hat{H}_0^{(2)} \rangle_t , \\ \sigma^{\text{pm}}(t, \tau) &= \frac{e^2 a^2}{\hbar^2} i \int_{\tau}^t d\tau' \langle \left[\left(\hat{H}_0^{(1)} \right)_{\hat{H}}(\tau'), \left(\hat{H}_0^{(1)} \right)_{\hat{H}}(t) \right] \rangle_{t_{\text{ini}}} . \end{aligned} \quad (\text{III.50})$$

If the problem is time-independent except for the electric field, then the response functions simplify to $\sigma^{\text{dia}}(t) \rightarrow \sigma^{\text{dia}}$ and $\sigma^{\text{pm}}(t, \tau) \rightarrow \sigma^{\text{pm}}(t - \tau)$. The Laplace-Fourier transformation is applied to transform the convolution to a multiplication,

$$f(\omega) = \mathcal{L}_{t \rightarrow -i\omega}(f(t)) = \int_0^{\infty} dt e^{(i\omega - \delta)t} f(t) , \quad \langle \hat{j} \rangle_{\omega} = E(\omega) \sigma(\omega) .$$

Our method computes the equilibrium conductivity in $O(g^2)$. The diamagnetic part has a zeroth and second-order term,

$$\begin{aligned} \sigma^{\text{dia}} &= \sigma^{\text{dia},(0)} + g^2 \sigma^{\text{dia},(2)} + O(g^3) , \quad \sigma^{\text{dia},(0)} = \frac{e^2 a^2}{\hbar^2} \langle \hat{H}_0^{(2)} \rangle_0 , \\ \sigma^{\text{dia},(2)} &= -\frac{e^2 a^2}{\hbar^2} \int_{-\infty}^0 dt_1 \int_{-\infty}^{t_1} dt_2 f(t_1) f(t_2) \langle \left[\left[V_I(t_2), \left[\hat{V}_I(t_1), \hat{H}_0^{(2)} \right] \right] \right] \rangle_0 , \end{aligned}$$

and we obtain for our Hubbard model ($\frac{e^2 a^2}{\hbar^2} \equiv 1$, $\hat{H}_0^{(2)} = -\hat{H}_0$, $g = U$, $t^* = 1$),

$$\sigma^{\text{dia},(0)} = -\langle \hat{H}_0 \rangle_0 = \frac{1}{2\sqrt{\pi}} , \quad \sigma^{\text{dia},(2)} = -E_{\text{kin}}^{(2)} = -\int_{\frac{1}{4}}^1 db \frac{a_4(b)}{2\sqrt{\pi^3 b^3}} \approx -0.0659 .$$

III PRETHERMALIZATION INDUCED BY WEAK INTERACTIONS

The expectation value from the paramagnetic conductivity is computed as

$$\begin{aligned} & \langle \left[\left(\hat{H}_0^{(1)} \right)_{\hat{H}} (\tau'), \left(\hat{H}_0^{(1)} \right)_{\hat{H}} (t) \right] \rangle_{t_{\text{ini}}} \\ &= -g^2 \int_{-\infty}^t dt_1 \int_{-\infty}^{\tau'} d\tau_1 f(t_1) f(\tau_1) \langle \left[\left[V_I(\tau_1), \hat{H}_0^{(1)} \right], \left[\hat{V}_I(t_1), \hat{H}_0^{(1)} \right] \right] \rangle_0 + O(g^3). \quad (\text{III.51}) \end{aligned}$$

We rewrite the expectation value analogously to equation (III.25),

$$\begin{aligned} & \langle \left[\left[V_I(\tau_1), \hat{H}_0^{(1)} \right], \left[\hat{V}_I(t_1), \hat{H}_0^{(1)} \right] \right] \rangle_0 \\ &= \langle \left[V, \hat{H}_0^{(1)} \right], \left[U_0^\dagger(t_1, \tau_1) \hat{V} U_0(t_1, \tau_1), \hat{H}_0^{(1)} \right] \rangle_0 - \langle \left[U_0(t_1, \tau_1) V U_0^\dagger(t_1, \tau_1), \hat{H}_0^{(1)} \right], \left[\hat{V}, \hat{H}_0^{(1)} \right] \rangle_0 \\ &= \langle \left[V, \hat{H}_0^{(1)} \right], \left[U_0^\dagger(t_1, \tau_1) \hat{V} U_0(t_1, \tau_1), \hat{H}_0^{(1)} \right] \rangle_0 - \langle \left[V, \hat{H}_0^{(1)} \right], \left[U_0^\dagger(t_1, \tau_1) \hat{V} U_0(t_1, \tau_1), \hat{H}_0^{(1)} \right] \rangle_0^* \\ &= - \sum_m e^{i \int_{\tau_1}^{t_1} d\tau \Delta E_m(\tau)} |V_{0m}|^2 (\Delta E_m^{(1)})^2 - \text{c.c.}, \end{aligned}$$

with $\hat{H}_0^{(1)} |\Psi_m\rangle = E_m^{(1)} |\Psi_m\rangle$, $\Delta E_m^{(1)} = E_m^{(1)} - E_0^{(1)}$ and $V_{nm} = \langle \Psi_n | \hat{V} | \Psi_m \rangle$. We can evaluate equation (III.50) as the eigenenergies are time-independent, $\Delta E_m(t) = \Delta E_m$. For that, we need the integral

$$\begin{aligned} \int_{-\infty}^{\tau'} d\tau_1 f(\tau_1) e^{-i\tau_1 \Delta E_m} &= \int_{-\infty}^0 d\tau_1 e^{\tau_1 \delta} e^{-i\tau_1 \Delta E_m} + \int_0^{\tau'} d\tau_1 e^{-i\tau_1 \Delta E_m} \\ &= \frac{e^{-i\tau' \Delta E_m} - 1}{-i\Delta E_m} + \frac{1}{-i\Delta E_m + \delta} = \frac{e^{-i\tau' \Delta E_m}}{-i\Delta E_m}. \end{aligned}$$

Then, the time integration gives

$$\begin{aligned} i \int_{\tau}^t d\tau' \int_{-\infty}^t dt_1 \int_{-\infty}^{\tau'} d\tau_1 f(t_1) f(\tau_1) e^{i \int_{\tau_1}^{t_1} d\tau \Delta E_m} + \text{c.c.} &= i \int_{\tau}^t d\tau' \frac{e^{it\Delta E_m} e^{-i\tau' \Delta E_m}}{i\Delta E_m - i\Delta E_m} + \text{c.c.} \\ &= \frac{e^{i(t-\tau)\Delta E_m} - 1}{\Delta E_m^3} + \text{c.c.} \end{aligned}$$

Thus, the model-independent result for equation (III.50) is

$$\begin{aligned} \sigma^{\text{pm}}(t, \tau) \stackrel{\partial_t \Delta E_m = 0}{=} \sigma^{\text{pm}}(t - \tau) &= g^2 \sigma^{\text{pm},(2)}(t - \tau) + O(g^3), \\ \sigma^{\text{pm},(2)}(t) &= \frac{e^2 a^2}{\hbar^2} \sum_m |V_{0m}|^2 2(\Delta E_m^{(1)})^2 \frac{\cos(\Delta E_m t) - 1}{\Delta E_m^3}. \end{aligned}$$

Application to our Hubbard model gives

$$\sigma^{\text{pm},(2)}(t) = \sum_m |D_{0m}|^2 2\Delta\bar{E}_m \frac{\cos(t\Delta E_m) - 1}{\Delta E_m^3}. \quad (\text{III.52})$$

We express the cosine function in its series form, and then every term is of type

$$\begin{aligned} & \sum_m |D_{0m}|^2 e^{i\tau_1\Delta E_m + i\tau_2\Delta\bar{E}_m} \frac{\Delta\bar{E}_m^2}{\Delta E_m^{3-2n_1}} \Bigg|_{\tau_1=\tau_2=0} \\ &= \left(\frac{\partial}{\partial i\tau_1} \right)^{-3+2n_1} \left(\frac{\partial}{\partial i\tau_2} \right)^2 \langle \hat{D} e^{i\tau_1\hat{H}_0 + i\tau_2\hat{H}_0} \hat{D} e^{-i\tau_1\hat{H}_0 - i\tau_2\hat{H}_0} \rangle_0 \Bigg|_{\tau_1=\tau_2=0} \\ &= (-1)^{1+n_1} \left(\frac{\partial}{\partial\tau_1} \right)^{-3+2n_1} \left(\frac{\partial}{\partial\tau_2} \right)^2 F(\tau_1, \tau_2)^4 \Bigg|_{\tau_1=\tau_2=0} \\ &\stackrel{(\text{III.45})}{=} (-1)^{1+n_1} \left(\frac{\partial}{\partial\tau_1} \right)^{2n_1} \frac{\partial^2 e^{-\tau_2^2}}{\partial\tau_2^2} \int_{\frac{1}{4}}^1 db \frac{a_4(b)}{\sqrt{b\pi^4}} \left(\frac{\sqrt{\pi}}{2} e^{-\frac{\tau_1^2}{4b}} + iD_+\left(\frac{\tau_1}{2\sqrt{b}}\right) \right) \Bigg|_{\tau_1=\tau_2=0}. \end{aligned}$$

The response function is real and thus the term with the Dawson function D_+ does not contribute. We take the derivatives with respect to τ_1 and τ_2 and then set them to zero. This gives rational factors and negative powers in b ,

$$-\frac{\partial^2 e^{-\tau_2^2}}{\partial\tau_2^2} \Bigg|_{\tau_2=0} = 2, \quad (-1)^{n_1} \frac{\partial^{2n_1} e^{-\frac{\tau_1^2}{4b}}}{\partial\tau_1^{2n_1}} \Bigg|_{\tau_1=0} = \frac{(2n_1 - 1)!!}{(2b)^{n_1}}.$$

The sum results in the exponential series,

$$\begin{aligned} \sigma^{\text{pm},(2)}(t) &= 2 \int_{\frac{1}{4}}^1 db \frac{a_4(b)}{\sqrt{b\pi^3}} \left(\sum_{n=1}^{\infty} \frac{(-1)^n t^{2n} (2n-1)!!}{2n! (2b)^n} \right) \\ &= 2 \int_{\frac{1}{4}}^1 db \frac{a_4(b)}{\sqrt{b\pi^3}} \left(\sum_{n=1}^{\infty} \frac{\left(-\frac{t^2}{4b}\right)^n}{n!} \right) \\ &= -2 \int_{\frac{1}{4}}^1 db \frac{a_4(b)}{\sqrt{b\pi^3}} \left(1 - e^{-\frac{t^2}{4b}} \right). \end{aligned}$$

III PRETHERMALIZATION INDUCED BY WEAK INTERACTIONS

The Fourier-Laplace transformation gives

$$\sigma(\omega) = \mathcal{L}_{t \rightarrow -i\omega}(\sigma(t)) = \int_0^{\infty} dt e^{(i\omega - \delta)t} \sigma(t), \quad \sigma^{\text{dia}}(\omega) = \frac{i\sigma^{\text{dia}}}{\omega + i\delta},$$

$$\sigma^{\text{pm},(2)}(\omega) = 2 \int_{\frac{1}{4}}^1 db \frac{a_4(b)}{\sqrt{b\pi^3}} \left(\frac{-i}{\omega + i\delta} + \sqrt{\pi b} e^{-\omega^2 b} + 2i\sqrt{b} D_+(\sqrt{b}\omega) \right). \quad (\text{III.53})$$

The diamagnetic conductivity is proportional to $\frac{i}{\omega + i\delta} = \pi\delta(\omega) + \frac{i}{\omega}$, which is the behavior

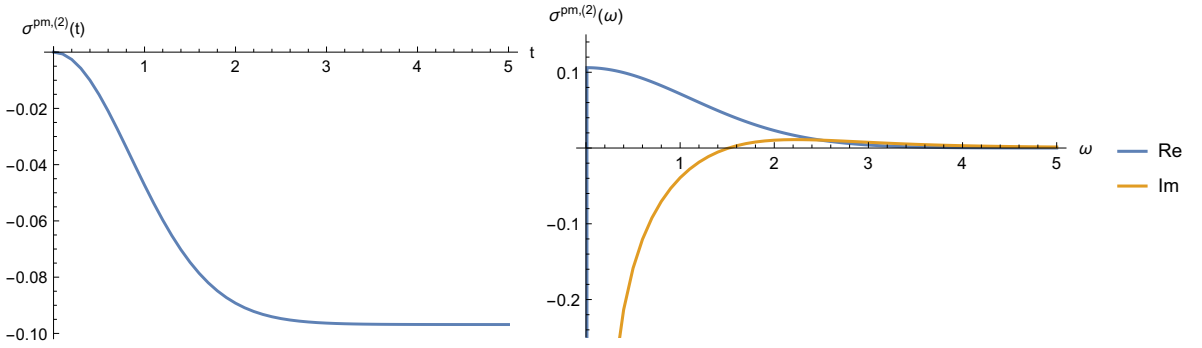


Figure 58: Paramagnetic conductivity in real time (left) and frequency (right)

of a perfectly metallic system. It stems from the noninteracting system and is renormalized by the interaction. The paramagnetic conductivity has qualitatively different terms due to the interaction. Our paramagnetic correction $\sigma^{\text{pm},(2)}$ is plotted in figure 58. We will see that the most important feature is the real, finite contributions for $\omega \neq 0$ as the $\delta(\omega)$ terms do not contribute to the conductivity with respect to the external field.

Conductivity with respect to external field

We have computed the conductivity with respect to the internal electric field and now we derive the conductivity with respect to the external electric field. The induced current generates an additional vector potential \mathbf{A}_{sys} by the Maxwell equation,

$$(\partial_t^2 - c^2 \nabla^2) \mathbf{A}_{\text{sys}}(\mathbf{r}, t) = 4\pi c \mathbf{j}_{\text{sys}}(\mathbf{r}, t) \Rightarrow \partial_t^2 \mathbf{A}_{\text{sys}}(t) = 4\pi c \mathbf{j}_{\text{sys}}(t).$$

The internal field is the superposition of the external field and the generated field,

$$\mathbf{A}(\mathbf{r}, t) = \mathbf{A}_{\text{ext}}(\mathbf{r}, t) + \mathbf{A}_{\text{sys}}(\mathbf{r}, t).$$

4 PHOTOINDUCED PRETHERMALIZATION

We include the current $\mathbf{j}(t)_{\text{sys}}$ as a classical quantity according to Skolimowski et al.¹⁰⁷ and set it equal to the expectation value of the quantum mechanical current,

$$\mathbf{j}_{\text{sys}}(t) = \langle \hat{\mathbf{j}} \rangle_t .$$

The computation of the conductivity with respect to the external field σ_{ext} is best done in frequency space ($\hat{\mathbf{j}} = \mathbf{e}_A \hat{j}$, $\mathbf{A}(t) = \mathbf{e}_A A(t)$, $\mathbf{E}(t) = \mathbf{e}_A E(t)$),

$$\begin{aligned} E(t) &= -c^{-1} \partial_t A(t) \Rightarrow E(\omega) = \frac{i\omega}{c} A(\omega) , \\ \langle \hat{\mathbf{j}} \rangle_\omega &= E_{\text{ext}}(\omega) \sigma_{\text{ext}}(\omega) = E(\omega) \sigma(\omega) , \\ \frac{cE(\omega)}{i\omega} &= \frac{cE_{\text{ext}}(\omega)}{i\omega} - \frac{4\pi c}{\omega^2} \langle \hat{\mathbf{j}} \rangle_\omega , \\ \Rightarrow \sigma_{\text{ext}}(\omega) &= \frac{\sigma(\omega)}{\epsilon(\omega)} , \quad \epsilon(\omega) = 1 + i \frac{4\pi}{\omega} \sigma(\omega) . \end{aligned} \quad (\text{III.54})$$

The conductivity with respect to the external field $\sigma_{\text{ext}}(\omega)$ is directly computed from

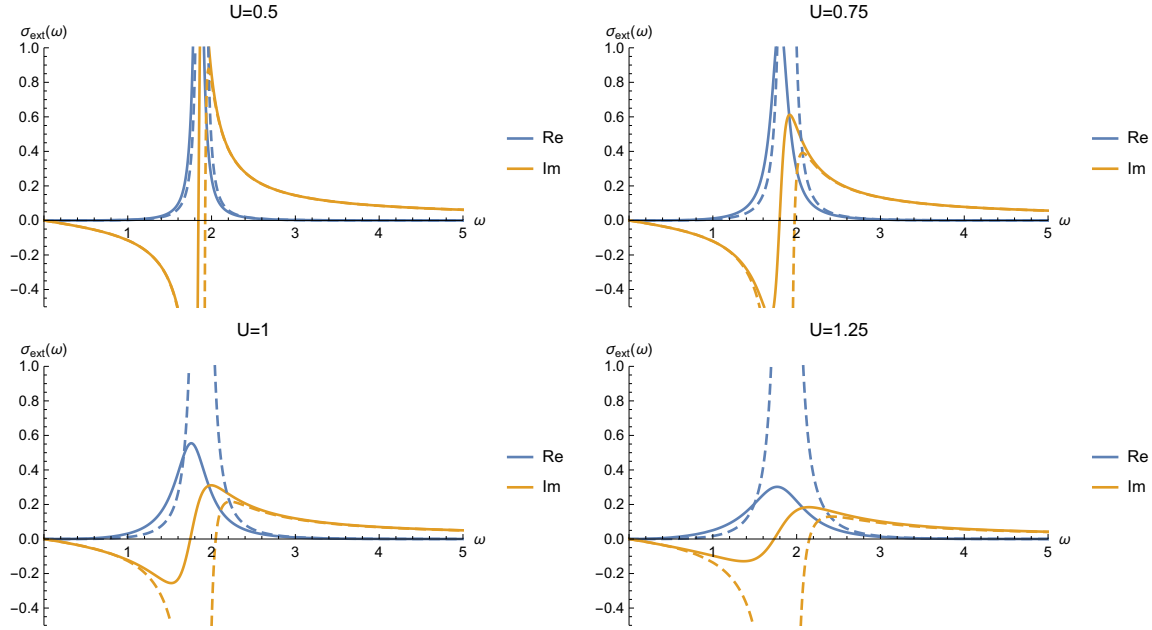


Figure 59: Conductivity with respect to the external field computed nonperturbatively (solid lines) or perturbatively (dashed lines) in U

the conductivity with respect to the internal field $\sigma(\omega)$. Our method expands the

III PRETHERMALIZATION INDUCED BY WEAK INTERACTIONS

conductivity to $O(U^2)$, $\sigma(\omega) = \sigma^{(0)}(\omega) + U^2\sigma^{(2)}(\omega) + O(U^3)$. When we compute $\sigma_{\text{ext}}(\omega)$, we have two options. First, we directly insert $\sigma^{(0)}(\omega) + U^2\sigma^{(2)}(\omega)$ in equation (III.54) and treat it nonperturbatively in U . Second, we expand to second order

$$\sigma_{\text{ext}}(\omega) = \frac{\sigma^{(0)}(\omega)}{1 + i\frac{4\pi}{\omega}\sigma^{(0)}(\omega)} + U^2\sigma^{(2)}(\omega) \left[\frac{\partial}{\partial x} \frac{\sigma^{(0)}(\omega) + x}{1 + i\frac{4\pi}{\omega}(\sigma^{(0)}(\omega) + x)} \right]_{x=0} + O(U^3)$$

and this is depicted in figure 59 as the dashed lines. The delta functions $\delta(\omega)$ are suppressed in both cases. The perturbative results (dashed lines) have a pole at $\omega = \sqrt{2}(\pi)^{1/4} \approx 1.88$ (in units of $t^* = 1$) and the nonperturbative results (solid lines) are analytic and have a finite peak. The nonperturbative results have the typical features of a Drude conductivity,³²

$$\sigma^{\text{Drude}}(\omega) = \frac{\sigma_0}{1 - i\omega\tau} , \quad \sigma_{\text{ext}}^{\text{Drude}}(\omega) = \frac{\sigma^{\text{Drude}}(\omega)}{1 + i\frac{4\pi}{\omega}\sigma^{\text{Drude}}(\omega)} .$$

Next, we quantify this similarity. We fit the two Drude parameters σ_0 and τ by the

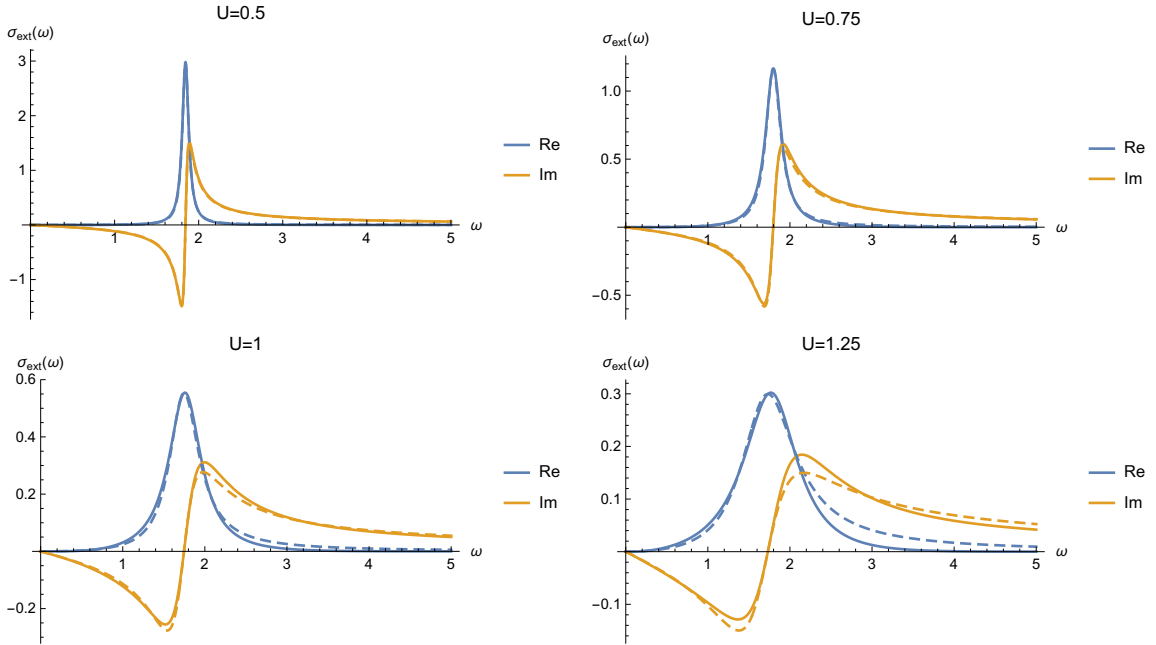


Figure 60: Conductivity with respect to the external field computed nonperturbatively (solid lines) or as Drude fit (dashed lines)

resonance peak,

$$\Im\{\sigma_{\text{ext}}(\omega_{\text{res}})\} = 0 , \quad \sigma_{\text{ext}}(\omega_{\text{res}}) = \sigma_{\text{ext}}^{\text{Drude}}(\omega_{\text{res}}) \Rightarrow \sigma_0 = \sigma_{\text{ext}}(\omega_{\text{res}}) , \quad \tau = \frac{4\pi\sigma_0}{\omega_{\text{res}}^2} .$$

The Drude fit is very accurate for $U \leq 1$ as we see in figure 60. Then it starts to deviate at the high-frequency tail and around the peaks of the imaginary part.

We have assumed in our computation that the pre- and post-pulse Hamiltonian are identical, $A(\tau > t_{\text{fin}}) = 0$. This requirement is realized for a metallic system even if the long-time limit of the external vector potential does not vanish $A_{\text{ext}}(t \rightarrow \infty) = \text{const.} \neq 0 \Rightarrow A_{\text{ext}}(\omega \rightarrow 0) \sim \frac{i}{\omega + i\delta}$. For a metallic material, the conductivity stays finite in the infrared limit $\sigma(\omega \rightarrow 0) \sim \omega^0$, e.g., the Drude conductivity is $\sigma(\omega) = \frac{\sigma_0}{1 - i\omega\tau}$. The relation between the internal and external vector potential gives

$$A(\omega) = \frac{A_{\text{ext}}(\omega)}{\epsilon(\omega)} \Rightarrow A(\omega \rightarrow 0) \sim \left(\pi\delta(\omega) + \frac{i}{\omega} \right) \omega = i \Rightarrow A(t \rightarrow \infty) = 0 .$$

The $\delta(\omega)$ contribute to $A(t)$ is suppressed by the factor ω , and thus the internal vector potential vanishes for large times. This argumentation is not valid for an insulator, as it has no dc-current, and then the external and internal vector potential are identical for $\omega \rightarrow 0$.

Generally, the response functions $\phi_{\hat{O}}(t - \tau)$ converge to a constant value for $t \rightarrow \infty$ and finite τ . Therefore, the linear response theory prediction vanishes in the long-time limit with $A(\tau > t_{\text{fin}}) = 0$,

$$\lim_{t \rightarrow \infty} \delta \langle \hat{O} \rangle_t = O(A^2) .$$

We have to include at least second-order terms in the field to capture a prethermal state. Next, we compute the pump-probe conductivity, which treats the pump pulse nonperturbatively and the probe pulse in linear response theory.

h) Pump-probe conductivity

Now, we consider a pump-probe scenario. Suppose that, a pump pulse excites the system, and the following probe pulse measures an altered conductivity. Below, we compute the conductivity for the probe pulse with equation (III.50), and the Hamiltonian includes the pump pulse.

III PRETHERMALIZATION INDUCED BY WEAK INTERACTIONS

We compute the change in the conductivity $\Delta\sigma(t, \tau)$, which is the conductivity of the probe pulse after the pump pulse minus the equilibrium conductivity,

$$\begin{aligned} \Delta\sigma(t, \tau) &= \sigma(t, \tau)|_{\hat{H}+\delta\hat{H}_0} - \sigma(t - \tau)|_{\hat{H}} , \quad \Delta\sigma^{\text{dia}}(t) = \frac{e^2 a^2}{\hbar^2} \left(\langle \hat{H}_0^{(2)} \rangle_t - \langle \hat{H}_0^{(2)} \rangle_{t_{\text{ini}}} \right) , \\ \Delta\sigma^{\text{pm}}(t, \tau) &= \frac{e^2 a^2}{\hbar^2} i \int_{\tau}^t d\tau' \left\langle \left[\left(\hat{H}_0^{(1)} \right)_{\hat{H}+\delta\hat{H}_0}(\tau'), \left(\hat{H}_0^{(1)} \right)_{\hat{H}+\delta\hat{H}_0}(t) \right] \right\rangle_{t_{\text{ini}}} \\ &\quad - \left\langle \left[\left(\hat{H}_0^{(1)} \right)_{\hat{H}}(\tau'), \left(\hat{H}_0^{(1)} \right)_{\hat{H}}(t) \right] \right\rangle_{t_{\text{ini}}} . \quad (\text{III.55}) \end{aligned}$$

We expect the dynamics of the diamagnetic conductivity to behave similarly to the kinetic energy. In our particular model, they are equal to each other except for a factor minus one, $\hat{H}_0^{(2)} = -\hat{H}_0$. This was investigated in subsection e) and f). We learned that the plateau scales linearly in duration and quadratic in field strength of the pump pulse. Next, we compute the change in the paramagnetic conductivity. We obtain the second-order term with equation (III.51) and rewrite the time-dependent contribution with equation (III.31),

$$\begin{aligned} &\left\langle \left[\left(\hat{H}_0^{(1)} \right)_{\hat{H}+\delta\hat{H}_0}(\tau'), \left(\hat{H}_0^{(1)} \right)_{\hat{H}+\delta\hat{H}_0}(t) \right] \right\rangle_{t_{\text{ini}}} \\ &= g^2 \sum_l |V_{0l}|^2 \left(\Delta E_l^{(1)} \right)^2 \underbrace{\int_{-\infty}^t dt_1 \int_{-\infty}^{\tau'} d\tau_1 f(t_1) f(\tau_1) \exp \left(i \int_{\tau_1}^{t_1} dt' (\Delta E_l + \delta e_l(t')) \right)}_{= e^{i(t-\tau')\Delta E_l} (\varphi_l^{(1)}(t))^* \varphi_l^{(1)}(\tau')} - \text{c.c.} + O(g^3) . \end{aligned}$$

We assume that the pump and the probe pulse have no overlap in time $t, \tau > t_{\text{fin}}$. Thus, the upper limit of the integrals in equation (III.31) are t_{fin} . We use equation (III.33),

$$\begin{aligned} \varphi_l^{(1)}(t > t_{\text{fin}}) &= \frac{-1}{\Delta E_l} + i e^{it\Delta E_l} h_l , \\ h_l &= \int_0^{t_{\text{fin}}} dt_1 e^{-it_1\Delta E_l} \left[e^{i \int_{t_1}^{t_{\text{fin}}} dt' \delta e_l(t')} - 1 \right] = - \int_0^{t_{\text{fin}}} dt_1 \frac{e^{-it_1\Delta E_l}}{\Delta E_l} e^{i \int_{t_1}^{t_{\text{fin}}} dt' \delta e_l(t')} \delta e_l(t_1) . \end{aligned}$$

Now, we compute the time-integration

$$\begin{aligned}
 & \left(\varphi_l^{(1)}(t) \right)^* i \int_{\tau}^t d\tau' e^{i(t-\tau')\Delta E_l} \varphi_l^{(1)}(\tau') + \text{c.c.} \\
 &= \left(\frac{-1}{\Delta E_l} - i e^{-it\Delta E_l} h_l^* \right) i \int_{\tau}^t d\tau' e^{i(t-\tau')\Delta E_l} \left(\frac{-1}{\Delta E_l} + i e^{i\tau'\Delta E_l} h_l \right) + \text{c.c.} \\
 &= \frac{e^{i(t-\tau)\Delta E_l} - 1}{\Delta E_l^3} + \frac{e^{i(t-\tau)\Delta E_l} - 1}{\Delta E_l^2} e^{-it\Delta E_l} i h_l^* + \frac{t - \tau}{\Delta E_l} e^{it\Delta E_l} h_l + \text{c.c.}
 \end{aligned}$$

and the first term gives the paramagnetic conductivity in equilibrium. Consequently, the other terms give the change of the paramagnetic conductivity,

$$\begin{aligned}
 \Delta\sigma^{\text{pm},(2)}(t, \tau) &= \frac{e^2 a^2}{\hbar^2} \int_0^{t_{\text{fin}}} dt_1 \sum_l |V_{0l}|^2 \frac{\left(\Delta E_l^{(1)} \right)^2}{\Delta E_l^2} e^{i \int_{t_1}^{t_{\text{fin}}} dt' \delta e_l(t')} \delta e_l(t_1) \\
 &\quad \times \left(i \frac{e^{i\tau\Delta E_l} - e^{it\Delta E_l}}{\Delta E_l} - e^{it\Delta E_l} (t - \tau) \right) + \text{c.c.} . \quad (\text{III.56})
 \end{aligned}$$

Every term has a factor $e^{it\Delta E_l}$ or $e^{i\tau\Delta E_l}$. Thus, the limit $\tau \rightarrow \infty$ ($t > \tau$) gives $\Delta\sigma^{\text{pm},(2)}(t, \tau) \rightarrow 0$. Next, we evaluate equation (III.56) within our particular Hubbard model,

$$\begin{aligned}
 \Delta\sigma^{\text{pm},(2)}(t, \tau) &= \int_0^{t_{\text{fin}}} dt_1 \sin(A(t_1)) B_{03}(t - \tau, \tau_1, \tau_2) - 2 \sin^2 \left(\frac{A(t_1)}{2} \right) B_{12}(t - \tau, \tau_1, \tau_2) , \\
 B_{n_1 n_2}(\Delta t, \tau_1, \tau_2) &= B_{n_2}^{(2)}(\tau_2) \left(\Delta t B_{n_1+1}^{(1)}(\tau_1) - B_{n_1}^{(1)}(\tau_1) + B_{n_1}^{(1)}(\tau_1 - \Delta t) \right) , \\
 B_n^{(1)}(x) &= \int_{\frac{1}{4}}^1 db \frac{a_4(b)}{\sqrt{\pi^3 b}} \left(\frac{\partial}{\partial x} \right)^n e^{-\frac{x^2}{4b}} , \quad B_n^{(2)}(y) = \left(\frac{\partial}{\partial y} \right)^n e^{-y^2} , \\
 \tau_1 &= t - t_{\text{fin}} + \int_{t_1}^{t_{\text{fin}}} d\tau \cos(A(\tau)) \quad \text{and} \quad \tau_2 = \int_{t_1}^{t_{\text{fin}}} d\tau \sin(A(\tau)) .
 \end{aligned}$$

Examples with fixed t are depicted in figure 61. The response is strongest directly after the pulse ($\tau = 10$) followed by a rapid decay. In our particular Hubbard model,

III PRETHERMALIZATION INDUCED BY WEAK INTERACTIONS

the terms vanish as a Gaussian function $\sim e^{-\tau^2/4}$. The pump-field strength E scales $\Delta\sigma^{\text{pm},(2)}(t, \tau)$ almost quadratically in the left plot of figure 61. Only, the line with $E = 2$ does not follow the scaling law strictly.

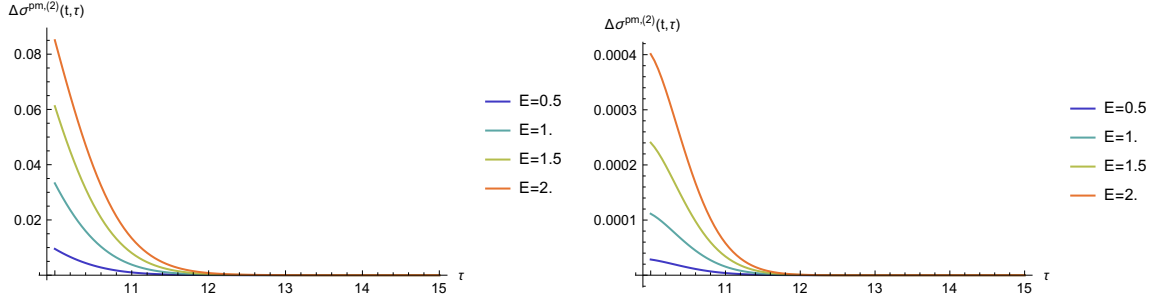


Figure 61: Change in paramagnetic conductivity after “simple” (left) or “realistic” (right) pump pulse with $T = 2$, $m = 5$, $t = 15$ and $\tau > Tm$

The term linear in $A(t)$ has a factor $(\Delta E_l^{(1)})^3$ in equation (III.56). Therefore, it is expected to vanish for initial states with zero global momentum. The expansion in pump-field strength gives in our model,

$$\begin{aligned} \Delta\sigma^{\text{pm},(2)}(t, \tau) = & \int_0^{t_{\text{fin}}} dt_1 \int_0^{t_1} dt_2 A(t_2)A(t_1)B_{04}(t - \tau, t - t_2, 0) \\ & - \int_0^{t_{\text{fin}}} dt_2 \frac{A(t_2)^2}{2} B_{12}(t - \tau, t - t_2, 0) + O(A^3) . \end{aligned} \quad (\text{III.57})$$

It is computed as a convolution of $B_{04}(t - \tau, t, 0)$ or $B_{12}(t - \tau, t, 0)$ with the pump field. These two functions are depicted in figure 62 and they converge to a universal line for relative short times ($t > 4$), which is computed as the long-time limit,

$$\lim_{t \rightarrow \infty} B_{n_1 n_2}(t - \tau, t, \tau_2) = B_{n_2}^{(2)}(\tau_2) B_{n_1}^{(1)}(\tau) .$$

The probe pulse acts during times τ and the functions $B_{n_1 n_2}(t - \tau, t, \tau_2)$ nearly decay to zero for $\tau > 4$. We conclude that if the time-delay between the pump and probe pulse is greater than 4, then the paramagnetic conductivity is unchanged in our model, $\Delta\sigma^{\text{pm},(2)} \rightarrow 0$. This tells us that a probe pulse shortly after the pump pulse has a pump-probe effect on the paramagnetic conductivity. A probe pulse long after the pump

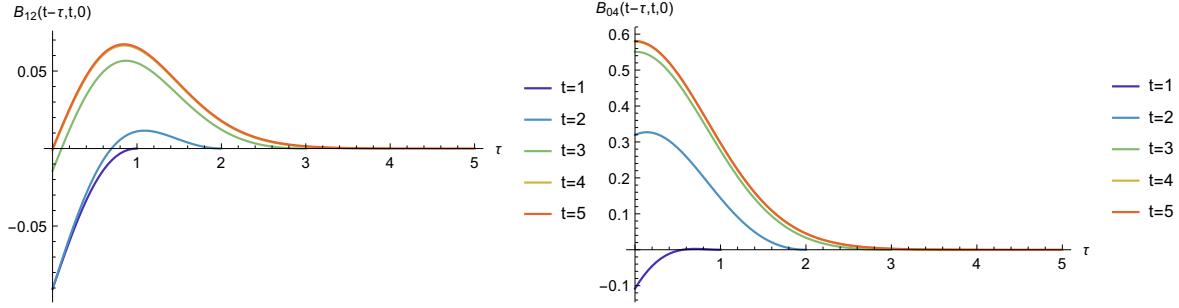


Figure 62: $O(A^2)$ contribution to the pump-probe paramagnetic conductivity

pulse has no effect in our model. The diamagnetic conductivity is proportional to the kinetic energy in our model. The kinetic energy relaxes to a plateau value, and thus the pump-probe conductivity relaxes to a plateau as well.

These results have the following consequences for the observation of the prethermal state. Typically, a measuring protocol would have three steps. First, the pump excites the system. Second, the system relaxes to the prethermal steady state. Finally, the probe pulse detects the nonthermal steady state. The kinetic energy is constant under quasi-particle scattering from the Boltzmann equation,^{45–47} which thermalizes the occupation numbers at a later stage. Therefore, the prethermal plateau value of the kinetic energy is equal to its equilibrium value after the pump pulse. This means that the conductivity is identical for the steady prethermal state and the thermal state. Therefore, the probe pulse would only detect the heating in our setup and does not resolve the nonthermal state.

In our protocol, the pump and the probe pulse have identical directions. To detect the prethermal state, we propose to pump and probe from different directions. If this shows no indication of the prethermal state, we suggest replacing the probe pulse with a momentum-resolved measuring technique. Improving our computational technique to include at least $O(g^4)$ terms could further resolve this. The thermal and the prethermal state have different momentum distributions in $O(g^2)$, which should give a deviation in the paramagnetic conductivity $O(g^4)$. In the next subsection, we encounter a resonance frequency at which the prethermal plateau is amplified. It would be worthwhile to calculate the conductivity for this amplified prethermal state and compare it to the conductivity in the thermal state.

i) Scaled prethermal plateau

At the end of subsection f), we observed that the energy absorption is proportional to the pulse duration and quadratic in field strength. Here, the proportionality factor is the real part of the conductivity.¹⁰⁷ First, we deduce this scaling behavior within a real-time framework and apply the analogous steps to the occupation numbers. This predicts a similar scaling behavior for the change in the distribution function as for the system's heating. Finally, we will give the model-independent proportionality factor in equation (III.60) and compute it in our perturbative method. Furthermore, it is straightforward to substitute the internal field with the applied external field to obtain the experimentally relevant response.

The linear response does not affect the long-time limit. Therefore, we neglect terms with a single time convolution. As we expand in the field, the second-order term is thus the most important one. The energy absorption of the system is computed as

$$\begin{aligned} \delta\hat{H}_0(t) &= -\frac{ea}{\hbar c}A(t)\hat{H}_0^{(1)} + O(A^2) , \\ \Delta\langle\hat{H}\rangle_t &= \frac{-1}{c^2} \int_{t_{\text{ini}}}^t dt_1 \int_{t_{\text{ini}}}^{t_1} dt_2 A(t_1)A(t_2) \underbrace{\frac{e^2 a^2}{\hbar^2} \langle [(\hat{H}_0^{(1)})_H(t_2), [(\hat{H}_0^{(1)})_H(t_1), \hat{H}]] \rangle_{t_{\text{ini}}}}_{= \frac{\partial^2 \sigma^{\text{pm}}(\tau)}{\partial \tau^2} \Big|_{\tau=t_1-t_2}} + O(A^3) . \end{aligned}$$

The expectation value is connected to paramagnetic conductivity. We apply the Fourier transformation and the pulse shall end at t_{fin} ,

$$\Delta\langle\hat{H}\rangle_{t>t_{\text{fin}}} = \int d\omega \frac{\omega^2 \Re\{\sigma^{\text{pm}}(\omega)\}}{c^2 \pi} \int_{t_{\text{ini}}}^{t_{\text{fin}}} dt_1 \int_{t_{\text{ini}}}^{t_1} dt_2 A(t_1)A(t_2) e^{i(t_1-t_2)(\omega+i\delta)} + O(A^3) ,$$

We assume that the electric field can be written as a superposition of sine and cosine functions,

$$E(t) = E(t)^* = \sum_j E_j e^{it\omega_j} \Rightarrow A(t) = A(t)^* = -c \sum_j \frac{E_j}{i\omega_j} e^{it\omega_j} , \quad (\text{III.58})$$

and compute the time integrals,

$$\frac{1}{c^2} \int_{t_{\text{ini}}}^{t_{\text{fin}}} dt_1 \int_{t_{\text{ini}}}^{t_1} dt_2 A(t_1)A(t_2) e^{i(t_1-t_2)(\omega+i\delta)} = \sum_j \frac{|E_j|^2}{\omega_j^2} \frac{i(t_{\text{fin}} - t_{\text{ini}})}{\omega + i\delta - \omega_j} + O((t_{\text{fin}} - t_{\text{ini}})^0) .$$

This gives one term which is proportional to the pulse duration and has a delta contribution, $(\omega + i\delta - \omega_j)^{-1} \rightarrow -i\pi\delta(\omega - \omega_j)$. The scaled long-time limit is

$$\lim_{t_{\text{fin}} \rightarrow \infty} \frac{\Delta \langle \hat{H} \rangle_{t > t_{\text{fin}}}}{t_{\text{fin}}} = \sum_j |E_j|^2 \Re\{\sigma^{\text{pm}}(\omega_j)\} + O(E^3). \quad (\text{III.59})$$

This a very general statement, and we apply it to our two classes of pulses,

$$\text{“simple”}: E_1(t) = E \sin\left(\frac{2\pi t}{T}\right) \Rightarrow E_j = \frac{\pm iE}{2}, \quad \omega_j = \pm \frac{2\pi}{T},$$

$$\text{“realistic”}: E_2(t) = E \sin\left(\frac{2\pi t}{T}\right) \sin\left(\frac{\pi t}{mT}\right) \Rightarrow E_j = \frac{\pm E}{4}, \quad \omega_j = \pm \frac{\pi(2m \pm 1)}{Tm}.$$

At the end of subsection f), we found scaled universal functions in figure 57. They are obtained by the limit $m \rightarrow \infty$ and the conductivity from equation (III.53),

$$\begin{aligned} \text{“simple”}: \quad \lim_{m \rightarrow \infty} \frac{\Delta \langle \hat{H}_0 \rangle_{t > Tm}}{Tm} &= \frac{E^2}{2} \Re\{\sigma^{\text{pm},(2)}(\omega)\}_{\omega = \frac{2\pi}{T}} + O(E^3), \\ \text{“realistic”}: \quad \lim_{m \rightarrow \infty} \frac{\Delta \langle \hat{H}_0 \rangle_{t > Tm}}{Tm} &= \frac{E^2}{4} \Re\{\sigma^{\text{pm},(2)}(\omega)\}_{\omega = \frac{2\pi}{T}} + O(E^3). \end{aligned}$$

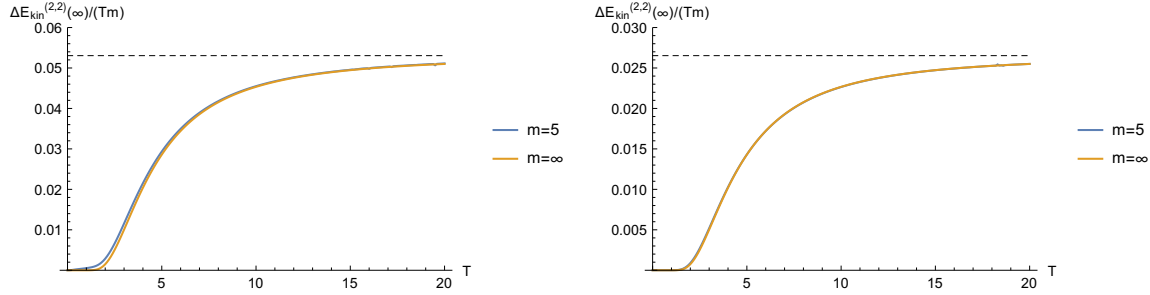


Figure 63: Plateau value of kinetic energy scaled by pulse duration Tm for “simple” (left) and “realistic” (right) pulse shape

The absorbed energy differs for our two different pulses by a factor of two, which is congruent to our finite pulses in figure 63. We expect that the prefactor for other pulse shapes is computed from the mean quadratic amplitude. It is established that the absorbed energy during one period of a monochromatic electromagnetic field is

III PRETHERMALIZATION INDUCED BY WEAK INTERACTIONS

proportional to the real part of the conductivity.¹⁰⁷ This is in congruence with our result in equation (III.59) as the diamagnetic conductivity is entirely imaginary.

We plotted the real part of the conductivity in figure 58 for our Hubbard model, which scales by U^2 . Next, we replace $E^2 \rightarrow E_{\text{ext}}^2/|\epsilon(\omega)|^2$ and compute the absorbed energy from the external field. Our results are displayed in figure 64, and the resonance peak increases for weaker interactions, which is a major difference to interaction drives. The heating rate for weak interaction drives scales with U^2 as discussed in subsection 3.f). We thus suggest photopumping a weakly interacting system at this resonance frequency. The absorbed energy indicates a highly nonthermal state. The interparticle scattering rate decreases with interaction strength, which we will discuss in subsection 6.a). The slow thermalization rate should stabilize the nonthermal state, and we expect a long-lived prethermal state.

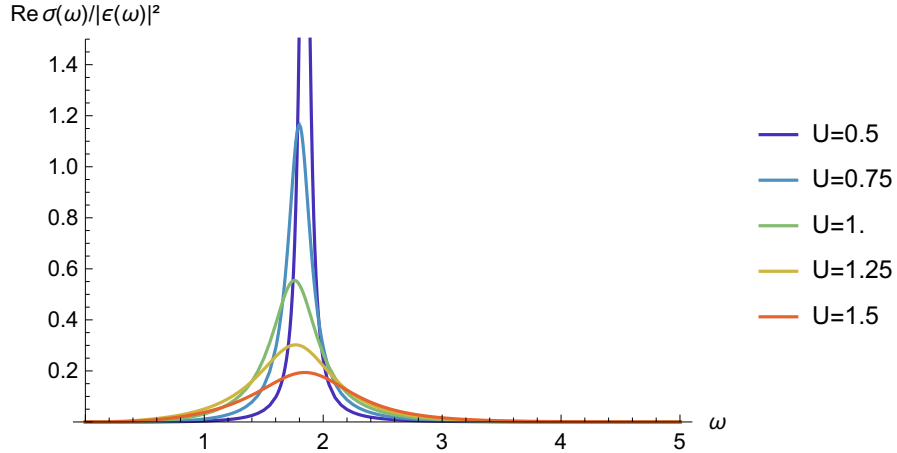


Figure 64: Energy absorption factor with respect to the external field

We apply the analogous steps to the momentum distribution to capture the features of the prethermal state. We neglect the single time convolutions, and the dominating term in the long-time limit is

$$\begin{aligned} \Delta \langle \hat{n}_{\sigma \mathbf{k}} \rangle_t &= \frac{-1}{c^2} \int_{t_{\text{ini}}}^t dt_1 \int_{t_{\text{ini}}}^{t_1} dt_2 A(t_1) A(t_2) \\ &\quad \times \frac{e^2 a^2}{\hbar^2} \langle \left[\left(\hat{H}_0^{(1)} \right)_H (t_2), \left[\left(\hat{H}_0^{(1)} \right)_H (t_1), (\hat{n}_{\sigma \mathbf{k}})_H (t) \right] \right] \rangle_{t_{\text{ini}}} + O(A^3) . \end{aligned}$$

We assume that the long-time limit of the Heisenberg operator is diagonal in the eigenbasis of \hat{H} , thus it commutes with the Hamiltonian,

$$\lim_{t \rightarrow \infty} (\hat{n}_{\sigma \mathbf{k}})_H(t) = \sum_m |\Psi_m\rangle\langle\Psi_m| \hat{n}_{\sigma \mathbf{k}} |\Psi_m\rangle\langle\Psi_m| \Rightarrow \left[\lim_{t \rightarrow \infty} (\hat{n}_{\sigma \mathbf{k}})_H(t), \hat{H} \right] = 0 .$$

Furthermore, the initial state is an eigenstate of \hat{H} and the expectation value's time-dependence simplifies to depend on the time difference $t_1 - t_2$,

$$\begin{aligned} \langle \left[\left(\hat{H}_0^{(1)} \right)_H(t_2), \left[\left(\hat{H}_0^{(1)} \right)_H(t_1), (\hat{n}_{\sigma \mathbf{k}})_H(t \rightarrow \infty) \right] \right] \rangle_{t_{\text{ini}}} \\ = \langle \left[\hat{H}_0^{(1)}, \left[\left(\hat{H}_0^{(1)} \right)_H(t_1 - t_2), (\hat{n}_{\sigma \mathbf{k}})_H(t \rightarrow \infty) \right] \right] \rangle_{t_{\text{ini}}} . \end{aligned}$$

Now, we apply the analogous steps and obtain for the distribution function,

$$\begin{aligned} \lim_{t_{\text{fin}} \rightarrow \infty} \frac{\Delta \langle \hat{n}_{\sigma \mathbf{k}} \rangle_{t > t_{\text{fin}}}}{t_{\text{fin}}} &= \sum_j \pi |E_j|^2 \frac{\tilde{n}_{\sigma \mathbf{k}}(\omega_j)}{\omega_j^2} + O(E^3) , \quad (\text{III.60}) \\ \tilde{n}_{\sigma \mathbf{k}}(\omega) &= -\frac{e^2 a^2}{\hbar^2} \int_{-\infty}^{\infty} \frac{d\tau}{2\pi} e^{-i\tau\omega} \langle \left[\hat{H}_0^{(1)}, \left[\left(\hat{H}_0^{(1)} \right)_H(\tau), (\hat{n}_{\sigma \mathbf{k}})_H(t \rightarrow \infty) \right] \right] \rangle_{t_{\text{ini}}} . \end{aligned}$$

As this term scales linear in pulse duration, the predicted ensemble is nonthermal. Equations (III.59) and (III.60) are general and not restricted to a specific model. The next goal is to compute this prethermal plateau prediction within second-order perturbation theory. We apply the expansion on the first,

$$\langle \left[\left(\hat{H}_0^{(1)} \right)_H(t_2), \dots \right] \rangle_{t_{\text{ini}}} = ig \int_{-\infty}^{t_2} d\tau_2 f(\tau_2) \langle \left[\left[\hat{V}_I(\tau_2), \hat{H}_0^{(1)} \right], \dots \right] \rangle_0 + O(g^2) ,$$

and second part of the expectation value,

$$\begin{aligned} &\left[\left(\hat{H}_0^{(1)} \right)_H(t_1), (\hat{n}_{\sigma \mathbf{k}})_H(t) \right] \\ &= ig \int_{-\infty}^{t_1} d\tau_1 f(\tau_1) \underbrace{\left[\left[\hat{V}_I(\tau_1), \hat{H}_0^{(1)} \right], \hat{n}_{\sigma \mathbf{k}} \right]}_{=-\left[\hat{H}_0^{(1)}, \left[\hat{V}_I(\tau_1), \hat{n}_{\sigma \mathbf{k}} \right] \right]} + ig \int_{-\infty}^t d\tau f(\tau) \left[\hat{H}_0^{(1)}, \left[\hat{V}_I(\tau), \hat{n}_{\sigma \mathbf{k}} \right] \right] + O(g^2) \\ &= ig \int_{t_1}^t d\tau \left[\hat{H}_0^{(1)}, \left[\hat{V}_I(\tau), \hat{n}_{\sigma \mathbf{k}} \right] \right] + O(g^2) . \end{aligned}$$

III PRETHERMALIZATION INDUCED BY WEAK INTERACTIONS

We insert the eigenstates of \hat{H}_0 to compute the expectation value,

$$\begin{aligned}
& \langle \left[\left[\hat{V}_I(\tau_2), \hat{H}_0^{(1)} \right], \left[\hat{H}_0^{(1)}, \left[\hat{V}_I(\tau), \hat{n}_{\sigma\mathbf{k}} \right] \right] \right] \rangle_0 \\
&= \langle \left[\left[\hat{V}, \hat{H}_0^{(1)} \right], \left[\hat{H}_0^{(1)}, \left[\hat{V}_I(\tau - \tau_2), \hat{n}_{\sigma\mathbf{k}} \right] \right] \right] \rangle_0 \\
&= \langle \left[\left[\hat{V}, \left(\hat{H}_0^{(1)} - \langle \hat{H}_0^{(1)} \rangle_0 \right) \right], \left[\left(\hat{H}_0^{(1)} - \langle \hat{H}_0^{(1)} \rangle_0 \right), \left[\hat{V}_I(\tau - \tau_2), (\hat{n}_{\sigma\mathbf{k}} - \langle \hat{n}_{\sigma\mathbf{k}} \rangle_0) \right] \right] \right] \rangle_0 \\
&= -\langle \hat{V} \left(\hat{H}_0^{(1)} - \langle \hat{H}_0^{(1)} \rangle_0 \right) \left(\hat{H}_0^{(1)} - \langle \hat{H}_0^{(1)} \rangle_0 \right) (\hat{n}_{\sigma\mathbf{k}} - \langle \hat{n}_{\sigma\mathbf{k}} \rangle_0) \hat{V}_I(\tau - \tau_2) \rangle_0 + \text{c.c.} \\
&= -\sum_m e^{i(\tau - \tau_2)\Delta E_m} |V_{0m}|^2 (\Delta E_m^{(1)})^2 \Delta n_{\sigma\mathbf{k},m} + \text{c.c.} .
\end{aligned}$$

Now, we evaluate the time-integration and the term with $e^{it\Delta E_m}$ vanishes in the long-time limit as the energies ΔE_m are generally continuously distributed,

$$\int_{t_1}^t d\tau \int_{-\infty}^{t_2} d\tau_2 f(\tau_2) e^{i(\tau - \tau_2)\Delta E_m} = \underbrace{\frac{e^{i(t-t_2)\Delta E_m}}{\Delta E_m^2}}_{\xrightarrow{t \rightarrow \infty} 0} - \frac{e^{i(t_1-t_2)\Delta E_m}}{\Delta E_m^2} .$$

The model-independent perturbative result is

$$\begin{aligned}
\tilde{n}_{\sigma\mathbf{k}}(\omega) &= g^2 \tilde{n}_{\sigma\mathbf{k}}^{(2)}(\omega) + O(g^3) , \\
\tilde{n}_{\sigma\mathbf{k}}^{(2)}(\omega) &= \frac{e^2 a^2}{\hbar^2} \int_{-\infty}^{\infty} \frac{d\tau}{2\pi} e^{-i\tau\omega} \left(\sum_m \frac{e^{i\tau\Delta E_m}}{\Delta E_m^2} |V_{0m}|^2 (\Delta E_m^{(1)})^2 \Delta n_{\sigma\mathbf{k},m} + \text{c.c.} \right) \\
&= \frac{e^2 a^2}{\hbar^2} \sum_m \delta(\Delta E_m \pm \omega) |V_{0m}|^2 \frac{(\Delta E_m^{(1)})^2 \Delta n_{\sigma\mathbf{k},m}}{\Delta E_m^2} .
\end{aligned}$$

We insert our particular Hubbard model, and the sum over all eigenstates gives ($\epsilon_{\mathbf{k}} \geq 0$)

$$\begin{aligned}
\sum_m e^{i\tau_1 \Delta E_m + i\tau_2 \Delta \bar{E}_m} |D_{0m}|^2 \frac{\Delta n_{\sigma\mathbf{k},m}}{\Delta E_m^2} &\stackrel{d \rightarrow \infty}{=} \left(\frac{\partial}{\partial i\tau_1} \right)^{-2} e^{i\tau_1 \epsilon_{\mathbf{k}} + i\tau_2 \bar{\epsilon}_{\mathbf{k}}} F(\tau_1, \tau_2)^3 \\
&\stackrel{\text{(III.46)}}{=} e^{i\tau_2 \bar{\epsilon}_{\mathbf{k}} - \frac{3\tau_2^2}{4}} \int_{\frac{1}{3}}^1 db a_3(b) \int_{\epsilon_{\mathbf{k}}}^{\infty} d\epsilon_0 \left(1 - \frac{\epsilon_{\mathbf{k}}}{\epsilon_0} \right)^2 \frac{e^{i\tau_1 \epsilon_0 - b\epsilon_0^2}}{\sqrt{\pi^3}} .
\end{aligned}$$

The main contribution to the plateau is given as ($\epsilon_{\mathbf{k}} \geq 0$)

$$\begin{aligned} \tilde{n}_{\sigma\mathbf{k}}^{(2)}(\omega) &= \left(\frac{3}{2} + \bar{\epsilon}_{\mathbf{k}}^2\right) \int_{\frac{1}{3}}^1 db a_3(b) \int_{\epsilon_{\mathbf{k}}}^{\infty} d\epsilon_0 \left(1 - \frac{\epsilon_{\mathbf{k}}}{\epsilon_0}\right)^2 \frac{e^{-b\epsilon_0^2}}{\sqrt{\pi^3}} \int_{-\infty}^{\infty} \frac{d\tau}{2\pi} e^{i\tau(\epsilon_0 - \omega)} + e^{i\tau(-\epsilon_0 - \omega)} \\ &= \Theta(|\omega| - \epsilon_{\mathbf{k}}) \left(\frac{3}{2} + \bar{\epsilon}_{\mathbf{k}}^2\right) \int_{\frac{1}{3}}^1 db a_3(b) \left(1 - \frac{\epsilon_{\mathbf{k}}}{|\omega|}\right)^2 \frac{e^{-b\omega^2}}{\sqrt{\pi^3}}. \end{aligned} \quad (\text{III.61})$$

This result applied to for the enveloped pulse. Equation (III.58) has an unexpected $\omega_j = 0$ contribution for the “simple” pulse and we need to take the $\omega_j = 0$ term into account as well

$$\text{“simple”}: \quad E_1(t) = E \sin\left(\frac{2\pi t}{T}\right) \Rightarrow A_1(t) = \left(\cos\left(\frac{2\pi t}{ET}\right) - 1\right) \frac{T}{2\pi} \neq -\sum_j \frac{E_j}{i\omega_j} e^{it\omega_j}$$

$$\lim_{m \rightarrow \infty} \frac{\Delta \langle \hat{n}_{\sigma\mathbf{k}} \rangle_{t > Tm}}{Tm} = \pi E^2 \frac{\tilde{n}_{\sigma\mathbf{k}}(\omega) + 2\tilde{n}_{\sigma\mathbf{k}}(0)}{2\omega^2} \Big|_{\omega = \frac{2\pi}{T}} + O(E^3)$$

$$\text{“realistic”}: \quad E_2(t) = E \sin\left(\frac{2\pi t}{T}\right) \sin\left(\frac{\pi t}{mT}\right) \Rightarrow A_2(t) = -\sum_j \frac{E_j}{i\omega_j} e^{it\omega_j}$$

$$\lim_{m \rightarrow \infty} \frac{\Delta \langle \hat{n}_{\sigma\mathbf{k}} \rangle_{t > Tm}}{Tm} = \frac{\pi E^2 \tilde{n}_{\sigma\mathbf{k}}(\omega)}{4\omega^2} \Big|_{\omega = \frac{2\pi}{T}} + O(E^3)$$

We observe a fast convergence to the long-pulse limit in figure 65 except in the high-

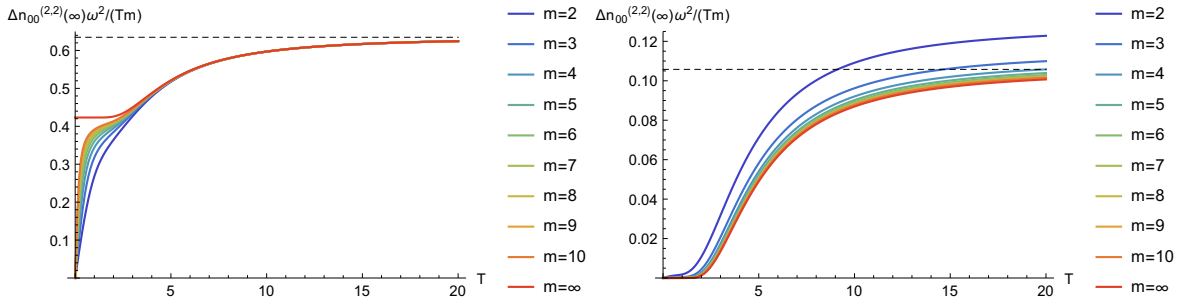


Figure 65: Plateau value of the occupation number with $\epsilon_{\mathbf{k}} = \bar{\epsilon}_{\mathbf{k}} = 0$ scaled by $\frac{\omega^2}{Tm}$ for “simple” (left) and “realistic” (right) pulse shape

frequency regime for the “simple” pulse shape. Therefore, the long-pulse limit is a valid

III PRETHERMALIZATION INDUCED BY WEAK INTERACTIONS

approximation for relatively brief pulses ($m \geq 5$). In the low-frequency regime, the functions relax to a constant value marked by a dotted line for $m = \infty$.

We are interested in prethermal state induced by an external electric field. The $\tilde{n}_{\sigma\mathbf{k}}(0)$ contribution for the “simple” pulse shape is therefore not relevant. Hence, we replace the internal with the external field ($E^2 \rightarrow E_{\text{ext}}^2/|\epsilon(\omega)|^2$),

$$\lim_{m \rightarrow \infty} \frac{\Delta \langle \hat{n}_{\sigma\mathbf{k}} \rangle_{t > Tm}}{Tm} \stackrel{\text{(III.54)}}{=} \frac{\pi s E_{\text{ext}}^2 \tilde{n}_{\sigma\mathbf{k}}(\omega)}{|\omega + 4\pi i \sigma(\omega)|^2} + O(E_{\text{ext}}^3). \quad (\text{III.62})$$

For the “realistic” pulse, the pulse-shape factor s is $1/4$ and would be different (but of $O(1)$) for other realistic pulse shapes. Equation (III.62) is one of our main results. It predicts a nonthermal distribution function if the thermalization rate is sufficiently slow. The perturbative results for our Hubbard model are displayed in figure 66. The right-side plot illustrates the scaling caused by the weak interactions U , which is independent of the momentum. It has the resonance peak at frequency $\omega \approx 1.88$, which increases and sharpens for weaker interactions. The left plot shows the \mathbf{k} -dependent term from equation (III.61), which is independent of the interaction strength. The excitations closer to the Fermi surface are more intense and vanish for $|\epsilon_{\mathbf{k}} - \epsilon_{\text{F}}| \geq \omega$. Occupations numbers with finite $\bar{\epsilon}_{\mathbf{k}}$ have an additional factor $(1 + \frac{2}{3}\bar{\epsilon}_{\mathbf{k}}^2)$, thus the states with \mathbf{k} along the field are amplified, $|\mathbf{k} \cdot \mathbf{e}_A|^2 \sim \bar{\epsilon}_{\mathbf{k}}^2$. In a thermal ensemble, the excitations should be independent of $\bar{\epsilon}_{\mathbf{k}}$. This highlights the nonthermal character of this distribution function.

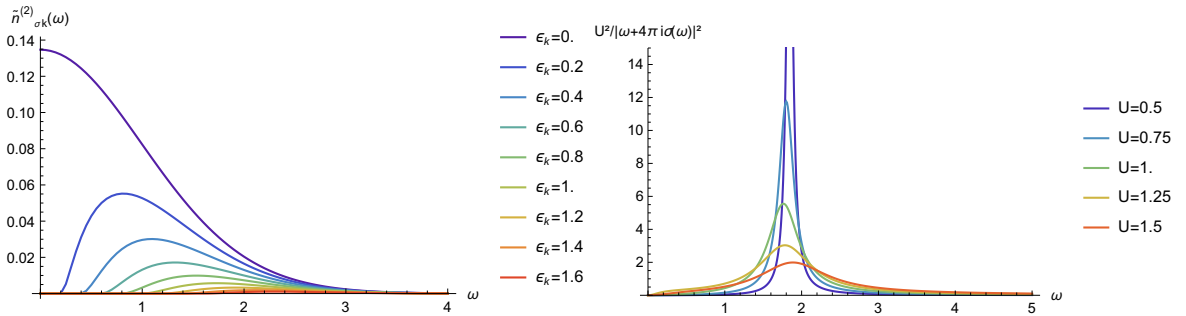


Figure 66: $\tilde{n}_{\sigma\mathbf{k}}^{(2)}(\omega)$ from equation (III.61) for $\bar{\epsilon}_{\mathbf{k}} = 0$ (left) gives multiplied with the scaling term (right) the prethermal plateau with respect to the external field

In this subsection, we learned that most details of the pump-pulse have a minor effect on the prethermal state. We suggest to computed the momentum distribution of the

prethermal state by equations (III.60) or (III.62) as it captures the major terms. Its numerical evaluation is easier than the real-time computations performed in subsection e) and f). The driving frequency enters in a nontrivial fashion, and the field strength squared times pulse duration scales the excitations. The pulse shape gives a shape factor of order unity. The interaction strength expansion factorises the problem into a \mathbf{k} -dependent term and an g -dependent term, e.g., results depicted in figure 66. The resonance presents an opportunity to create a highly nonthermal state in a weakly interacting system. Driving at the resonance frequency generates a pronounced nonthermal ensemble according to equation (III.62). The thermalization rate is slowed down for sufficiently small interactions, as discussed in outlook subsection 6.a). Therefore, we propose to photopump at resonance frequency to generate a nonthermal distribution function, which will be stabilized for sufficiently small interactions.

5 Summary for weakly interacting systems

Let us summarize the main insights from this chapter. First, the Dirac representation gives directly the formal series expansion in interaction strength g . It can be applied to any time-dependent expectation value for any nonequilibrium protocol. For the interaction quench and the mode occupation numbers, it reproduces the established expressions^{73,80,85} for the prethermalization plateau. Furthermore, we can study initially interacting states if we prepend an adiabatic switching to the Hamiltonian. One main result of this dissertation are the generalized prethermalization formulas in equations (III.5) and (III.7).

We define the prethermalization regime as the time scale where the leading order expansion gives an accurate result. The deviation increases with interaction strength g and time t . Hence, the perturbative expansion is only applicable within a certain time window, even for weakly interacting systems. The perturbative terms relax to a constant value called prethermalization plateau for general systems and processes.

The Boltzmann equation^{45–47} governs the thermalization on a larger times scale. We discuss it in the subsection 6.a) below. The dynamics can be approximated by a two-step process for weakly interacting systems. First, one computes occupation numbers in the prethermalization regime and then inserts them into the Boltzmann equation (III.67). This leads to a relaxation to a Fermi distribution determined by the kinetic energy, which is a constant of motion in the Boltzmann dynamics. Hence, the kinetic energy in the prethermal steady state determines the eventual thermal distribution.

We assign the observables into two classes, whether the $O(g)$ term in the perturbative expansion vanishes or not. The observables with finite $O(g)$ are called “first-order” observables by us. The other ones are called “second-order” observables as $O(g^2)$ is the leading order.

The prethermalization dynamics of first-order observables are qualitatively equal for initially interacting and noninteracting states. Thus, the change in interaction strength has the strongest the impact. Furthermore, the plateau is independent of the explicit nonequilibrium protocol and relates to perturbative terms in equilibrium. Therefore, it is very likely to encounter crossing points for fixed final and varying initial interaction strength. These crossing points are expected in most first-order observables, but the crossing time depends on the chosen observable and protocol. If the interaction is treated nonperturbatively, then the crossing point distributes into a region. The region

becomes sharper for weaker interactions and for shorter crossing times.

Second-order observables exhibit new features. First, the prethermalization dynamics are computed by the summation of two terms. The dynamics concerning the noninteracting state plus a second “mixing”-term for initially interacting states. This “mixing”-term behaves similar to a first-order observable. Regarding the noninteracting state, the term relaxes to a plateau value,^{73,80,84} grows logarithmic for low dimensional systems^{82,83} or linearly for driven systems.⁸⁹

Constants of motion for an interacting Hamiltonian are generated from the constants of the free Hamiltonian, which we obtain by adiabatic transformations. The perturbative evaluation is done by applying the series expansion in interaction strength. The prethermalization plateaus after a nonequilibrium process are described by the generalized Gibbs ensemble (GGE) constructed from these constants of motion. This was previously established for the quench,⁸⁵ and we generalized it to arbitrary nonequilibrium protocols in subsection 2.c).

As an application, we considered the Hubbard model in infinite dimensions at half-filling, as it is a generic and computational feasible system. For nonequilibrium protocols with time-dependent interaction, only the density of states (d.o.s.) enters the computational scheme. Our method computes efficiently for quenches,^{73,80,85} ramps,⁸⁴ and periodically driven systems.⁸⁹ It has access to all times within the prethermal regime and can handle initially interacting states. The dynamics are similar for initially interacting states as for uncorrelated states. Furthermore, we derive the equations of motion in a more direct fashion and reproduce previous results.

The occupation probabilities behave similarly for various ramps and d.o.s.. Occupied states decrease, and initially unoccupied states increase during the ramp or quench. Then, they relax with damped oscillations to their prethermalization plateau. For different d.o.s. and observables, we find different relaxation laws. Generally, they decay with t^{-3} or faster, as determined by the d.o.s. at the band edges. The quench plateau value of the occupation numbers is twice the adiabatic value.^{73,80,85} Finite ramps connect these two limits.⁸⁴ States towards the band edges converge faster to the adiabatic limit than states near the Fermi surface. Our calculations indicate that increasing ramping time is the only available tool to prevent heating, while ramping more smoothly does not.

We observe two different regimes in a periodically driven system,⁸⁹ determined by the relation of the driving frequency to the bandwidth. The system relaxes to a prether-

III PRETHERMALIZATION INDUCED BY WEAK INTERACTIONS

malization plateau with steady oscillations for fast driving. The observables increase linearly, and no relaxation is predicted for slow driving. The critical driving frequency is not affected by initial interactions. At a certain time, the linear growing observables reach unphysical values. Our approximation breaks down at this point and marks the definite end of the prethermalization regime.

In the last section, we computed the expectation values for the Hubbard model hit by a homogeneous field pulse. Our electric field pulse scenario established several new features. In some cases, the current relaxes to a finite plateau value. When we apply an enveloping function to the pulse or linearize in field strength, the plateau vanishes. The occupation numbers relax to steady nonthermal values. We evaluate the linear and pump-probe response functions. If the delay between pump and probe pulse is short ($\Delta t \approx W^{-1}$), then the probe response function is affected nontrivially by the pump pulse. If the delay time is large ($\Delta t \gg W^{-1}$), then the diamagnetic conductivity is changed due to the increased kinetic energy. In this setup, the measured conductivity of the prethermal and thermalized states are identical. Including the higher-order terms should lead to a different paramagnetic conductivity for the thermal and prethermal states as both have different momentum distributions. Furthermore, we suggest pumping and probing from different directions to detect the prethermal steady state in the probe conductivity.

It is sufficient and more efficient to expand in the first few orders in electric field strength. It is necessary to include at least second-order terms to obtain a finite shift because linear response theory always predicts the return to the initial thermal value. Our expansion in electric field strength indicates that the plateau values of kinetic energy and occupation numbers scale linearly in duration and quadratic in field strength. The change in kinetic energy determines the heating of the system. In the high-frequency limit, the heating vanishes, and in the low-frequency limit, the heating becomes frequency independent. The current is essentially linear in the electric field and vanishes in the long-time limit. If we assume it as linear and set it equal to the classical current, Maxwell's equations relate the internal to the external electric field in frequency space. This enables us to compute the dominating contributions to the prethermal state for the external field. Electronic systems with weak interactions have a pronounced Drude peak, which provides an opportunity to drive into a highly excited state. The weak interparticle scattering slows down thermalization and increases the stability of the prethermal state. Our method should be extended to arbitrary d.o.s. and electric-field orientations. We expect the distinction into a high and low-frequency regime for a d.o.s. with finite bandwidth. As for periodically driven interactions,⁸⁹ we expect linear heating

5 SUMMARY FOR WEAKLY INTERACTING SYSTEMS

in the low-frequency regime and no linear heating in the high-frequency regime.

The prethermal and thermalization regime are described within the weak-correlations approximation, which we discuss below in subsection 6.a). This approximation was computed for the Hubbard model with infinite spatial dimensions⁷⁴ and a one-dimensional system.^{115,116} The kinetic equations simplify when formulated as local in time, as discussed in subsection 6.b).

6 Outlook: From prethermalization to thermalization

a) Derivation of the Boltzmann equation

As an outlook, we derive the Boltzmann equation for weakly interacting fermionic systems. The Boltzmann equation describes the dynamics after the prethermal regime as it thermalizes a nonthermal distribution function. We extract the thermalization time scale during the derivation. We use the method developed here, but follow the major steps found in previous work.^{45,46} It is possible to derive the Boltzmann equation within the DMFT framework, which gives proper results even for strongly interacting systems.¹¹⁷ In one dimension, the Boltzmann equation captures the long-time thermalization if there is a finite next-to-nearest neighbor hopping amplitude.¹¹⁸

We start the derivation with equation (III.4) and the particle occupation numbers are given in the interaction picture by

$$\begin{aligned}
 \langle \hat{n}_\nu \rangle_t &= \langle \hat{n}_\nu \rangle_{t_{\text{ini}}} + \sum_{n=2}^{\infty} (ig)^n \int_{t_{\text{ini}}}^t dt_1 \dots \int_{t_{\text{ini}}}^{t_{n-1}} dt_n \langle [\hat{H}_{1,I}(t_n), \dots [\hat{H}_{1,I}(t_1), \hat{n}_\nu] \dots] \rangle_{t_{\text{ini}}} \\
 &= \langle \hat{n}_\nu \rangle_{t_{\text{ini}}} - g^2 \int_{t_{\text{ini}}}^t dt_1 \int_{t_{\text{ini}}}^{t_1} dt_2 \sum_{n=0}^{\infty} (ig)^n \int_{t_{\text{ini}}}^{t_2} d\tau_1 \dots \int_{t_{\text{ini}}}^{\tau_{n-1}} d\tau_n \\
 &\quad \times \langle [\hat{H}_{1,I}(\tau_n), \dots [\hat{H}_{1,I}(\tau_1), [\hat{H}_{1,I}(t_2), [\hat{H}_{1,I}(t_1), \hat{n}_\nu]]]] \dots] \rangle_{t_{\text{ini}}} \\
 &= \langle \hat{n}_\nu \rangle_{t_{\text{ini}}} - g^2 \int_{t_{\text{ini}}}^t dt_1 \int_{t_{\text{ini}}}^{t_1} dt_2 \langle [\hat{H}_{1,I}(t_2), [\hat{H}_{1,I}(t_1), \hat{n}_\nu]] \rangle_{t_2} . \tag{III.63}
 \end{aligned}$$

If \hat{n}_ν commutes with the unperturbed Hamiltonian \hat{H}_0 and the initial state is an eigenstate of \hat{n}_ν and \hat{H}_0 , then the first-order term vanishes and equation (III.63) is applicable. Now, we assume that the expectation value on the right side is evaluated by an uncorrelated state, however all occupation numbers are computed self-consistently. Then, it becomes a function of all $\langle \hat{n}_\alpha \rangle_{t_2}$. We call this approximation weak-correlation approximation,

$$\langle [\hat{H}_{1,I}(t_2), [\hat{H}_{1,I}(t_1), \hat{n}_\nu]] \rangle_{t_2} \longrightarrow \langle [\hat{H}_{1,I}(t_2), [\hat{H}_{1,I}(t_1), \hat{n}_\nu]] \rangle_{t_{\text{ini}}} \Big|_{\langle \hat{n}_\alpha \rangle_{t_{\text{ini}}} \rightarrow \langle \hat{n}_\alpha \rangle_{t_2}} . \tag{III.64}$$

A strength of this approximation is that it includes arbitrary orders of interaction strength g and computes all single-particle observables self-consistently. A drawback is that a complicated Volterra integrodifferential equation must be solved

$$\frac{\partial \langle \hat{n}_\nu \rangle_t}{\partial t} = -g^2 \int_{t_{\text{ini}}}^t dt_2 \langle [\hat{H}_{1,I}(t_2), [\hat{H}_{1,I}(t), \hat{n}_\nu]] \rangle_{t_{\text{ini}}} \Big|_{\langle \hat{n}_\alpha \rangle_{t_{\text{ini}}} \rightarrow \langle \hat{n}_\alpha \rangle_{t_2}} . \quad (\text{III.65})$$

The numerical evaluation of (III.65) was done for the infinite-dimensional Hubbard model⁷⁴ and a one-dimensional model.^{115,116} To derive the Boltzmann equation, we take a few additional steps. First, the Hamiltonian stays constant after a certain point in time, which we set as time zero,

$$\hat{H}(t > 0) = \hat{H}_0 + \hat{V} .$$

Second, the time evolution up to time zero gives corrections of $O(g^2)$,

$$\frac{\partial \langle \hat{n}_\nu \rangle_t}{\partial t} = -g^2 \int_0^t dt_2 \langle [\hat{V}, [\hat{V}_I(t-t_2), \hat{n}_\nu]] \rangle_{t_{\text{ini}}} \Big|_{\langle \hat{n}_\alpha \rangle_{t_{\text{ini}}} \rightarrow \langle \hat{n}_\alpha \rangle_{t_2}} + O(g^2 t^0) .$$

The third step is to rescale the time to $\tau = tg^2$ and assume the existence of an analytic function $N_\nu(\tau) = \langle \hat{n}_\nu \rangle_{\frac{\tau}{g^2}}$ for small g ,

$$\frac{\partial N_\nu(\tau)}{\partial \tau} = - \int_0^{\frac{\tau}{g^2}} dt_2 \langle [\hat{V}, [\hat{V}_I(\frac{\tau}{g^2} - t_2), \hat{n}_\nu]] \rangle_{t_{\text{ini}}} \Big|_{\langle \hat{n}_\alpha \rangle_{t_{\text{ini}}} \rightarrow \langle \hat{n}_\alpha \rangle_{t_2}} + O(g^2) .$$

Next, we partially integrate,

$$\begin{aligned} & \int_0^{\frac{\tau}{g^2}} dt_2 \langle [\hat{V}, [\hat{V}_I(\frac{\tau}{g^2} - t_2), \hat{n}_\nu]] \rangle_{t_{\text{ini}}} \Big|_{\langle \hat{n}_\alpha \rangle_{t_{\text{ini}}} \rightarrow \langle \hat{n}_\alpha \rangle_{t_2}} \\ &= \int_0^{\frac{\tau}{g^2}} dt_2 \langle [\hat{V}, [\hat{V}_I(\frac{\tau}{g^2} - t_2), \hat{n}_\nu]] \rangle_{t_{\text{ini}}} \Big|_{\langle \hat{n}_\alpha \rangle_{t_{\text{ini}}} \rightarrow N_\alpha(\tau)} \\ & \quad - \underbrace{\int_0^{\frac{\tau}{g^2}} dt_1 \int_0^{t_1} dt_2 \frac{\partial}{\partial t_1} \langle [\hat{V}, [\hat{V}_I(\frac{\tau}{g^2} - t_2), \hat{n}_\nu]] \rangle_{t_{\text{ini}}} \Big|_{\langle \hat{n}_\alpha \rangle_{t_{\text{ini}}} \rightarrow \langle \hat{n}_\alpha \rangle_{t_1}}}_{=O(g^2)} . \end{aligned}$$

III PRETHERMALIZATION INDUCED BY WEAK INTERACTIONS

The second term is $O(g^2)$ because it is linear in the time derivative of the occupation numbers. The expectation value is real and thus it is symmetric in t_2 . We symmetrize the time integration t_2 and take the limit $g \rightarrow 0$,

$$\lim_{g \rightarrow 0} \frac{\partial N_\nu(\tau)}{\partial \tau} = -\frac{1}{2} \int_{-\infty}^{\infty} dt_2 \langle [\hat{V}, [\hat{V}_I(t_2), \hat{n}_\nu]] \rangle_{t_{\text{ini}}} \Big|_{\langle \hat{n}_\alpha \rangle_{t_{\text{ini}}} \rightarrow N_\alpha(\tau)} . \quad (\text{III.66})$$

Up to now, we have not specified a certain model. Thus, we can interpret equation (III.66) as a generalization of the Boltzmann equation. In this derivation, we copied the essential steps of previous work,^{45,46,74} but skipped the initial step of assuming a specific Hamiltonian. Equation (III.66) governs the dynamics on the time scale $t = \frac{\tau}{g^2}$. Even systems with infinitesimal small interactions g can thus exhibit dynamics beyond the hopping time scale.

The final step is to insert a free particle Hamiltonian for \hat{H}_0 and a two-particle interaction for \hat{V} ,

$$\hat{H}_0 = \sum_{\nu} \epsilon_{\nu} \hat{n}_{\nu} , \quad \hat{V} = \sum_{\alpha, \beta, \gamma, \delta} V_{\alpha\beta\gamma\delta} \hat{c}_{\alpha}^{\dagger} \hat{c}_{\beta}^{\dagger} \hat{c}_{\gamma} \hat{c}_{\delta} .$$

Then, the expectation value for an uncorrelated ensemble $\hat{\rho}_0$ is

$$\begin{aligned} \langle [\hat{V}, [\hat{V}_I(t), \hat{n}_\nu]] \rangle_0 &= \sum_{\beta\gamma\delta} |V_{\nu\beta\gamma\delta}|^2 \cos(t(\epsilon_{\nu} + \epsilon_{\beta} - \epsilon_{\gamma} - \epsilon_{\delta})) \\ &\quad \times \left(\langle \hat{n}_{\nu} \rangle_0 \langle \hat{n}_{\beta} \rangle_0 (1 - \langle \hat{n}_{\gamma} \rangle_0) (1 - \langle \hat{n}_{\delta} \rangle_0) \right. \\ &\quad \left. - \langle \hat{n}_{\gamma} \rangle_0 \langle \hat{n}_{\delta} \rangle_0 (1 - \langle \hat{n}_{\nu} \rangle_0) (1 - \langle \hat{n}_{\beta} \rangle_0) \right) . \end{aligned}$$

The step by step computation of the expectation value is done in subsection 3.b). The time integration in (III.66) transforms the cosine function into a delta function,

$$\begin{aligned} \lim_{g \rightarrow 0} \frac{\partial N_\nu(\tau)}{\partial \tau} &= -\pi \sum_{\beta, \gamma, \delta} |V_{\nu\beta\gamma\delta}|^2 \delta(\epsilon_{\nu} + \epsilon_{\beta} - \epsilon_{\gamma} - \epsilon_{\delta}) \\ &\quad \times \left(N_{\nu}(\tau) N_{\beta}(\tau) (1 - N_{\gamma}(\tau)) (1 - N_{\delta}(\tau)) \right. \\ &\quad \left. - N_{\gamma}(\tau) N_{\delta}(\tau) (1 - N_{\nu}(\tau)) (1 - N_{\beta}(\tau)) \right) \\ &= \pi J_{\hat{n}_{\nu}}(\epsilon = 0) \Big|_{\langle \hat{n}_\alpha \rangle_{t_{\text{ini}}} \rightarrow N_\alpha(\tau)} . \end{aligned} \quad (\text{III.67})$$

Equation (III.67) is the Boltzmann equation^{45,46} and $J_{\hat{n}_{\nu}}(\epsilon)$ was defined in equation (III.6). The Boltzmann equation describes a two-particle scattering process in which

6 OUTLOOK: FROM PRETHERMALIZATION TO THERMALIZATION

two occupied particles scatter into two unoccupied states. The delta function conserves energy for the scattering processes, and the interaction potential $|V_{\nu\beta\gamma\delta}|^2$ conserves quantum numbers, e.g., momentum for isotropic interactions. Thus, the Boltzmann equation redistributes the occupation numbers until they reach a steady state. It is established that the Fermi distribution governs the occupation numbers for the steady state,^{45,73,74}

$$N_\nu(\tau) = \frac{1}{1 + e^{-\beta(\epsilon_\nu - \mu)}} .$$

The Fermi distribution is the thermal distribution of a noninteracting system. Therefore, the Boltzmann equation thermalizes the distribution for $g \rightarrow 0$. Furthermore, the Boltzmann equation conserves the kinetic energy,^{73,74}

$$\begin{aligned} \lim_{g \rightarrow 0} \frac{\partial \langle \hat{H}_0 \rangle_\tau}{\partial \tau} &= -\pi \sum_{\alpha, \beta, \gamma, \delta} \epsilon_\alpha |V_{\alpha\beta\gamma\delta}|^2 \delta(\epsilon_\alpha + \epsilon_\beta - \epsilon_\gamma - \epsilon_\delta) \\ &\quad \times \left(N_\alpha(\tau) N_\beta(\tau) (1 - N_\gamma(\tau)) (1 - N_\delta(\tau)) \right. \\ &\quad \left. - N_\gamma(\tau) N_\delta(\tau) (1 - N_\alpha(\tau)) (1 - N_\beta(\tau)) \right) \\ &= 0 . \end{aligned}$$

The total particle number is conserved in the weak-correlation approximation and therefore in the Boltzmann equation as well. When we compute the time evolution with respect to the Boltzmann equation (III.67), then we can predict the long-time limit with these two constants. First, we compute the kinetic energy at the initial time. In the long-time limit, it will converge to a Fermi distribution. The parameters inverse temperature β and the chemical potential μ are determined from these two conserved quantities,

$$\langle \hat{N} \rangle_\infty = \sum_\alpha \frac{1}{1 + e^{-\beta(\epsilon_\alpha - \mu)}} , \quad \langle \hat{H}_0 \rangle_\infty = \sum_\alpha \frac{\epsilon_\alpha}{1 + e^{-\beta(\epsilon_\alpha - \mu)}} .$$

The kinetic energy has to lie below the infinite temperature ensemble. Otherwise, no appropriate Fermi distribution exists.

Weak interaction quenches are fully captured by the following two-step method.^{73,74} First, the occupation numbers are computed by the leading-order expansion during the prethermal regime. Second, we insert the occupation numbers of the prethermal plateau predicted from equation (III.5) at $\tau = 0$, and the Boltzmann equation computes the thermalization dynamics. In figure 67, we display an example of how the Boltzmann equation redistributes the occupation numbers. The main feature is the closing of the

III PRETHERMALIZATION INDUCED BY WEAK INTERACTIONS

gap at the Fermi energy.

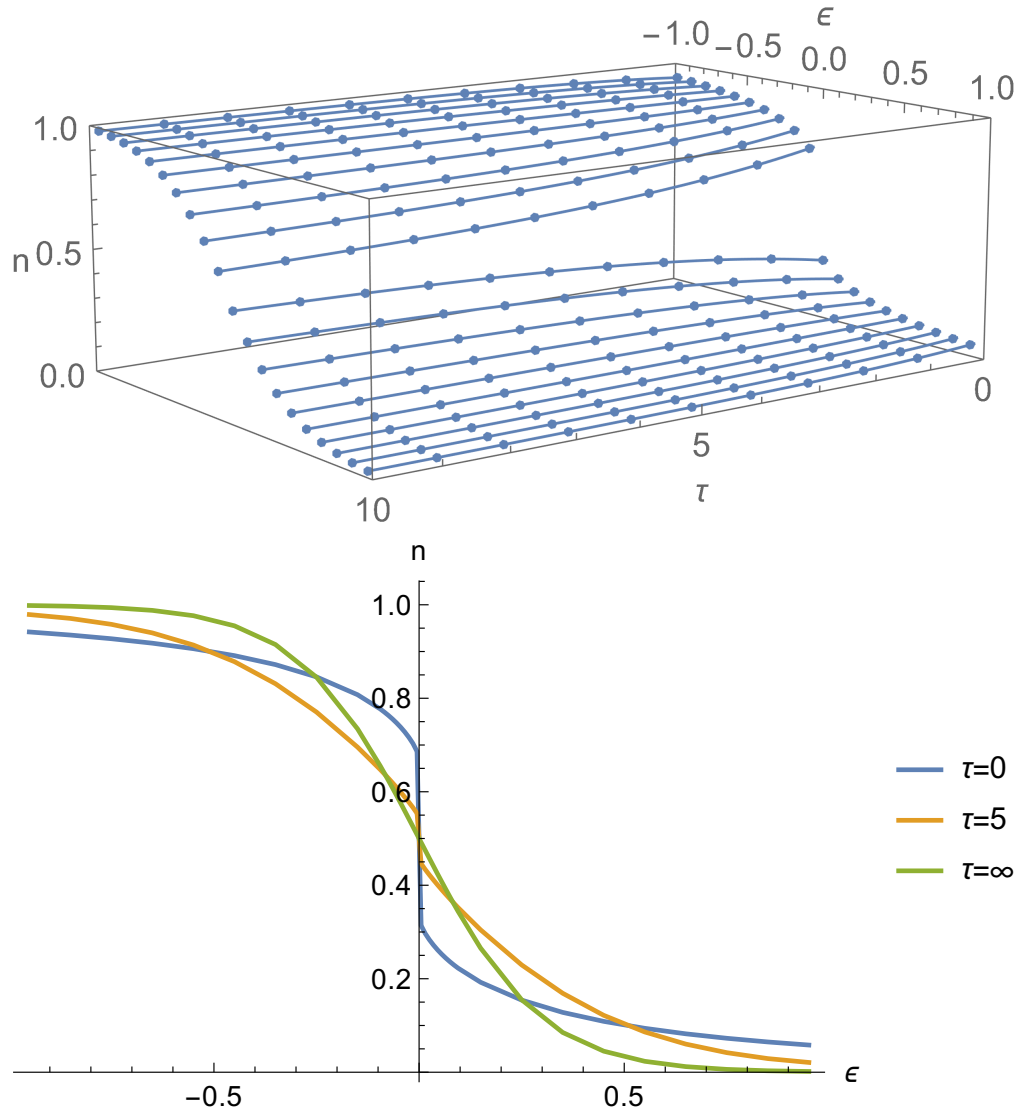


Figure 67: Evolution with Boltzmann equation for half-filled Hubbard model with infinite spatial dimension and semi-elliptic d.o.s. starting from the quench prethermalization plateau with $U = 1$

When the instantaneous occupation numbers are further away from the Fermi distribution, then the redistribution due the Boltzmann equation is more rapid. Therefore,

this scheme predicts faster thermalization for stronger interaction quenches. In the small U and late τ regime, the Fermi gap closes exponentially $\Delta n_F(t) \propto \exp(\gamma_F t)$ with $\gamma_F = O(U^4)$.⁷⁴ This method gives unphysical results when the interaction is larger than g_{crit} . We determine g_{crit} as the interaction strength, when the kinetic energy at $\tau = 0$ is equal to that of the infinite temperature ensemble,

$$E_0(T = \infty) = E_0(t = 0) + g_{\text{crit}}^2 E_{\text{kin}}^{(2)}(t = \infty) . \quad (\text{III.68})$$

DMFT found at $U_c^{\text{dyn}} = 3.2$ ¹¹⁹ the fastest thermalization after an interaction quench away from the uncorrelated ground state. For stronger quenches, collapse-and-revival oscillations characterize the dynamics and the gap at the Fermi surface closes at later times.¹¹⁹ Therefore, U_c^{dyn} marks the distinction point between two qualitatively different regimes of weak and strong interaction quenches. Equation (III.68) gives $U_{\text{crit}} = 3.189$ for this problem. The agreement of U_c^{dyn} and U_{crit} is surprisingly good. Therefore, we propose U_{crit} as an approximation to U_c^{dyn} .

b) Local in time formulation

In this outlook, we reformulate the weak-correlation approximation local in time. At the end of this subsection, we point out the benefits of the reformulation for future projects. Our general idea is to consider other of self-consistent quantities. We start from the equations of motions (III.63), which was deduced in the previous subsection a). It is free of approximations, and the new quantities are

$$\tilde{N}_\nu(t, \epsilon) = -g^2 \int_{-\infty}^{\infty} \frac{d\tau}{2\pi} e^{-i\epsilon(t-\tau)} \int_{t_{\text{ini}}}^t dt_2 \langle [\hat{H}_{1,I}(t_2), [\hat{H}_{1,I}(\tau), \hat{n}_\nu]] \rangle_{t_2} .$$

They are related to the time-derivative of the occupation numbers

$$\int d\epsilon \tilde{N}_\nu(t, \epsilon) = -g^2 \int_{t_{\text{ini}}}^t dt_2 \langle [\hat{H}_{1,I}(t_2), [\hat{H}_{1,I}(t), \hat{n}_\nu]] \rangle_{t_2} = \frac{\partial \langle \hat{n}_\nu \rangle_t}{\partial t} .$$

They are initially zero and follow the differential equation,

$$\frac{\partial \tilde{N}_\nu(t, \epsilon)}{\partial t} = -i\epsilon \tilde{N}_\nu(t, \epsilon) - g^2 \int_{-\infty}^{\infty} \frac{d\tau}{2\pi} e^{-i\epsilon(t-\tau)} \langle [\hat{H}_{1,I}(t), [\hat{H}_{1,I}(\tau), \hat{n}_\nu]] \rangle_t .$$

Now, we apply the weak-correlation approximation as in equation (III.64). It replaces the expectation value of the exact correlated state by a time-dependent uncorrelated state.

III PRETHERMALIZATION INDUCED BY WEAK INTERACTIONS

The new equations of motion are local in time. We depict them for a time-independent interaction ($\hat{H}_1(t) \rightarrow \hat{V}$),

$$\begin{aligned} \frac{\partial \tilde{N}_\nu(t, \epsilon)}{\partial t} &= -i\epsilon \tilde{N}_\nu(t, \epsilon) + g^2 J_{\hat{n}_\nu}(\epsilon) \Big|_{\langle \hat{n}_\alpha \rangle_{t_{\text{ini}}} \rightarrow \langle \hat{n}_\alpha \rangle_t} , \\ J_{\hat{n}_\nu}(\epsilon) &= \int_{-\infty}^{\infty} \frac{d\tau}{2\pi} e^{-i\epsilon\tau} \langle [\hat{V}, [\hat{V}_I(\tau), \hat{n}_\nu]] \rangle_{t_{\text{ini}}} , \\ \frac{\partial \langle \hat{n}_\nu \rangle_t}{\partial t} &= \int d\epsilon \tilde{N}_\nu(t, \epsilon) . \end{aligned} \tag{III.69}$$

If we compute the time-dependent interaction expectation value as

$$\langle \hat{V} \rangle_t = \langle \hat{V} \rangle_{t_{\text{ini}}} + ig \int_{t_{\text{ini}}}^t d\tau \langle [\hat{V}_I(\tau), \hat{V}_I(t)] \rangle_{t_{\text{ini}}} \Big|_{\langle \hat{n}_\alpha \rangle_{t_{\text{ini}}} \rightarrow \langle \hat{n}_\alpha \rangle_t} ,$$

then the energy expectation value is constant in time,

$$\frac{\partial \langle \hat{H}_0 \rangle_t}{\partial t} + g \frac{\partial \langle \hat{V} \rangle_t}{\partial t} = 0 .$$

The computation in the weak-correlation approximation can be executed in two ways. The first method is the evaluation of the Volterra integrodifferential equation (III.65). For times shortly after the uncorrelated state, we expect equation (III.65) to be efficient. With increasing time, the computational cost increases. The new second method is to evaluate the integrodifferential equation (III.69). For later times, we expect our new formalism to outperform the old one as the computational cost stays constant in time.

Furthermore, we may be able to find equilibrium “ensembles” in the weak-correlation approximation. These ensembles are described by a set of $\langle \hat{n}_\nu \rangle_t$ and $\tilde{N}_\nu(t, \epsilon)$ which have $\partial_t \langle \hat{n}_\nu \rangle_t = 0$. In the limit of $g \rightarrow 0$, these ensembles are governed by the Fermi distribution as equation (III.69) becomes the Boltzmann equation. Thus, they are equal to the thermal ensembles of the noninteracting system. For a finite g , we expect to obtain ensembles, which resemble thermal ensembles of a weakly correlated system.

As a future project, we propose to study equation (III.69) for the infinite-dimensional Hubbard model in equilibrium and nonequilibrium. The local-in-time formulation should be help to include initially interacting states, ramps, and electric field pulses.

IV Conclusion

We investigated a variety of different nonequilibrium protocols for systems close to an integrable point. We assumed a weak interaction strength g , which broke the integrability of the system. We investigated the expectation values of certain operators which correspond to physical observables. We explicitly computed the first nontrivial contribution from the expansion in g and predicted relaxation to a steady state, which is nonthermal in general. The further relaxation to the thermal state is not described by this method, but can be calculated self-consistently as discussed in subsection III.6.a).

We evaluated different terms in g depending on the operator and the nonequilibrium protocol, namely the zeroth-, first- or second-order terms. The different orders had distinct features, and thus we categorized the operators into different classes, resulting in zeroth-, first- or second-order observables. Generally, the classification of observable changes with the kind of nonequilibrium protocol and the system under investigation. For example, in chapter II, we computed the local density for a locally perturbed system. This was a zeroth-order observable. On the other hand, the double occupation was a first-order observable for the spatially homogeneous perturbations in chapter III. There, the mode occupation numbers were second-order observables.

In chapter II, we developed an efficient formalism to compute the Friedel oscillations after quenching the potential energy of a single site. We treated the model as noninteracting because we investigated a zeroth-order observable. The dynamics were fully determined by the local Green function of the initial translationally invariant system. When we represented the lattice in the shell-symmetric basis, the problem became effectively one-dimensional. If the impurity strength exceeded a critical value a localized eigenstate emerged. We computed this threshold for the Bethe and the hyper-cubic lattice. It was finite for higher dimensional systems and infinitesimally small for the simple chain and the square lattice. Hence, in these low-dimensional systems, every finite impurity potential induced a localized state. This is a fundamental difference between a low and a high-dimensional system. The single-particle states showed steady oscillations in the presence of the localized state, but canceled each other out for a many-particle state. Then, the density relaxed to a constant value, captured by a generalized Gibbs ensemble (GGE). If there was no localized eigenstate, the GGE was equal to the zero-temperature ensemble, and direct thermalization was observed. In absence of the localized state, there was an additional conservation law, and thermalization in a reduced Hilbert space was observed. We termed this phenomenon generalized thermalization.^{38,72} We observed an exact agreement of GGE and the long-time limit for the thermodynamic limit. The

IV CONCLUSION

deviation between GGE and long-time limit decreases for finite systems with their size.^{12, 13, 38, 72}

In chapter III, we investigated global homogeneous perturbations. There, the local density remained constant in time. Other local observables, e.g., the double occupation, were affected due to the local interactions. The first-order term of the mode occupation number vanished, and we classified them as second-order observables. The first-order observables' prethermalization plateau solely depended on the final Hamiltonian and was equal to equilibrium perturbation theory. The plateau value for second-order observables depended on the protocol. For the quench, it is twice the equilibrium correction.^{37, 73, 74} The finite ramping values lay between the quench value and the value of adiabatic switching, which is equal to the equilibrium correction. Generally, the plateau value is described by a GGE, and the constants of motion can be constructed by adiabatic dressing as discussed in subsection III.2.b).

We computed the expectation values for the Hubbard model in infinite spatial dimensions. There, the momentum conservation simplifies, and the problem is feasible but nonintegrable. Our equations of motions are more general than in previous work.^{73, 80, 84, 85} In addition, we appended an optional adiabatic switching process, which generalized the method to interacting initial states. Our results for quenches, ramps, and periodic driving were computed efficiently and not restricted to stroboscopic times. Furthermore, we successfully studied an electric field pulse hits a weakly interacting Hubbard system. The interaction strength was constant, and the eigenenergies of the noninteracting Hamiltonian changed due to the electric field. This problem was more challenging to evaluate, but allowed to describe the field nonperturbatively.

If we add small interactions, the system shifts away from the noninteracting integrable point, and relaxation to a thermal ensemble is expected. A mean-field description was derived in reference⁷⁵ predicting thermalization at the time scale of $\tau = t/g$ for local observables. On the other hand, mode occupation numbers as nonlocal observables thermalize due to quasiparticle scattering on the time scale $\tau = t/g^2$.⁴⁵⁻⁴⁷ Thus, the thermalization time scale should strongly depend on the observable.

There are different approaches to generate a stationary prethermal state. The two aspects of interest are the deviation from the thermal state on the one hand and its lifetime on the other hand. We may extend the thermalization time scale by decreasing g , so that the lifetime of the prethermalization plateau is prolonged. We found that the scaling is more favorable for global perturbations than for local ones. The deviation is

$O(g^0)$ for local and $O(g^2)$ for global perturbations. We conclude that local quenches should be as close to the integrable point as possible. This increases the lifetime, and the deviation from the thermal is not affected. For global perturbations, an intermediate g should be chosen because the impact must be strong enough to be detectable and the lifetime long enough to apply a measuring procedure. However, resonant photopumping can bypass the $O(g^2)$ scaling law for global perturbations. The resonance peak sharpens and heightens for weaker interactions. If we pump at the resonance frequency of the Drude peak, then the momentum distribution deviates more from its equilibrium value. The main obstacle is that the driving rate is multiplied by the small factor $\frac{E^2 e^2 a^2}{\hbar^2 \omega^2}$, which emerges from the second-order expansion in field strength.

We see two general directions for further progress. The first is the engineering of certain desirable features in prethermal states. This could elevate prethermal states to promising candidates for technological applications. The other is to further develop theoretical methods. More refined methods should cover the prethermalization and the thermalization time scale. This allows us to investigate the dynamic transition between these two regimes. We suggest focusing on the weak-correlation approximation to achieve this, which was introduced in subsection III.6.a). This approximation includes self-consistently arbitrary orders in interaction strength and continuously connects the two regimes of prethermalization and thermalization.

In conclusion, we presented a combination of analytical and numerical methods for the prethermal regime and applied it to the Hubbard model for various nonequilibrium protocols. we developed a general and efficient method, addressed several essential questions, and suggested further perspectives, so that this dissertation may serve as a comprehensive guide on the topic of prethermalization.

IV CONCLUSION

V Appendix

1 Evaluation of $a_3(b)$ and $a_4(b)$

In this appendix, we compute analytically the functions $a_3(b)$ and $a_4(b)$. They are first defined in equation (III.17). We introduce the generalized function

$$a_3(\alpha, \beta) = \int_0^\infty dx \int_0^\infty dy \int_0^\infty dz \delta(\alpha - (x + y + z)) \delta(\beta - (x^2 + y^2 + z^2)) .$$

We compute $a_4(b)$ by integrating over $a_3(\alpha, \beta)$,

$$a_4(\beta) = \int_0^\infty dx a_3(1 - x, \beta - x^2) . \quad (\text{V.1})$$

The easiest way to compute $a_3(\alpha, \beta)$ is to calculate the cut between a triangle with corner points $(\alpha, 0, 0)$, $(0, \alpha, 0)$ and $(0, 0, \alpha)$ with a sphere of radius $\sqrt{\beta}$ at the origin. We multiply the result by $(2\sqrt{3\beta})^{-1}$. The factor originates from the integration over the delta functions $\delta(\alpha - (x + y + z))$ and $\delta(\beta - (x^2 + y^2 + z^2))$,

$$a_3(\alpha, \beta) = \Theta(\alpha) \Theta(\alpha^2 - \beta) \Theta(3\beta - \alpha^2) \sqrt{3} \left(\frac{\pi}{3} - \Theta(2\beta - \alpha^2) \arccos \left(\frac{\alpha}{\sqrt{6\beta - 2\alpha^2}} \right) \right) .$$

We obtain $a_4(b)$ by evaluating the integral in equation (V.1). The arccos function we deform into a root by partial integration,

$$\frac{d}{dx} \arccos(x) = \frac{-1}{\sqrt{1-x^2}} \quad \text{for } -1 < x < 1 .$$

After respective shifts in the integration variable x , two types of integrals remain. They are found in a table of integrals,¹²⁰

$$\begin{aligned} R &= a + bx + cx^2 , \\ \Delta &= 4ac - b^2 , \\ \int \frac{dx}{\sqrt{R}} &= \frac{-1}{\sqrt{-c}} \arcsin \left(\frac{2cx + b}{\sqrt{-\Delta}} \right) \quad \text{for } [c < 0, \Delta < 0] , \\ \int \frac{dx}{x\sqrt{R}} &= \frac{1}{\sqrt{-a}} \arcsin \left(\frac{2a + bx}{x\sqrt{-\Delta}} \right) \quad \text{for } [a < 0, \Delta < 0] . \end{aligned}$$

V APPENDIX

Further simplifications lead to the solution,

$$a_4(x) = \begin{cases} \pi\sqrt{x - \frac{1}{4}} & \text{for } \frac{1}{4} < x < \frac{1}{3} \\ \frac{\pi}{\sqrt{3}} - \pi\sqrt{x - \frac{1}{4}} & \text{for } \frac{1}{3} < x < \frac{1}{2} \\ -\frac{\pi}{2\sqrt{3}} - \pi\sqrt{x - \frac{1}{4}} + a_{4h}(x) & \text{for } \frac{1}{2} < x < 1 \\ 0 & \text{else} \end{cases},$$

$$a_{4h}(x) = \sqrt{3} \arcsin\left(\frac{1}{\sqrt{6x-2}}\right) + 3\sqrt{x - \frac{1}{4}} \arcsin\left(\frac{\sqrt{1-6x+8x^2}}{3x-1}\right).$$

$a_4(b)$ is depicted together with $a_3(b)$ in figure 68. The functions $a_n(b)$ are nonzero only in the interval from $\frac{1}{n}$ to 1. They have positive values there. Furthermore, they are nonanalytic at the points $b = \frac{1}{m}$ with integers $1 \leq m \leq n$.

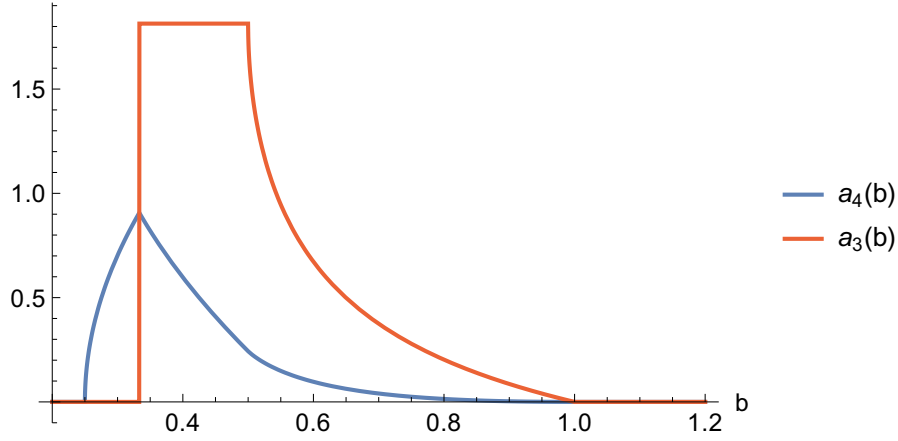


Figure 68: Graphical representation of $a_4(b)$ and $a_3(b)$

References

- ¹ M. Rigol, V. Dunjko, and M. Olshanii, *Thermalization and its mechanism for generic isolated quantum systems*, Nature **452**, 854 (2008).
- ² M. C. Bañuls, J. I. Cirac, and M. B. Hastings, *Strong and Weak Thermalization of Infinite Nonintegrable Quantum Systems*, Phys. Rev. Lett. **106**, 050405 (2011).
- ³ G. Biroli, C. Kollath, and A. M. Läuchli, *Effect of Rare Fluctuations on the Thermalization of Isolated Quantum Systems*, Phys. Rev. Lett. **105**, 250401 (2010).
- ⁴ P. Calabrese, F. H. L. Essler, G. Mussardo, A. D. Luca, M. Fagotti, J. Cardy, M. A. Cazalilla, M.-C. Chung, D. Bernard, B. Doyon, J.-S. Caux, L. Vidmar, M. Rigol, R. Vasseur, J. E. Moore, T. Langen, T. Gasenzer, J. Schmiedmayer, E. Ilievski, M. Medenjak, T. Prosen, and L. Zadnik, *Special issue on Quantum Integrability in Out of Equilibrium Systems*, Journal of Statistical Mechanics: Theory and Experiment **2016**, 064001 (2016).
- ⁵ M. Srednicki, *Chaos and quantum thermalization*, Phys. Rev. E **50**, 888 (1994).
- ⁶ J. M. Deutsch, *Quantum statistical mechanics in a closed system*, Phys. Rev. A **43**, 2046 (1991).
- ⁷ M. Rigol and M. Srednicki, *Alternatives to Eigenstate Thermalization*, Phys. Rev. Lett. **108**, 110601 (2012).
- ⁸ M. Rigol, V. Dunjko, and M. Olshanii, *Thermalization and its mechanism for generic isolated quantum systems*, Nature **452**, 854 (2008).
- ⁹ M. Srednicki, *The approach to thermal equilibrium in quantized chaotic systems*, Journal of Physics A: Mathematical and General **32**, 1163 (1999).
- ¹⁰ E. T. Jaynes, *Information Theory and Statistical Mechanics*, Phys. Rev. **106**, 620 (1957).
- ¹¹ R. Balian, *From Microphysics to Macrophysics: Methods and Applications of Statistical Physics*, volume Vol.1, Springer, Berlin, 1991.
- ¹² M. Rigol, A. Muramatsu, and M. Olshanii, *Hard-core bosons on optical superlattices: Dynamics and relaxation in the superfluid and insulating regimes*, Phys. Rev. A **74**, 053616 (2006).

REFERENCES

- ¹³ M. Rigol, V. Dunjko, V. Yurovsky, and M. Olshanii, *Relaxation in a Completely Integrable Many-Body Quantum System: An Ab Initio Study of the Dynamics of the Highly Excited States of 1D Lattice Hard-Core Bosons*, Phys. Rev. Lett. **98**, 050405 (2007).
- ¹⁴ H. Aoki, N. Tsuji, M. Eckstein, M. Kollar, T. Oka, and P. Werner, *Nonequilibrium dynamical mean-field theory and its applications*, Rev. Mod. Phys. **86**, 779 (2014).
- ¹⁵ L. E. Sadler, J. M. Higbie, S. R. Leslie, M. Vengalattore, and D. M. Stamper-Kurn, *Spontaneous symmetry breaking in a quenched ferromagnetic spinor Bose-Einstein condensate*, Nature **443**, 312 (2006).
- ¹⁶ S. Ritter, A. Öttl, T. Donner, T. Bourdel, M. Köhl, and T. Esslinger, *Observing the Formation of Long-Range Order during Bose-Einstein Condensation*, Phys. Rev. Lett. **98**, 090402 (2007).
- ¹⁷ A. Widera, S. Trotzky, P. Cheinet, S. Fölling, F. Gerbier, I. Bloch, V. Gritsev, M. D. Lukin, and E. Demler, *Quantum Spin Dynamics of Mode-Squeezed Luttinger Liquids in Two-Component Atomic Gases*, Phys. Rev. Lett. **100**, 140401 (2008).
- ¹⁸ T. Kinoshita, T. Wenger, and D. S. Weiss, *A quantum Newton's cradle*, Nature **440**, 900 (2006).
- ¹⁹ S. Hofferberth, I. Lesanovsky, B. Fischer, T. Schumm, and J. Schmiedmayer, *Non-equilibrium coherence dynamics in one-dimensional Bose gases*, Nature **449**, 324 (2007).
- ²⁰ S. Trotzky, Y.-A. Chen, A. Flesch, I. P. McCulloch, U. Schollwöck, J. Eisert, and I. Bloch, *Probing the relaxation towards equilibrium in an isolated strongly correlated one-dimensional Bose gas*, Nature Physics **8**, 325 (2012).
- ²¹ T. Kitagawa, A. Imambekov, J. Schmiedmayer, and E. Demler, *The dynamics and prethermalization of one-dimensional quantum systems probed through the full distributions of quantum noise*, New Journal of Physics **13**, 073018 (2011).
- ²² M. Gring, M. Kuhnert, T. Langen, T. Kitagawa, B. Rauer, M. Schreitl, I. Mazets, D. A. Smith, E. Demler, and J. Schmiedmayer, *Relaxation and Prethermalization in an Isolated Quantum System*, Science **337**, 1318 (2012).
- ²³ D. A. Smith, M. Gring, T. Langen, M. Kuhnert, B. Rauer, R. Geiger, T. Kitagawa, I. Mazets, E. Demler, and J. Schmiedmayer, *Prethermalization revealed by the*

- relaxation dynamics of full distribution functions*, New Journal of Physics **15**, 075011 (2013).
- ²⁴ O. Madelung, *Introduction to solid state theory*, Springer, New York, 1996.
- ²⁵ P. W. Anderson, *Basic notions of condensed matter physics*, Reading, Mass. : Addison-Wesley, 1997, The Advanced book program.
- ²⁶ P. Fulde, *Electron Correlations in Molecules and Solids*, Electron correlations in molecules and solids, Springer Berlin Heidelberg, 1995.
- ²⁷ G. Stefanucci and R. van Leeuwen, *Nonequilibrium Many-Body Theory of Quantum Systems: A Modern Introduction*, Cambridge University Press, 2013.
- ²⁸ J. Hubbard, *Electron Correlations in Narrow Energy Bands*, Proceedings of the Royal Society of London Series A **276**, 238 (1963).
- ²⁹ J. Kanamori, *Electron Correlation and Ferromagnetism of Transition Metals*, Progress of Theoretical Physics **30**, 275 (1963).
- ³⁰ M. C. Gutzwiller, *Effect of Correlation on the Ferromagnetism of Transition Metals*, Phys. Rev. Lett. **10**, 159 (1963).
- ³¹ H. Tasaki, *The Hubbard model - an introduction and selected rigorous results*, Journal of Physics: Condensed Matter **10**, 4353 (1998).
- ³² N. W. Ashcroft and j. a. Mermin, N. David, *Solid state physics*, New York Holt, Rinehart and Winston, 1976, Includes bibliographical references.
- ³³ F. Gebhard, *Metal—Insulator Transitions*, pages 1–48, Springer Berlin Heidelberg, Berlin, Heidelberg, 1997.
- ³⁴ M. Kollar and M. Eckstein, *Relaxation of a one-dimensional Mott insulator after an interaction quench*, Phys. Rev. A **78**, 013626 (2008).
- ³⁵ M. Rigol, *Breakdown of Thermalization in Finite One-Dimensional Systems*, Phys. Rev. Lett. **103**, 100403 (2009).
- ³⁶ M. Rigol, *Quantum quenches and thermalization in one-dimensional fermionic systems*, Phys. Rev. A **80**, 053607 (2009).
- ³⁷ D. M. Kennes, J. C. Pommerening, J. Diekmann, C. Karrasch, and V. Meden, *Small quenches and thermalization*, Phys. Rev. B **95**, 035147 (2017).

REFERENCES

- ³⁸ L. Vidmar and M. Rigol, *Generalized Gibbs ensemble in integrable lattice models*, Journal of Statistical Mechanics: Theory and Experiment **2016**, 064007 (2016).
- ³⁹ M. Mierzejewski and L. Vidmar, *Quantitative impact of integrals of motion on the eigenstate thermalization hypothesis*, Physical Review Letters **124**, 040603 (2020).
- ⁴⁰ T. Mori, T. N. Ikeda, E. Kaminishi, and M. Ueda, *Thermalization and prethermalization in isolated quantum systems: a theoretical overview*, Journal of Physics B: Atomic, Molecular and Optical Physics **51**, 112001 (2018).
- ⁴¹ J. Berges, *Introduction to nonequilibrium quantum field theory*, AIP Conf. Proc. **739**, 3 (2004).
- ⁴² S. Wall, D. Brida, S. R. Clark, H. P. Ehrke, D. Jaksch, A. Ardavan, S. Bonora, H. Uemura, Y. Takahashi, T. Hasegawa, H. Okamoto, G. Cerullo, and A. Cavalleri, *Quantum interference between charge excitation paths in a solid-state Mott insulator*, Nature Physics **7**, 114 (2011).
- ⁴³ Y. H. Wang, H. Steinberg, P. Jarillo-Herrero, and N. Gedik, *Observation of Floquet-Bloch States on the Surface of a Topological Insulator*, Science **342**, 453 (2013).
- ⁴⁴ S. Braun, J. P. Ronzheimer, M. Schreiber, S. S. Hodgman, T. Rom, I. Bloch, and U. Schneider, *Negative Absolute Temperature for Motional Degrees of Freedom*, Science **339**, 52 (2013).
- ⁴⁵ N. M. Hugenholtz, *Derivation of the Boltzmann equation for a Fermi gas*, Journal of Statistical Physics **32**, 231 (1983).
- ⁴⁶ L. Erdős, M. Salmhofer, and H.-T. Yau, *On the Quantum Boltzmann Equation*, Journal of Statistical Physics **116**, 367 (2004).
- ⁴⁷ J. Lukkarinen and H. Spohn, *Not to Normal Order—Notes on the Kinetic Limit for Weakly Interacting Quantum Fluids*, Journal of Statistical Physics **134**, 1133 (2009).
- ⁴⁸ J. Berges, A. Rothkopf, and J. Schmidt, *Nonthermal Fixed Points: Effective Weak Coupling for Strongly Correlated Systems Far from Equilibrium*, Phys. Rev. Lett. **101**, 041603 (2008).
- ⁴⁹ N. Strohmaier, D. Greif, R. Jördens, L. Tarruell, H. Moritz, T. Esslinger, R. Sensarma, D. Pekker, E. Altman, and E. Demler, *Observation of Elastic Doublon Decay in the Fermi-Hubbard Model*, Phys. Rev. Lett. **104**, 080401 (2010).

- ⁵⁰ M. Heyl, *Dynamical quantum phase transitions: a review*, Reports on Progress in Physics **81**, 054001 (2018).
- ⁵¹ K. Nasu, *Photoinduced Phase Transitions*, World Scientific Publishing Company, 2004.
- ⁵² H. Zeiger, J. Vidal, T. Cheng, E. Ippen, G. Dresselhaus, and M. Dresselhaus, *Theory for displacive excitation of coherent phonons*, Physical Review B **45**, 768 (1992).
- ⁵³ J. Friedel, *Metallic alloys*, Il Nuovo Cimento (1955-1965) **7**, 287 (1958).
- ⁵⁴ J. M. Zhang and Y. Liu, *Dynamical Friedel oscillations of a Fermi sea*, Phys. Rev. B **97**, 075151 (2018).
- ⁵⁵ J. M. Zhang and H.-T. Yang, *Sudden jumps and plateaus in the quench dynamics of a Bloch state*, EPL **116**, 10008 (2016).
- ⁵⁶ J. M. Zhang and H.-T. Yang, *Cusps in the quench dynamics of a Bloch state*, EPL **114**, 60001 (2016).
- ⁵⁷ W. Metzner and D. Vollhardt, *Correlated Lattice Fermions in $d = \infty$ Dimensions*, Phys. Rev. Lett. **62**, 324 (1989).
- ⁵⁸ A. Georges, G. Kotliar, W. Krauth, and M. J. Rozenberg, *Dynamical mean-field theory of strongly correlated fermion systems and the limit of infinite dimensions*, Rev. Mod. Phys. **68**, 13 (1996).
- ⁵⁹ P. Lunts, A. Georges, E. M. Stoudenmire, and M. Fishman, *Hubbard model on the Bethe lattice via variational uniform tree states: Metal-insulator transition and a Fermi liquid*, Phys. Rev. Research **3**, 023054 (2021).
- ⁶⁰ E. Economou, *Green's Functions in Quantum Physics*, Springer Series in Solid-State Sciences, Springer, 2006.
- ⁶¹ M. Sherafati and S. Satpathy, *Impurity states on the honeycomb and the triangular lattices using the Green's function method*, physica status solidi (b) **248**, 2056 (2011).
- ⁶² H. A. Bethe, *Statistical Theory of Superlattices*, Proceedings of the Royal Society of London Series A **150**, 552 (1935).
- ⁶³ G. D. Mahan, *Energy bands of the Bethe lattice*, Phys. Rev. B **63**, 155110 (2001).
- ⁶⁴ M. Eckstein, personal communication, 2004.

REFERENCES

- ⁶⁵ H. Yorikawa, *Density of states of the Cayley tree*, Journal of Physics Communications **2**, 125009 (2018).
- ⁶⁶ D. Aryal and S. Kettemann, *Complete solution of the tight binding model on a Cayley tree: strongly localised versus extended states*, Journal of Physics Communications **4**, 105010 (2020).
- ⁶⁷ M. Ostilli, C. G. Bezerra, and G. M. Viswanathan, *Spectrum of the tight-binding model on Cayley Trees and comparison with Bethe Lattices*, 2021.
- ⁶⁸ M. van den Berg, T. C. Dorlas, and V. B. Priezzhev, *The boson gas on a Cayley tree*, Journal of Statistical Physics **69**, 307 (1992).
- ⁶⁹ B. A. Lippmann and J. Schwinger, *Variational Principles for Scattering Processes. I*, Phys. Rev. **79**, 469 (1950).
- ⁷⁰ M. Eckstein, M. Kollar, K. Byczuk, and D. Vollhardt, *Hopping on the Bethe lattice: Exact results for densities of states and dynamical mean-field theory*, Phys. Rev. B **71**, 235119 (2005).
- ⁷¹ N. Blümer, *Mott-Hubbard Metal-Insulator Transition and Optical Conductivity in High Dimensions*, PhD thesis, Shaker Verlag, 2003.
- ⁷² A. C. Cassidy, C. W. Clark, and M. Rigol, *Generalized Thermalization in an Integrable Lattice System*, Phys. Rev. Lett. **106**, 140405 (2011).
- ⁷³ M. Moeckel and S. Kehrein, *Interaction Quench in the Hubbard Model*, Phys. Rev. Lett. **100**, 175702 (2008).
- ⁷⁴ M. Stark and M. Kollar, *Kinetic description of thermalization dynamics in weakly interacting quantum systems*, arXiv: **1308.1610v2** (2013).
- ⁷⁵ B. Bertini, F. H. L. Essler, S. Groha, and N. J. Robinson, *Prethermalization and Thermalization in Models with Weak Integrability Breaking*, Phys. Rev. Lett. **115**, 180601 (2015).
- ⁷⁶ J. Viti, J.-M. Stéphan, J. Dubail, and M. Haque, *Inhomogeneous quenches in a free fermionic chain: Exact results*, EPL (Europhysics Letters) **115**, 40011 (2016).
- ⁷⁷ M. Knap, A. Shashi, Y. Nishida, A. Imambekov, D. A. Abanin, and E. Demler, *Time-Dependent Impurity in Ultracold Fermions: Orthogonality Catastrophe and Beyond*, Phys. Rev. X **2**, 041020 (2012).

- ⁷⁸ P. W. Anderson, *Infrared Catastrophe in Fermi Gases with Local Scattering Potentials*, Phys. Rev. Lett. **18**, 1049 (1967).
- ⁷⁹ T. Morita, *Useful Procedure for Computing the Lattice Green's Function-Square, Tetragonal, and bcc Lattices*, Journal of Mathematical Physics **12**, 1744 (1971).
- ⁸⁰ M. Moeckel and S. Kehrein, *Real-time evolution for weak interaction quenches in quantum systems*, Annals of Physics **324**, 2146 (2009).
- ⁸¹ P. Reimann and L. Dabelow, *Typicality of prethermalization*, Physical review letters **122**, 080603 (2019).
- ⁸² S. A. Hamerla and G. S. Uhrig, *Dynamical transition in interaction quenches of the one-dimensional Hubbard model*, Phys. Rev. B **87**, 064304 (2013).
- ⁸³ S. A. Hamerla and G. S. Uhrig, *Interaction quenches in the two-dimensional fermionic Hubbard model*, Phys. Rev. B **89**, 104301 (2014).
- ⁸⁴ M. Moeckel and S. Kehrein, *Crossover from adiabatic to sudden interaction quenches in the Hubbard model: prethermalization and non-equilibrium dynamics*, New Journal of Physics **12**, 055016 (2010).
- ⁸⁵ M. Kollar, F. A. Wolf, and M. Eckstein, *Generalized Gibbs ensemble prediction of prethermalization plateaus and their relation to nonthermal steady states in integrable systems*, Phys. Rev. B **84**, 054304 (2011).
- ⁸⁶ M. Born and V. Fock, *Beweis des Adiabatenatzes*, Zeitschrift für Physik **51**, 165 (1928).
- ⁸⁷ T. Kato, *On the Adiabatic Theorem of Quantum Mechanics*, Journal of the Physical Society of Japan **5**, 435 (1950).
- ⁸⁸ J. E. Avron and A. Elgart, *Adiabatic Theorem without a Gap Condition*, Communications in Mathematical Physics **203**, 445 (1999).
- ⁸⁹ E. Canovi, M. Kollar, and M. Eckstein, *Stroboscopic prethermalization in weakly interacting periodically driven systems*, Phys. Rev. E **93**, 012130 (2016).
- ⁹⁰ C. P. Enz, *A Course on Many-Body Theory Applied to Solid-State Physics*, WORLD SCIENTIFIC, 1992.
- ⁹¹ A. Tokmakoff, *5.74 Introductory Quantum Mechanics II*, 2009, Massachusetts Institute of Technology: MIT OpenCourseWare.

REFERENCES

- ⁹² V. Jakšić and C.-A. Pillet, *Mathematical Theory of Non-Equilibrium Quantum Statistical Mechanics*, Journal of Statistical Physics **108**, 787 (2002).
- ⁹³ S. Iso, H. Ohta, and T. Suyama, *Secular terms in Dyson series to all orders of perturbation*, Progress of Theoretical and Experimental Physics **2018**, 083A01 (2018).
- ⁹⁴ E. Schrödinger, *Quantisierung als Eigenwertproblem*, Annalen der Physik **385**, 437 (1926).
- ⁹⁵ F. Schwabl, *Approximation Methods for Stationary States*, pages 203–214, Springer Berlin Heidelberg, Berlin, Heidelberg, 2007.
- ⁹⁶ W. Pauli, *Approximation Methods*, pages 79–102, Springer Berlin Heidelberg, Berlin, Heidelberg, 1980.
- ⁹⁷ H. G. Evertz and F. Maislinger, personal communication, 2020.
- ⁹⁸ N. Chandra, M. Kollar, and D. Vollhardt, *Nearly universal crossing point of the specific heat curves of Hubbard models*, Phys. Rev. B **59**, 10541 (1999).
- ⁹⁹ M. Eckstein, M. Kollar, and D. Vollhardt, *Isosbestic Points in the Spectral Function of Correlated Electrons*, Journal of Low Temperature Physics **147**, 279 (2007).
- ¹⁰⁰ M. Greger, M. Kollar, and D. Vollhardt, *Isosbestic points: How a narrow crossing region of curves determines their leading parameter dependence*, Phys. Rev. B **87**, 195140 (2013).
- ¹⁰¹ Microsoft, *Smoothstep at Microsoft Developer Network*, 2018.
- ¹⁰² J. Kessenich, *The OpenGL® Shading Language*, 2009.
- ¹⁰³ Unity Technologies, *Unity game engine SmoothStep documentation*.
- ¹⁰⁴ Advanced Micro Devices (AMD), *ATI R3x0 Pixel Shaders*, 2012.
- ¹⁰⁵ Wikipedia, *Smoothstep - Wikipedia, The Free Encyclopedia*, 2020, [Online; accessed 31-March-2020].
- ¹⁰⁶ M. Bukov, L. D’Alessio, and A. Polkovnikov, *Universal high-frequency behavior of periodically driven systems: from dynamical stabilization to Floquet engineering*, Advances in Physics **64**, 139 (2015).

- ¹⁰⁷ J. Skolimowski, A. Amaricci, and M. Fabrizio, *Misuse of the minimal coupling to the electromagnetic field in quantum many-body systems*, Physical Review B **101**, 121104 (2020).
- ¹⁰⁸ V. Turkowski and J. K. Freericks, *Nonlinear response of Bloch electrons in infinite dimensions*, Phys. Rev. B **71**, 085104 (2005).
- ¹⁰⁹ R. Peierls, *Zur Theorie des Diamagnetismus von Leitungselektronen*, Zeitschrift für Physik **80**, 763 (1933).
- ¹¹⁰ J. M. Luttinger, *The Effect of a Magnetic Field on Electrons in a Periodic Potential*, Phys. Rev. **84**, 814 (1951).
- ¹¹¹ E. Müller-Hartmann, *Correlated fermions on a lattice in high dimensions*, Zeitschrift für Physik B Condensed Matter **74**, 507 (1989).
- ¹¹² E. Müller-Hartmann, *The Hubbard model at high dimensions: some exact results and weak coupling theory*, Zeitschrift für Physik B Condensed Matter **76**, 211 (1989).
- ¹¹³ P. G. J. van Dongen and D. Vollhardt, *Exact mean-field Hamiltonian for fermionic lattice models in high dimensions*, Phys. Rev. Lett. **65**, 1663 (1990).
- ¹¹⁴ M. Eckstein and M. Kollar, *Theory of time-resolved optical spectroscopy on correlated electron systems*, Physical Review B **78**, 205119 (2008).
- ¹¹⁵ B. Bertini and M. Fagotti, *Pre-relaxation in weakly interacting models*, Journal of Statistical Mechanics: Theory and Experiment **2015**, P07012 (2015).
- ¹¹⁶ B. Bertini, F. H. L. Essler, S. Groha, and N. J. Robinson, *Thermalization and light cones in a model with weak integrability breaking*, Phys. Rev. B **94**, 245117 (2016).
- ¹¹⁷ M. Wais, M. Eckstein, R. Fischer, P. Werner, M. Battiato, and K. Held, *Quantum Boltzmann equation for strongly correlated systems: Comparison to dynamical mean field theory*, Physical Review B **98**, 134312 (2018).
- ¹¹⁸ F. R. Biebl and S. Kehrein, *Thermalization rates in the one-dimensional Hubbard model with next-to-nearest neighbor hopping*, Physical Review B **95**, 104304 (2017).
- ¹¹⁹ M. Eckstein, M. Kollar, and P. Werner, *Thermalization after an Interaction Quench in the Hubbard Model*, Phys. Rev. Lett. **103**, 056403 (2009).
- ¹²⁰ I. S. Gradshteyn and I. M. Ryzhik, *Table of Integrals, Series, and Products*, Academic Press, seventh edition, 2007.